

Institute of Theoretical Physics, Wrocław University  
of Science and Technology  
Department of Physics, University of Ottawa

---

# Optical Properties of Correlated Electrons in Two-Dimensional Crystals

---

Katarzyna Sadecka

PhD thesis prepared under supervision of  
Prof. Arkadiusz Wójs  
Prof. Paweł Hawrylak

© Katarzyna Sadecka, Wrocław, Poland, 2025



# Acknowledgements

*"Gratitude is when memory is stored in the heart and not in the mind."*

– Lionel Hampton.

Not a thousand words would be enough to fully capture my gratitude to everyone who supported me throughout this long and not always joyful journey. I trust that those close to my heart already know how much their encouragement, warm and kind words, and unwavering support meant to me during this process. With that in mind, I want to keep this expression of deep appreciation brief.

To my supervisors, Prof. Arkadiusz Wójs and Prof. Paweł Hawrylak, my collaborators, friends, and family, I want to say – though it might seem simple, yet in truth, with all my heart and in its deepest meaning – for everything,

*thank you.*



# Abstract

In recent years, two-dimensional (2D) van der Waals crystals, such as bilayer graphene (BLG) and transition metal dichalcogenides (TMDCs), have emerged as promising platforms for exploring novel physical phenomena at the atomic scale. These materials hold significant potential for advancing quantum technologies due to their unique electronic, optical, and mechanical properties. However, the role of many-body effects—particularly in the optical response—remains not fully understood. This dissertation develops and extends the theoretical framework for modeling electron–electron interactions in 2D crystals, focusing on the formation and evolution of neutral and charged excitonic complexes in 2D electron gases in these materials.

We investigate the optical properties of gated BLG quantum dots (QDs), where electrical gating opens an energy gap, transforming BLG into an electrically tunable semiconductor, with both electrons and holes confined by lateral gates. The BLG QDs are modeled using an atomistic tight-binding (TB) approach, enabling the calculation of confined electron and hole states in structures containing over a million atoms. Coulomb matrix elements and self-energies are computed to capture many-body effects, and the Bethe-Salpeter equation (BSE) is solved for both neutral and charged excitons. The resulting emission and absorption spectra provide insight into the optical response. Our results show that excitons in BLG QDs differ from those in conventional semiconductor QDs, with their energy tunable by voltage across a broad range, from terahertz (THz) to far infrared. The conservation of spin, valley, and orbital angular momentum leads to a fine structure in the excitons, characterized by a band of dark low-energy states. We also explore negatively charged excitons (trions), which, unlike in conventional QDs, exhibit a rich fine structure. Furthermore, we predict the existence of bright low-energy emission states and propose that temperature-dependent emission spectra could be used to extract the fine structure of the trion.

The research also explores the behavior of excitonic complexes in TMDC monolayers in high magnetic fields, focusing on how charge density and magnetic field strength influence the formation and properties of magnetoexcitons. Single layers of TMDCs, with their unique electronic and optical characteristics driven by strong spin-orbit coupling (SOC), broken inversion symmetry, and direct band gaps in the visible spectrum, provide a versatile platform for investigating many-body effects. A high magnetic field alters the energy spectrum of TMDC monolayers, leading to the formation of quantized Landau levels, along with spin and valley Zeeman splittings. These phenomena significantly enhance light-matter interactions and the optical response of the material. The electronic structure is first obtained through *ab initio* calculations, which are then used to parameterize a material-specific model incorporating both SOC and magnetic field effects. To study the optical response, the BSE is solved for magnetoexcitons—bound electron-hole pairs that form under the influence of the magnetic field. Special emphasis is placed on the impact of charge density and magnetic field strength on the excitonic spectrum, allowing for a detailed analysis of

many-body effects and the resulting optical transitions.

The electronic properties of MoSe<sub>2</sub>/WSe<sub>2</sub> heterostructures are also studied, with a focus on the effects of vertical electric fields on interlayer coupling and band alignment. *Ab initio* calculations reveal a type-II band alignment, with conduction band minima at the  $K$  and  $Q$  points in the Brillouin zone and valence band maxima at the  $K$  and  $\Gamma$  points. Analyzing the Kohn-Sham wave functions reveals the contributions from layer, spin, and orbital degrees of freedom. A TB model based on these results is then constructed to provide a deeper understanding of interlayer interactions. The effect of a vertical electric field is explored, showing that vertical gating allows control over the valleys' extrema and their occupancy. Additionally, the study investigates laterally gated QDs within the heterostructure, analyzing how a perpendicular electric field influences their energy spectrum. The results demonstrate that tuning the electric field enables selective control over the valley character of the QD states, localizing them in either the  $K$  or  $Q$  valleys, as evidenced by characteristic degeneracies and wave functions. This approach reveals the tunability of confined QD states, offering new strategies for controlling optical transitions in 2D material heterostructures.

Ultimately, this dissertation advances the understanding of the optical properties of 2D materials by providing a comprehensive theoretical description of many-body effects in excitons and trions. The insights gained into the control and manipulation of excitonic states—under the influence of electric and magnetic fields, interlayer coupling, and valley-dependent interactions—offer new perspectives for tuning optical responses at the nanoscale. These findings lay the groundwork for the development of next-generation optoelectronic and quantum devices, including exciton-based transistors, high-efficiency light emitters, and scalable quantum information platforms. By deepening our knowledge of correlated states in low-dimensional materials, this work contributes both to fundamental science and to the design of novel quantum materials and photonic technologies.

# Streszczenie

W ostatnich latach dwuwymiarowe (*ang. two-dimensional 2D*) kryształy van der Waalsa, takie jak dwuwarstwa grafenu (*ang. bilayer graphene BLG*) oraz dichalkogenki metali przejściowych (*ang. transition metal dichalcogenides TMDCs*), ukazały się jako obiecujące platformy do badania nowych zjawisk fizycznych w skali atomowej. Dzięki unikalnym właściwościom elektronicznym, optycznym i mechanicznym materiały te oferują istotny potencjał dla rozwoju technologii kwantowych. Jednym z kluczowych, choć wciąż nie do końca poznanych aspektów tych materiałów, są efekty wielociałowe — a w szczególności ich wpływ na odpowiedź optyczną. Niniejsza rozprawa rozwija i rozszerza teoretyczne możliwości modelowania oddziaływań elektron–elektron w materiałach dwuwymiarowych, koncentrując się na formowaniu i ewolucji neutralnych oraz naładowanych kompleksów ekscytonowych w dwuwymiarowych gazach elektronowych.

W pierwszej części pracy analizowane są właściwości optyczne kropki kwantowej opartej na dwuwarstwie grafenu z niezerową przerwą energetyczną indukowaną zewnętrznym polem elektrycznym. Takie pole przekształca BLG w półprzewodnik o regulowanej przerwie energetycznej, umożliwiając jednocześnie uwięzienie elektronów i dziur w potencjale generowanym przez boczne elektrody. BLG modelowany jest z wykorzystaniem atomistycznego podejścia — przybliżenia ciasnego wiązania (*ang. tight-binding TB*) — co pozwala na analizę struktur zawierających ponad milion atomów. Następnie obliczane są elementy macierzowe oddziaływań kulombowskich oraz energie własne stanów elektronowych i dziurowych, a także rozwiązywane jest równanie Bethe-Salpetera (*ang. Bethe-Salpeter equation BSE*) zarówno dla ekscytonów neutralnych, jak i naładowanych (trionów). Otrzymane widma emisji i absorpcji pozwalają na szczegółową analizę odpowiedzi optycznej. Pokazano, że ekscytony w takich układach istotnie różnią się od tych znanych z konwencjonalnych półprzewodnikowych kropek kwantowych — ich energie można precyzyjnie modulować za pomocą pola elektrycznego w zakresie od teraherców po daleką podczerwień. Zachowanie spinu, doliny i orbitalnego momentu pędu prowadzi do struktury subtelnej ekscytonów, w której pojawia się pasmo ciemnych stanów niskoenergetycznych. Przeanalizowano również ekscytony naładowane ujemnie, które — w odróżnieniu od trionów w konwencjonalnych półprzewodnikach — wykazują złożoną strukturę subtelną. Ponadto pokazano istnienie jasnych stanów niskoenergetycznych w widmie emisji oraz zaproponowano metodę identyfikacji struktury subtelnej poprzez analizę zmian widm emisji w funkcji temperatury.

W kolejnej części rozprawy zbadano zachowanie kompleksów ekscytonowych w monowarstwach TMDCs pod wpływem silnych pól magnetycznych, ze szczególnym uwzględnieniem wpływu gęstości ładunku i siły pola na formowanie się oraz właściwości magnetoekscytonów. Monowarstwy TMDCs, dzięki silnemu sprzężeniu spin–orbita, złamanej symetrii inwersyjnej oraz prostej przerwie energetycznej w zakresie światła widzialnego, stanowią wyjątkową platformę do badania efektów wielociałowych. Silne pole magnetyczne prowadzi do formowania dyskretnych poziomów Landaua oraz do spinowego i dolinowego rozszczepienia Zeemana, co znacząco modyfikuje oddziaływania

światło–materia i wpływa na odpowiedź optyczną materiału. Struktura elektronowa badanych monowarstw została najpierw wyznaczona metodami *ab initio*, a następnie wykorzystana do parametryzacji modelu uwzględniającego zarówno oddziaływanie spin-orbita, jak i efekty pola magnetycznego. Odpowiedź optyczna wyznaczana jest poprzez rozwiązanie równania Bethe-Salpetera dla magnetoekscytonów — związanych stanów elektron-dziura powstających pod wpływem pola magnetycznego. W szczególności analizowano wpływ gęstości ładunku oraz natężenia pola magnetycznego na spektrum ekscytonowe. Uzyskane wyniki podkreślają istotną rolę efektów wielociałowych w przejściach optycznych w monowarstwach TMDCs w silnych polach magnetycznych.

W ostatniej części pracy przeanalizowano właściwości elektronowe heterostruktury  $\text{MoSe}_2/\text{WSe}_2$ , ze szczególnym uwzględnieniem wpływu pola elektrycznego prostopadłego do warstw na oddziaływanie międzywarstwowe oraz charakter pasm energetycznych. Obliczenia *ab initio* wykazały, że badana heterostruktura jest typu II, z minimami pasma przewodnictwa w punktach  $K$  i  $Q$  oraz maksimami pasma walencyjnego w punktach  $K$  i  $\Gamma$  strefy Brillouina. Analiza funkcji falowych Kohn-Shama pozwoliła określić wkłady warstwowe, spinowe oraz orbitalne do struktury pasmowej. Na podstawie tych wyników skonstruowano model ciasnego wiązania, który umożliwia dokładny opis oddziaływań międzywarstwowych. Zbadano wpływ pola elektrycznego na położenie ekstremów dolinowych, co daje możliwość ich kontrolowanej manipulacji. Przeanalizowano również właściwości kropki kwantowej utworzonej w tej heterostrukturze, ze szczególnym uwzględnieniem wpływu pola na widmo energetyczne. Wyniki wskazują, że odpowiednia modulacja pola elektrycznego umożliwia selektywną kontrolę dolinowego charakteru stanów kropki, prowadząc do ich lokalizacji w dolinach  $K$  lub  $Q$ , co odzwierciedla się w degeneracjach energetycznych i charakterze funkcji falowych. Przedstawione podejście otwiera nowe możliwości sterowania przejściami optycznymi w heterostrukturach materiałów dwuwymiarowych.

Niniejsza rozprawa wnosi istotny wkład w zrozumienie właściwości optycznych materiałów dwuwymiarowych, oferując szczegółowy opis teoretyczny efektów wielociałowych w ekscytonach i tryonach. Uzyskane wyniki pokazują, że możliwe jest precyzyjne sterowanie stanami ekscytonowymi za pomocą pól elektrycznych i magnetycznych, oddziaływań międzywarstwowych oraz dolinowych. Wnioski płynące z tej analizy tworzą podstawy dla przyszłych zastosowań w zakresie nowoczesnych urządzeń optoelektronicznych i technologii kwantowych — w tym tranzystorów ekscytonowych, wydajnych źródeł światła czy skalowalnych platform do przetwarzania informacji kwantowej. Zrozumienie skorelowanych stanów w materiałach niskowymiarowych przyczynia się do pogłębienia wiedzy z zakresu fizyki podstawowej oraz dostarcza narzędzi do projektowania nowych materiałów i technologii fotonowych.

# Statement of Originality

This dissertation presents original research conducted under the supervision of Prof. Arkadiusz Wójs, Rector of Wrocław University of Science and Technology, Member of the Polish Academy of Sciences, and Member of Academia Europaea, as well as Prof. Paweł Hawrylak, Group Leader of the Quantum Theory Group and University Research Chair in Quantum Theory of Materials, Nanostructures, and Devices at the University of Ottawa. The research draws on theoretical and computational methods developed within the Quantum Theory Group, with significant independent implementation and methodological advancement forming the basis of the original results presented herein.

This work has benefited from scientific collaboration with the following researchers, each of whom contributed to specific aspects of the research:

- Dr. Marek Korkusiński (Security and Disruptive Technologies, National Research Council of Canada, Ottawa, Canada) – provided insightful guidance and contributed to the development and validation of the theoretical framework.
- Dr. Yasser Saleem (formerly at the Department of Physics, University of Ottawa, Canada) – collaborated on the modeling and interpretation of the electronic and optical properties of gated bilayer graphene quantum dots.
- Dr. Ludmiła Szulakowska (formerly at the Department of Physics, University of Ottawa, Canada) – participated in collaborative studies on transition metal dichalcogenide monolayers in high magnetic fields.
- Dr. Jarosław Pawłowski (Institute of Theoretical Physics, Wrocław University of Science and Technology, Poland) – assisted in the verification of theoretical predictions and provided guidance on electrostatic potential modeling within the MoSe<sub>2</sub>/WSe<sub>2</sub> heterostructure project.
- Dr. Maciej Bieniek (Institute of Theoretical Physics, Wrocław University of Science and Technology, Poland) – contributed to discussions and modeling strategies related to the electronic and optical properties of transition metal dichalcogenides.

The dissertation includes original theoretical and computational contributions to the field of excitonic physics in atomically thin materials. The work combines *ab initio* electronic structure methods with effective models based on tight-binding (TB) and massive Dirac Fermion (mDF) approximations, to investigate excitons, trions, and correlated electronic states in monolayer and bilayer graphene (BLG), transition metal dichalcogenide (TMDC) monolayers, TMDC-based heterostructures and their quantum dots (QDs).

A significant part of the research involved performing advanced Density Functional Theory (DFT) simulations using the ABINIT software, including structural relaxation, band structure analysis, and post-DFT wave function analysis. I used ABINIT to obtain electronic properties of TMDC monolayers and their heterostructures, including energy dispersion of electrons and holes, bandgaps, spin splittings, and valley degrees of freedom. I also developed custom post-processing

tools in Fortran to extract spin, orbital, and layer contributions from Kohn–Sham states. These methods were applied to understand spin and orbital characteristics of TMDC monolayers, as well as valley-dependent features and interlayer hybridization in MoSe<sub>2</sub>/WSe<sub>2</sub> heterostructures.

While DFT offers a detailed and accurate description of electronic states, it becomes computationally expensive for large systems, such as those with millions of atoms. To tackle this problem, I employed first-principles-based simplified methods, namely TB and mDF models. These models are useful for describing the electronic structure of large nanostructures and systems subjected to external fields, particularly when dealing with the complexity and size of materials like van der Waals heterostructures.

The TB model serves as an efficient, computationally feasible tool to describe the electronic structure of TMDC monolayers and their heterostructures. It captures essential electronic properties while significantly reducing the computational cost. I re-derived and implemented the existing TB models and extended them to incorporate features relevant to TMDC heterostructures, including SOC, valley splitting, and interlayer interactions. In particular, I derived the interlayer coupling elements to account for the hybridization between adjacent layers in type-II TMDC heterostructures. I tackled multidimensional minimization problems, refining the TB parameters to match the results from DFT calculations. This step was critical for ensuring that the TB model was capable of accurately predicting the electronic band structure and excitonic properties, even in large, complex systems.

In addition to the TB model, I also employed the mDF model, which is particularly suited for describing the low-energy electronic properties of materials such as TMDC monolayers. The mDF model provides an efficient approximation for the electronic structure, allowing to capture the spin-orbit interactions and valley splitting. I derived and applied the mDF model to study the electronic properties of TMDC monolayers, including the effects of magnetic fields on the Landau levels spectrum. The mDF model was further used for studying the behavior of excitons, trions and the 2D electron gas (2DEG) in TMDC monolayers in high magnetic fields.

By combining DFT, TB, and mDF models, this work provides a comprehensive framework for studying the electronic structure and optical properties of 2D materials and heterostructures. The efficiency of these models allows for the investigation of large-scale systems, which would be challenging to study using first-principles methods alone. The TB models developed in this work were further extended to study confined systems, specifically QDs composed of millions of atoms. These models can incorporate both lateral and vertical gate-defined confinement.

To go beyond mean-field approximations and capture the essential role of electron–electron interactions in 2D materials, I developed and applied a configuration interaction (CI) approach capable of treating many-body correlations in finite systems. Starting from single-particle states obtained via DFT, TB, or mDF models, I constructed a correlated many-body basis and implemented exact diagonalization of the full interacting Hamiltonian. To manage the exponential growth of the Hilbert space, I introduced project-specific approximations that ensured computational tractability while preserving the accuracy of the results. I also computed atomistic Coulomb matrix elements (CMEs), including both unscreened and screened interactions, and adapted screening models such as the Rytova–Keldysh formalism to various dielectric environments and material systems. Additionally, I implemented the methodology required to include magnetic fields in the treatment of correlated states.

Next, to describe excitonic effects, I derived and implemented the Bethe-Salpeter equation (BSE) for both neutral and charged excitons in 2D materials, enabling the computation of corre-

lated electron-hole eigenstates and wave functions. I performed exact diagonalization of the BSE Hamiltonian using single-particle energies and wave functions from atomistic models, along with computed atomistic CMEs, which allowed for a detailed analysis of exciton and trion spectra. This analysis included the effects of self-energies, direct (electron-hole attraction) and exchange (electron-hole repulsion) interactions, as well as their evolution in external electric and magnetic fields. I applied this framework to BLG QDs, TMDC monolayers, heterostructures, and their confined systems, demonstrating how exciton and trion energies can be tuned via gate voltages, offering nanoscale control over optical properties.

To investigate the optical properties of 2D materials, I developed a framework to describe light-matter interactions, focusing on both the  $\vec{p} \cdot \vec{A}$  and  $\vec{E} \cdot \vec{r}$  formalisms. For periodic systems, I employed the  $\vec{p} \cdot \vec{A}$  formalism, which uses Bloch wave functions to describe electronic states. For confined systems, such as QDs, I applied the  $\vec{E} \cdot \vec{r}$  approach, enabling the direct computation of dipole matrix elements and transition probabilities between discrete, spatially localized states. I also extended the  $\vec{p} \cdot \vec{A}$  framework to include magnetic fields, allowing for the analysis of magneto-optical effects. Additionally, I derived the optical selection rules for hexagonal lattices, providing a deeper understanding of the symmetry properties of 2D materials. Using this framework, I calculated the absorption and emission spectra of systems like BLG QDs and TMDC monolayers, employing Fermi's golden rule to determine the transition probabilities and analyze the optical response of these systems.

Throughout the dissertation, I independently developed the computational workflows, derived theoretical models, and implemented numerical schemes needed to address the physics of Coulomb-correlated quasiparticles in complex 2D materials and nanostructures. Together, these contributions form a cohesive and original body of research that deepens the theoretical understanding of excitonic behavior, tunability, and confinement in 2D crystals.

The core findings have been disseminated in peer-reviewed publications, listed below with the full authorship and contributions summarized:

1. **K. Sadecka**, *Inter- and Intralayer Excitonic Spectrum of MoSe<sub>2</sub>/WSe<sub>2</sub> Heterostructure*, Acta Physica Polonica A **141**, 2 (2022).

Transition metal dichalcogenide heterostructures enable the formation of excitons composed of electrons and holes in distinct layers. In this work I have studied the electronic and optical properties of a transition metal dichalcogenide MoSe<sub>2</sub>/WSe<sub>2</sub> heterostructure. Using a combination of density functional theory, the *ab initio*-based effective mass model and the Bethe-Salpeter theory I have investigated the spectra of inter- and intralayer excitons, predicting a rich variety of interlayer optical transitions.

2. M. Bieniek, **K. Sadecka**, L. Szulakowska, P. Hawrylak, *Theory of excitons in atomically thin semiconductors: tight-binding approach*, Nanomaterials **12**, 9, 1582 (2022).

I contributed to this work by investigating the electronic properties of 2D transition metal dichalcogenide crystals (both monolayers and their heterostructures) using the density functional theory methods and the *ab initio*-based tight-binding model. With the constructed models we studied the effect of interactions on the optical properties of transition metal dichalcogenide 2D crystals. The effect of the screening of electron-electron interactions was studied with the use of different screening models. Furthermore, we studied the topological properties of transition metal dichalcogenides manifested in the excitonic spectrum, the effect of a Berry curvature on the *2p* and *3d* shell splittings.

3. Y. Saleem, **K. Sadecka**, M. Korkusiński, P. Hawrylak, *Excitons in Gated Bilayer Graphene Quantum Dots*, Nano Letters **23**, 2998-3004 (2023).

It has been shown that bilayer graphene quantum dots can combine the ability to confine both electrons and holes of semiconductor self-assembled quantum dots with the tunability of laterally gated semiconductor quantum dots, thus enabling the existence of gate-tunable excitons in such nanostructures (Nano Lett. 23, 2998 (2023)). My contribution to this work consists of generating independently the single-particle and exciton states in gated bilayer graphene quantum dots. We demonstrated that excitons formed in such systems are highly tunable electrostatically with energies from terahertz to far infrared, thus being excellent candidates for quantum emitters in these ranges. Furthermore, we found a complex sequence of dark and bright low-energy states in the exciton, showing promise for optical memories. All this shows an extreme promise of bilayer graphene systems for nanooptics, which only begins to be tapped experimentally.

4. **K. Sadecka**, Y. Saleem, D. Miravet, M. Albert, M. Korkusiński, G. Bester, P. Hawrylak, *Electrically tunable fine structure of negatively charged excitons in gated bilayer graphene quantum dots*, Physical Review B **109**, 085434 (2024).

In this work I derived the effective Hamiltonian for trions in gated bilayer quantum dots, and used the CI tools to obtain the trion spectra. Similar to neutral excitons, trions are highly tunable electrostatically. I also found a rich fine structure of the charged exciton, in contrast to similar complexes in materials such as InAs.

5. M. Albert, D. Miravet, Y. Saleem, **K. Sadecka**, M. Korkusiński, G. Bester, P. Hawrylak, *Optical properties of gated bilayer graphene quantum dots with trigonal warping*, Physical Review B **110**, 155421 (2024).

When trigonal warping is included, the gated bilayer graphene energy spectrum is characterized by two  $K$ -valleys surrounded by three minivalleys with energies depending on the applied vertical electric field. My contribution to this study involves independent determination of the electronic and optical properties of gated bilayer graphene quantum dots with trigonal warping. Using the tight-binding approximation, we computed the single-particle bulk and quantum dot states and analyzed the influence of trigonal warping on the energy spectrum. I calculated the Coulomb matrix elements, solved numerically the Bethe-Salpeter equation and determined the effect of trigonal warping on the exciton spectrum.

6. D. Miravet, L. Szulakowska, M. Bieniek, **K. Sadecka**, M. Korkusiński, P. Hawrylak, *Theory of excitonic complexes in gated WSe<sub>2</sub> quantum dots*, Physical Review B **110**, 235404 (2024).

My contribution to this work involved determining independently the single-particle properties of gated WSe<sub>2</sub> quantum dots. We started with determining the electronic properties of WSe<sub>2</sub> monolayer using an *ab initio*-based tight-binding approach. Next, we computed the single-particle states of a gate-defined quantum dot within a computational box comprising over one million atoms, where holes are electrostatically confined and electrons repelled, or vice versa. These single-particle energies and wave functions were utilized to develop the Bethe-Salpeter theory of an interacting electron-hole pair. The confinement of excitons involves a delicate balance of the repulsion of electrons due to the gate potential with the attraction caused by the Coulomb interaction with a hole localized in the quantum dot. The absorption spectrum of such an exciton is the central result of this work.

7. **K. Sadecka**, M. Bieniek, P. E. Faria Junior, A. Wójs, P. Hawrylak, J. Pawłowski, *Electrically tunable MoSe<sub>2</sub>/WSe<sub>2</sub> heterostructure-based quantum dot*, Physical Review B **111**, 115421 (2025).

Van der Waals heterostructures allow for tuning their electronic properties beyond their monolayer counterparts. In this study I performed the density functional theory analysis of transition metal dichalcogenide heterostructures and created an *ab initio*-based tight-binding model comprehensively describing the properties of MoSe<sub>2</sub>/WSe<sub>2</sub> heterostructure, such as band nesting, the massive Dirac Fermion character of electrons, the degenerate *K* and *Q* conduction band valleys, as well as the tunability of the electronic structure of the system with an applied electric field showing that local gating enables control of valleys extrema and their occupancy. This model was further used to study a laterally gated MoSe<sub>2</sub>/WSe<sub>2</sub> heterostructure-based quantum dot and its tunability with applied vertical electric field.

8. **K. Sadecka**, M. Bieniek, P. E. Faria Junior, A. Wójs, P. Hawrylak, J. Pawłowski, *Electrically tunable Q-valley qutrit in MoSe<sub>2</sub>/WSe<sub>2</sub> heterostructure, in preparation*.

Following on our previous study, we propose a *Q*-valley qutrit in a gated MoSe<sub>2</sub>/WSe<sub>2</sub> heterostructure-based quantum dot.

9. **K. Sadecka**, M. Korkusiński, L. Szulakowska, P. Hawrylak, *Electronic and optical properties of 2D electron gas in transition metal dichalcogenide crystals in high magnetic fields, in preparation*.

This article involves determining the single-particle spectrum of 2D crystals in a high magnetic field, focusing on the example of a single layer of transition metal dichalcogenides. With the use of a massive Dirac Fermion model, we analyzed the optical selection rules, the effect of non-equivalent valleys and spin-orbit interactions. Finally, with the inclusion of interactions, we study the properties of magnetoexcitons as a function of electron density and determine the emission spectra.



# Thesis Chapter Summary

This dissertation investigates the electronic and optical properties of correlated electrons in atomically thin 2D van der Waals (vdW) materials, with particular emphasis on the role of electron–electron interactions. The research advances theoretical understanding of many-body phenomena in 2D systems and explores their potential for next-generation quantum and optoelectronic technologies. The thesis is organized into six chapters: an introductory chapter, a detailed methodology chapter, three research-focused chapters, and a concluding chapter, followed by an appendix containing supplementary material.

## *Chapter 1: Introduction*

The opening chapter provides a broad overview of low-dimensional vdW materials, emphasizing their electronic and optical characteristics as well as common fabrication techniques. It begins with a discussion of monolayer graphene and its relativistic electronic structure featuring massless Dirac fermions, followed by bilayer graphene (BLG), where an external electric field induces a tunable bandgap. Light–matter interactions in these systems are considered, including exciton formation, optical absorption, and their potential in quantum optics applications. The discussion then shifts to carbon-based quantum dots (QDs), covering both monolayer and bilayer graphene implementations, fabrication methods, and their quantum confinement and excitonic properties.

The second half of the chapter focuses on monolayer transition metal dichalcogenides (TMDCs), highlighting strong spin–orbit coupling, broken inversion symmetry, and direct optical band gaps. Excitonic complexes and their role in light–matter interactions are addressed, along with fabrication methods such as exfoliation and chemical vapor deposition. The chapter concludes by introducing advanced concepts including moiré superlattices, twistrionics, and the implementation of TMDC-based QDs, with emphasis on how reduced dimensionality and many-body interactions govern the optical response under external perturbations.

## *Chapter 2: Computational and Theoretical Methods*

This chapter outlines the computational and theoretical framework underpinning the thesis. It opens with electronic structure techniques, including density functional theory (DFT) and post-DFT approaches for extracting spin, orbital, and layer-resolved properties in 2D materials. Tight-binding (TB) models are introduced—using graphene as a case study—and applied to develop massive Dirac fermion (mDF) models tailored for BLG and TMDCs, with generalizations to systems in vertical magnetic fields.

Attention then turns to many-body physics. The configuration interaction (CI) method is introduced, alongside methods for computing Coulomb matrix elements and effective electron–electron interactions in reduced dimensions. Concepts such as static dielectric screening and the Rytova–Keldysh potential are discussed in detail.

Finally, the modeling of correlated excitonic states via the Bethe-Salpeter equation (BSE) is

presented, including an extension to charged excitons. Optical response modeling—both absorption and emission—is treated comprehensively, including the magnetic-field-induced phenomena and selection rules for light-matter coupling.

### *Chapter 3: Optical Properties of Bilayer Graphene Quantum Dots*

Electrostatically defined BLG QDs under a perpendicular electric field are studied here. The vertical field opens a tunable bandgap, turning BLG into a voltage-controlled semiconductor in which both electrons and holes are confined. An atomistic TB model is employed to describe QD structures containing over a million atoms. The combined influence of trigonal warping and gating on the low-energy spectrum is analyzed, revealing electrically controllable optical transitions.

Neutral excitonic states are explored by solving the BSE using Coulomb matrix elements derived from the atomistic basis. The absorption spectra exhibit a fine structure of confined excitons, with a dark band of low-energy states governed by angular momentum, spin, and valley conservation.

The chapter concludes with a study of negatively charged excitons (trions). Unlike in conventional semiconductor QDs, trions in BLG QDs display a rich fine structure. Emission spectra indicate the existence of bright low-energy states, which could be accessed via temperature-dependent photoluminescence. These findings position gated BLG QDs as a viable platform for tunable excitonic states and infrared quantum light sources.

### *Chapter 4: Magnetoexcitons in TMDC Monolayers*

Excitonic behavior in TMDC monolayers under strong perpendicular magnetic fields is the focus of this chapter. First-principles band structure calculations form the basis for constructing an effective mDF model that captures key features such as Landau quantization, spin-orbit coupling, and valley-specific behavior.

The optical response is examined by solving the BSE at varying carrier densities. Charge-density effects on the many-body corrections are analyzed, alongside the influence of magnetic fields on neutral and charged excitonic states. Both neutral and negatively charged magnetoexcitons (trions) are investigated across different regimes. In doped systems, optical emission spectra reveal pronounced many-body effects. These results highlight the tunability of magneto-optical phenomena in monolayer TMDCs.

### *Chapter 5: MoSe<sub>2</sub>/WSe<sub>2</sub> Heterostructure QDs*

Electronic and optical properties of vertically biased MoSe<sub>2</sub>/WSe<sub>2</sub> heterostructures and laterally gated QDs are analyzed in this chapter. Starting from *ab initio* calculations, the system is shown to possess a type-II band alignment with hybridized conduction-band states at the *Q*-valley. These insights inform the development of a TB model that captures spin, orbital, and interlayer coupling degrees of freedom.

The response to vertical electric fields is explored within both full and simplified TB frameworks. Field-induced changes to the band alignment and interlayer hybridization are compared with DFT benchmarks to validate the model.

Quantum confinement in gated heterostructure-based QDs is then investigated. The resulting confined states exhibit tunable valley and layer character, and their optical transitions can be modulated by external fields. These findings underscore the potential of MoSe<sub>2</sub>/WSe<sub>2</sub> heterostructure QDs for valleytronic and optoelectronic applications with electrical control.

### *Chapter 6: Conclusions*

The final chapter synthesizes the key findings of the thesis, highlighting how the developed

theoretical models offer a unified framework for understanding tunable excitonic complexes in atomically thin systems. Particular emphasis is placed on the role of external electric and magnetic fields, spatial confinement, and interlayer coupling in shaping excitonic spectra and enabling control over optical responses. The chapter also outlines future research directions, including the exploration of quantum-confined states in engineered 2D heterostructures and the design of optoelectronic platforms based on gate-tunable excitons and trions.

*Appendix*

Supporting material includes an analysis of topological effects in TMDCs, such as Berry curvature contributions manifested in the excitonic spectrum.



# Contents

<b>Acknowledgements</b>	<b>iii</b>
<b>Abstract</b>	<b>v</b>
<b>Streszczenie</b>	<b>vii</b>
<b>Statement of Originality</b>	<b>ix</b>
<b>Thesis Chapter Summary</b>	<b>xv</b>
<b>List of Acronyms</b>	<b>xxiv</b>
<b>1 Introduction to Low-Dimensional Crystals</b>	<b>1</b>
1.1 Graphene and Bilayer Graphene . . . . .	2
1.1.1 Electronic Structure and Relativistic Effects in Monolayer Graphene . . . . .	2
1.1.2 Electronic Structure of Bilayer Graphene: From Dirac Fermions to Bandgap Engineering . . . . .	4
1.1.3 Graphene and Bilayer Graphene Interacting with Light: Excitons, Absorption, and Quantum Optics . . . . .	5
1.2 Carbon-Based Quantum Dots . . . . .	7
1.2.1 Monolayer Graphene Quantum Dots . . . . .	7
1.2.2 Bilayer Graphene as a Platform for the Realization of Tunable Quantum Dots	8
1.2.3 Optical Properties of Graphene and Bilayer Graphene Quantum Dots . . . .	10
1.3 Transition Metal Dichalcogenides . . . . .	11
1.3.1 Electronic Properties of Transition Metal Dichalcogenide Monolayers . . . . .	13
1.3.2 Excitonic Effects in Monolayer Transition Metal Dichalcogenides . . . . .	14
1.4 2D Transition Metal Dichalcogenide Heterostructures . . . . .	17
1.4.1 Electronic Behavior of Transition Metal Dichalcogenide van der Waals Heterostructures . . . . .	18
1.4.2 Optical Properties of Transition Metal Dichalcogenide Bilayers . . . . .	20
1.4.3 Moiré Superlattices and Twistronics in Transition Metal Dichalcogenide Multi-Layers . . . . .	22
1.5 Transition Metal Dichalcogenide-Based Quantum Dots . . . . .	25
<b>2 Methodology</b>	<b>29</b>
2.1 Numerical Methods for the Electronic Structure Calculation . . . . .	30
2.1.1 Density Functional Theory . . . . .	31

2.1.2	Post-DFT Analysis of Spin, Orbital, and Layer Contributions . . . . .	34
2.1.2.1	Spin-Resolved Contribution to the Charge Density . . . . .	35
2.1.2.2	Orbital Contribution to the Charge Density . . . . .	35
2.1.2.3	Layer-Resolved Contributions for Heterostructure Systems . . . . .	36
2.1.3	Tight-Binding Method . . . . .	36
2.1.3.1	Tight-Binding Model on the Example of Graphene . . . . .	38
2.1.4	Massive Dirac Fermion Model and the Effect of Vertical Magnetic Field . . . . .	42
2.1.4.1	Massless Dirac Fermions in Graphene . . . . .	42
2.1.4.2	Massive Dirac Fermions in Transition Metal Dichalcogenides . . . . .	43
2.1.4.3	Inclusion of the Vertical Magnetic Field . . . . .	45
2.2	Electron-Electron Interactions in 2D Crystals . . . . .	47
2.2.1	Configuration Interaction Method . . . . .	48
2.2.2	Coulomb Matrix Elements in Atomistic Basis . . . . .	50
2.2.3	Electron-Electron Scattering Matrix Elements in an External Magnetic Field . . . . .	52
2.2.4	Effective Coulomb Interaction in Low-Dimensional Systems . . . . .	55
2.2.4.1	Static Screening . . . . .	55
2.2.4.2	Rytova-Keldysh Screening Model . . . . .	56
2.3	Theory of Correlated Electrons in 2D Crystals . . . . .	62
2.3.1	Single Electron-Hole Excitations. Bethe-Salpeter Equation . . . . .	63
2.3.2	Charged Excitons . . . . .	68
2.4	Optical Response of 2D Crystals . . . . .	69
2.4.1	Optical Selection Rules in Hexagonal Crystals via the $\vec{p} \cdot \vec{A}$ Formalism. Inclusion of a magnetic field . . . . .	69
2.4.1.1	Excitation with Circularly Polarized Light . . . . .	70
2.4.1.2	Transition Rates and Fermi's Golden Rule . . . . .	72
2.4.1.3	Optical Selection Rules for TMDC Monolayers at High Magnetic Fields . . . . .	73
2.4.1.4	Transition Rate with Magnetic Field . . . . .	76
2.4.2	Dipole Moments for Optical Transitions . . . . .	77
2.4.3	Optical Absorption . . . . .	78
2.4.4	Optical Emission . . . . .	78
<b>3</b>	<b>Optical Properties of Gated Bilayer Graphene Quantum Dots</b> . . . . .	<b>81</b>
3.1	Single-Particle Properties of Bilayer Graphene and BLG QDs . . . . .	82
3.1.1	Tight-Binding Model for Bulk Bilayer Graphene . . . . .	82
3.1.2	The Effect of Vertical Electric Field on the Electronic Structure of Bilayer Graphene . . . . .	86
3.1.3	Laterally Gated Bilayer Graphene Quantum Dot Spectrum . . . . .	87
3.1.4	Optical Transitions in a Bilayer Graphene Quantum Dot . . . . .	89
3.2	Electrically Tunable Neutral Excitons . . . . .	92
3.2.1	Excitonic Spectrum and the Effect of Coulomb Interactions . . . . .	92
3.2.2	Optical Absorption . . . . .	94
3.3	Negatively Charged Excitons . . . . .	96
3.3.1	Fine Structure of Trions in Bilayer Graphene Quantum Dots . . . . .	96
3.3.2	Optical Absorption . . . . .	100

3.3.3	Emission Spectrum . . . . .	101
3.4	Conclusions . . . . .	103
<b>4</b>	<b>Optical Response of Transition Metal Dichalcogenide Monolayers in High Magnetic Fields</b>	<b>105</b>
4.1	First Principles Electronic Structure . . . . .	106
4.2	<i>Ab Initio</i> -Based Massive Dirac Fermion Model . . . . .	108
4.2.1	Massive Dirac Fermion Model for MoS <sub>2</sub> Monolayer . . . . .	108
4.2.2	The Effect of an External Magnetic Field . . . . .	109
4.3	Coulomb Interaction and Self-Energy Correction . . . . .	112
4.4	Optical Emission as a Function of Finite Charge Density . . . . .	115
4.4.1	The Effect of the External Magnetic Field on the Spectrum of a Neutral Exciton . . . . .	115
4.4.2	Magnetoexcitons in the Presence of $\nu = 1$ Charge Density . . . . .	119
4.4.3	Negatively Charged $K'$ -Valley Magnetoexcitons . . . . .	123
4.5	Conclusions . . . . .	126
<b>5</b>	<b>Electrically Tunable MoSe<sub>2</sub>/WSe<sub>2</sub> Heterostructure-Based Quantum Dots</b>	<b>127</b>
5.1	<i>Ab Initio</i> Band Structure of MoSe <sub>2</sub> /WSe <sub>2</sub> . . . . .	128
5.2	Tight-Binding Model . . . . .	130
5.2.1	Orbital Basis . . . . .	131
5.2.2	Spinfull Monolayer Hamiltonian . . . . .	132
5.2.3	Heterostructure Hamiltonian . . . . .	137
5.2.4	Interlayer Coupling . . . . .	137
5.2.5	Full Tight-Binding Model Dispersion and Spin-Layer-Orbital Properties . . . . .	140
5.2.6	Simplified Tight-Binding Model . . . . .	141
5.3	Electric Field Effect . . . . .	144
5.3.1	Tight-Binding Model in Electric Field . . . . .	144
5.3.2	Effect of an Electric Field on the TMDC Heterostructure: DFT and Full TB Comparison . . . . .	146
5.3.3	Simplified TB Approach with Vertical Electric Field . . . . .	148
5.4	Electrically Tunable Laterally Gated Quantum Dot . . . . .	150
5.5	Conclusions . . . . .	152
	<b>Conclusions</b>	<b>155</b>
	<b>Appendix</b>	<b>157</b>
A	Topological Effects in TMDC Crystals . . . . .	157
	<b>Bibliography</b>	<b>159</b>



# Acronyms

$X^+$	positively charged exciton
$X^-$	negatively charged exciton
$X^0$	neutral exciton
<b>2D</b>	two-dimensional
<b>2DEG</b>	2D electron gas
<b>3D</b>	three-dimensional
<b>BLG</b>	bilayer graphene
<b>BSE</b>	Bethe-Salpeter equation
<b>BZ</b>	Brillouin zone
<b>CB</b>	conduction band
<b>CI</b>	configuration interaction
<b>CME</b>	Coulomb matrix element
<b>CVD</b>	chemical vapor deposition
<b>DE</b>	differential evolution
<b>DF</b>	Dirac Fermion
<b>DFT</b>	Density Functional Theory
<b>DME</b>	dipole matrix elements
<b>ED</b>	exact diagonalization
<b>FIR</b>	far infrared
<b>GGA</b>	generalized gradient approximation
<b>GO</b>	graphite oxide
<b>GS</b>	ground state
<b>hBN</b>	hexagonal boron nitride
<b>IQHE</b>	integer quantum Hall effect
<b>JDOS</b>	joint optical density of states
<b>LCAO</b>	linear combination of atomic orbitals
<b>LED</b>	light emitting diodes
<b>LL</b>	Landau level
<b>mDF</b>	massive Dirac Fermion
<b>NN</b>	nearest neighbour
<b>NNN</b>	next nearest neighbours
<b>PAW</b>	projector augmented wave
<b>PBE</b>	Perdew-Burke-Ernzerhof
<b>PL</b>	photoluminescence
<b>PP</b>	pseudopotential
<b>QD</b>	quantum dot

**QED** quantum electrodynamics  
**QHE** quantum Hall effect  
**RPA** random phase approximation  
**SOC** spin-orbit coupling  
**TB** tight-binding  
**TDSE** time-dependent Schrödinger equation  
**THz** terahertz  
**TMDC** transition metal dichalcogenide  
**TW** trigonal warping  
**UC** unit cell  
**VB** valence band  
**vdW** van der Waals  
**XC** exchange-correlation

# List of Figures

1.1	Atomic structure of TMDCs . . . . .	11
2.1	Post-DFT Analysis of Orbital Contributions . . . . .	34
2.2	Honeycomb lattice geometry . . . . .	39
2.3	CI configurations . . . . .	49
2.4	Schematic picture of the different dielectric environments of the TMDC mono- and bilayers . . . . .	60
2.5	One-pair excitation scheme . . . . .	64
2.6	Schematic representation of optical selection rules for TMDC monolayers . . . . .	73
3.1	Electronic properties of gated Bernal-stacked BLG . . . . .	83
3.2	Single-particle spectrum of a BLG QD . . . . .	89
3.3	Dipole moments for optical transitions . . . . .	91
3.4	Excitonic energy spectra of a BLG QD in different stages of including Coulomb interactions . . . . .	93
3.5	Optical absorption spectrum of an exciton in the gated lateral BLG QD . . . . .	95
3.6	Low-energy trion configurations . . . . .	97
3.7	BLG QD trion energy spectra in different stages of including Coulomb interactions . . . . .	98
3.8	Trion absorption and emission spectra . . . . .	101
3.9	Temperature-dependent trion emission for the low-energy states . . . . .	102
4.1	Transition metal dichalcogenides monolayer geometry . . . . .	106
4.2	DFT electronic structures of the MoS <sub>2</sub> monolayer. . . . .	107
4.3	wave functions coefficients for a TMDC monolayer in magnetic field . . . . .	109
4.4	Spin-resolved LLs spectrum as a function of the vertical magnetic field for a MoS <sub>2</sub> monolayer . . . . .	110
4.5	Scheme of optical selection rules for MoS <sub>2</sub> in the mDF model with an external magnetic field . . . . .	112
4.6	Schematic representation of the available spin configurations of a neutral exciton . . . . .	116
4.7	$X^0$ spectrum: spin-bright vs. spin-dark configurations with and without inter-valley coupling . . . . .	117
4.8	Exciton spectrum evolution for neutral $X^0$ in MoS <sub>2</sub> with magnetic field . . . . .	118
4.9	Schematic representation of the recombination process for a neutral exciton and an exciton interacting with $\nu = 1$ . . . . .	119
4.10	Schematic representation of the spin configurations of a neutral exciton interacting with $\nu = 1$ . . . . .	120

4.11	Exciton spectrum evolution for $X^{\text{inter}}$ interacting with $\nu = 1$ . . . . .	122
4.12	Spectrum of an intraband exciton . . . . .	123
4.13	Optical response of a MoS <sub>2</sub> monolayer in a magnetic field . . . . .	124
4.14	Single-valley trion spectrum for MoS <sub>2</sub> in an external magnetic field . . . . .	125
5.1	Geometry of the TMDC heterostructure in AB stacking . . . . .	128
5.2	DFT electronic structure and orbital composition of MoSe <sub>2</sub> /WSe <sub>2</sub> . . . . .	129
5.3	Electronic structure of MoSe <sub>2</sub> /WSe <sub>2</sub> in the TB model . . . . .	142
5.4	Effect of a vertical electric field on the electronic structure of MoSe <sub>2</sub> /WSe <sub>2</sub> in the full TB model . . . . .	147
5.5	Effect of a vertical electric field on the electronic structure of MoSe <sub>2</sub> /WSe <sub>2</sub> in the simplified TB model . . . . .	149
5.6	The effect of vertical electric field on the laterally gated MoSe <sub>2</sub> /WSe <sub>2</sub> -based QD . . . . .	151
A.1	Topological splitting of excitonic shells in a TMDC monolayer. . . . .	158

# List of Tables

1.1	Bandgap values for selected TMDCs in monolayer and bulk form . . . . .	13
1.2	Comparison of exciton properties in monolayer TMDCs encapsulated in hBN. . . . .	15
5.1	DFT orbital contributions for the MoSe <sub>2</sub> /WSe <sub>2</sub> heterostructure . . . . .	131
5.2	Slater-Koster parameters for the MoSe <sub>2</sub> /WSe <sub>2</sub> heterostructure in the TB model . . . . .	141
5.3	Orbital contributions from the full TB model . . . . .	143



# Chapter 1

## Introduction to Low-Dimensional Crystals

The discovery of low-dimensional vdW materials—one-atom-thick layers extracted from layered bulk crystals—has had a significant impact on condensed matter physics and materials science. These materials exhibit unique electronic, optical, and mechanical properties that arise from their reduced spatial dimensions. In-plane 2D quantum confinement of charge carriers leads to the emergence of new quantum states, while their thin, atomically flat structure exposes a large proportion of atoms at the surface, amplifying surface-related effects and interactions. These altered interactions with light, magnetic fields, and electric fields enable a range of applications, including ultra-sensitive detectors, high-performance transistors, and efficient light-emitting devices. As a result, these materials hold strong potential for constructing quantum computing, optoelectronic, and energy harvesting devices [1–7]. Compared to their three-dimensional (3D) counterparts, 2D crystals exhibit fundamentally different behaviors, driven by the confinement of charge carriers and the emergence of physical phenomena absent in bulk materials.

Among low-dimensional materials, graphene [1–4] and TMDCs [5–7] have garnered particular attention due to their distinctive properties. Graphene, a single layer of carbon atoms arranged in a honeycomb lattice, is characterized by high electrical conductivity and mechanical strength [3]. In contrast, band gaps of TMDCs materials, such as MoS<sub>2</sub>, MoSe<sub>2</sub>, WS<sub>2</sub> and WSe<sub>2</sub>, can be engineered [8–13], making them well-suited for optoelectronic applications. Recent advances in fabrication techniques, such as mechanical exfoliation and chemical vapor deposition (CVD), have enabled the precise creation of these materials, allowing for in-depth investigations of their properties. Moreover, combining graphene and TMDCs in vdW heterostructures has opened new possibilities for engineering their electronic and optical behaviors, with applications in flexible electronics and photodetectors [14].

This chapter begins with a discussion of *graphene* and *bilayer graphene* in Sec. 1.1. In Sec. 1.1.1, the *electronic properties* of monolayer graphene are explored, focusing on the relativistic behavior of charge carriers and its unique band structure. Sec. 1.1.2 shifts to *bilayer graphene*, where the electronic structure and the possibility of bandgap tuning through external fields and inter-layer interactions are examined. The *optical response* of both materials, including excitonic effects and quantum light-matter interactions, is examined in Sec. 1.1.3. In Sec. 1.2, the focus shifts to *carbon-based quantum dots*. *Graphene-based quantum dots* are discussed in Sec. 1.2.1. Particular attention is paid to the *optical characteristics* and *quantum confinement effects* of *bilayer graphene*

*quantum dots*, which are explored in Sections 1.2.2 and 1.2.3. The following section, Sec. 1.3, introduces *monolayer transition metal dichalcogenides*, highlighting their distinct *electronic properties* in Sec. 1.3.1 and strong *excitonic phenomena* in Sec. 1.3.2. Finally, in Sec. 1.4, we explore 2D *TMDC heterostructures*, where interlayer interactions give rise to novel *electronic* and *optical* behaviors, discussed in Sections 1.4.1 and 1.4.2. Furthermore, Sec. 1.4.3 extends the discussion into *moiré superlattices and twistrionics*. Together, these sections provide an overview of the key properties and applications of atomically thin materials, which are the focus of this thesis.

## 1.1 Graphene and Bilayer Graphene

Atomically thin carbon-based materials—such as graphene and BLG—have become important to the study of condensed matter physics due to their rich electronic properties and unique physical behavior. While both systems are based on carbon atoms arranged in a hexagonal lattice, they exhibit distinctly different electronic characteristics: monolayer graphene hosts massless Dirac Fermions (DFs) with a linear energy dispersion, whereas BLG features a tunable finite band gap and finite effective mass of charge carriers. This section introduces the fundamental properties, fabrication methods, and quantum phenomena associated with graphene, followed by an in-depth discussion of BLG, including its enhanced tunability and interaction effects. Additionally, the optical response of both materials, including excitonic phenomena and applications in quantum optics, will be explored.

### 1.1.1 Electronic Structure and Relativistic Effects in Monolayer Graphene

Graphene [1, 3], a single layer of carbon atoms arranged in a hexagonal lattice, has attracted significant interest in the scientific community due to its exceptional electronic, optical, and mechanical properties. The research journey into graphene is rooted in early theoretical studies. One of the pioneering works was conducted by Philip Russell Wallace in 1947 [15], at the National Research Council of Canada’s Chalk River Laboratory. Wallace analyzed the band structure of graphite by beginning with a single atomic layer—what we now call graphene. He accurately identified the hexagonal lattice composed of two inequivalent carbon sublattices and developed a TB model to describe its electronic properties. His calculations revealed that the conduction and valence bands of graphene meet at two distinct points in the Brillouin zone (BZ), showing that graphene is a semimetal with an unconventional linear energy dispersion. This characteristic mirrors the behavior of massless relativistic particles, as described by the Dirac and Weyl equations [16, 17], leading to the term “Dirac electrons” for graphene’s charge carriers. It was not until nearly 60 years later that these DFs were experimentally observed in graphene [18].

Thin layers of graphite—essentially graphene—were first observed by Hanns-Peter Boehm and colleagues in 1962 [19]. By chemically reducing graphite oxide (GO), they were able to isolate and identify individual carbon layers, some of which corresponded to single-layer graphene. Over the following decades, various attempts were made to obtain ultrathin carbon-based films, taking advantage of the weak vdW forces between layers that allow for mechanical separation. Both experimental and theoretical studies of graphite intercalation compounds highlighted the importance of domain structures and layer transformation kinetics, with models offering insight into interlayer decoupling mechanisms that would later inform approaches to bilayer and few-layer graphene iso-

lation [20]. A breakthrough came with the development of mechanical exfoliation using adhesive tape, a method refined by Andre’s Geim group. In 2004, Geim and co-workers successfully exfoliated thin graphite flakes and transferred them onto a silicon substrate configured as a transistor. They demonstrated ambipolar field-effect behavior in these graphene flakes under ambient conditions [1]. Perhaps the most striking outcome of their work was not just the isolation of graphene itself, but the discovery that it exhibited unexpectedly high conductivity even when exposed to air [2]. This indicated that the atomic layers retained their integrity and electrical performance in non-vacuum environments. In recognition of these achievements, the 2010 Nobel Prize in Physics was awarded to Andre Geim and Konstantin Novoselov for their “*groundbreaking experiments regarding the two-dimensional material graphene*” [1].

Various methods for fabricating graphene have since been developed, each offering unique advantages and challenges. The aforementioned mechanical exfoliation, pioneered by Geim and Novoselov [1], involves peeling layers from graphite using adhesive tape, producing high-quality graphene but with limited sample size for practical applications. Using CVD, graphene is grown by decomposing carbon precursors on metal surfaces such as nickel or copper, allowing control over layer number and enabling larger-area samples [21]. Thermal decomposition of SiC produces graphene by heating silicon carbide, yielding high-quality graphene with the advantage of patterned films and insulating substrates [22]. Finally, the reduction of GO involves chemically modifying graphite to create GO, which is then reduced to graphene through thermal or electrochemical processes. This provides a low-cost, scalable method, though typically at the expense of structural quality due to defects [23].

Although the possibility of isolating a monolayer of graphene was considered as early as the 1970s, it wasn’t until the 1990s—spurred by advances in carbon nanotubes and other 2D materials—that researchers began to fully appreciate graphene’s theoretical significance [24, 25]. Graphene’s linear energy dispersion relation, causing electrons to behave as massless DFs, gives rise to its high electrical conductivity and ultrafast charge transport. Charge carriers in graphene—both electrons and holes—exhibit a linear energy-momentum relationship, leading to relativistic quantum phenomena such as the quantum Hall effect (QHE) [2] and Klein tunneling [26]. By the early 2000s, predictions of the QHE in graphene [2, 3, 27–30] were experimentally confirmed. The integer quantum Hall effect (IQHE) in graphene differs significantly from that in conventional semiconductors with parabolic band dispersion. In graphene, Hall plateaus occur at half-integer filling factors, and the energy of the Landau levels (LLs) scales with the square root of the magnetic field. Additionally, the unit of quantized conductance in graphene is four times larger than that in traditional systems due to its fourfold degeneracy (accounting for spin and valley degrees of freedom). In 2007, the room-temperature observation of the IQHE in graphene was reported [3, 31], enabled by high-quality samples and large cyclotron gaps in the LL spectrum due to the relativistic nature of charge carriers.

Klein tunneling is a quantum mechanical phenomenon observed in graphene, where charge carriers can traverse high potential barriers with unexpectedly high efficiency. This counterintuitive behavior arises from the combination of linear dispersion and the chiral nature of massless DFs. At energies near the Dirac point, an energy barrier for electrons effectively becomes a potential well for holes, allowing wavefunction continuity and near-perfect transmission [26, 32]. This phenomenon, rooted in the relativistic-like motion of electrons—with an effective speed approximately 300 times lower than that of light in vacuum [33–35]—poses a challenge for electrostatic confinement using metallic gates, while enabling novel device architectures based on quantum tunneling.

Beyond its unique electronic properties, graphene exhibits material characteristics that make it highly attractive for practical applications in flexible electronics, sensors, and energy-efficient devices. Its thermal conductivity, measured to exceed 5300 W/m·K [36, 37], ensures efficient heat dissipation critical for nanoscale integration. Mechanically, graphene combines remarkable strength, elasticity, and structural stability; it possesses a Young’s modulus of approximately 1 TPa [37] and a tensile strength surpassing 130 GPa [38], all while maintaining flexibility and integrity under ambient conditions. This unique convergence of electrical, thermal, and mechanical performance positions graphene as a leading candidate for next-generation technologies, including wearable electronics, nanoelectromechanical systems, and energy-efficient computing platforms [2, 30]. Graphene’s superior conductivity, coupled with excellent thermal stability [39], also positions it as a promising material for nanoelectronics, energy storage systems, and optoelectronic devices. Its mechanical strength [38], along with intrinsic flexibility, makes it particularly attractive for flexible electronics, wearable sensors, and structural composites requiring enhanced strength-to-weight ratios.

Graphene’s unique electronic and mechanical properties highlight its potential for the next generation of quantum technologies, including quantum transistors and photonic devices. The ability to control its electronic states via external parameters, such as electric fields or mechanical strain, provides a versatile platform for quantum device engineering. Graphene is also widely explored for sensing applications, where its high surface area and electrical sensitivity allow for the detection of gases, biomolecules, and other analytes with exceptional precision [40, 41]. In quantum metrology, graphene-based sensors have been proposed for detecting weak magnetic fields, enabling advancements in quantum magnetometry and THz sensing [42–44]. Graphene’s role in quantum technologies is rapidly expanding, particularly in hybrid systems that integrate graphene with superconducting materials and other 2D heterostructures [45]. As research continues, advancements in fabrication techniques and theoretical understanding will ensure that graphene remains a key material in the development of next-generation electronic and quantum devices.

Despite its many advantages, several challenges remain in the practical implementation of graphene-based technologies. Large-scale synthesis of high-quality graphene with uniform properties remains difficult, especially for applications requiring precise control over electronic behavior. Additionally, while the high mobility of charge carriers in graphene is advantageous, its intrinsic lack of a bandgap limits its suitability for certain electronic devices, such as digital transistors. Research efforts are focused on overcoming this limitation through the application of external electric fields, chemical functionalization, and heterostructure engineering with other 2D materials [4, 29, 46–48].

### 1.1.2 Electronic Structure of Bilayer Graphene: From Dirac Fermions to Bandgap Engineering

While graphene’s impressive properties make it a versatile material for many applications, one of its main limitations is the absence of a band gap. Since in its pristine form graphene behaves as a gapless semimetal, its use in digital electronics—where a controllable band gap is essential for switching behavior—is limited. To overcome this limitation, one can vertically stack two graphene layers, creating bilayer graphene (BLG) [1]. In the most stable configuration, known as AB (Bernal) stacking, the atoms of the A sublattice in the top layer align with the B sublattice atoms in the bottom layer, while the remaining atoms lie above the centers of hexagons. The addition of the

second layer introduces interlayer coupling absent in monolayer graphene. This coupling removes the linear dispersion near the Dirac points, resulting in a low-energy band structure described by massive chiral Fermions with approximately quadratic dispersion [4]. Although pristine BLG remains gapless at the Fermi level, its electronic properties differ significantly from those of monolayer graphene, making it a valuable platform for further band gap engineering.

The application of an external electric field can open an energy gap in BLG, and importantly, the magnitude of this gap can be continuously tuned by adjusting the field strength [46, 47, 49–53]. This tunability marks a significant advantage over monolayer graphene, as it allows BLG to function as a semiconducting material with a controllable band gap. It has important implications for various electronic applications, particularly in low-power and high-performance devices. Unlike conventional semiconductors, which have a fixed bandgap, BLG allows for dynamic control of its electronic states. This makes BLG highly suitable for designing logic devices, infrared photodetectors, and tunable electronic circuits [54]. Furthermore, the interlayer coupling in BLG gives rise to significant interactions between carriers confined on different layers, which play a key role in emergent quantum phenomena such as excitonic condensation and correlated insulating phases [53, 55]. These properties position BLG as a promising material for next-generation quantum electronics and other advanced technological applications.

Beyond its electronic versatility, BLG maintains graphene’s impressive mechanical and thermal performance [4]. Although the two layers are bound by relatively weak vdW forces, the interlayer interaction adds structural stability without compromising flexibility. The material remains stiff, with a Young’s modulus close to 1 TPa, and continues to exhibit high thermal conductivity—measured above 2000 W/m·K—which is important for heat dissipation in electronic devices. This combination of strength, flexibility, and thermal efficiency makes BLG a strong candidate for flexible electronics, high-speed transistors, and other nanoscale technologies.

BLG additionally exhibits strong coupling between the electronic states of its layers, leading to many-body effects such as valley and spin polarization, exciton formation, plasmons, and topological phases [48, 56–62]. These effects are important for a variety of applications, and the strong light-matter interactions in BLG make it particularly promising for optoelectronics. A more detailed discussion of the optical properties and potential device applications will follow in the next subsection.

Interestingly, BLG can be integrated into hybrid systems with other 2D materials such as hexagonal boron nitride (hBN) and TMDCs, enabling the engineering of new material phases with enhanced functionalities for quantum and electronic applications [51, 53]. By stacking BLG with materials such as TMDCs, graphene oxide, or hBN, researchers can create heterostructures that exhibit emergent properties not present in individual layers. These heterostructures hold the potential for creating more efficient transistors, sensors, and flexible electronic devices, as well as exploring novel quantum effects that arise from the interactions between different 2D materials [45].

### 1.1.3 Graphene and Bilayer Graphene Interacting with Light: Excitons, Absorption, and Quantum Optics

In addition to its impressive electronic and mechanical properties, graphene exhibits unique optical properties, making it a promising material for optoelectronic applications. While bulk graphene has no bandgap, graphene nanoribbons can exhibit a tunable bandgap, ranging from 0 eV up to values comparable to that of benzene, depending on their width. This tunability allows

graphene nanoribbons to absorb light across a broad portion of the solar spectrum [63]. Furthermore, despite being only a single atomic layer thick, graphene absorbs approximately 2.3–2.4% of incident light uniformly across the visible and infrared spectrum—a value resulting from its gapless linear dispersion and universal optical conductivity [64, 65]. Notably, this absorption remains nearly unaffected by excitonic effects in the low-energy regime due to the vanishing joint density of states near the Dirac point [66]. This intrinsic optical response, combined with high electrical conductivity, enables a range of applications in transparent conductive films, broadband photodetectors, and optical modulators [67, 68]. Additionally, the tunability of graphene’s electronic structure provides a pathway for engineering light–matter interactions, particularly in relation to excitonic phenomena [69, 70].

The addition of a second graphene layer markedly alters the material’s optical behavior. In BLG, excitons begin to play a more prominent role, particularly under an applied electric field. While early studies focused on single-particle models [55, 71], later works also incorporated electron-hole interactions [66, 72], revealing that excitonic effects, though negligible at low energies in intrinsic BLG, become significant when a bandgap is introduced [58, 59, 73–76]. In this context, the optical response shows tunable excitonic features, with resonances predicted both near the Dirac point and in the ultraviolet range [3, 48, 66, 77]. These observations highlight the relevance of many-body interactions for understanding and engineering the optoelectronic properties of BLG.

The electronic band structure of BLG gives rise to excitonic behavior that significantly differs from semiconductors such as GaAs. In 2010, Cheol-Hwan Park and Steven G. Louie [57] employed many-body *ab initio* calculations using the GW–Bethe-Salpeter formalism and demonstrated that BLG can support bound excitonic states. This behavior is driven by the peculiar “one-dimensional” joint optical density of states (JDOS) and a continuously tunable bandgap in biased BLG. The study revealed that the exciton properties—such as level degeneracy and optical selection rules—are governed by pseudospin effects and Berry phase phenomena, making them fundamentally different from those of a 2D hydrogen atom. Moreover, the binding energy of these excitons is tunable with an external bias, ranging from zero to several tens of millielectronvolts under laboratory conditions. It was also predicted that the optical response is dominated by bound excitons, with a distinct absorption spectrum characterized by a single symmetric peak, which contrasts with the typical interband transition behavior. Notably, Park and Louie identified two bright excitonic states in the low-energy absorption spectrum, arising from transitions between nearly parallel conduction and valence bands near the  $K$  and  $K'$  points. This finding challenges the conventional assumption that strong excitonic features require a significant bandgap and highlights the importance of band nesting and electron-hole correlations in modifying the optical response of BLG. These theoretical predictions were later supported by experimental work from Long Ju *et al.* [48], who used photocurrent spectroscopy to observe two distinct excitonic absorption peaks in gated BLG. Their results matched the predicted excitonic signatures. The tunability of exciton binding energies via electrostatic gating was also confirmed.

In 2014, a microscopic study by Faris Kadi and Ermin Malic [78] investigated the optical properties of Bernal-stacked BLG, with particular emphasis on the momentum dependence of both optical and Coulomb matrix elements. Using a density matrix formalism combined with TB wave functions, they identified key features in the absorption spectrum: a distinct low-energy absorption peak originating from cross transitions at the Dirac point, and two closely spaced ultraviolet peaks associated with interband transitions near the saddle points of the BZ. Their work also highlighted the role of the carrier-light coupling element in governing optical selection

rules and transition strengths. Importantly, they demonstrated that Coulomb interactions lead to significant energy renormalizations and promote the formation of electron-hole pairs at the saddle points, offering insight into the complex excitonic landscape of BLG and its implications for optoelectronic applications.

Additional theoretical studies [79, 80] further validated the presence and tunability of low-energy excitons in BLG, highlighting its potential for optoelectronic and photonic applications. By modulating interlayer asymmetry, dielectric environment, and carrier doping, excitonic resonances can be precisely engineered, enabling electrically switchable light-matter interactions in the infrared and terahertz regimes. This tunability has significant implications for quantum optoelectronics, including the development of gate-controlled quantum light sources such as single-photon emitters and entangled photon pair generators [77, 81]. Furthermore, graphene-based photodetectors and modulators leverage these properties to achieve high-speed, broadband performance [67, 82, 83], positioning BLG as a promising platform for next-generation tunable infrared and terahertz photonic devices [84, 85].

The unique properties of BLG make it an ideal platform for studying a range of quantum effects. The gate-tunability enables the exploration of gate-dependent interband transitions, exciton formation [86], and gate-induced insulating states [46, 47, 51–53, 86], all of which are of interest for the development of quantum technologies. Additionally, the valley-dependent Berry phase in BLG [87, 88], a hallmark feature of this material, leads to effects not typically observed in conventional semiconductors [89]. Ongoing research into the excitonic properties of BLG, especially when integrated with other vdW materials such as hBN and TMDCs, is likely to uncover novel optical phenomena, particularly in the domain of strong light-matter interactions. This could pave the way for significant advancements in optoelectronics, photonic quantum technologies, and tunable light-matter interactions [87, 90, 91].

## 1.2 Carbon-Based Quantum Dots

Nanostructures that exhibit confinement in both in-plane directions are called quantum dots (QDs) [85, 92–94]. Over the years, QDs—both in conventional semiconductor materials [95–100] and in 2D materials like graphene [64, 69, 70, 84, 85, 101–110] and BLG [56, 111–120]—have attracted significant attention for their unique electronic and optical properties.

Semiconductor QDs, including those formed by self-assembly or lateral gating, are key components in applications like light emission, detection, and coherent control of excitons. While laterally gated QDs provide high tunability of electronic properties, they are limited to confining only one type of charge carrier (either electrons or holes). Self-assembled QDs, in contrast, confine both types of carriers simultaneously, but their size, shape, and electronic properties are defined by growth conditions and are difficult to tune once the dots are created [121–128].

### 1.2.1 Monolayer Graphene Quantum Dots

Among the various material platforms, graphene is of particular interest due to its unique electronic and optical properties. Graphene-based QDs provide an alternative to conventional semiconductor systems. Quantum confinement in graphene QDs leads to discrete electronic states that are not present in bulk graphene, allowing for control over charge, spin, and valley degrees of freedom [48, 70, 129]. This makes these dots promising candidates for qubits in quantum

computing [58, 70, 130], with graphene’s long spin coherence times further enhancing their potential for spintronic and valleytronic quantum applications [3, 29, 70, 86].

The inherent gapless band structure of graphene presents challenges for practical applications like switching devices, as the current cannot be fully turned off. To address this, reducing graphene’s lateral dimensions to the QD regime leads to the emergence of a bandgap due to quantum confinement effects. This size-dependent energy gap transforms graphene from a semimetal into a semiconductor [63]. In particular, graphene nanoribbons and graphene QDs have garnered significant interest due to the enhanced electronic tunability stemming from these confinement effects [85].

Multiple fabrication strategies have been developed to realize these structures [70, 108, 131–133]. Chemical synthesis provides a bottom-up approach to graphene QDs comprising several hundred atoms [131, 133]. However, electronic and optoelectronic applications often require QDs with larger sizes and precise control over shape and edge termination. In such cases, top-down techniques, including those involving atomic force microscopy, offer promising alternatives [132]. Transport measurements on such structures have revealed Coulomb blockade phenomena, and analysis of the gate-dependent oscillations has confirmed the presence of extended QDs beneath the electrode regions.

The role of edge termination in graphene QDs has also been extensively studied. It has been demonstrated that edge structure strongly influences the electronic and optical properties [134–136]. In particular, graphene QDs with zigzag edges can host edge-localized states that collapse into a degenerate shell at the Fermi level [134, 137–140]. The degeneracy of this shell has been linked to the imbalance between the two graphene sublattices [137]. Triangular graphene QDs, which naturally support such degeneracies, have been a focal point of theoretical studies [134, 137, 140]. For half-filled degenerate shells in triangular graphene QDs, the ground state has been shown to feature spin-polarized edges and a finite magnetic moment that scales with the degree of degeneracy [137, 138].

Quantum confinement effects in graphene QDs become particularly significant for diameters below 100 nm [141]. In this regime, Coulomb blockade peak oscillations with irregular spacings have been observed, consistent with the predictions for chaotic Dirac billiards. Theoretical studies by Patrik Recher and Björn Trauzettel have further predicted an exponential dependence of the energy gap on the dot diameter for DFs [142]. In few-nanometer-scale QDs with well-defined edges, scanning tunneling microscopy (STM) has revealed high-symmetry standing wave patterns [143], in agreement with TB and DFT calculations. Jaakko Akola *et al.* have demonstrated the emergence of shell and supershell structures in the energy spectra of both circular and triangular QDs [144]. According to their results, triangular QDs with edge lengths of at least  $\sim 40$  nm are required to resolve the first supershell. Furthermore, TB calculations predict a tunable energy gap for graphene QDs of arbitrary shape, with the gap decreasing exponentially with the number of atoms. This decay is strongly influenced by the edge type, with zigzag edges supporting localized states that significantly alter the electronic structure [136].

## 1.2.2 Bilayer Graphene as a Platform for the Realization of Tunable Quantum Dots

While monolayer graphene QDs offer a rich platform to study quantum confinement and edge-related phenomena, their gapless bulk nature and limited electrostatic tunability remain significant

challenges. These limitations have motivated the exploration of alternative 2D materials, among which BLG has emerged as a particularly promising candidate for realizing quantum-confined structures with enhanced control over their electronic properties.

Beyond its role in extended systems, BLG can also serve as a platform for quantum-confined structures. In recent years, BLG has emerged as a promising candidate for realizing highly tunable lateral QDs [56, 145–147]. Unlike conventional semiconductors, where laterally gated QDs [56, 145–147] often confine only one type of charge carrier, BLG allows for the simultaneous confinement of both electrons and holes within the same QD [85, 124–129], owing to its unique electronic structure [4, 46, 47, 51, 53, 86]. The massive nature of charge carriers in BLG gives rise to a tunable band structure that can be modulated by an external electric field [4, 46–48, 51, 53, 55, 80, 86, 87, 148–151], offering a practical mechanism for tuning QD properties [152]. In particular, the field-induced tunability of the band gap enables dynamic control over the confinement potential, providing a high degree of flexibility in device design [56].

Several experimental works on QDs in BLG have explored electron-electron interactions, including the study of two-electron complexes. In particular, work on the spin-triplet and valley-singlet states has demonstrated unique behavior that is distinct from that seen in conventional semiconductors [115, 130, 146]. These findings highlight the potential of BLG in QD-based quantum computing and quantum information processing.

One of the observed features of BLG QDs is the coexistence and tunability of spin and valley degrees of freedom, which opens a path toward encoding quantum information in multicomponent qubit bases. In 2021, Luca Banszerus *et al.* [113] demonstrated the experimental observation of spin-valley coupling in single-electron BLG QDs. Using transport-spectroscopy in a perpendicular magnetic field, they observed a splitting of the fourfold spin-valley degeneracy—commonly expected in graphene-based systems—attributed to intrinsic spin-orbit coupling of Kane-Mele type. The measured splitting was on the order of  $60 \mu\text{eV}$ , while intervalley scattering remained below the experimental resolution ( $<20 \mu\text{eV}$ ), reflecting the high crystallographic quality of the encapsulated BLG. These results underscore the capacity of BLG QDs to host quantum states with long coherence times and minimal disorder-induced valley mixing, both of which are promising for implementing spin- and valley-based quantum bits.

The complexity of electron interactions becomes even more apparent in the few-electron regime. Samuel Möller *et al.* [120] extended the picture by investigating the energy spectrum of two-electron BLG QDs, where Coulomb interactions play a central role. Through finite-bias transport spectroscopy, they resolved two distinct sets of multiplet states: six orbitally symmetric states and ten antisymmetric ones, in agreement with theoretical predictions based on two-particle wavefunction symmetries. The symmetric multiplet was found to lie  $0.4\text{--}0.8\text{meV}$  lower in energy than the antisymmetric one. Furthermore, a finer internal splitting of  $0.15\text{--}0.5 \text{meV}$  within the symmetric multiplet was observed, attributed to short-range interactions. These detailed spectroscopic fingerprints provide a microscopic window into the interplay between Coulomb repulsion, spin-valley entanglement, and quantum confinement. Altogether, these findings firmly establish gate-defined BLG QDs as a robust and highly tunable solid-state platform for exploring correlated quantum states and for the potential realization of electrically controlled spin-valley qubits.

In addition to the tunability of BLG through vertical electric fields, in 2007 João Milton Pereira Junior, Panagiotis Vasilopoulos, and Francois Peeters [145] proposed a lateral confining potential realized through position-dependent doping, which could confine both an electron and a hole simultaneously. They showed that the pseudospin winding number of 2 in BLG plays a significant

role in the angular momentum dependence of the QD spectrum, leading to new effects that are not observed in conventional semiconductors. The tunability along with the ability to confine both types of charge carriers positions BLG as a powerful candidate for QD-based quantum technologies, such as quantum sensors or qubits [56].

Following the theoretical proposal [145], recent advances in nanoscale device fabrication have enabled the realization of high-quality gate-defined QDs in BLG. Several experimental studies demonstrated the realization of gated lateral QDs in BLG, which successfully confined either electrons or holes [56, 112].

BLG offers a promising platform for advancing quantum technologies, including quantum computation, optoelectronics, and quantum information processing [56, 113, 120], where tunable and controllable QDs are important components. Furthermore, QDs in BLG have shown promise in applications such as single-photon detection [153–156], where the material’s unique properties can enable high-performance detectors for quantum cryptography, communication, and secure information processing. The enhanced tunability of BLG QDs provides significant advantages in the development of photonic quantum technologies, allowing for more precise control of photon emission and detection, important for advancing quantum networks and computing systems.

### 1.2.3 Optical Properties of Graphene and Bilayer Graphene Quantum Dots

Graphene and BLG QDs present a unique platform for studying and utilizing advanced optical properties in nanostructures. While monolayer graphene lacks a bandgap and exhibits strong screening, which typically suppresses tightly bound excitonic states, excitonic features have still been observed in graphene QDs, where spatial confinement enhances Coulomb interactions [57, 58].

Due to the infinite Bohr radius of excitons in graphene, graphene QDs exhibit quantum confinement effects regardless of their size [92]. This results in a finite bandgap and photoluminescence (PL) upon excitation. The absorption spectrum of graphene QDs typically features a strong peak near 230 nm, attributed to  $\pi \rightarrow \pi^*$  excitation of graphene’s  $\pi$ -bonds [157]. The presence of functional groups at the edges can influence both absorption features and PL, an effect known as the “edge effect” [158]. Reported PL quantum yields vary widely, with values up to 28% [92]. Compared to traditional semiconductor QDs, graphene QDs exhibit broader PL spectra, red-shifting and decreasing in intensity with increasing excitation wavelength [92]. Furthermore, some studies have reported up-conversion luminescence in graphene QDs. The mechanism has been suggested to involve anti-Stokes transitions [159].

In BLG QDs, the combination of quantum confinement, many-body interactions, and gate-defined potentials enables highly tunable optical properties. External electric fields not only open and modulate the bandgap, but also influence exciton and trion binding energies, allowing dynamic control over recombination dynamics and emission characteristics [57–59, 103, 113, 145, 160]. Unlike self-assembled QDs, this electrostatic confinement provides real-time adjustability of optical transitions. Moreover, the interplay between spin, valley, and orbital degrees of freedom opens pathways for encoding quantum information across multiple channels [56]. The tunable bandgap in BLG, spanning the THz to far infrared (FIR) range [44], supports low-energy excitations relevant for quantum sensing and long-coherence-time qubit platforms. Intrinsic properties such as pseudospin and Berry phase (with a winding number of 2) influence selection rules and

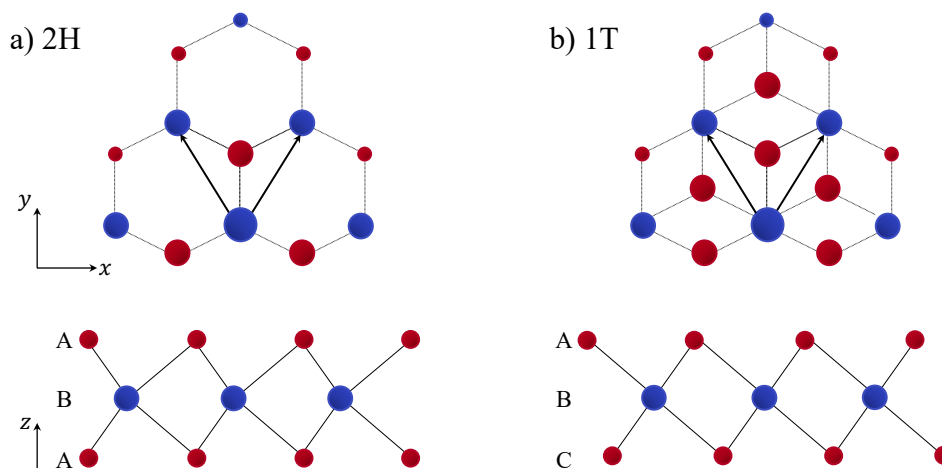


**Figure 1.1:** Atomic structure of single layers of TMDCs in their (a) trigonal prismatic (2H) and (b) distorted octahedral (1T) phase.

valley-dependent transitions, enabling the observation of valley-polarized excitons shaped by confinement, Coulomb interactions, and pseudospin dynamics [105, 147, 161].

The ability to control photon energy, emission intensity, and polarization with gate voltages makes BLG QDs especially attractive for quantum photonic applications. Their tunable response enables use in photodetectors, LEDs, single-photon sources, and emitters for secure quantum communication [127–129]. In particular, valley-polarized excitons offer a route to encode and manipulate information using the valley degree of freedom—a key concept in emerging valleytronic-based quantum technologies.

As fabrication techniques improve and theoretical understanding deepens, BLG QDs are increasingly recognized as promising platforms for highly controllable quantum devices. Alongside monolayer graphene, BLG enables the design of QDs with tunable electronic, spin, and optical properties, offering potential in quantum optics, computing, sensing, and communication [1, 29, 56, 162, 163]. In particular, the ability of BLG to host both semiconducting and metallic phases under different conditions highlights its versatility. Continued research on graphene-based systems is expected to drive progress in scalable quantum technologies and expand the possibilities of nanoscale device engineering.

### 1.3 Transition Metal Dichalcogenides

Research on graphene and other 2D crystals has emerged in recent years as one of the leading topics in condensed matter physics and materials science. Following the successful isolation of graphene, interest in alternative 2D materials has grown significantly [164, 165]. Approximately 2000 stable, exfoliable 2D crystals have been identified in nature [166]. Among these, a significant subset—about 20%—corresponds to compounds with the general chemical formula  $AB_2$ , which includes roughly 40 transition metal dichalcogenides (TMDCs) [167]. TMDCs are layered materials with the chemical composition  $MX_2$ , where  $M$  is a transition metal (e.g., Mo, W) and  $X$  is a chalcogen (e.g., S, Se, Te). Their diverse structural phases and tunable electronic properties have positioned them as key candidates for a range of applications beyond what graphene alone can offer.

Unlike graphene, which lacks an intrinsic bandgap, TMDCs form a class of layered materials with diverse and tunable electronic properties, making them highly attractive for applications in next-generation electronic and optoelectronic devices. Furthermore, while BLG allows for bandgap engineering via external electric fields, TMDCs possess intrinsic bandgaps even in their monolayer form, often in the visible range. This intrinsic semiconducting nature simplifies their use in optoelectronic applications and enables strong light–matter interactions without the need for electrostatic gating. Structurally, these materials consist of a transition metal layer sandwiched between two chalcogen layers, resulting in strong in-plane covalent bonding and weak interlayer vdW interactions—similar to the interlayer coupling seen in BLG, yet with far greater chemical diversity and structural anisotropy.

The ability to isolate 2D  $\text{MX}_2$  compounds has played a pivotal role in enabling the exploration of the fundamental properties of TMDCs. Bulk TMDC crystals are indirect-gap semiconductors composed of vdW-bonded  $X - M - X$  units [168]. Each monolayer consists of two hexagonal planes of  $X$  chalcogen atoms and an intermediate hexagonal plane of  $M$  metal atoms, arranged in a trigonal prismatic structure with ionic-covalent interactions between the layers [169]. The weak interlayer interactions, combined with strong intralayer bonding, enable the production of ultrathin TMDCs crystals via micromechanical cleavage, as demonstrated by Konstantin Novoselov *et al.* [169, 170]. While this technique produces high-quality monolayers suitable for fundamental studies, it faces limitations in scalability due to the restricted size and quantity of the flakes produced. To address these challenges, alternative bottom-up strategies have been developed, such as CVD, which allows for the synthesis of large-area, high-quality 2D materials [171]. CVD methods have successfully been used to produce various TMDCs and their alloys, offering better scalability for potential applications in electronics and optoelectronics. However, despite the advantages, both exfoliation and CVD methods require careful optimization to balance quality with scalability. Furthermore, solution-based exfoliation methods, which use chemical intercalation or mechanical sonication, can produce large quantities of flakes, but often introduce defects and impurities that may limit the material’s performance in precision-driven applications. These methods, however, show promise for photo- and electrocatalytic applications [165, 171].

TMDCs exhibit several distinct structural phases, primarily determined by the coordination of transition metal atoms within their crystal lattices [5]. The two most common phases are the trigonal prismatic (2H) and octahedral (1T) phases, which differ in the stacking arrangement of the atomic layers (chalcogen–metal–chalcogen), as presented in Fig. 1.1. In the 2H phase, the chalcogen atoms in different layers occupy the same position (ABA stacking), shown in Fig. 1.1(a), whereas in the 1T phase, the stacking follows an ABC pattern, depicted in Fig. 1.1(b). The thermodynamically stable phase varies depending on the transition metal (Mo, W, etc.) and chalcogen (S, Se, Te), with the 2H phase typically being stable for many group VI TMDCs, and the 1T phase being metastable. Notably,  $\text{WTe}_2$  is an exception, where the stable phase is orthorhombic  $1\text{T}_d$  at room temperature. Additionally, distortions in the structure can occur, leading to more complex phases such as  $1\text{T}'$  or charge density wave phases, which exhibit intriguing physical properties and are central to the rich phase diagrams of TMDCs.

Single layers of TMDCs combine atomic-scale thickness, direct bandgaps, strong SOC, and unique electronic and mechanical properties, making them ideal for both fundamental research and a wide range of applications. These materials are particularly promising for fields such as high-end flexible electronics, spintronics, optoelectronics, energy harvesting [5] or medicine, where they can be used for DNA sequencing or in drug delivery processes [172]. With their unique

**Table 1.1:** Bandgap values for selected TMDCs in monolayer and bulk forms, determined theoretically (theory) and experimentally (exp.), respectively.

Material	Bulk $E_g$ (eV)		Monolayer $E_g$ (eV)	
	Theory [176]	Exp. [177]	Theory [178]	Exp. [12]
MoS <sub>2</sub>	1.46	1.28	1.59	1.87
MoSe <sub>2</sub>	1.30	1.10	1.34	1.52
WS <sub>2</sub>	1.45	1.38	1.58	1.99
WSe <sub>2</sub>	1.26	1.24	1.27	1.62

characteristics, TMDCs are at the forefront of materials research, offering new insights into novel physical phenomena and enabling advances in nanoelectronic, nanophotonic, and nanoscale sensing and actuation devices [5].

### 1.3.1 Electronic Properties of Transition Metal Dichalcogenide Monolayers

Due to the diversity of chemical compositions and structural phases, TMDCs exhibit a broad range of electronic properties, which become particularly apparent when reduced to monolayers. In the following description we focus on the TMDCs formed by group VI transition metals Mo and W combined with S and Se. In their bulk form, TMDCs display an indirect bandgap, where the minimum of the conduction band (CB) and the maximum of the valence band (VB) do not occur at the same momentum  $\vec{k}$ . However, when the material is thinned down to a monolayer (in their thermodynamically stable 2H phase), this indirect bandgap transitions into a direct energy gap [5, 169, 173–175], a phenomenon that enhances suitability of TMDCs monolayers for optoelectronic applications, including light emitting diodes (LEDs), photodetectors, and solar cells. This transition to a direct bandgap has been demonstrated for several TMDCs such as MoS<sub>2</sub>, MoSe<sub>2</sub>, WS<sub>2</sub>, and WSe<sub>2</sub>. The values of bulk and monolayer energy gaps are collected in Tab. 1.1.

The transition from an indirect to a direct bandgap in monolayer TMDCs is driven by quantum confinement effects, which become more pronounced as the material thickness is reduced. In bulk TMDCs, the interlayer coupling between individual layers results in reduced electronic interaction between the layers, leading to the indirect nature of the bandgap. As the number of layers decreases to a monolayer, the interlayer coupling is diminished, and the material’s electronic structure is modified, resulting in a direct bandgap [5–7]. Moreover, the direct bandgap of monolayer TMDCs can be modified through external factors such as strain [11], applied electric fields, or doping [10], offering a versatile platform for controlling their electronic properties for various applications.

One of the most distinctive features of monolayer TMDCs is their valley-dependent electronic structure, which arises from the presence of two inequivalent but energetically degenerate valleys located at the  $K$  and  $K'$  points—corresponding to the corners of the hexagonal BZ (see Sec. 2.1.3.1, Fig. 2.2).

Another important characteristic of monolayer 2H-phase TMDCs is the absence of inversion symmetry, which, combined with strong SOC—the interaction between an electron’s spin and its momentum—leads to spin splitting of the electronic bands. Moreover, at the  $K$  and  $K'$  points

in the BZ, spin degeneracy is lifted. This effect is especially visible in the VB, where the spin splitting ranges from approximately 0.15 eV in 2H-MoS<sub>2</sub> to about 0.46 eV in 2H-WSe<sub>2</sub> [179], following the expected trend with increasing atomic number of the transition metal. Although the CB exhibits a much smaller spin splitting—typically an order of magnitude lower [178]—it remains relevant. Moreover, due to time-reversal symmetry, the spin splitting at  $K$  and  $K'$  has opposite signs, resulting in spin–valley locking: the spin orientation of charge carriers is intrinsically linked to their valley index [7, 180].

This coupling enables the conversion of valley polarization into spin polarization, providing a route to spintronic devices that do not require magnetic components [181]. As the spin and valley degrees of freedom are intrinsically coupled, monolayer TMDCs allow for selective excitation of electrons in a given valley using circularly polarized light. This lays the foundation for valleytronics, a field in which information is encoded and manipulated using the valley index, analogous to the role of charge in conventional electronics.

The combination of tunable bandgap, valley-dependent physics, and spin-valley coupling in monolayer TMDCs presents new opportunities for creating novel quantum devices, including quantum sensors, quantum light sources, and integrated photonic circuits. These unique properties, along with their relatively simple fabrication and scalability, make monolayer TMDCs a highly promising material system for future optoelectronic and quantum technologies [5–7].

### 1.3.2 Excitonic Effects in Monolayer Transition Metal Dichalcogenides

In the case of monolayer TMDC crystals, the absence of inversion symmetry and the transition from 3D to 2D dimensionality result in the aforementioned direct bandgap located at the  $K$  and  $K'$  points of the hexagonal BZ. This direct bandgap enables efficient optical generation of excitons [6, 182–222]—bound states of an electron in the CB and a hole in the VB, interacting via Coulomb attraction, often modeled using a hydrogen-like picture [7].

Compared to their bulk counterparts and previously discussed low-dimensional systems such as BLG and its QDs, monolayer TMDCs present a significantly richer landscape of electronic and optical phenomena. Notably, these atomically thin crystals exhibit no broken bonds at their surfaces, minimizing interfacial defects, dangling bonds, or electronic trap states—features that often limit the performance of conventional semiconductor heterostructures. Moreover, the reduced dielectric screening in monolayer systems leads to enhanced Coulomb interactions, giving rise to large exciton binding energies and strongly bound excitonic states, which dominate their optical response [6].

Due to the strictly 2D nature of TMDC monolayers, the excitons formed in these materials are extremely strongly bound compared to those in conventional 3D semiconductors. Binding energies of excitons in monolayer TMDCs can reach values as high as several hundred meV [174, 223–227], which is approximately two orders of magnitude larger than the binding energies in typical bulk semiconductors, where values are often only a few meV at low temperatures [45, 228–230]. This large binding energy in monolayer TMDCs stems from the significantly reduced dielectric screening in the 2D limit, which allows the Coulomb attraction between the electron and hole to remain effective over longer distances.

The excitonic spectrum in these vdW crystals is often modeled as hydrogen-like, comprising a ground state and a series of excited states. However, due to the modified screening environment in 2D materials, this series deviates from the ideal hydrogenic model, and the energy level spacing

**Table 1.2:** A compilation of experimentally determined exciton binding energies  $E_b$  in hBN-encapsulated systems, along with first-principles-calculated exciton lifetimes  $\tau$  (understood as the recombination time of a bound electron–hole pair) at low and room temperatures. Additionally, theoretical energies of A and B excitons in monolayer TMDCs, calculated using many-body perturbation theory, are included for comparison.

Monolayer	$E_b$ (meV) [231]	$\tau$ (ns) [232]	A/B Exciton Energies (eV) [233]
MoS <sub>2</sub>	221	3.7 (4 K) 0.27 (300 K)	1.78 / 2.02
MoSe <sub>2</sub>	231	5.0 (4 K) 0.38 (300 K)	1.65 / 1.87
WS <sub>2</sub>	180	2.3 (4 K) 0.17 (300 K)	2.06 / 2.39
WSe <sub>2</sub>	167	3.8 (4 K) 0.29 (300 K)	1.83 / 2.14

is nonuniform. Importantly, the large exciton binding energy results in a substantial difference between the free-particle bandgap (i.e., the energy required to generate an unbound electron–hole pair) and the optical bandgap (i.e., the energy associated with the creation of a bound exciton). The difference between these two energy scales defines the exciton binding energy.

To experimentally determine this quantity, one typically combines scanning tunneling spectroscopy to measure the quasiparticle or free-particle bandgap with optical techniques such as PL spectroscopy or reflectance contrast to extract the optical gap. This dual approach enables accurate estimation of the binding energy in monolayer TMDCs, as summarized in Tab. 1.2.

Exciton lifetimes, which characterize the time an exciton remains in its bound state before recombining radiatively or non-radiatively, are highly sensitive to environmental conditions and material quality. In monolayer TMDCs, these lifetimes span a broad range—from just a few picoseconds up to several hundred picoseconds—depending on factors such as substrate material, temperature, excitation density, and sample disorder [234–239] (see Tab. 1.2). At low temperatures and low excitation powers, radiative recombination dominates, and exciton lifetimes are relatively long due to the narrow linewidth and reduced phonon interactions. However, as temperature increases or under high carrier densities, scattering with phonons and other excitons, as well as interactions with charged defects, can lead to accelerated non-radiative recombination and shorter lifetimes.

Due to the reduced dielectric screening and the resulting strong Coulomb interactions in monolayer TMDCs, a rich variety of excitonic species contribute to their optical response [6, 7]. Among these are bright excitons, which arise from spin-allowed, momentum-direct transitions from the top of the VB to the bottom of the CB at the  $K$  and  $K'$  points of the BZ. These are referred to as A excitons [233, 240]. A second peak in the absorption spectrum, known as the B exciton, arises from transitions involving the lower spin-split VB and the same-spin CB minimum [233, 240]. This splitting reflects the strength of SOC in the VB and varies across different compounds. While B excitons are also optically active, they typically exhibit lower oscillator strength than A excitons. The A and B exciton energies for selected monolayer TMDCs are listed in Tab. 1.2.

Dark excitons may also form when the electron and hole are located at different points in

momentum space—such as  $K-K'$  or  $K-Q$  (also referred to as  $\Lambda$ )—resulting in a nonzero center-of-mass momentum that suppresses direct radiative recombination [220–222, 241]. Spin-forbidden dark excitons can additionally occur when the electron and hole have opposite spin orientations within the same valley, rendering the transition dipole-forbidden. The interplay of bright and dark excitonic species underlies a range of phenomena, including spin–valley locking, where spin polarization can be coupled to valley pseudospin [7].

In addition to these well-known species, various other bound electron–hole configurations can emerge depending on the material and experimental conditions, further enriching the excitonic landscape of these materials. The excitonic states can be strongly coupled with phonons, leading to additional fine structures in the optical response, such as phonon-assisted recombination and intervalley scattering. These effects contribute to the temperature dependence of exciton lifetimes and can even give rise to phenomena such as Rydberg excitons, where the exciton binding energy becomes comparable to its energy level spacing, leading to unusually long-lived and highly correlated excitonic states [220–222]. Thus, the ability to tune the excitonic landscape through material engineering, strain, and external fields presents unique opportunities for optoelectronic and valleytronic applications in monolayer TMDCs.

In addition to neutral excitons, charged excitonic complexes, known as trions [6, 211, 242, 243], have also been observed in monolayer TMDCs. They consist of an electron and two holes, forming a positively charged trion, or two electrons and a hole, forming a negatively charged trion [6, 211, 242, 243]. Due to the reduced dielectric screening in 2D materials, trions in TMDCs are highly bound and exhibit optical characteristics distinct from those of neutral excitons [7]. Furthermore, they possess unique absorption and emission spectra, which can be separated from those of neutral excitons, allowing them to be optically distinguished. The energy difference between the trion and exciton resonances is primarily determined by the Coulomb interaction between the additional charge carriers in the trion [6, 242]. These complexes exhibit a variety of behaviors, such as distinct photoluminescence peaks and modified lifetimes, which depend on factors like carrier concentration, temperature, and the presence of external electric or magnetic fields [194, 195, 243].

The study of trions is important for understanding charge transport and recombination processes in monolayer TMDCs. Their presence can influence the material’s optical and electronic properties, particularly in devices where charge carrier dynamics are of paramount importance, such as in photodetectors, light-emitting diodes, and photovoltaic cells. Trions are also believed to play a significant role in the development of 2D-based optoelectronic applications, as their behavior can be tuned by manipulating parameters like carrier density or the application of external fields [200, 204, 205].

In addition, the interaction between excitons and trions can provide insights into the interplay between neutral and charged excitations in 2D materials. The complex nature of these interactions may open up avenues for the design of novel quantum devices that leverage both excitons and trions.

The study of excitonic effects in monolayer TMDCs is not only relevant for fundamental physics but also for practical applications in optoelectronics, including photodetectors, light-emitting devices, and solar cells. Moreover, the strong Coulomb interactions in these materials enable the creation of novel quantum states, such as exciton-polaritons and Bose-Einstein condensates of excitons, which could find applications in quantum computing and quantum information processing [182–188].

Furthermore, valley-selective excitation of excitons in monolayer TMDCs offers exciting possibilities for valleytronic applications, where the information is encoded in the valley index [189–194].

This valley-dependent behavior, coupled with the strong SOC in TMDCs, could lead to spin-valley locked states, where the spin of the electron is correlated with its valley index. Such phenomena offer exciting prospects for developing spintronic devices that can exploit both spin and valley degrees of freedom for advanced applications in information storage and processing.

Overall, excitonic effects in monolayer TMDCs provide a rich platform for exploring fundamental physics and developing novel optoelectronic and quantum devices. The combination of strong Coulomb interactions, large binding energies, tunable optical properties, and valley-dependent physics places monolayer TMDCs at the forefront of research in 2D materials.

## 1.4 2D Transition Metal Dichalcogenide Heterostructures

Beyond monolayers, stacking TMDCs in various configurations enables the construction of vdW heterostructures, where interlayer interactions give rise to novel physical phenomena. To construct vdW heterostructures, atomically thin layers—obtained via exfoliation or CVD—must be carefully stacked in a desired sequence. This can be achieved using either top-down or bottom-up assembly techniques.

In the top-down approach, state-of-the-art alignment transfer methods rely on microscope stages with micromanipulators to align micrometre-scale flakes. A first 2D material layer is placed on a substrate, and a second is aligned and transferred—typically using a polymer stamp supported on a transparent material. While direct polymer dissolution enables two-layer stacking, polymer residues limit multilayer assembly. To avoid this, advanced “pick-up” or “peel-off” techniques have been developed for residue-free interfaces, enabling the fabrication of complex stacks with atomically sharp boundaries. These methods can be performed even in inert environments (e.g., glove boxes), making them compatible with air-sensitive materials. Despite its flexibility, exfoliation-based stacking is time-consuming and not scalable.

Bottom-up synthesis, such as direct CVD growth of stacked layers, offers a scalable alternative but suffers from strict growth conditions, making the synthesis of mixed-material vdW heterostructures more challenging. One significant advantage of mechanical stacking is control over twist angle between layers—unlike CVD growth, which typically locks layers in fixed orientations. This twist degree of freedom allows for the intentional formation of moiré patterns and structural transitions, enabling further tailoring of the electronic properties of the heterostructure.

The ability to stack monolayers of various 2D materials, including TMDCs, graphene, hBN, and others, has led to the development of heterostructures [45, 244] with unique electronic, optical, and mechanical properties. These materials, when layered in a vdW fashion, maintain their individual crystal lattices and do not require lattice matching, which allows for more flexibility in choosing combinations of materials. The interactions between the layers are dominated by vdW forces, resulting in new material phases with emergent properties not present in the individual components.

Furthermore, the ability to engineer band alignments in TMDC heterostructures [245] can be used as another tool for device applications. Depending on the specific combination of materials and stacking configurations, these systems can exhibit type-I, type-II, or type-III band alignments. In type-I (straddling) alignment, both the CB minimum and VB maximum of one material lie within the band gap of the other, confining both electrons and holes in the same layer—favorable for light-emitting devices. Type-II (staggered) alignment places the CB minimum and VB maximum in different layers, facilitating charge separation and making it useful for photovoltaics and photodetectors. Type-III (broken-gap) alignment occurs when the VB maximum of one material

lies above the CB minimum of the other, enabling tunneling behavior that can be exploited in tunnel field-effect transistors. Type-II heterostructures, in particular, are attractive for optoelectronic applications, as they promote efficient charge separation and reduced recombination. Such heterostructures hold great promise for applications in quantum computing, optoelectronics, and energy harvesting.

TMDC heterostructures offer highly tunable electronic and optical properties, which can be modulated through stacking order, twist angle, or external perturbations such as strain, electric fields, and dielectric environments [165, 246–248]. The strong Coulomb interactions and reduced dielectric screening in these systems enhance excitonic effects, leading to the formation of long-lived interlayer excitons with valley-specific optical selection rules and potential relevance for optoelectronics and quantum information technologies [249–253]. Interestingly, small rotational misalignments between layers give rise to moiré superlattices, which can host flat bands and correlated electronic states—enabling phenomena such as correlated insulators, superconductivity, and unconventional excitonic behavior, in analogy to twisted bilayer graphene [45]. The electronic band structure, excitonic spectrum, and moiré-induced phenomena will be discussed in more detail in the following sections. Beyond their electronic and optical features, TMDC heterostructures also exhibit notable mechanical flexibility and thermoelectric properties, broadening their technological relevance. Taken together, these characteristics make TMDC heterostructures an ideal platform for exploring emergent physical phenomena and for developing next-generation electronic and photonic devices.

#### 1.4.1 Electronic Behavior of Transition Metal Dichalcogenide van der Waals Heterostructures

The electronic behavior of TMDC vdW heterostructures is one of the more interesting aspects of 2D materials research. By stacking monolayers of TMDCs together or combining them with other 2D materials (such as graphene, black phosphorus or boron nitride), it is possible to create heterostructures with enhanced electronic properties, including tunable bandgaps, modified electronic band structures, and improved light-matter interactions [254]. These properties can be precisely controlled by altering the stacking sequence [255], the relative alignment between layers (introducing the mutual twist angle between the layer, thus creating twisted bilayers) [246, 252], or by applying external fields, e.g., electric [247, 248, 253] or magnetic fields. Such tunability is one of the key advantages of vdW heterostructures, as it allows for the engineering of electronic properties for specific applications.

The electronic properties of TMDC heterostructures can be tuned through the modulation of the interlayer coupling, which can vary significantly depending on the specific combination of materials used in the heterostructure [245, 246]. The interlayer interactions are particularly sensitive to the specific combination of 2D materials, and this has been shown to result in a wide range of electronic phenomena, including changes in the band structure [247], valley polarization effects [248], and the emergence of novel quantum states [256]. This tunability is significant in applications requiring precise control over the bandgap, such as in photodetectors or transistors [165].

Recent theoretical approaches using DFT and TB approximation have provided deep insights into the electronic structure of TMDC vdW heterostructures [247, 257, 258]. The stacking order of the monolayers plays an important role in determining the electronic properties of the heterostructures. Out-of-plane heterostructures, depending on their minimal energy stacking configurations,

often exhibit indirect bandgaps with type-II band alignment. In contrast, in-plane heterostructures maintain direct bandgaps, which are beneficial for efficient light absorption and emission. Moreover, moderate tensile strain has been shown to induce direct bandgaps in specific heterostructures, such as MoSe<sub>2</sub>-WSe<sub>2</sub> and MoTe<sub>2</sub>-WTe<sub>2</sub>, opening up new possibilities for tunable optoelectronic properties [257].

Vertically stacked TMDC heterostructures, in particular, exhibit a strong dependence of their electronic properties on the stacking configuration of the individual monolayers. As demonstrated in first-principles calculations performed in 2014 by Jiangang He *et al.* [245], the relative orientation and atomic registry of the layers significantly influence the band structure, especially near the  $K$  point of the BZ. Variations in stacking can modify the VB maximum splitting, impact the direct or indirect nature of the bandgap, and alter the strength and character of interlayer excitonic transitions. For instance, while some stacking configurations maintain a direct bandgap, others induce a transition to an indirect bandgap regime. These effects underscore the importance of stacking order in tailoring the electronic landscape of vertical TMDC heterostructures for targeted optoelectronic and quantum applications.

In addition to the vertical stacking of materials, lateral heterojunctions [259–261], which involve combining different 2D materials side-by-side in a single monolayer, provide another degree of control over the electronic properties. These lateral heterostructures offer the advantage of engineered interfaces where the properties of the materials can vary spatially, leading to the creation of region-specific electronic behaviors. For instance, lateral junctions between different types of TMDC monolayers can result in a gradual change in band alignment, allowing for the creation of electronic devices like tunnel diodes or photodetectors with highly controllable responses. The use of lateral heterojunctions also enables the development of devices with new functionalities that rely on the unique properties of the individual materials in different regions, such as lateral exciton transport or high-speed electronic switching.

These insights into the electronic behavior of TMDC heterostructures are of high importance for their use in advanced technologies. The ability to precisely tailor their electronic properties allows for the development of devices with highly controllable size and type of the energy gap, which are essential for applications in quantum computing, optoelectronics, and spintronics. The modification of the electronic structure through interlayer coupling and strain can lead to the creation of novel quantum devices, such as topological quantum computers and spintronic devices that utilize electron spin for data storage and processing. Additionally, the tunability of these properties in TMDC heterostructures makes them ideal candidates for next-generation optoelectronic devices, such as photodetectors, light-emitting diodes, and lasers, where precise control over excitonic and charge transport dynamics is important [8, 262–268].

Furthermore, recent studies have revealed a rich variety of phenomena arising from the interlayer interactions in TMDC heterostructures, significantly influencing their electronic properties. These interactions enable bandgap engineering, spin-polarized states, and valley polarization effects. For example, in lateral heterostructures such as MoSe<sub>2</sub>/WSe<sub>2</sub>, valley polarization can be simultaneously manipulated in both materials within the same heterostructure [269], offering a platform for valleytronic applications, where control of carriers in specific valleys is utilized for information encoding. Additionally, TMDC heterostructures exhibit spin-polarized states due to strong SOC which can be further manipulated by applying external perturbations, such as electric fields or strain. For instance, recent studies have demonstrated that strain can induce nonlinear Hall effects in MoSe<sub>2</sub>/WSe<sub>2</sub> heterostructures, highlighting the role of strain in tuning the elec-

tronic properties of TMDC materials [270]. This phenomenon is of great interest for spintronic devices, where the spin degree of freedom is leveraged for data storage and processing. The ability to control both spin and valley polarization in these materials opens up exciting opportunities for developing advanced electronic and quantum devices.

The electronic behavior of TMDC vdW heterostructures offers rich possibilities for creating devices with customizable electronic properties. The ability to tailor the interlayer coupling, strain, and alignment between monolayers provides a versatile platform for designing novel quantum materials and optoelectronic devices with unprecedented levels of control and functionality.

### 1.4.2 Optical Properties of Transition Metal Dichalcogenide Bilayers

Similar to monolayers, the optical properties of TMDC bilayers are strongly influenced by excitonic effects and exhibit enhanced light-matter interactions, which are important for developing efficient optoelectronic devices. Furthermore, the vdW interactions between layers can modify the excitonic properties of each monolayer, leading to stronger and more tunable exciton binding energies. This behavior is particularly important for applications in light-emitting devices, where the control of exciton dynamics is essential for device efficiency. In TMDC heterostructures, there are two types of excitons, referred to as intralayer and interlayer (sometimes indirect) excitons. Intralayer excitons are confined within a single layer of the homo- or heterostructure, with a structure analogous to excitons observed in an isolated monolayer of TMDCs. A particularly interesting phenomenon is the formation of interlayer excitons. These optical complexes involve a bound state formed by an electron in the CB of one monolayer and a hole in the VB of the other layer. Interlayer excitons exhibit unique properties [8–10, 216, 217, 262–268, 271–288] and can play a significant role in photovoltaic and optoelectronic industries [289, 290].

In 2015, Pasqual Rivera *et al.* [249] demonstrated that the lifetime of a bright interlayer exciton in a MoSe<sub>2</sub>/WSe<sub>2</sub> heterobilayer reaches 1.8 ns at 20 K—three orders of magnitude longer than the typical exciton lifetime in monolayer TMDCs, which is on the order of a few picoseconds [234, 236]. This observation aligns with theoretical predictions, which suggest exciton lifetimes of around 5.9 ns for MoS<sub>2</sub>/MoS<sub>2</sub> bilayers, 205 ns for MoS<sub>2</sub>/WS<sub>2</sub>, and as high as 175 ns for MoSe<sub>2</sub>/WSe<sub>2</sub> at cryogenic temperatures [232, 249]. At room temperature, these values drop significantly, e.g., to 0.44 ns for MoS<sub>2</sub>/MoS<sub>2</sub>, 15 ns for MoS<sub>2</sub>/WS<sub>2</sub>, and 12.8 ns for MoSe<sub>2</sub>/WSe<sub>2</sub>. Experiments in subsequent years [291–293] confirmed that interlayer excitons generally exhibit significantly extended lifetimes compared to their intralayer counterparts. Moreover, lifetimes can vary across a broad range—up to several hundred nanoseconds—depending on the specific heterostructure studied [292–294]. An important factor influencing these timescales is the twist angle between the layers. Junho Choi *et al.* [295] showed that the interlayer exciton lifetime in twisted MoSe<sub>2</sub>/WSe<sub>2</sub> heterobilayers changes by an order of magnitude when the angle is varied between 1° and 3.5°. This behavior arises from two mechanisms: the transition from direct to indirect optical gaps due to twisting, and the formation of a moiré potential landscape that modifies carrier localization and recombination dynamics.

Experiments on interlayer excitons in semiconductor heterostructures based on GaAs have revealed numerous interesting physical effects, such as spin currents in a coherent excitonic gas [296] and spontaneous coherence and condensation of interlayer excitons [297]. However, due to their low binding energies ( $E_b$ ), interlayer excitons in GaAs heterostructures can exist only at low temperatures, approximately  $E_b/k_B$  (where  $k_B$  is the Boltzmann constant). In contrast, vdW

heterostructures constructed from atomically thin layers of TMDCs offer the advantage of studying materials with precisely tunable properties, including excitons with remarkably high binding energies. Interlayer excitons in TMDC crystal heterostructures are characterized by binding energies reaching several hundred meV, making them stable at room temperature [298–303]. The high binding energies of interlayer excitons in vdW heterostructures made of TMDC crystals could enable studies of high-temperature quantum Bose gases of interlayer excitons. As with lifetime, an additional factor influencing the binding energy of interlayer excitons is the twist angle between the layers [304].

A thorough understanding of the properties of excitons in TMDCs heterostructures and the ability to control these optical complexes is important for studying the physics of multi-particle systems and their applications in the photonic device industry. At the beginning of 2020, Erica Calman *et al.* [251] conducted an analysis of the luminescence lines of interlayer excitons in the heterostructure MoSe<sub>2</sub>/WSe<sub>2</sub>. The bilayer TMDC was covered with hBN, and the entire structure was placed on a graphite substrate. It was observed that while the energy of the intralayer exciton remains almost constant as a function of applied voltage, the energy of the interlayer exciton changes significantly when a voltage of 3 V is applied (the difference between 0 V and 3 V is approximately 20 meV). A similar property was recently shown by Etienne Lorchat *et al.* [305] analyzing the MoS<sub>2</sub> bilayer. This effect provides the possibility of controlling the energy of the interlayer exciton.

One of the more innovative developments in recent years has been the construction of a dual-gate system that enables selective control of the charge density in individual layers of a MoSe<sub>2</sub>/WSe<sub>2</sub> heterostructure [300]. This setup allows for the manipulation of neutral interlayer exciton motion via applied voltage, offering enhanced control over multi-particle complexes such as trions.

Shortly after the discovery of large-radius excitons, the existence of “exciton molecules”, also referred to as charged excitons, and now commonly known as trions, was predicted [306]. In a simplified picture, these are three-particle optical complexes formed by two carriers with the same charge and one with the opposite charge. Two electrons with a hole form a negatively charged exciton ( $X^-$ ), while two holes and one electron form a positively charged exciton ( $X^+$ ). They can be understood analogously to hydrogen ions, where ( $H^-$ ) describes a system of two electrons and a proton, and ( $H_2^+$ ) corresponds to two protons bound with one electron. The binding energy of trions in 3D semiconductor materials is quite small. However, it has been shown that with the reduction of dimensions (transition from bulk materials to their 2D counterparts), the binding energy of the trion increases significantly [307–309]. This has allowed for the observation of trions in CdTe and GaAs quantum wells, leading to the development of experimental research and theoretical analyses of charged excitons in various semiconductor materials [310, 311].

In 2013, Kin Fai Mak *et al.* [312] observed in TMDC heterostructures trions characterized by large binding energy ( $\sim 20$  meV, relative to the exciton energy). Moreover, these quasiparticles can be optically created from valley- and spin-polarized holes, which is not the case in conventional semiconductors. It is also important to note that, unlike neutral excitons in monolayers, the motion of trions in such a system can be controlled by an electric field. The presence of strongly bound trions, in which the valley and spin degrees of freedom of the hole can be controlled, opens new possibilities in the field of multi-particle complex physics, such as the control of carriers by light (carrier-exciton interaction via trions). An important issue for understanding the physics of charged excitons is the analysis (both theoretical and experimental) of the fine structure of these optical complexes in TMDC crystals. These studies have made it possible to investigate,

among other things, the  $2s$  states of trions appearing energetically below the  $2s$  states of neutral excitons [313], as well as the fine structure and valley polarization of charged excitons [314] for monolayer  $\text{WS}_2$ . The obtained results highlight the important role of trions in the full excitation spectrum in 2D semiconductor crystals.

Questions related to the formation mechanism of trions and their manifestation in the optical properties of systems, as well as interesting physical properties of charged excitons, have contributed to the growing interest in these optical complexes and the expansion of research areas to multilayer systems (vdW heterostructures) [251, 299, 300, 315, 316]. Research conducted on the  $\text{MoSe}_2/\text{WSe}_2$  bilayer has not only allowed the analysis of the previously described properties of the interlayer exciton, but also, based on the measurement of energy splitting and the dependence of luminescence lines on temperature, the observation of the interlayer charged exciton, i.e., the so-called interlayer trion [251]. The formation of the charged interlayer exciton was later observed by other groups [299, 300]. It is worth noting that, similarly to the interlayer exciton, the binding energy of the interlayer trion has also been shown to be controllable by a gate (with an energy difference of about 10 meV for a voltage change from 0 V to 3 V) [251].

### 1.4.3 Moiré Superlattices and Twistronics in Transition Metal Dichalcogenide Multi-Layers

Atomically thin layers of 2D materials can be also used to create heterostructures with mismatched lattice constants or layers twisted at arbitrary angles [45, 164, 246]. In such homo- and heterostructures, a periodicity known as a moiré superlattice emerges [317–319]. The presence of moiré patterns can lead to the occurrence of interesting physical effects. When the layers have the same lattice constants, electrons can be described directly by Bloch bands for the appropriately set unit cell (UC) of the analyzed bilayer. However, in the case of lattice mismatch, the presence of moiré patterns causes the low-energy structure to be described in a significantly reduced BZ. This phenomenon is seen, for example, in the graphene/hBN systems [320, 321]. A particularly interesting effect arising from the presence of moiré bands can be observed in twisted bilayer graphene structures [322–324], where a transition from an insulator to a superconductor is possible for so-called “magic” twist angles [325].

In numerous theoretical analyses conducted in recent years for bilayer TMDC, the effects of lattice mismatch between the individual layers forming the considered heterostructure were often neglected. However, in general, it can be shown that the vdW interaction between such monolayers is not strong enough to lead to coherence of the lattice constants, and the mismatch will lead to the formation of moiré patterns [326, 327]. In such a structure, the mutual arrangement of atoms belonging to the individual layers differs at different points of the system. In 2013, Jun Kang *et al.* [326] showed that this leads to a spatial variation of the interlayer interaction strength and the electrostatic potential, and additionally, the effect of moiré pattern formation allows for the localization of the full hole wavefunction, while the electron wavefunction is weakly localized. This phenomenon also significantly impacts the character of the material’s electronic structure, which will differ at different points of the superlattice. It is also possible to analyze systems with additionally twisted layers [328]. In 2019, Vladimir Fal’ko *et al.* [329] suggested that the effects arising from the presence of moiré patterns should be weak for arbitrary twist angles, but dominant for angles close to  $\theta = 0^\circ$  and  $\theta = 60^\circ$ , resulting in, among other things, the appearance of narrow minibands near the actual band edges. In recent years, moiré superlattices occurring in TMDC

crystal heterostructure systems have been increasingly observed and experimentally analyzed [330–336], allowing for the observation of phenomena such as domain structure formation or piezoelectric texture.

An interesting topic is the analysis of optical complexes in the presence of moiré superlattices. Moiré patterns in vdW heterostructures lead to the presence of superlattice potentials. Numerous theoretical analyses [328, 336–339] predict that in such structures, both intra- and interlayer excitons (referred to as moiré excitons) will exhibit exotic properties. In 2017, Hongyi Yu *et al.* [336] showed that interlayer excitons in moiré superlattices exhibit a large spin-orbit splitting of the excitonic bands (depending on the center-of-mass momentum of the exciton), as well as the presence of Dirac and Weyl nodal points in the low-energy structure of these bands. This leads to the appearance of spin-momentum localized edge states resulting from the combined hopping integral between the moiré lattice nodes, which depends on spin. This quantity in the superlattice potentials can be controlled by a perpendicular electric field or appropriate modulation of the moiré lattice periodicity, which enables the use of such systems in optoelectronic device industries (single-photon emitters, high-efficiency semiconductor lasers, entangled photon sources), and also provides a possibility to analyze new quantum phases of matter. The combination of moiré potentials, exciton Zeeman fields, electron-hole exchange interactions, and Berry phase valley effects can lead to the formation of so-called topological excitonic bands with nonzero Chern numbers [337]. An important issue is also the theory of optical absorption of interlayer excitons. The periodic potential arising from the presence of moiré stripes causes mixing of momentum states separated by moiré reciprocal lattice vectors, leading to the appearance of peaks in the absorption spectrum or multiple resonance peaks in the photoluminescence spectrum [328]. It is also possible to analyze transitions between different excitonic phases in the moiré potential and their impact on the optical properties of bilayer TMDCs [338]. Additionally, it is worth noting that, as mentioned earlier, the twist angle directly affects the lifetime of interlayer excitons [295, 340–343]. In recent years, numerous experiments have allowed the observation and detailed analysis of moiré exciton properties [295, 344–354]. The presence of moiré trions in twisted MoSe<sub>2</sub> bilayer has also been demonstrated [355].

An interesting physical phenomenon is also the possibility of so-called exciton trapping in interlayer moiré potential barriers. Scanning tunneling microscopy and spectroscopy have allowed the direct observation and measurement of moiré patterns in 2D semiconductor heterostructures, showing periodically varying layer separations and energy gaps [327]. When the superlattice period of the moiré pattern formed due to lattice mismatch or mutual twisting of the layers exceeds the Bohr radius of the interlayer exciton (around 1 nm), such an exciton will experience a spatially modulated periodic potential, which leads to the formation of a system analogous to a Bose-Einstein condensate on optical lattices [356]. The minimum of the moiré potential can act like a structure similar to a QD. A unique feature of trapping potentials using moiré lattices is the fact that they preserve C<sub>3</sub> symmetry [328, 336]. For this reason, interlayer excitons “trapped” in such a potential should exhibit valley-dependent properties, distinguishing them from excitons bound by randomly formed trapping potentials. Interlayer excitons trapped in the moiré potential were first observed in 2019 by Kyle L. Seyler *et al.* [250] in MoSe<sub>2</sub>/WSe<sub>2</sub> bilayer, and since then, they have been increasingly studied experimentally [357–362]. The exciton trapping effect in moiré superlattice potentials allows for the construction of new quantum optical devices, including so-called Hubbard model simulators.

Recently, it has been shown that the presence of moiré patterns enables the trapping not only

of neutral interlayer excitons but also of charged excitons, i.e., trions. Interlayer trions trapped in the moiré potential were observed in early 2021 in MoSe<sub>2</sub>/WSe<sub>2</sub> bilayer [363, 364].

There is currently interest in monolayers of TMDC materials due to their semiconductor nature, which allows their use in the development of electronic and optoelectronic devices. However, it should be noted that the ability to create heterostructures made from 2D TMDC crystals also makes it possible to expect the occurrence of other states of matter, such as (unconventional) superconducting states [365] or exciton condensates [366, 367]. Additional twisting of the layers leads to the formation of flat bands, which may enable the occurrence of a Mott insulator phase [368–370], spin liquid [369, 371], or the predicted topological insulator [372].

TMDC bilayers belong to the class of materials characterized by two unique features. First, they possess a coupled spin-valley-layer degree of freedom, and second, their crystal structure is globally centrosymmetric, but locally non-centrosymmetric. The combination of these properties can lead to a rich phase diagram for unconventional superconductivity and the occurrence of exotic physical effects, such as the appearance of the Fulde-Ferrell-Larkin-Ovchinnikov phase in the presence of a strong magnetic field [365, 373]. In recent years, superconductivity has been observed experimentally in TMDC bilayers [374]. Analyses of the superconducting state induced by voltage in MoS<sub>2</sub> crystals with different dimensionalities (from bulk material to bilayer, and up to monolayer) have shown that this state depends on the thickness (number of layers) of the material, being weakest for the 2D crystal (monolayer) [375]. The transition to the superconducting state for the MoS<sub>2</sub> bilayer occurs at a critical temperature of  $T_C \approx 7$  K, which is much higher than for the monolayer. Interestingly, it was also observed that the type of gate applied to the MoS<sub>2</sub> bilayer influences the superconducting properties [374].

A Bose-Einstein condensate is the ground state of a bosonic gas, which can consist, for example, of atoms cooled to temperatures close to absolute zero. Numerous analyses have predicted that excitons in systems of 2D bilayer crystals made of carriers with an effective mass much smaller than that of an atom can undergo a transition to an excitonic condensate at relatively high temperatures [376]. vdW heterostructures, characterized by the presence of interlayer excitons with high binding energies, are ideal systems for studying excitonic condensates [377, 378]. Theoretical analyses considering both TMDC/hBN/TMDC systems [379, 380] and bilayers with a dielectric barrier [303] have predicted the occurrence of high-temperature Bose-Einstein condensates of excitonic states. In 2019, Zefang Wang *et al.* [366] analyzed the MoSe<sub>2</sub>/WSe<sub>2</sub> bilayer system with a high density of correlated electron-hole states, without the presence of an external magnetic field. Measurements allowed for the observation of a threshold dependence of electroluminescence on exciton density, sensitivity to charge imbalance, and the occurrence of critical fluctuations, which are characteristic of an excitonic condensate. Moreover, these effects persist up to temperatures as high as 100 K, which is consistent with earlier theoretical predictions [303, 379, 380]. This opens the possibility of studying excitonic condensates at high-energy scales and suggests the potential for high-temperature excitonic superconductivity [381, 382]. Interestingly, the excitonic condensate phase has recently been predicted and observed in twisted TMDC bilayers [362, 367].

A particularly promising direction is the journey to the twisted bilayer world. Introducing a nonzero twist angle between layers leads to numerous interesting effects. Theoretical analyses predict that certain precisely defined twist angles will lead to the flattening of bands in the system's electronic structure [369–371, 383]. This phenomenon, combined with doping the flat bands with holes, can lead to the occurrence of a Mott insulator phase at half-filling of the band in twisted MoS<sub>2</sub> bilayers, as well as spin liquid states or a quantum anomalous Hall insulator phase for

certain specific filling factors. It is worth noting that, unlike twisted bilayer graphene, where the formation of flat bands can only be observed near the so-called “magic angle” [323, 384, 385], twisted TMDC bilayers are predicted to show this effect over a wide range of twist angles [369]. In recent years, analyses have shown the occurrence of flat bands in twisted homostructures of  $\text{WSe}_2/\text{WSe}_2$ , which appear for various twist angles, including  $3^\circ$ ,  $4^\circ$ - $5.1^\circ$ , and  $57.5^\circ$  [386–388]. The possibility of engineering flat bands across a continuous range of twist angles for  $\text{WSe}_2$  layers has been demonstrated [386, 388]. By mapping the wave functions, it was observed that, in accordance with first-principles calculations, the localization of the flat bands differs for twist angles close to zero and for twist angles of nearly  $60^\circ$  [387]. The phase diagram for twist angles from about  $4^\circ$  to  $5.2^\circ$  shows the occurrence of both an insulating phase and a metallic phase [388]. Thus, it is important to note that the wide possibilities for modifying the electronic structure of TMDC bilayers allow for the analysis of various model systems. An interesting aspect is also the change in the type of surrounding layers. Although the most commonly studied system is of the type  $\text{hBN}/\text{TMDC}/\text{TMDC}/\text{hBN}$ , other systems in which the band flattening effect also occurs are being analyzed, such as  $\text{CrBr}_3/\text{WSe}_2/\text{WSe}_2/\text{CrBr}_3$  [383].

The emergence of moiré superlattices in twisted and lattice-mismatched TMDC heterostructures has opened up a rich landscape of novel physical phenomena. These include the formation of moiré excitons and trions, exciton trapping in periodic potentials, and the engineering of flat electronic bands that enable correlated and topological quantum phases. Twistrionics allows unprecedented control over optical, electronic, and excitonic properties, facilitating the exploration of exotic states such as exciton condensates, Mott insulators, and unconventional superconductivity. As experimental techniques advance, moiré-engineered TMDC bilayers continue to serve as a versatile platform for both fundamental research and future quantum technologies.

## 1.5 Transition Metal Dichalcogenide-Based Quantum Dots

The development of TMDC-based QDs adds another dimension to their unique properties and potential applications. The strong quantum confinement in these nanostructures further modifies their optical and electronic properties, enabling their use in quantum computing, single-photon emitters, and nanoscale optoelectronic devices [14].

TMDC-based QDs represent a new class of low-dimensional materials with unique electronic and optical properties. Unlike bulk TMDCs or even their monolayer counterparts, QDs introduce quantum confinement effects that lead to discrete energy levels and size-dependent optical transitions. These properties make TMDC QDs highly promising for applications in quantum optics, photodetectors, and optoelectronic devices [14, 389–393].

Several theoretical studies of TMDC-based QDs have explored how quantum confinement and edge termination influence their electronic properties. Notably, Andor Kormányos *et al.* [394] developed an effective Hamiltonian to describe electrons in the CB of monolayer TMDCs under perpendicular electric and magnetic fields. Their analysis revealed that intrinsic and Bychkov-Rashba SOC lead to significant spin splitting, resulting in all QD states being both valley and spin split. This unique spin-valley coupling suggests the feasibility of utilizing such QDs as valley-spin filters and for implementing spin-valley (Kramers) qubits. The study underscores the potential of monolayer TMDCs in quantum computing applications, where control over spin and valley degrees of freedom is important.

Sladán Pavlović and Francois Peeters [389] investigated the electronic properties of triangular

and hexagonal MoS<sub>2</sub> QDs using a TB model. Their findings indicate that the shape and edge termination of the QDs significantly influence their electronic structure. Triangular QDs exhibit degenerate edge states near the Fermi level, leading to an enhanced density of states, whereas hexagonal QDs display a more uniform energy level distribution. This contrast in edge-state behavior highlights the importance of geometric considerations in tailoring the electronic properties of TMDC-based nanostructures for quantum and optoelectronic applications.

In 2017, Matthew Brooks and Guido Burkard [395] investigate the spin and valley degrees of freedom in monolayer TMDC QDs, focusing on overcoming the limitations imposed by strong SOC. In the absence of an external magnetic field, the spin and valley states form Kramers pairs, leading to a fourfold degeneracy. The study identifies specific regimes where this degeneracy can be preserved, enabling the realization of pure spin qubits. These regimes are achievable in materials like MoS<sub>2</sub>, where the SOC is sufficiently low and of the appropriate sign, allowing for the isolation of a single valley and tuning to a spin-degenerate regime within that valley. The article highlights the potential of monolayer TMDC QDs for spin-based quantum computing applications, emphasizing the importance of material choice and QD design in achieving desired spin properties.

These studies, along with numerous others, demonstrate the growing interest in exploring spin and valley qubits in TMDC-based QDs, highlighting their potential for quantum computing and spintronic applications. Advances in graphene and TMDC materials, along with the development of lateral gating strategies [121, 394], have made it possible to fabricate gated QDs [396, 397].

The synthesis of TMDC QDs can be achieved through various approaches, which generally fall into two categories: top-down and bottom-up methods. Top-down techniques involve breaking down bulk TMDC materials into nanoscale structures, often using liquid-phase exfoliation, laser ablation, or chemical etching. These processes enable the production of monolayer and few-layer QDs with controlled size and thickness. In contrast, bottom-up methods focus on the direct synthesis of QDs from molecular precursors. CVD, colloidal synthesis, and hydrothermal techniques allow for more precise control over the shape and composition of the resulting QDs. The choice of synthesis method directly influences the material's properties, particularly in terms of size distribution, defect density, and surface chemistry, all of which play a critical role in determining their optical and electronic behavior.

In 2018 Riccardo Pisoni *et al.* [396] demonstrated the fabrication of a high-quality, gate-tunable QD in a monolayer MoS<sub>2</sub> vdW heterostructure. The device consists of a monolayer MoS<sub>2</sub> encapsulated between hBN layers, with metallic ohmic contacts established through a pre-patterned hBN layer. This structure exhibits an electron mobility up to 3000 cm<sup>2</sup>/Vs at a carrier density of  $7 \times 10^{12}$  cm<sup>-2</sup> and a temperature of 1.7 K. Shubnikov-de Haas oscillations are observed at magnetic fields as low as 3.3 T, indicating high sample quality. By implementing a single QD gate structure atop the hBN, the researchers achieve electron confinement in the MoS<sub>2</sub> layer, observing Coulomb blockade effects. Furthermore, tuning the middle gate voltage allows the transition to a double dot regime, evidenced by the characteristic honeycomb pattern in the charge stability diagram. This work highlights the potential of TMDC-based heterostructures for quantum electronic applications.

Later on, Sagar Bhandari *et al.* [397] have shown the direct imaging of QD formation in monolayer MoS<sub>2</sub> nanostructures. A cooled scanning probe microscope operating at 4.2 K was used to spatially map conductance in a MoS<sub>2</sub> channel. By capacitively coupling the movable tip of the microscope to the 2D material, they locally modulate the electron density and observe Coulomb blockade phenomena manifesting as concentric ring patterns, indicative of localized electron states.

These “bullseye” features correspond to charging events of single QDs, enabling estimates of dot size and position using a capacitive model. At reduced carrier densities, the formation of multiple QDs is observed, attributed to disorder-induced potential fluctuations within the material. This work demonstrates a powerful method for probing localized electronic states in TMDC systems and provides insight into the role of disorder and electrostatic confinement in the formation of QDs in atomically thin semiconductors.

One of the most defining characteristics of TMDC monolayer and heterostructure-based QDs is their strong excitonic effects, driven by reduced dielectric screening and enhanced Coulomb interactions in low-dimensional systems. These properties result in high exciton binding energies and significant photoluminescence enhancement, making them ideal candidates for single-photon sources and light-emitting devices [14, 391]. Recent studies have further explored the tunable electronic and optical properties of TMDC-based QDs. It has been demonstrated that TMDC QDs exhibit size-dependent energy levels and exciton binding energies, making them highly tunable for optoelectronic applications [398]. Fanyao Qu *et al.* [399] further highlighted the ability to control the absorption spectrum of MoS<sub>2</sub>-based QDs through spatial and magnetic quantization, revealing their potential for spin and valley-polarized devices. The emission wavelength of QDs can be precisely controlled by varying their diameter, further enhancing their versatility for device engineering [389, 392].

Given their tunable properties, TMDC QDs have found applications in several technological fields. In quantum optics, their discrete energy levels allow for single-photon emission, which is essential for quantum cryptography and secure communication systems. Their strong light-matter interactions make them highly suitable for photodetectors, light-emitting diodes, and flexible optoelectronic devices [390, 392]. Furthermore, their biocompatibility and stable photoluminescence have positioned them as promising candidates for bioimaging and sensing applications. Unlike conventional fluorescent dyes, TMDC QDs offer greater stability and resistance to photobleaching, making them ideal for long-term imaging studies. Beyond optics, their edge-rich structure enhances catalytic activity, particularly in hydrogen evolution reactions and electrochemical energy storage, thus opening up possibilities for energy-related applications.

A promising direction in the field of TMDC QDs is the use of heterostructures, such as MoSe<sub>2</sub>/WSe<sub>2</sub>, which offer significant tunability of the QD’s electronic properties through external electric fields [248]. In particular, TMDC heterostructure-based QDs exhibit type-II band alignment, providing control over the energy levels and enabling valley- and spin-polarized effects, which are of interest for quantum devices. This ability to precisely tune the QD properties opens up new avenues for the development of optoelectronic devices that rely on quantum effects.

Despite their potential, several challenges remain in the widespread adoption of TMDC QDs. Achieving precise size control and uniformity is still a significant hurdle, as variability in QD dimensions affects their optoelectronic properties. Additionally, surface defects and oxidation can degrade their performance, necessitating improved passivation and encapsulation strategies. The integration of QDs into large-scale electronic and photonic devices also requires a deeper understanding of charge transport and inter-dot coupling effects. Addressing these challenges through advancements in fabrication techniques and theoretical modeling will be key to unlocking the full potential of TMDC QDs, positioning them as fundamental components in future quantum technologies and nanoscale devices.



## Chapter 2

# Methodology

Theoretical description of interacting electrons, particularly their correlations and interactions with light, remains one of the central challenges in condensed matter physics. This chapter outlines the methodology employed in this thesis to tackle these challenges, combining different computational techniques for electronic structure calculations with the theoretical frameworks necessary to understand the electronic correlations and optical properties of 2D materials.

The approach taken in this work relies on a combination of *ab initio* techniques, particularly the Density Functional Theory (DFT), alongside simplified models such as the tight-binding (TB) and mDF models, which are needed to describe large nanostructures and the effects of magnetic fields. These models are complemented by many-body theoretical approaches, including the Bethe-Salpeter equation (BSE) and configuration interaction (CI) methods, also known as non-perturbative exact diagonalization (exact diagonalization (ED)) techniques. Together, these tools enable the prediction of both electronic and optical properties of 2D materials, with an emphasis on high-performance computational methods that facilitate the study of large, atomically thin systems, such as twisted van der Waals (vdW) heterostructures and complex nanostructures.

The first step in the methodology involves determining the electronic structure from first principles using the DFT. Following this, the Kohn-Sham wave functions are analyzed—a process that is computationally challenging due to the large matrix sizes and the need to evaluate numerous integrals. In the next step, the *ab initio*-based TB or mDF models are constructed, offering an efficient approach for studying complex materials while capturing key electronic properties. This process however includes tackling multidimensional minimization problems to optimize the mDF and TB model parameters. The computational efficiency of these models is especially important when dealing with systems such as twisted vdW heterostructures or nanostructures with millions of atoms, where DFT methods would be prohibitively expensive.

The primary focus of this work is the theoretical exploration of optical properties of 2D materials, with an emphasis on electronic structure and many-body interactions. To address excitations in 2D crystals, the many-body calculations are performed using approximate screened electron-electron interactions within the BSE framework. A numerical challenge arises from the rapid growth of the many-body Hilbert space, where the number of configurations scales combinatorially with the number of particles and available single-particle states. To control this growth, the size of the Hilbert space is restricted by selecting a truncated single-particle basis. Finally, the absorption and emission spectra are calculated by determining the exciton spectra and dipole matrix elements, providing insight into the optical response of the materials.

This chapter is structured as follows: Sec. 2.1 introduces the numerical methods used for electronic structure calculations. It begins with a summary of *Density Functional Theory* in Sec. 2.1.1, followed by an approach to analyze spin, orbital, and layer contributions beyond DFT in Sec. 2.1.2. Next, the *tight-binding method* is introduced in Sec. 2.1.3, while the *massive Dirac fermion model* is discussed in Sec. 2.1.4. Sec. 2.2 then focuses on electron-electron interactions in 2D crystals. It begins with the *configuration interaction* method described in Sec. 2.2.1, followed by a discussion of *atomistic-based Coulomb matrix elements* in Sec. 2.2.2 and *electron-electron scattering in an external magnetic field* in Sec. 2.2.3. Various approaches for the *effective Coulomb interaction in low-dimensional systems* are considered in Sec. 2.2.4. Building on this, Sec. 2.3 introduces the theoretical framework for *correlated electron-hole states*, such as neutral and charged excitons, in 2D materials. It starts with the *Bethe-Salpeter equation for single electron-hole excitations* in Sec. 2.3.1, followed by the formalism for *charged excitons (trions)* in Sec. 2.3.2. Finally, Sec. 2.4 presents the theoretical methods used to describe the *optical response of 2D crystals*. This includes the derivation of *optical selection rules via the  $\vec{p} \cdot \vec{A}$  formalism* in Sec. 2.4.1, followed by a discussion of *dipole moments for optical transitions* in Sec. 2.4.2. The chapter concludes with an analysis of *optical absorption* and *optical emission*, presented in Sections 2.4.3 and 2.4.4, respectively.

## 2.1 Numerical Methods for the Electronic Structure Calculation

Understanding the electronic properties of materials requires a combination of theoretical models and numerical techniques that capture both the intrinsic quantum-mechanical behavior of electrons and the influence of material-specific interactions and external perturbations. This section provides an overview of the numerical methods employed in this thesis to investigate the electronic structure of 2D materials, as well as signatures of topology and correlated phases.

A multiscale approach is adopted, combining first-principles calculations with effective low-energy models. In Sec. 2.1.1, we discuss the principles of DFT, which serves as the benchmark method for accurate ground state (GS) electronic structure calculations. By solving the many-electron problem approximately with an effective Hartree and exchange-correlation (XC) potential, DFT provides reliable predictions of GS properties such as total energy, structural parameters, and electron density distributions. However, standard DFT is not suited for describing excited-state phenomena or optical response functions without additional corrections. Due to these limitations, and the computational cost of more sophisticated methods, alternative approaches are often required to accurately capture low-energy excitations and emergent quasiparticle behavior.

In Sec. 2.1.3, we introduce the TB model, a powerful yet computationally efficient method for describing electronic states in materials using the atomistic basis. By expressing the Hamiltonian in terms of hopping parameters between atomic orbitals, the TB model provides an intuitive understanding of band formation. In particular, the crystal symmetry influences the overlap between atomic orbitals, determining which electronic states can couple and how they contribute to the overall band structure. This results in a set of electronic states that reflect both the atomic-scale interactions and the symmetry constraints of the material. This approach allows to study large-scale systems, heterostructures, and moiré superlattices, where full DFT calculations are computationally prohibitive. Furthermore, it serves as a bridge to approximate theories, where the semiconductor medium is treated as continuous, enabling simplified and often quasianalytical

descriptions of the low-energy electronic properties.

Finally, in Sec. 2.1.4, we discuss the mDF model, useful in capturing the physics of materials with Dirac-like dispersion, such as graphene and TMDCs. By expanding the TB Hamiltonian around high-symmetry points, one arrives at an effective Dirac equation incorporating key features such as linear  $\vec{k} \cdot \vec{p}$  terms, mass terms, SOC, and Berry curvature effects. This model provides insights into valley-selective optical transitions, excitonic effects, and topological properties, making it a central tool for studying optoelectronic applications and quantum transport phenomena.

Together, these methods offer complementary tools for the electronic structure calculation, allowing for both accurate material-specific predictions and generalizable low-energy descriptions. The synergy between DFT, TB, and mDF approaches provides a robust theoretical framework for exploring the rich electronic behaviors that arise in quantum materials.

### 2.1.1 Density Functional Theory

Theoretical modelling of electronic properties in solids often relies on the DFT [400–410], a quantum-mechanical approach that reformulates the complex many-electron problem into one based on the electron density. DFT provides a practical balance between accuracy and computational cost, offering reliable predictions for GS properties such as lattice constants, elastic moduli, and VB levels. Although the theory is, in principle, exact, practical implementations require approximations that generally represent the many-body state by a single Slater determinant of effective orbitals, obtained through a self-consistent procedure.

The formal foundation of DFT is given by the two Hohenberg–Kohn theorems [411]. These theorems establish that the GS properties of an interacting electron system are uniquely determined by the electron density, depending only on the spatial coordinates. As a consequence, all observables are functionals of the GS density, reducing the many-body problem to an effective single-particle description in an external potential. The Hamiltonian of the system can be thus written as:

$$\hat{H}^{HK} = \hat{T} + \hat{V} + \hat{U}. \quad (2.1)$$

In Eq. (2.1) the notation following the original work by Hohenberg and Kohn was introduced, where each term is defined as follows:

$$\hat{T} = -\frac{\hbar^2}{2m_0} \int d\vec{r} \Psi^\dagger(\vec{r}) \Delta \Psi(\vec{r}); \quad (2.2)$$

$$\hat{V} = \int d\vec{r} V(\vec{r}) \Psi^\dagger(\vec{r}) \Psi(\vec{r}); \quad (2.3)$$

$$\hat{U} = \frac{e^2}{2\epsilon_0} \int d\vec{r} \int d\vec{r}' \frac{1}{|\vec{r} - \vec{r}'|} \Psi^\dagger(\vec{r}) \Psi^\dagger(\vec{r}') \Psi(\vec{r}') \Psi(\vec{r}). \quad (2.4)$$

Here,  $\hat{T}$  is the kinetic energy,  $\hat{V}$  describes the external potential, and  $\hat{U}$  is the Coulomb operator defining the Coulomb interactions between particles.  $\Psi(\vec{r})$  corresponds to the field operators allowing to define the electronic density as:

$$\hat{n}(\vec{r}) = \Psi^\dagger(\vec{r}) \Psi(\vec{r}). \quad (2.5)$$

In the Hohenberg-Kohn formalism, the electronic density  $n(\vec{r})$  is treated as the central quantity, allowing to describe completely all properties of the system. The electronic wave functions can be defined as functionals of the density,  $|\Psi[n]\rangle$ , and the expectation value of any observable  $\hat{O}$  can be written as  $O = \langle \Psi[n] | \hat{O} | \Psi[n] \rangle$ . In particular, the energy of electrons moving in an external

potential of atomic nuclei can be expressed as:

$$E[n] = \langle \Psi[n] | \hat{H}^{HK} | \Psi[n] \rangle, \quad (2.6)$$

thus being a unique functional of the electronic density  $n$ . Eq. (2.6) is the second Hohenberg-Kohn theorem. Furthermore, for a non-degenerate GS the functional of total energy  $E[n]$  has a global minimum defined by the electronic density of the GS. It has been proven that  $E_{GS} = E[n_0(\vec{r})]$  (with  $n_0(\vec{r})$  being the GS density) when  $n_0(\vec{r})$  minimises the functional  $E[n]$  and when it is normalised such that  $N[n] = \int d\vec{r} n(\vec{r}) = N$  with  $N$  corresponding to the number of electrons in the system.

The procedure of minimisation of the total energy as a functional of the electronic densities  $E[n]$  has been introduced by Walter Kohn and Lu Jeu Sham in 1965 [412], allowing to obtain the GS energy and the density of the system. It is important to the computational efficiency of DFT methods. To derive the Kohn-Sham equations we start with the formula describing the GS energy of an interacting inhomogeneous electron gas in a static potential  $V(\vec{r})$ , that is a solution of Eq. (2.6) for the GS density  $n(\vec{r})$ :

$$E[n] = \hat{V} + \hat{U} + G[n] = \int V(\vec{r}) n_0(\vec{r}) + \frac{e^2}{2\epsilon} \int d\vec{r} \int d\vec{r}' \frac{n(\vec{r}) n(\vec{r}')}{|\vec{r} - \vec{r}'|} + G[n], \quad (2.7)$$

with  $G[n]$  is a universal functional of the density  $n(\vec{r})$ . This functional can be determined in an approximate way as:

$$G[n] = T[n] + E_{XC}[n], \quad (2.8)$$

with  $T[n]$  being the kinetic energy of a system of non-interacting electrons with density  $n$ , and  $E_{XC}[n]$  is exchange and correlation energy of an interacting system with density  $n$ , called XC potential (energy). There is no simple, general expression for defining  $E_{XC}[n]$  exactly; however, for sufficiently slowly varying densities  $n$ , it has been shown that the XC potential can be written as:

$$E_{XC}[n] = \int n(\vec{r}) \epsilon_{XC}[n(\vec{r})] d\vec{r}, \quad (2.9)$$

with  $\epsilon_{XC}$  being the exchange and correlation energy per electron of a uniform electron gas of density  $n$ , and it is regarded as known from theories of the homogeneous electron gas [413]. Now the total energy functional  $E[n]$  defined in Eq. (2.7) can be minimised with respect to the density  $n$ . From the stationary property of  $E[n]$ , and with the condition that the total number of electrons remains fixed:

$$\int d\vec{r} \delta n(\vec{r}) = 0 \quad (2.10)$$

we obtain the condition:

$$\int \delta n(\vec{r}) \left( V(\vec{r}) + \frac{e^2}{2\epsilon_0} \int d\vec{r}' \frac{n(\vec{r}')}{|\vec{r} - \vec{r}'|} + \frac{\delta T[n]}{\delta n(\vec{r})} + \mu_{XC}[n(\vec{r})] \right) d\vec{r} = 0. \quad (2.11)$$

In the above equation we have the XC contribution to the chemical potential for the electron gas defined as  $\mu_{XC}[n(\vec{r})] = \frac{d(n\epsilon_{XC}[n(\vec{r})])}{dn(\vec{r})}$ . To solve Eq. (2.11), the many-body ground state is approximated by a single Slater determinant composed of effective single-particle orbitals  $\phi_i(\vec{r})$ . The electronic density is then expressed as a functional of these orbitals. Within this approximation, the problem reduces to solving the following effective single-particle Schrödinger equation:

$$\left( V(\vec{r}) + \frac{e^2}{2\epsilon} \int d\vec{r}' \frac{n(\vec{r}')}{|\vec{r} - \vec{r}'|} - \frac{\hbar^2}{2m_0} \Delta + \mu_{XC}[n(\vec{r})] \right) \phi_i(\vec{r}) = E_i \phi_i(\vec{r}), \quad (2.12)$$

Hence, the considered problem is the one of an electron moving in the mean field coming from the external potential  $V(\vec{r})$ , the direct Coulomb repulsion with all other electrons, and the chemical potential  $\mu_{XC}$  taking into account both the exchange and correlation effects. Furthermore, the wavefunction  $\phi_i(\vec{r})$  is the state, ground and excited, of the Kohn-Sham particle. Thus the electronic density of a single Slater determinant, GS, is obtained by filling up Kohn-Sham orbitals with  $N$  electrons yielding electronic density  $n(r)$ :

$$n(\vec{r}) = \sum_{i=1}^N |\phi_i(\vec{r})|^2. \quad (2.13)$$

Solving the problem of a single electron is computationally significantly easier than solving the full many-body problem. The Kohn-Sham formalism, by simplifying the expensive many-body calculation, enables the study of 3D crystals, 2D materials, and vdW heterostructures, as discussed in this work.

A further approximation to the problem of many electrons was introduced in 1934 by Hans Hellmann [414]. In this approach, the volume of the solid is divided into regions close to the lattice ions (the ion core regions) and regions between the lattice sites. Furthermore, we distinguish between the mobile (conduction) electrons, which are only weakly bound to the cores, and the core electrons, which occupy the lower shells of the lattice atoms and are strongly bound to them. The wave functions of conduction electrons are usually smoothly varying in the region between the ion cores, but they have a complicated nodal structure near the cores. Outside of the core regions, the potential acting on conduction electrons is relatively weak, corresponding to the screened Coulomb potential of the ion cores. In this outer region, the conduction orbitals can be approximated as plane waves, and the energy of a free electron depends on the wavevector  $\vec{k}$  as  $E_{\vec{k}} = \hbar^2 k^2 / 2m$ . However, inside the core regions, the strong, spherically symmetric core potential dominates, the plane-wave approximation breaks down, and the wave functions are no longer simply characterized by  $\vec{k}$ . This observation opens the possibility of replacing the true core potential by an effective potential reproducing the correct wave functions outside the core, known as the pseudopotential (PP) approximation [415]. The PP approach allows for a significant reduction in both the basis set size and the number of explicitly treated electrons.

Two main types of PPs are commonly used in modern plane-wave electronic structure codes: the norm-conserving PPs proposed by D. R. Hamann, M. Schlüter, and C. Chiang in 1979 [416], and the ultrasoft PPs introduced by David Vanderbilt in 1990 [417]. A related technique, building upon the pseudopotential idea, is the projector augmented wave (PAW) method developed by Peter E. Blöchl in 1994 [418, 419]. In our work, we employ the PAW method [418] combined with the Perdew-Burke-Ernzerhof (PBE) parametrization of the generalized gradient approximation (GGA) for the exchange-correlation potentials [420], along with the DFT-D3 functional for the inclusion of vdW interactions, as implemented in the ABINIT package. While DFT has been extraordinarily successful, it is still an active area of research. One major challenge is accurately describing systems with strong electron correlations, which can lead to significant deviations from the predictions of traditional DFT approximations. To address this, methods such as DFT+U, which introduces a Hubbard correction to the exchange-correlation functional [421–423], and hybrid functionals, which mix exact exchange with DFT [424, 425], have been developed to improve accuracy.

Additionally, time-dependent DFT [426] has emerged as a powerful tool for studying excited-state properties and dynamic processes. TDDFT extends the traditional DFT formalism to include the response of the electron density to time-dependent perturbations, making it invaluable for studying optical properties, excited-state dynamics, and electron transport in materials.

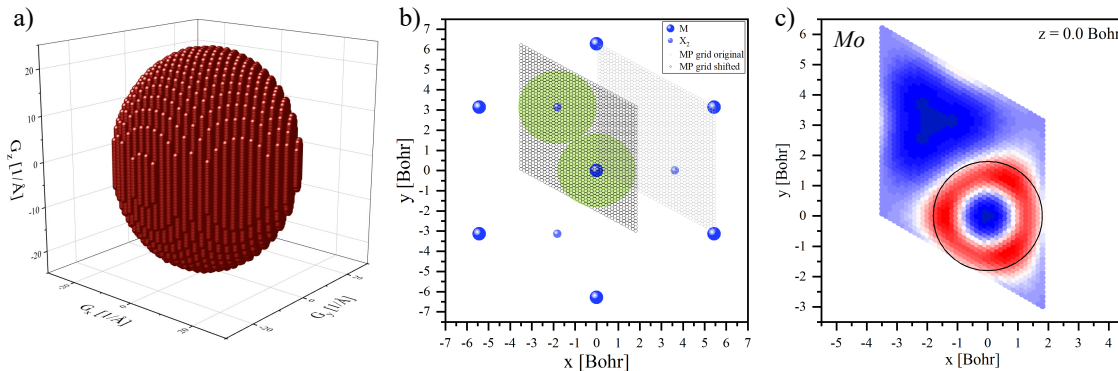


**Figure 2.1:** (a) Basis set of plane-wave  $\vec{G}$  vectors, shown in  $\text{\AA}^{-1}$  units and reduced coordinates. (b) Schematic representation of the projection spheres (green) surrounding metal ( $M$ ) atoms and chalcogen dimers ( $X_2$ ) within the UC, used for decomposing the DFT wave functions. The Monkhorst-Pack (MP) grid points are indicated as open circles. (c) Example of orbital decomposition for a Mo atom in a MoSe<sub>2</sub> monolayer at the VB  $K$ -point.

An important aspect of DFT calculations is the optimization of atomic geometries, ensuring that the system reaches a stable configuration corresponding to a global minimum on the potential energy surface. This is achieved by iteratively minimizing the total energy and atomic forces using numerical optimization techniques such as the Broyden–Fletcher–Goldfarb–Shanno (BFGS) algorithm [427], conjugate gradient methods, or damped molecular dynamics [428, 429]. The optimization process is governed by convergence criteria, typically defined in terms of energy differences between consecutive steps, maximum force thresholds, and atomic displacement tolerances. Proper geometry optimization is essential for obtaining reliable electronic and structural properties, as the final atomic configuration directly influences computed band structures, charge densities, and response functions.

In this work, DFT serves as the foundation for investigating the electronic structure of 2D materials. After obtaining the Kohn-Sham wave functions from DFT, we perform a post-DFT analysis to evaluate the contributions of spin, orbital, and layer degrees of freedom to the energy bands. These contributions are important for constructing TB models that are then used to study the effect of electron-electron interactions and predict optical properties. While DFT provides essential information about the GS electronic structure, the post-DFT analysis allows for a deeper understanding of the material’s electronic properties, which is key to exploring new materials with novel characteristics.

### 2.1.2 Post-DFT Analysis of Spin, Orbital, and Layer Contributions

Following the initial DFT calculations, it is furthermore possible to perform a post-DFT analysis to gain deeper insights into the contributions of spin, orbital character, and individual layers to the energy bands. While the Kohn-Sham wave functions provide essential information about the electronic structure, further decomposition is necessary to investigate specific features of the material, such as spin polarization and orbital hybridization. The post-DFT analysis involves several steps, which we describe in detail below.

Before discussing the details of the Kohn-Sham wave functions and charge densities, we first define the basic geometric elements used throughout this work. The system is assumed to exhibit

periodicity, hence the UC of the crystal can be defined by the primitive translation vectors  $\vec{a}_1$ ,  $\vec{a}_2$ , and  $\vec{a}_3$ . The corresponding reciprocal lattice vectors  $\vec{b}_1$ ,  $\vec{b}_2$ , and  $\vec{b}_3$  are given explicitly by:

$$\begin{aligned}\vec{b}_1 &= 2\pi \frac{\vec{a}_2 \times \vec{a}_3}{\vec{a}_1 \cdot (\vec{a}_2 \times \vec{a}_3)}, \\ \vec{b}_2 &= 2\pi \frac{\vec{a}_3 \times \vec{a}_1}{\vec{a}_2 \cdot (\vec{a}_3 \times \vec{a}_1)}, \\ \vec{b}_3 &= 2\pi \frac{\vec{a}_1 \times \vec{a}_2}{\vec{a}_3 \cdot (\vec{a}_1 \times \vec{a}_2)}.\end{aligned}\tag{2.14}$$

These reciprocal lattice vectors define the space in which wavevectors  $\vec{k}$  are constructed, enabling the description of the wave-like behavior of electrons in the periodic crystal.

We can now define the set of vectors  $\vec{G}$  that form the plane-wave basis using the reciprocal lattice vectors  $\vec{b}_i$  as:

$$\vec{G} = h\vec{b}_1 + k\vec{b}_2 + l\vec{b}_3\tag{2.15}$$

where  $h, k, l$  are integers. The magnitude of these vectors is limited by the cutoff condition  $|\vec{G}| < |\vec{G}_{\text{cutoff}}|$ .

### 2.1.2.1 Spin-Resolved Contribution to the Charge Density

To investigate the spin-polarized contributions to the charge density, we calculate the spin-resolved charge densities for each Kohn-Sham wave function  $\phi_{n,k}^{\uparrow/\downarrow}(x, y, z)$ , with  $x, y, z$  indicating the spatial coordinates within the UC. The quantity  $|\phi_{n,k}^{\uparrow/\downarrow}(x, y, z)|^2$  gives the probability density of finding an electron at a specific position within the UC. The spin-resolved charge density  $\rho_{n,k}^{\uparrow/\downarrow}$  for a wavevector  $k$ , representing the momentum of the electron in reciprocal space, and a band index  $n$ , which distinguishes the specific energy bands in the system, is given by:

$$\rho_{n,k}^{\uparrow/\downarrow} = \iint_{UC} |\phi_{n,k}^{\uparrow/\downarrow}(x, y, z)|^2 dx dy\tag{2.16}$$

The spin components are denoted as  $\uparrow$  and  $\downarrow$ , corresponding to the spin-up and spin-down contributions to the charge density, respectively. The integral is performed over the entire 2D UC of the material.

This approach allows us to examine the spin-up and spin-down charge densities, revealing spin-polarized features in the band structure. Such an analysis is important for understanding magnetic properties, such as the spin polarization of specific bands or regions of the BZ.

### 2.1.2.2 Orbital Contribution to the Charge Density

In addition to the spin contributions, we investigate the orbital contributions by projecting the wave functions onto a set of atomic orbitals or predefined basis sets. This provides an orbital-resolved density, which enables us to analyze orbital hybridization and the interplay between different orbital characters within the bands.

The Kohn-Sham spinor wave function, which includes both spin-up and spin-down components, is expressed in the plane wave basis, as implemented in the ABINIT code. It is thus given by a spinor:

$$\phi_{n,\vec{k}}(x, y, z) = \sum_{\vec{G}}^{|\vec{G}| < |\vec{G}_{\text{cutoff}}|} c_{n,\vec{k}}^{\sigma=\uparrow}(\vec{G}) e^{i(\vec{k}+\vec{G})\cdot\vec{r}} \cdot \begin{bmatrix} 1 \\ 0 \end{bmatrix} + \sum_{\vec{G}}^{|\vec{G}| < |\vec{G}_{\text{cutoff}}|} c_{n,\vec{k}}^{\sigma=\downarrow}(\vec{G}) e^{i(\vec{k}+\vec{G})\cdot\vec{r}} \cdot \begin{bmatrix} 0 \\ 1 \end{bmatrix}\tag{2.17}$$

The basis of  $\vec{G}$  vectors is presented in Fig. 2.1(a).

The normalization condition for the wave function is expressed as:

$$\sum_{\sigma} \sum_{|\vec{G}| < |\vec{G}_{\text{cutoff}}|} |c_{n,\vec{k}}^{\sigma}(\vec{G})|^2 = 1. \quad (2.18)$$

However, it is important to note that DFT software may not satisfy the normalization condition perfectly, and thus, the Kohn-Sham spinor wave functions might require a normalization procedure to ensure accuracy in subsequent calculations.

The projection of the wave functions onto atomic orbitals is performed within the spheres surrounding the atoms in the UC, as illustrated in Fig. 2.1(b).

For the orbital-resolved decomposition, we use localized Slater-like orbitals  $\varphi_{\alpha,\mu}$  to project the wave functions. These Slater orbitals are defined as [430]:

$$\varphi_{\alpha,\mu}(\vec{r}) = R_n(r)Y_{L,\mu}(\theta, \phi), \quad (2.19)$$

with  $\alpha$  being a composite index,  $\alpha = (n, L)$ , denoting the orbital type within the UC, and  $L$  represents the orbital angular momentum. For example, for a MoSe<sub>2</sub> monolayer,  $\alpha = 1$  denotes a Mo atom with  $L = 2$ , and  $\mu \in \{-2, 0, +2\}$ , while  $\alpha = 2$  corresponds to Se atoms with  $L = 1$  and  $\mu \in \{-1, 0, +1\}$ . The radial function  $R_n(r)$  is expressed as:

$$R_n(r) = \frac{(2\zeta_{n,L,m})^{n+\frac{1}{2}}}{\sqrt{(2n)!}} r^{n-1} e^{-\zeta_{n,L,m} \cdot r}, \quad (2.20)$$

where  $\zeta_{n,L,m}$  is the Slater parameter, taken from an isolated atom model [430]. The spherical harmonics  $Y_{L,\mu}(\theta, \phi)$  are given by:

$$Y_{L,\mu} = \sqrt{\frac{2L+1}{4\pi} \frac{(L-m)!}{(L+m)!}} P_L^m(\cos \theta) e^{im\theta}, \quad (2.21)$$

where  $P_L^m$  are the associated Legendre polynomials and the Condon-Shortley phase factor  $(-1)^m$  is included in the definition of these polynomials.

The projection of the wave functions onto these Slater orbitals provides a detailed information about the orbital character of the material's electronic states. Specifically, this procedure is performed within spherical regions around each atom in the UC, as shown in Fig. 2.1(b). For instance, the projection of the wave function for the Mo atom in the MoSe<sub>2</sub> monolayer at the  $K$ -point VB is shown in panel Fig. 2.1(c).

### 2.1.2.3 Layer-Resolved Contributions for Heterostructure Systems

For the vdW heterostructures, which consist of multiple layers of different materials, we also perform a layer-resolved decomposition of the charge density. This decomposition allows us to explore layer-dependent effects such as interlayer coupling, band structure variations due to stacking, and electronic effects specific to individual layers. This layer-resolved analysis is particularly important for understanding the unique properties of layered materials, such as the strong influence of layer number on their electronic and optical characteristics.

### 2.1.3 Tight-Binding Method

The TB approximation, also referred to as the linear combination of atomic orbitals (LCAO) method, starts with the atomic wave functions of isolated atoms. In this model, we assume that

an electron moving in the potential  $U(\vec{r})$  of an isolated atom is described by the atomic orbital  $\varphi_\alpha(\vec{r})$ , where the index  $\alpha$  enumerates different orbitals on the same atom.

In the following, we focus on the application of the TB methodology to periodic solids. As demonstrated in Sec. 2.1.2, such systems allow the definition of a reciprocal space, indexed by the wave vector  $\vec{k}$  (see Eq. (2.14)), which belongs to the BZ. The most general form of a single-particle wavefunction in a periodic system is then constructed as a linear combination of atomic orbitals:

$$\psi_{\vec{k}}(\vec{r}) = \sum_{j,\alpha} c_{\vec{k},j,\alpha} \varphi_\alpha(\vec{r} - \vec{r}_j), \quad (2.22)$$

where the summation runs over all atoms  $j$ , and  $\alpha$  denotes the orbital index. This wavefunction represents a superposition of atomic orbitals centered at different lattice sites in the crystal.

To determine the coefficients  $c_{\vec{k},j,\alpha}$  appearing in Eq. (2.22), we employ a systematic procedure based on Bloch's theorem. This approach involves expressing the total wavefunction as a linear combination of Bloch sums constructed for each atomic orbital within the UC. The Bloch sum corresponding to orbital  $\alpha$  is defined as:

$$\psi_{\vec{k},\alpha}(\vec{r}) = \frac{1}{\sqrt{N}} \sum_{\vec{R}_j} e^{i\vec{k}\cdot(\vec{R}_j + \vec{\tau}_\alpha)} \varphi_\alpha(\vec{r} - (\vec{R}_j + \vec{\tau}_\alpha)), \quad (2.23)$$

where  $\vec{R}_j$  denotes the lattice vector of the  $j$ -th UC,  $\vec{\tau}_\alpha$  is the position of orbital  $\alpha$  within the UC and  $N$  is the total number of UCs in the crystal. The exponential factor encodes the translational symmetry, while the orbital function  $\varphi_\alpha$  remains localized around each atomic site. By construction, this form satisfies the periodic boundary conditions of a crystal. The total single-particle wavefunction can now be expressed as a linear combination of these Bloch sums:

$$\psi_{\vec{k}}(\vec{r}) = \sum_{\alpha} c_{\vec{k},\alpha} \psi_{\vec{k},\alpha}(\vec{r}), \quad (2.24)$$

where the summation is over all atomic orbitals within the UC, and the coefficients  $c_{\vec{k},\alpha}$  now carry the full information about the band structure at a given  $\vec{k}$ .

To determine the single-electron energy in state  $\psi_{\vec{k}}(\vec{r})$ , we now proceed by inserting the wavefunction given in Eq. (2.24) into the Schrödinger equation:

$$\hat{H}\psi_{\vec{k}}(\vec{r}) = E_{\vec{k}}\psi_{\vec{k}}(\vec{r}). \quad (2.25)$$

By projecting onto the Bloch sums  $\psi_{\vec{k},\alpha}(\vec{r})$ , we get the matrix equation:

$$\langle \psi_{\vec{k},\alpha} | \hat{H} | \psi_{\vec{k}} \rangle = E_{\vec{k}} \langle \psi_{\vec{k},\alpha} | \psi_{\vec{k}} \rangle. \quad (2.26)$$

This equation must be satisfied for each orbital  $\alpha$ , yielding a system of coupled equations for the coefficients  $c_{\vec{k},\alpha}$  and the band energies  $E_{\vec{k}}$ . Thus, for each Bloch sum  $\psi_{\vec{k},\alpha}$ , Eq. (2.26) yields one equation in the system, and the full set of these equations determines the spectrum and eigenstates at a given  $\vec{k}$ -point.

There are two types of matrix elements in Eq. (2.26). The first corresponds to the right-hand side of the equation and can be expanded using Eqs. (2.24) and (2.23):

$$\langle \psi_{\vec{k},\alpha} | \psi_{\vec{k}} \rangle = \frac{1}{N} \sum_{\vec{R}_j, \vec{R}_m} e^{i\vec{k}\cdot(\vec{R}_j + \vec{\tau}_\alpha)} \sum_{\beta} c_{\vec{k},\beta} e^{i\vec{k}\cdot(\vec{R}_m + \vec{\tau}_\beta)} \langle \varphi_\alpha(\vec{r} - (\vec{R}_j + \vec{\tau}_\alpha)) | \varphi_\beta(\vec{r} - (\vec{R}_m + \vec{\tau}_\beta)) \rangle. \quad (2.27)$$

The terms  $\langle \varphi_\alpha(\vec{r} - (\vec{R}_j + \vec{\tau}_\alpha)) | \varphi_\beta(\vec{r} - (\vec{R}_m + \vec{\tau}_\beta)) \rangle$  represent the wavefunction overlap matrices. When the basis of Bloch sums is orthogonal, these overlap matrices satisfy  $\langle \psi_{\vec{k},\alpha} | \psi_{\vec{k},\beta} \rangle = \delta_{\alpha\beta}$ . The

second type of matrix elements corresponds to the left-hand side of the equation,  $\langle \psi_{\vec{k},\alpha} | \hat{H} | \psi_{\vec{k}} \rangle$ , which are the Hamiltonian matrix elements. For a given orbital  $\alpha$ , this matrix element can be expressed in terms of the localized atomic orbitals as:

$$\langle \psi_{\vec{k},\alpha} | \hat{H} | \psi_{\vec{k}} \rangle = \frac{1}{N} \sum_{\vec{R}_j, \vec{R}_m} e^{i\vec{k} \cdot (\vec{R}_j + \vec{\tau}_\alpha)} \sum_{\beta} c_{\vec{k},\beta} e^{i\vec{k} \cdot (\vec{R}_m + \vec{\tau}_\beta)} \langle \varphi_\alpha(\vec{r} - (\vec{R}_j + \vec{\tau}_\alpha)) | \hat{H} | \varphi_\beta(\vec{r} - (\vec{R}_m + \vec{\tau}_\beta)) \rangle. \quad (2.28)$$

In the above equation, the matrix element  $t_{\alpha\beta} = \langle \varphi_\alpha(\vec{r} - (\vec{R}_j + \vec{\tau}_\alpha)) | \hat{H} | \varphi_\beta(\vec{r} - (\vec{R}_m + \vec{\tau}_\beta)) \rangle$  quantifies the coupling between orbitals  $\alpha$  and  $\beta$  located at lattice sites  $\vec{R}_j + \vec{\tau}_\alpha$  and  $\vec{R}_m + \vec{\tau}_\beta$ , respectively. They define the hopping parameters  $t$ , representing the probability amplitude for electron tunneling between orbitals. These hopping elements depend on both the distance and the direction between lattice sites, as well as on the orbital character, and they typically decay with increasing interatomic separation. In systems with complex orbital structures or nontrivial symmetries, their directional dependence can significantly affect the resulting band structure.

For multi-orbital systems or materials with spin and orbital degrees of freedom, the general TB Hamiltonian in second quantization includes both diagonal (for  $\alpha = \beta$ , referred to as onsite) and off-diagonal (hopping) terms, and can be written as:

$$\hat{H} = \sum_{i,\alpha,\sigma} \varepsilon_{i,\alpha} \hat{c}_{i,\alpha,\sigma}^\dagger \hat{c}_{i,\alpha,\sigma} + \sum_{i,j,\alpha,\alpha',\sigma,\sigma'} \left( t_{i,j,\alpha,\alpha',\sigma,\sigma'} \hat{c}_{i,\alpha,\sigma}^\dagger \hat{c}_{j,\alpha',\sigma'} + \text{h.c.} \right), \quad (2.29)$$

where  $\varepsilon_{i,\alpha}$  denotes the onsite energy for orbital  $\alpha$  at site  $i$ , and  $\alpha$  and  $\sigma$  refer to orbital and spin indices, respectively. The hopping amplitudes  $t_{i,j,\alpha,\alpha',\sigma,\sigma'}$  account for tunneling processes between orbitals and include effects such as SOC.

In systems with translational symmetry and identical atoms at each site (e.g., graphene),  $\varepsilon_{i,\alpha} = \varepsilon$  can be treated as constant across the lattice. Since this uniform shift affects all bands equally, it is often set to zero without loss of generality. In this case, the Hamiltonian simplifies to the spinless, single-orbital TB model with nearest neighbour (NN) hopping:

$$\hat{H}_{\text{TB}} = \sum_{\langle i,j \rangle} t_{i,j} \hat{c}_i^\dagger \hat{c}_j + \text{h.c.}, \quad (2.30)$$

where  $\langle i,j \rangle$  denotes NN site pairs.

The TB approach provides a computationally efficient framework for modeling the electronic structure of materials, particularly when electron-electron interactions can be neglected or treated perturbatively. The band structure derived from this Hamiltonian reveals the key features governing the transport and optical properties of crystalline solids.

### 2.1.3.1 Tight-Binding Model on the Example of Graphene

As an example that will be central to our later analysis, we derive the TB Hamiltonian for monolayer graphene [431]. The electronic properties of graphene and related 2D materials can be effectively described by a TB model involving  $p_z$  orbitals arranged on a honeycomb lattice. This geometry, composed of two interpenetrating triangular sublattices labeled  $A$  and  $B$ , gives rise to bonding and antibonding states that span a band structure. Notably, the conduction and VBs touch at the  $K$  and  $K'$  points of the BZ, forming conical intersections (Dirac points) that result in a gapless, semimetallic dispersion.

Graphene consists of carbon atoms arranged in a 2D honeycomb lattice, as illustrated in Fig. 2.2(a). Each carbon atom contributes a single  $p_z$  orbital, which participates in delocalized

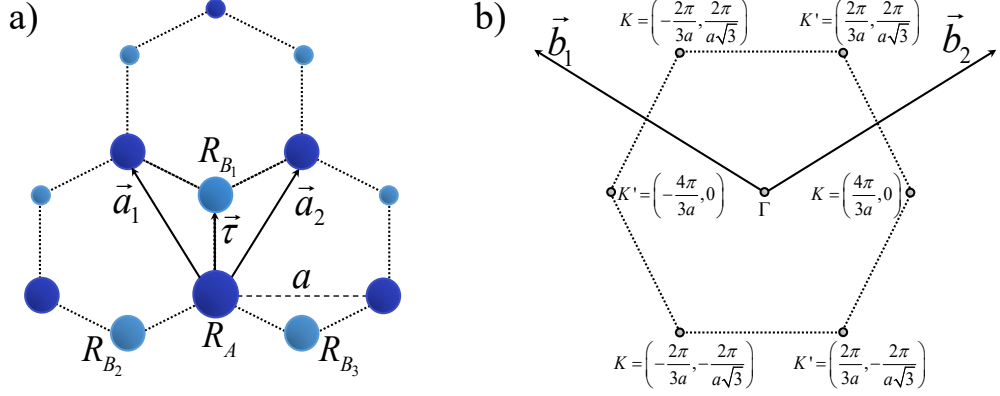


**Figure 2.2:** Honeycomb lattice geometry. (a) Honeycomb lattice in real space, showing the carbon atoms arranged in two sublattices (denoted A, dark blue, and B, light blue). The lattice constant is denoted by  $a$ . The lattice vectors are chosen as  $\vec{a}_1 = a \left(-\frac{1}{2}, \frac{\sqrt{3}}{2}\right)$  and  $\vec{a}_2 = a \left(\frac{1}{2}, \frac{\sqrt{3}}{2}\right)$ . The interatomic distance is defined as  $\vec{\tau} = a \left(0, \frac{\sqrt{3}}{2}\right)$ . (b) Corresponding BZ, with the high-symmetry points  $K$  and  $K'$  located at the corners of the hexagonal BZ, as marked.

$\pi$ -bonding responsible for the low-energy electronic structure near the Fermi level. The dominant coupling arises from NN hopping between adjacent  $p_z$  orbitals.

The lattice vectors are defined as  $\vec{a}_1 = a \left(-\frac{1}{2}, \frac{\sqrt{3}}{2}\right)$  and  $\vec{a}_2 = a \left(\frac{1}{2}, \frac{\sqrt{3}}{2}\right)$ , where  $a$  is the lattice constant. The displacement between  $A$  and  $B$  sites is given by  $\vec{\tau} = a \left(0, \frac{\sqrt{3}}{2}\right)$ . The corresponding reciprocal lattice forms a hexagonal BZ, shown in Fig. 2.2(b), with  $K$  and  $K'$  at its corners.

The general TB Hamiltonian introduced in Eq. (2.29) can be adapted to the case of graphene by considering only the  $p_z$  orbitals and restricting to NN hopping. This yields a simplified Hamiltonian:

$$\hat{H}_{\text{TB}} = -t \sum_{\langle i,j \rangle} c_i^\dagger c_j + \text{H.c.}, \quad (2.31)$$

where  $t$  is the hopping amplitude and  $\langle i,j \rangle$  denotes NN pairs.

We begin with a real-space formulation of this Hamiltonian for electrons in a periodic potential:

$$\hat{H} = \frac{\vec{p}^2}{2m} + \sum_{\vec{R}_A} V_A(\vec{r} - \vec{R}_A) + \sum_{\vec{R}_B} V_B(\vec{r} - \vec{R}_B), \quad (2.32)$$

where  $\vec{R}_{A/B}$  are the atomic positions on sublattices  $A$  and  $B$ , and  $V_{A/B}$  are the corresponding atomic potentials. We write the electronic wave function as a linear combination of Bloch states:

$$\Psi_{\vec{k}}(\vec{r}) = A(\vec{k})\psi_A(\vec{k}, \vec{r}) + B(\vec{k})\psi_B(\vec{k}, \vec{r}), \quad (2.33)$$

with Bloch functions defined by:

$$\psi_{A/B}(\vec{k}, \vec{r}) = \frac{1}{\sqrt{N}} \sum_{\vec{R}_{A/B}} e^{i\vec{k} \cdot \vec{R}_{A/B}} \phi_{A/B}(\vec{r} - \vec{R}_{A/B}), \quad (2.34)$$

where  $\phi_{A/B}(\vec{r})$  are localized atomic orbitals. Inserting this into the Schrödinger equation and projecting onto the sublattice Bloch states leads to a  $2 \times 2$  matrix Hamiltonian:

$$H_{\text{TB}}(\vec{k}) = \begin{bmatrix} \langle \psi_A | \hat{H} | \psi_A \rangle & \langle \psi_A | \hat{H} | \psi_B \rangle \\ \langle \psi_B | \hat{H} | \psi_A \rangle & \langle \psi_B | \hat{H} | \psi_B \rangle \end{bmatrix}. \quad (2.35)$$

In pristine graphene, the sublattices  $A$  and  $B$  are chemically and structurally identical, meaning they have the same onsite potential  $V_A = V_B$ . Consequently, the diagonal terms in the TB Hamiltonian, which represent the onsite energies of the  $p_z$  orbitals, are equal. These constant diagonal terms contribute an overall energy shift to the system but do not affect the relative energy differences between states. Since only these relative energies are physically meaningful for the band structure, we can eliminate this constant energy shift by redefining the energy origin. Specifically, we set the diagonal matrix elements of the Hamiltonian to zero, effectively choosing the zero of energy to correspond to the average energy of the  $p_z$  orbitals. To show it explicitly we will calculate the diagonal matrix element  $\langle \psi_A | \hat{H} | \psi_A \rangle$ , starting with substituting the Hamiltonian  $\hat{H}$  given in Eq. (2.32) into the matrix element:

$$\langle \psi_A | \hat{H} | \psi_A \rangle = \langle \psi_A | \frac{\vec{p}^2}{2m} + \sum_{\vec{R}_A} V_A(\vec{r} - \vec{R}_A) | \psi_A \rangle + \langle \psi_A | \sum_{\vec{R}_B} V_B(\vec{r} - \vec{R}_B) | \psi_A \rangle. \quad (2.36)$$

The term  $\langle \psi_A | \sum_{\vec{R}_B} V_B(\vec{r} - \vec{R}_B) | \psi_A \rangle$  represents the interaction between the  $A$ -type orbital and the potential generated by the  $B$ -type atoms. The diagonal term given in Eq. (2.36) defines the onsite energy  $E_A$  corresponding to the  $A$ -type orbital. For simplicity, we set  $E_A = 0$  to eliminate the overall energy shift.

We now need to compute the off-diagonal matrix element  $\langle \psi_A | \hat{H} | \psi_B \rangle$ , which describes the amplitude for an electron to hop from a state localized on the  $B$  sublattice to one on the  $A$  sublattice. We begin by expressing the matrix element explicitly using the full single-particle Hamiltonian:

$$\langle \psi_A | \hat{H} | \psi_B \rangle = \langle \psi_A | \frac{\vec{p}^2}{2m} + \sum_{\vec{R}_A} V_A(\vec{r} - \vec{R}_A) | \psi_B \rangle + \langle \psi_A | \sum_{\vec{R}_B} V_B(\vec{r} - \vec{R}_B) | \psi_B \rangle. \quad (2.37)$$

The first term contains the kinetic energy and the potential from atoms on the  $A$  sublattice:

$$\begin{aligned} & \langle \psi_A | \frac{\vec{p}^2}{2m} + \sum_{\vec{R}_A} V_A(\vec{r} - \vec{R}_A) | \psi_B \rangle = \\ &= \frac{1}{N} \sum_{\vec{R}_A, \vec{R}_B} e^{-i\vec{k} \cdot \vec{R}_A} e^{i\vec{k} \cdot \vec{R}_B} \int d^3r \phi_A^*(\vec{r} - \vec{R}_A) \left( \frac{\vec{p}^2}{2m} + \sum_{\vec{R}'_A} V_A(\vec{r} - \vec{R}'_A) \right) \phi_B(\vec{r} - \vec{R}_B) \\ &= \frac{1}{N} \sum_{\vec{R}_A, \vec{R}_B} e^{-i\vec{k} \cdot \vec{R}_A} e^{i\vec{k} \cdot \vec{R}_B} \int d^3r \phi_A^*(\vec{r} - \vec{R}_A) \underbrace{\left( \frac{\vec{p}^2}{2m} + V_A(\vec{r} - \vec{R}_A) \right)}_{\text{single-particle eigenenergy } E_A} \phi_B(\vec{r} - \vec{R}_B) \\ &+ \underbrace{\frac{1}{N} \sum_{\vec{R}_A, \vec{R}_B} e^{-i\vec{k} \cdot \vec{R}_A} e^{i\vec{k} \cdot \vec{R}_B} \int d^3r \phi_A^*(\vec{r} - \vec{R}_A) \sum_{\substack{\vec{R}'_A \neq \vec{R}_A \\ \vec{R}'_A \neq \vec{R}_B}} V_A(\vec{r} - \vec{R}'_A) \phi_B(\vec{r} - \vec{R}_B)}_{\text{3-center integral (negligible)}} \end{aligned} \quad (2.38)$$

Since  $\psi_A$  is constructed from atomic orbitals that are eigenstates of the operator  $\frac{\vec{p}^2}{2m} + V_A$ , the first term corresponds to the single-particle eigenenergy  $E_A$ , which we set to zero by convention. Furthermore, because  $\psi_A$  and  $\psi_B$  are formed from orbitals centered on different sublattices and assumed to have negligible spatial overlap (i.e.,  $\langle \phi_A | \phi_B \rangle \approx 0$ ), the second term represents a three-center integral, which can be safely neglected. This is a standard approximation in the TB model for orthonormal, localized orbitals. Thus, the first contribution  $\langle \psi_A | \frac{\vec{p}^2}{2m} + \sum_{\vec{R}_A} V_A(\vec{r} - \vec{R}_A) | \psi_B \rangle = 0$  and we are left with the second contribution, which arises from the potential of the  $B$  sublattice:

$$\langle \psi_A | \sum_{\vec{R}_B} V_B(\vec{r} - \vec{R}_B) | \psi_B \rangle = \frac{1}{N} \sum_{\vec{R}_A, \vec{R}_B} e^{i\vec{k} \cdot (\vec{R}_B - \vec{R}_A)} \sum_{\vec{R}'_B} \langle \phi_A(\vec{r} - \vec{R}_A) | V_B(\vec{r} - \vec{R}'_B) | \phi_B(\vec{r} - \vec{R}_B) \rangle. \quad (2.39)$$

The sum over  $\vec{R}_A$  and  $\vec{R}_B$  runs over all UC positions of the two sublattices, while the sum over  $\vec{R}'_B$  accounts for the contribution from all potential centers on sublattice  $B$ . However, due to the strong spatial localization of the atomic orbitals, the matrix element

$$\langle \phi_A(\vec{r} - \vec{R}_A) | V_B(\vec{r} - \vec{R}'_B) | \phi_B(\vec{r} - \vec{R}_B) \rangle \quad (2.40)$$

is only appreciable when  $\vec{R}_A$  and  $\vec{R}_B$  correspond to NN atoms. Therefore, we restrict the double sum to such NN pairs, yielding:

$$\langle \psi_A | \sum_{\vec{R}_B} V_B(\vec{r} - \vec{R}_B) | \psi_B \rangle = \frac{1}{N} \sum_{\langle \vec{R}_A, \vec{R}_B \rangle} e^{i\vec{k}(\vec{R}_B - \vec{R}_A)} \sum_{\vec{R}'_B} \langle \phi_A(\vec{r} - \vec{R}_A) | V_B(\vec{r} - \vec{R}'_B) | \phi_B(\vec{r} - \vec{R}_B) \rangle. \quad (2.41)$$

We now introduce the hopping parameter  $t$ , defined by:

$$\sum_{\vec{R}'_B} \langle \phi_A(\vec{r} - \vec{R}_A) | V_B(\vec{r} - \vec{R}'_B) | \phi_B(\vec{r} - \vec{R}_B) \rangle = t, \quad (2.42)$$

which quantifies the strength of the quantum mechanical coupling between neighboring atoms on the  $A$  and  $B$  sublattices. A negative value of  $t$  indicates that the bonding orbital lies lower in energy than the antibonding orbital, as is typical for bonding interactions in solids. The hopping parameter  $t$  is taken to be real and constant for all NN pairs due to lattice symmetry. There are three such NN vectors in the honeycomb lattice,  $\vec{R}_{B_i} - \vec{R}_A$  for  $i = 1, 2, 3$ , as denoted in Fig. 2.2(a). Hence, the sum over NN pairs becomes:

$$\langle \psi_A | \sum_{\vec{R}_B} V_B(\vec{r} - \vec{R}_B) | \psi_B \rangle = t \left( e^{i\vec{k}(\vec{R}_{B_1} - \vec{R}_A)} + e^{i\vec{k}(\vec{R}_{B_2} - \vec{R}_A)} + e^{i\vec{k}(\vec{R}_{B_3} - \vec{R}_A)} \right). \quad (2.43)$$

We can simplify this expression using the displacement vector  $\vec{\tau}$  from the  $A$  site to its nearest  $B$  neighbor in the UC, and lattice vectors  $\vec{a}_1, \vec{a}_2$  connecting neighboring UC. This yields the compact expression:

$$\langle \psi_A | \hat{H} | \psi_B \rangle = t e^{i\vec{k}\vec{\tau}} \left( 1 + e^{-i\vec{k}\vec{a}_1} + e^{-i\vec{k}\vec{a}_2} \right). \quad (2.44)$$

We now define the structure factor:

$$f(\vec{k}) = e^{i\vec{k}\vec{\tau}} \left( 1 + e^{-i\vec{k}\vec{a}_1} + e^{-i\vec{k}\vec{a}_2} \right), \quad (2.45)$$

which contains all the geometric information about the hopping between sublattices in reciprocal space. Therefore, the off-diagonal element of the Hamiltonian becomes:

$$\langle \psi_A | \hat{H} | \psi_B \rangle = t f(\vec{k}), \quad (2.46)$$

which will later enter the Bloch Hamiltonian matrix and play a role in determining the band structure of graphene.

The above calculation yields the final form of the TB Hamiltonian:

$$H_{\text{TB}}(\vec{k}) = \begin{bmatrix} 0 & t \cdot f(\vec{k}) \\ t \cdot f^*(\vec{k}) & 0 \end{bmatrix}. \quad (2.47)$$

Thus, we have derived the TB Hamiltonian for graphene by considering NN hopping between  $p_z$  orbitals on the two sublattices. This simplified model captures the essential low-energy behavior of graphene, particularly the linear dispersion near the Dirac points ( $K$  and  $K'$ ) in the BZ. The resulting Hamiltonian provides a robust foundation for exploring more complex phenomena in graphene and related systems, such as electron-electron interactions, disorder, or the influence of external fields.

### 2.1.4 Massive Dirac Fermion Model and the Effect of Vertical Magnetic Field

Expanding the TB Hamiltonian in the vicinity of the  $K$  and  $K'$  points leads to an effective low-energy theory described by massless DFs in 2D [85, 432]. This approximation captures key features of the electronic spectrum in graphene, such as the linear dispersion, pseudospin degree of freedom, and Berry phase effects, while significantly simplifying the mathematical structure of the problem.

When inversion or sublattice symmetry is broken — for example, through substrate effects, intrinsic SOC, or structural asymmetry — a gap opens at the Dirac points. In this case, the low-energy physics is governed by a massive Dirac Hamiltonian. This generalization describes a wide class of 2D semiconductors, including monolayer TMDCs, where the Dirac mass is finite and valley and spin degrees of freedom are strongly coupled [180, 433, 434].

The massive Dirac Fermion (mDF) model thus provides a compact and symmetry-based description of single-particle excitations near the band extrema in these materials. It retains essential features of the underlying lattice structure while offering analytical tractability and intuitive access to phenomena such as valley-dependent optical selection rules, Berry curvature, and magnetic response. In what follows, we systematically derive and analyze the mDF model starting from the lattice-scale TB Hamiltonian.

In the following section, we present detailed derivations of both the massless and massive Dirac Fermion models, alongside the methodology used to incorporate magnetic field effects into the mDF framework [435].

#### 2.1.4.1 Massless Dirac Fermions in Graphene

To analyze the low-energy excitations in graphene, we expand the TB Hamiltonian derived in Eq. (2.47) around the Dirac points in the BZ. These points, labeled  $K$  and  $K'$ , are located at the corners of the hexagonal BZ and are defined as:

$$\vec{K} = \frac{4\pi}{3a} (1, 0), \quad \vec{K}' = \frac{4\pi}{3a} (-1, 0), \quad (2.48)$$

where  $a$  is the lattice constant. We denote both points collectively as  $\vec{K}_\nu$  with  $\nu = \pm 1$  for the  $K$  and  $K'$  valleys, respectively. Letting  $\vec{k} = \vec{K}_\nu + \vec{q}$ , where  $\vec{q}$  is a small momentum deviation from the Dirac point, we expand the function  $f(\vec{k})$  to first order in  $\vec{q}$ :

$$f(\vec{K}_\nu + \vec{q}) = 1 + e^{-i(\vec{K}_\nu + \vec{q}) \cdot \vec{a}_1} + e^{-i(\vec{K}_\nu + \vec{q}) \cdot \vec{a}_2} \quad (2.49)$$

$$\approx 1 + e^{-i\vec{K}_\nu \cdot \vec{a}_1} (1 - i\vec{q} \cdot \vec{a}_1) + e^{-i\vec{K}_\nu \cdot \vec{a}_2} (1 - i\vec{q} \cdot \vec{a}_2). \quad (2.50)$$

At the Dirac points, the sum of phase factors vanishes due to destructive interference:

$$1 + e^{-i\vec{K}_\nu \cdot \vec{a}_1} + e^{-i\vec{K}_\nu \cdot \vec{a}_2} = 0, \quad (2.51)$$

which simplifies the expansion to:

$$f(\vec{K}_\nu + \vec{q}) \approx -i \left[ e^{-i\vec{K}_\nu \cdot \vec{a}_1} \vec{q} \cdot \vec{a}_1 + e^{-i\vec{K}_\nu \cdot \vec{a}_2} \vec{q} \cdot \vec{a}_2 \right]. \quad (2.52)$$

This linear dependence of  $f(\vec{k})$  on  $\vec{q}$  leads directly to the effective low-energy Hamiltonian near the Dirac points. Substituting the expansion into the TB Hamiltonian, we obtain the Dirac Hamiltonian in two dimensions:

$$\hat{H}_{\text{DF}} = \hbar v_F (\nu q_x \sigma_x + q_y \sigma_y), \quad (2.53)$$

where  $\sigma_{x,y}$  are Pauli matrices acting on the sublattice (pseudospin) degree of freedom, and the Fermi velocity is given by  $\hbar v_F = \frac{3}{2}ta$ . The valley index  $\nu = \pm 1$  accounts for the  $K$  and  $K'$  points.

The eigenvalues of this Hamiltonian are:

$$E_{\pm} = \pm \hbar v_F |\vec{q}|, \quad (2.54)$$

describing a conical, linear dispersion relation characteristic of massless DFs. This result captures several hallmark features of graphene, including its high carrier mobility, the chiral nature of quasi-particles, and the presence of a nontrivial Berry phase, which underlies the anomalous quantum Hall effect [2].

#### 2.1.4.2 Massive Dirac Fermions in Transition Metal Dichalcogenides

Unlike graphene, monolayer TMDCs exhibit a direct band gap at the  $K$  and  $K'$  valleys due to the presence of strong spin-orbit interaction and the absence of inversion symmetry, resulting from the fact that the two sublattices of the honeycomb lattice are occupied by two different atom types—a transition metal and a chalcogen—which breaks the inversion symmetry of the crystal. The general TB and DFT models reveal that the low-energy physics of TMDCs can still be effectively captured by a Dirac-like Hamiltonian. However, in contrast to graphene, this model includes a mass term that opens a band gap and additional spin-valley coupling [302] induced by spin-orbit effects:

$$\hat{H}_{\text{mDF}} = \hbar v_F (\nu k_x \sigma_x + k_y \sigma_y) + \frac{\Delta}{2} \sigma_z + \lambda \nu s_z \sigma_z, \quad (2.55)$$

where  $\Delta$  denotes the band gap,  $\lambda$  is the spin-orbit coupling parameter,  $\nu = \pm 1$  distinguishes the  $K$  and  $K'$  valleys,  $s_z$  is the spin index, and  $\sigma_i$  are Pauli matrices acting in the pseudospin space. This effective Hamiltonian describes massive DFs with spin-valley locking, which plays a key role in the valley-selective optical and transport properties of monolayer TMDCs. The Hamiltonian in Eq. (2.55) can now be written in matrix form, neglecting SOC, for the two low-energy bands—namely, the CB and the VB—as:

$$\hat{H}_{\text{mDF}} = \begin{bmatrix} \frac{\Delta}{2} & \hbar v_F (\nu q_x - i q_y) \\ \hbar v_F (\nu q_x + i q_y) & -\frac{\Delta}{2} \end{bmatrix}, \quad (2.56)$$

The presence of the mass term  $\Delta$  modifies the linear energy dispersion characteristic of graphene. Diagonalizing the Hamiltonian in Eq. (2.56) yields the energy eigenvalues:

$$E = \pm \sqrt{(\hbar v_F)^2 |\vec{q}|^2 + \left(\frac{\Delta}{2}\right)^2}, \quad (2.57)$$

where  $|\vec{q}|$  is the magnitude of the wavevector measured from the valley center. The resulting band structure exhibits an energy gap of magnitude  $\Delta$ , indicating that the carriers behave as massive DFs with an effective rest energy of  $\Delta/2$ .

To find the wave functions, we solve the eigenvalue problem for the matrix Hamiltonian in Eq. (2.56). The eigenstates for the conduction and VBs at the  $K$  and  $K'$  points take the form:

$$\begin{aligned} K : \quad |\psi^{\text{CB}}\rangle &= \frac{1}{N^{\text{CB/VB}}} \begin{pmatrix} \frac{\Delta}{2} + |E| \\ \hbar v_F |\vec{q}| e^{i\theta} \end{pmatrix}, \quad |\psi^{\text{VB}}\rangle = \frac{1}{N^{\text{CB/VB}}} \begin{pmatrix} -\hbar v_F |\vec{q}| e^{-i\theta} \\ \frac{\Delta}{2} + |E| \end{pmatrix}, \\ K' : \quad |\psi^{\text{CB}}\rangle &= \frac{1}{N^{\text{CB/VB}}} \begin{pmatrix} \frac{\Delta}{2} + |E| \\ -\hbar v_F |\vec{q}| e^{-i\theta} \end{pmatrix}, \quad |\psi^{\text{VB}}\rangle = \frac{1}{N^{\text{CB/VB}}} \begin{pmatrix} \hbar v_F |\vec{q}| e^{i\theta} \\ \frac{\Delta}{2} + |E| \end{pmatrix}, \end{aligned} \quad (2.58)$$

where  $\theta$  is the polar angle of the wavevector  $\vec{q}$  and  $N^{\text{CB/VB}} = \sqrt{2|E|(|E| + \Delta/2)}$  is the normalization factor ensuring  $\langle \psi | \psi \rangle = 1$ . The presence of two non-equivalent sublattices,  $A$  and  $B$ , is reflected in the spinor form of the wave functions, where each component corresponds to one of the sublattices in the honeycomb lattice of TMDCs. This structure is described using the concept of pseudospin, which refers to the degree of freedom associated with the occupation of the sublattices. Similar to real spin, pseudospin can take one of two states, corresponding to the occupation of the  $A$  or  $B$  sublattice. The valley index  $\nu = \pm 1$  (for the  $K$  and  $K'$  valleys) is associated with the chirality of the wave function. In the  $K$  valley, the wave function exhibits left-handed chirality, with the phase rotating counterclockwise, whereas in the  $K'$  valley, the chirality is right-handed, with the phase rotating clockwise. This valley-dependent chirality is reflected in the form factors  $f(\vec{k})$ , where the opposite sign of the valley index  $\nu$  results in the corresponding opposite chirality. This chirality plays an important role in the material's response to external fields, such as optical or magnetic fields, and is key to the unique properties of TMDCs.

The Hamiltonian given in Eq. (2.56) can be furthermore extended to account for the spin degrees of freedom, thus incorporating the SOC effects into the mDF model, which is important for understanding the valley- and spin-dependent phenomena in TMDC monolayers, such as the Valley Zeeman effect and the spin-polarized optical transitions. The SOC-modified Hamiltonian can be written as:

$$\hat{H}_{\text{SOC}} = \begin{bmatrix} \frac{\Delta}{2} + \frac{\Delta_{\text{SOC}}^{\text{CB}}}{2} & v_F(\nu q_x - iq_y) & 0 & 0 \\ v_F(\nu q_x + iq_y) & -\frac{\Delta}{2} - \frac{\Delta_{\text{SOC}}^{\text{VB}}}{2} & 0 & 0 \\ 0 & 0 & \frac{\Delta}{2} - \frac{\Delta_{\text{SOC}}^{\text{CB}}}{2} & v_F(\nu q_x - iq_y) \\ 0 & 0 & v_F(\nu q_x + iq_y) & -\frac{\Delta}{2} + \frac{\Delta_{\text{SOC}}^{\text{VB}}}{2} \end{bmatrix} \quad (2.59)$$

where  $\Delta_{\text{SOC}}^{\text{CB}}$  and  $\Delta_{\text{SOC}}^{\text{VB}}$  are the SOC splittings at the top of the VB and the bottom of the CB, respectively. The energies of the four spin-resolved low-energy bands can be obtained by diagonalizing the Hamiltonian in Eq. (2.59). The resulting energy spectrum is given by:

$$E = \frac{\Delta_{\text{SOC}}^{\text{CB}} - \Delta_{\text{SOC}}^{\text{VB}}}{4} \pm \nu \frac{1}{2} \sqrt{\left(\Delta + \frac{\Delta_{\text{SOC}}^{\text{CB}} + \Delta_{\text{SOC}}^{\text{VB}}}{2}\right)^2 + 3t^2 a^2 |\vec{q}|^2}. \quad (2.60)$$

The presence of both a mass term and strong spin-orbit interaction enables rich valley- and spin-dependent phenomena in monolayer TMDCs, including valley-selective optical transitions and spin-valley locking, with promising implications for applications in valleytronic devices [433, 434].

The transition from the massless to the mDF model is central to capturing the low-energy electronic properties of various 2D materials. In graphene, the effective low-energy Hamiltonian around the  $K$  and  $K'$  points reduces to a massless Dirac equation due to the combination of sublattice symmetry and negligible intrinsic SOC. However, in materials such as monolayer TMDCs, strong SOC and broken inversion symmetry, along with the fact that the sublattices are composed of different atoms (with sublattice  $A$  consisting of metal atoms and sublattice  $B$  consisting of chalcogenide dimers), lead to the emergence of a finite Dirac mass term. This mass modifies the band structure by opening an energy gap at the Dirac points, transforming the system into a direct-gap semiconductor. From a modeling perspective, the mDF Hamiltonian provides a computationally efficient and analytically tractable approximation of the band edges in 2D semiconductors, and it forms the foundation for exploring spin-valley coupling, Berry curvature effects, and valley-selective optical transitions. These features are particularly relevant for understanding the optoelectronic and valleytronic response of 2D materials in both equilibrium and driven regimes.

### 2.1.4.3 Inclusion of the Vertical Magnetic Field

In the next step, building upon the methodology presented above, we include the magnetic field into the description of the single-particle states. Both massless and massive Dirac fermion models provide a convenient starting point for studying the influence of external magnetic fields. When a magnetic field  $B$  is applied, the system undergoes Landau quantization, where the continuous electronic spectrum is replaced by discrete LLs. The magnetic field enters the Hamiltonian through the vector potential  $\vec{A}$ , which modifies the momentum operator as  $\vec{p} \rightarrow \vec{p} + e\vec{A}$ .

For graphene, the LL spectrum derived from Eq. (2.53) with the inclusion of magnetic field according to  $\vec{q} \rightarrow \vec{q} + e\vec{A}$  is characterized by the energies [2, 436, 437]:

$$E_n = \frac{\hbar v_F}{l_B} \sqrt{2n}, \quad (2.61)$$

where  $n$  is the LL index, and  $l_B = \sqrt{\hbar/eB}$  is the magnetic length. The characteristic square-root dependence on the LL index  $n$  is a hallmark of massless DFs.

In contrast, for TMDCs, the inclusion of the mass term modifies the LL structure, reflecting the finite mass of the carriers, resulting in a quantum Hall effect with integer quantization, distinct from graphene. Moreover, the interplay of SOC and valley degrees of freedom gives rise to valley-contrasting magnetic responses, enabling selective valley polarization under circularly polarized light [14].

We start by incorporating the vector potential  $\vec{A}(t)$  into the mDF Hamiltonian defined in Eq. (2.56) (for now we neglect the SOC). In the presence of an external magnetic field, chosen as  $\vec{B} = [0, 0, B]$ , the momentum operator  $\vec{q}$  is replaced by  $\vec{p} + |e|\vec{A}$ . We use the symmetric gauge for the vector potential,  $\vec{A} = \left[-\frac{By}{2}, \frac{Bx}{2}, 0\right]$ , which leads to the following form for both valleys:

$$\hat{H}_B = \begin{bmatrix} \frac{\Delta}{2} & v_F \left( \nu \left( p_x - \frac{eB}{2\hbar} y \right) - i \left( p_y + \frac{eB}{2\hbar} x \right) \right) \\ v_F \left( \nu \left( p_x + \frac{eB}{2\hbar} y \right) + i \left( p_y - \frac{eB}{2\hbar} x \right) \right) & -\frac{\Delta}{2} \end{bmatrix}, \quad (2.62)$$

where  $\nu$  corresponds to the valley index, with  $\nu = +1$  for the  $K$  valley and  $\nu = -1$  for the  $K'$  valley. Here,  $\Delta$  is the energy gap of the system and  $v_F$  represents the Fermi velocity.

The canonical momentum is given by  $\vec{p} = -i\hbar\nabla$ . Substituting these into the Hamiltonian, we obtain:

$$\hat{H}_B = \begin{bmatrix} \frac{\Delta}{2} & v_F \left( -\nu i \partial_x - \partial_y - \frac{eB}{2\hbar} (\nu y + ix) \right) \\ v_F \left( -\nu i \partial_x + \partial_y - \frac{eB}{2\hbar} (\nu y - ix) \right) & -\frac{\Delta}{2} \end{bmatrix}. \quad (2.63)$$

To diagonalize the Hamiltonian in Eq. (2.63), we introduce the ladder operators [438, 439]:

$$\begin{aligned} \hat{a} &= \frac{l_B}{\sqrt{2}} \left( \partial_x - \partial_y + \frac{1}{2l_B^2} (-iy + x) \right), \\ \hat{a}^\dagger &= \frac{l_B}{\sqrt{2}} \left( -\partial_x - \partial_y + \frac{1}{2l_B^2} (iy + x) \right), \end{aligned} \quad (2.64)$$

where  $l_B = \sqrt{\frac{\hbar}{eB}}$  is the magnetic length, and the commutation relation  $[\hat{a}, \hat{a}^\dagger] = 1$  holds. Using these ladder operators, we can express the Hamiltonian for both valleys as:

$$\hat{H}_B(K) = \begin{bmatrix} \frac{\Delta}{2} & -i \frac{v_F \sqrt{2}}{l_B} \hat{a} \\ i \frac{v_F \sqrt{2}}{l_B} \hat{a}^\dagger & -\frac{\Delta}{2} \end{bmatrix} \quad \text{and} \quad \hat{H}_B(K') = \begin{bmatrix} \frac{\Delta}{2} & -i \frac{v_F \sqrt{2}}{l_B} \hat{a}^\dagger \\ i \frac{v_F \sqrt{2}}{l_B} \hat{a} & -\frac{\Delta}{2} \end{bmatrix}. \quad (2.65)$$

Diagonalizing the Hamiltonian, we obtain the energy spectrum of the LLs. The energy eigenvalues for the CB and VB are:

$$E_n^{\text{VB/CB}} = \pm \sqrt{\left( \frac{v_F \sqrt{2}}{l_B} \right)^2 n + \left( \frac{\Delta}{l_B} \right)^2}, \quad (2.66)$$

where the “+” sign corresponds to the CB states and the “-” sign to the VB states, respectively. The index  $n$  represents the LL index, which takes integer values  $n = 0, 1, 2, \dots$ , respectively.

To fully describe the wave functions in a 2D system under a perpendicular magnetic field, we must account for two quantum numbers (two chiralities). The previously defined ladder operators  $\hat{a}$  and  $\hat{a}^\dagger$  raise and lower the LL index  $n$ , associated with radial excitations. Meanwhile, a second set of ladder operators  $\hat{b}$  and  $\hat{b}^\dagger$  account for the second quantum number index  $m$ , reflecting the degeneracy within each LL. These are defined analogously as:

$$\begin{aligned}\hat{b} &= \frac{l_B}{\sqrt{2}} \left( \partial_y + \frac{1}{l_B^2} (ix - y) \right), \\ \hat{b}^\dagger &= \frac{l_B}{\sqrt{2}} \left( -\partial_y + \frac{1}{l_B^2} (ix + y) \right).\end{aligned}\quad (2.67)$$

These operators satisfy the commutation relation  $[\hat{b}, \hat{b}^\dagger] = 1$ , and commute with  $\hat{a}$  and  $\hat{a}^\dagger$ . Together,  $\hat{a}$  and  $\hat{b}$  define the full Fock space of the 2D harmonic oscillator in the presence of a magnetic field. Importantly,  $\hat{b}$  and  $\hat{b}^\dagger$  also commute with the Hamiltonian, which depends only on  $\hat{a}$  and  $\hat{a}^\dagger$ . This leads to the characteristic LL degeneracy, as the energy eigenvalues depend solely on the action of  $\hat{a}$  and  $\hat{a}^\dagger$ , while different  $\hat{b}$ -states remain degenerate.

The wave functions are the solutions of the 2D harmonic oscillator and can be now written as:

$$\begin{aligned}\hat{a} |n, m\rangle &= \sqrt{n} |n-1, m\rangle, & \hat{a}^\dagger |n, m\rangle &= \sqrt{n+1} |n+1, m\rangle; \\ \hat{b} |n, m\rangle &= \sqrt{m} |n, m-1\rangle, & \hat{b}^\dagger |n, m\rangle &= \sqrt{m+1} |n, m+1\rangle.\end{aligned}\quad (2.68)$$

For both valleys, these wave functions can be written as:

$$|\psi_{n,m}^{\text{VB/CB}}(K)\rangle = \begin{pmatrix} \alpha_n^{\text{VB/CB}} |n-1, m\rangle \\ \beta_n^{\text{VB/CB}} |n, m\rangle \end{pmatrix} \quad \text{and} \quad |\psi_{n,m}^{\text{VB/CB}}(K')\rangle = \begin{pmatrix} \alpha_n^{\text{VB/CB}} |n, m\rangle \\ \beta_n^{\text{VB/CB}} |n-1, m\rangle \end{pmatrix}. \quad (2.69)$$

The coefficients  $\alpha$  and  $\beta$  are derived by diagonalizing the mDF Hamiltonian with the included magnetic field, as given in Eq. (2.64), yielding the following expressions:

$$\alpha_n^{\text{VB/CB}} = -i \frac{v_F \sqrt{2} \sqrt{n}}{l_B N_n^{\text{VB/CB}}}, \quad \beta_n^{\text{VB/CB}} = \frac{E_n^{\text{VB/CB}} - \frac{\Delta}{2}}{N_n^{\text{VB/CB}}}, \quad (2.70)$$

where  $N_n^{\text{VB/CB}}$  is the normalization constant, defined as  $N_n^{\text{VB/CB}} = \sqrt{E_n^{\text{VB/CB}} (2E_n^{\text{VB/CB}} - \Delta)}$ .

Next, we can incorporate the effects of SOC. The magnetic Hamiltonian, as given in Eq. (2.65), can be rewritten in the spin-resolved basis for the low-energy bands,  $\{\text{CB } \downarrow, \text{VB } \downarrow, \text{CB } \uparrow, \text{VB } \uparrow\}$ , and takes the following form:

$$\begin{aligned}\hat{H}_B(K) &= \begin{bmatrix} \frac{\Delta}{2} + \frac{\Delta_{\text{SOC}}^{\text{CB}}}{2} & -ic\hat{a} & 0 & 0 \\ ic\hat{a}^\dagger & -\frac{\Delta}{2} - \frac{\Delta_{\text{SOC}}^{\text{VB}}}{2} & 0 & 0 \\ 0 & 0 & \frac{\Delta}{2} - \frac{\Delta_{\text{SOC}}^{\text{CB}}}{2} & -ic\hat{a} \\ 0 & 0 & ic\hat{a}^\dagger & -\frac{\Delta}{2} + \frac{\Delta_{\text{SOC}}^{\text{VB}}}{2} \end{bmatrix} \\ \hat{H}_B(K') &= \begin{bmatrix} \frac{\Delta}{2} + \frac{\Delta_{\text{SOC}}^{\text{CB}}}{2} & -ic\hat{a}^\dagger & 0 & 0 \\ ic\hat{a} & -\frac{\Delta}{2} - \frac{\Delta_{\text{SOC}}^{\text{VB}}}{2} & 0 & 0 \\ 0 & 0 & \frac{\Delta}{2} - \frac{\Delta_{\text{SOC}}^{\text{CB}}}{2} & -ic\hat{a}^\dagger \\ 0 & 0 & ic\hat{a} & -\frac{\Delta}{2} + \frac{\Delta_{\text{SOC}}^{\text{VB}}}{2} \end{bmatrix}.\end{aligned}\quad (2.71)$$

For simplicity, we define  $c = \frac{v_F \sqrt{2}}{l_B}$ . The energy expression now becomes:

$$E_{n,s,v}^{\text{VB/CB}} = -\nu_s \frac{\Delta_{\text{SOC}}^{\text{CB}} - \Delta_{\text{SOC}}^{\text{VB}}}{4} \pm \sqrt{c^2 n + \frac{1}{4} \left( \Delta + \frac{\Delta_{\text{SOC}}^{\text{CB}} + \Delta_{\text{SOC}}^{\text{VB}}}{2} \right)^2}. \quad (2.72)$$

The mDF model is useful in describing the electronic properties of materials like graphene and TMDCs. Unlike graphene, which features massless DFs with linear energy dispersion, TMDC monolayers exhibit a finite bandgap due to SOC and inversion symmetry breaking. The mDF Hamiltonian incorporates these effects, leading to valley-selective optical transitions.

When an external magnetic field is introduced, Landau quantization occurs, transforming the continuous electronic spectrum into discrete LLs. For massless DFs in graphene, the LL spectrum follows a characteristic square-root dependence, leading to an anomalous quantum Hall effect. In contrast, in TMDCs, the presence of the Dirac mass term modifies the LL structure, resulting in a more complicated magnetic field dependence of the LL energies and valley-dependent magnetic responses. These effects are important for understanding SOC, valley polarization under circularly polarized light, and potential applications in valleytronics and optoelectronic devices.

## 2.2 Electron-Electron Interactions in 2D Crystals

Thus far, we have focused on the single-particle properties of 2D systems, treating electron-electron interactions at the mean-field level. In this approximation, each electron is assumed to move independently in an effective potential, neglecting the full complexity of many-body correlations. However, to accurately describe the electronic, optical, and magnetic properties of low-dimensional materials, electron-electron interactions beyond the mean-field approximation must be explicitly included. This is important in 2D systems, where reduced dielectric screening enhances Coulomb interactions and amplifies correlation effects.

The challenge in incorporating these interactions arises from the exponential growth of the Hilbert space when considering many-electron configurations. A full treatment of the interacting system requires constructing a many-body basis composed of antisymmetrized states built from single-particle orbitals, such as Slater determinants. This approach forms the foundation of configuration interaction (CI) methods, where the many-electron wavefunction is expressed as a linear combination of such configurations. While conceptually straightforward, the number of configurations increases combinatorially with the number of electrons and available orbitals, quickly making brute-force diagonalization of the full Hamiltonian computationally unfeasible.

In addition to the sheer size of the Hilbert space, mean-field theories neglect some essential physical effects that arise from electron-electron interactions. These include some aspects of screening, whereby the spatial distribution of charge carriers alters the potential landscape experienced by other electrons, as well as collective excitations such as plasmons and excitons that emerge from correlated charge dynamics. Such phenomena are particularly pronounced in 2D materials, where the reduced dimensionality and confinement amplify the role of Coulomb interactions and lead to a range of unconventional electronic and optical behaviors.

To describe these effects, the full interacting Hamiltonian must be considered. In the formalism of second quantization, the many-body Hamiltonian takes the form:

$$\hat{H}_C = \sum_i \epsilon_i \hat{c}_i^\dagger \hat{c}_i + \frac{1}{2} \sum_{i,j,k,l} \langle i, j | V_C | k, l \rangle \hat{c}_i^\dagger \hat{c}_j^\dagger \hat{c}_k \hat{c}_l. \quad (2.73)$$

Here, the first term describes the single-particle energies  $\epsilon_i$  and corresponding creation and annihilation operators  $\hat{c}_i^\dagger$  and  $\hat{c}_i$ , while the second term encodes the electron-electron interactions through the Coulomb matrix elements (CMEs)  $\langle i, j | V_C | k, l \rangle$ . These matrix elements quantify the amplitude for two electrons in orbitals  $k$  and  $l$  to scatter into orbitals  $i$  and  $j$ , mediated by the Coulomb potential.

An exact diagonalization of this Hamiltonian is generally impractical for realistic systems, necessitating the development of efficient and scalable approximations that capture the essential physics of electron correlation while remaining computationally tractable. In the following sections, we introduce the CI method as a framework for constructing and solving many-body wavefunctions from a selected basis of configurations, presented in Sec. 2.2.1. We then in Sec. 2.2.2 describe how CMEs can be evaluated in atomistic models, followed by a treatment of how magnetic fields influence electron-electron scattering in confined systems, as shown in Sec. 2.2.3. Finally, in Sec. 2.2.4, we present approaches for modeling screening effects in low-dimensional materials, including the conventional static screening approximation—which treats screening as a uniform, frequency-independent dielectric response—and the more refined Rytova-Keldysh model, which captures the nonlocal and environment-dependent static screening characteristic of 2D crystals. Both approaches are essential for accurately describing effective interactions governing correlated behavior in these systems.

## 2.2.1 Configuration Interaction Method

To determine the eigenstates of the many-body Hamiltonian defined in Eq. (2.73), we employ the CI method. In this approach, many-body wavefunctions are expressed as linear combinations of Slater determinants, where each determinant corresponds to a distinct arrangement of electrons in a set of single-particle orbitals.

Let us consider a set of orthonormal single-particle states  $\{\psi_i\}$ , which represent quantum states (such as orbitals or energy levels) that electrons can occupy. These states are obtained as a solution of the single-particle problem, for example via the TB or mDF approach, as described in Sec. 2.1. For each single-particle state  $\psi_i$ , we define creation and annihilation operators  $\hat{c}_i^\dagger$  and  $\hat{c}_i$ , which respectively add or remove an electron to/from the state  $\psi_i$ . These operators obey the standard anticommutation relations:

$$\{\hat{c}_i^\dagger, \hat{c}_j^\dagger\} = \{\hat{c}_i, \hat{c}_j\} = 0, \quad \{\hat{c}_i, \hat{c}_j^\dagger\} = \delta_{ij}. \quad (2.74)$$

A many-body configuration with  $N$  electrons occupying the single-particle states  $\psi_{i_1}, \psi_{i_2}, \dots, \psi_{i_N}$  is constructed by applying the corresponding creation operators to the vacuum state:

$$|\Phi_\alpha\rangle = \hat{c}_{i_1}^\dagger \hat{c}_{i_2}^\dagger \cdots \hat{c}_{i_N}^\dagger |0\rangle, \quad (2.75)$$

where the indices are ordered as  $i_1 < i_2 < \dots < i_N$ . This specific ordering is essential because the fermionic creation operators obey anticommutation relations, ensuring that exchanging any two electrons changes the sign of the wavefunction, thereby guaranteeing its antisymmetric nature. In real-space representation, this antisymmetric wavefunction corresponds exactly to a Slater determinant.

To better illustrate this construction, let us consider a model system of three spin-degenerate single-particle orbitals:  $\psi_1$ ,  $\psi_2$ , and  $\psi_3$ . Each orbital supports two spin states,  $\uparrow$  and  $\downarrow$ , leading to six single-particle spin-orbitals:

$$\psi_1^\uparrow, \psi_1^\downarrow, \psi_2^\uparrow, \psi_2^\downarrow, \psi_3^\uparrow, \psi_3^\downarrow. \quad (2.76)$$

These spin-orbitals are indexed as:

$$\begin{aligned} \psi_1^\uparrow &\rightarrow i = 1, & \psi_1^\downarrow &\rightarrow i = 2, \\ \psi_2^\uparrow &\rightarrow i = 3, & \psi_2^\downarrow &\rightarrow i = 4, \\ \psi_3^\uparrow &\rightarrow i = 5, & \psi_3^\downarrow &\rightarrow i = 6. \end{aligned} \quad (2.77)$$

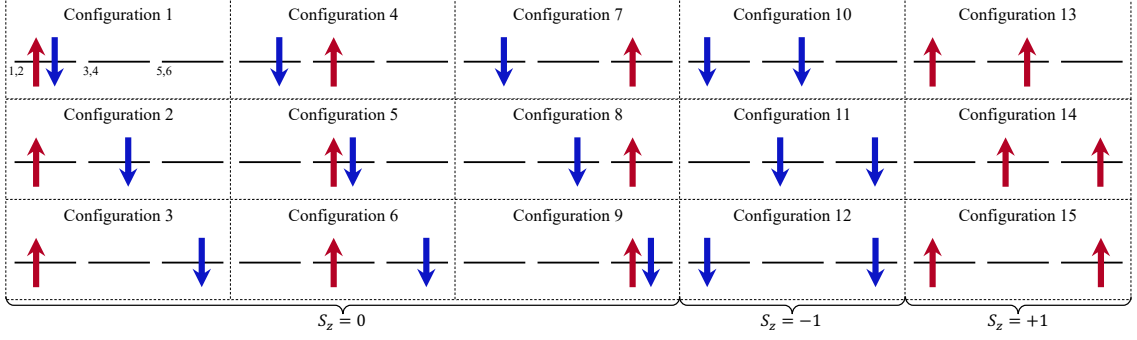


**Figure 2.3:** Schematic representation of all possible two-electron configurations in a system with three spin-degenerate single-particle orbitals. Each horizontal line corresponds to an orbital ( $\psi_1$ ,  $\psi_2$ ,  $\psi_3$ ), and arrows indicate electron occupation. Spin-up and spin-down electrons are represented by arrows of different colors (red for spin-up, blue for spin-down). The 15 possible configurations are grouped according to their total spin projection  $S_z$ : configurations with  $S_z = 0$  (one spin-up and one spin-down),  $S_z = -1$  (both spins down), and  $S_z = +1$  (both spins up).

Let us now enumerate all possible ways of placing two electrons in these six states. Since electrons are fermions, each configuration must involve two distinct indices  $i < j$ :

$$|\Phi_{ij}\rangle = \hat{c}_i^\dagger \hat{c}_j^\dagger |0\rangle, \quad 1 \leq i < j \leq 6. \quad (2.78)$$

There are  $\binom{6}{2} = 15$  such antisymmetric configurations. These can be grouped according to the total spin projection  $S_z$  of the configuration:

- 9 configurations with one spin-up and one spin-down electron ( $S_z = 0$ ),
- 3 configurations with both electrons spin-down ( $S_z = -1$ ),
- 3 configurations with both electrons spin-up ( $S_z = +1$ ).

This classification is useful when exploiting spin symmetries or analyzing singlet and triplet excitations.

As an example, one of the  $S_z = 0$  configurations is:

$$|\Phi_{1,4}\rangle = \hat{c}_1^\dagger \hat{c}_4^\dagger |0\rangle \quad (\text{electrons in } \psi_1^\uparrow, \psi_2^\downarrow \equiv \text{configuration 2}), \quad (2.79)$$

which corresponds to the Slater determinant:

$$\langle \vec{r}_1, \vec{r}_2 | \Phi_{1,4} \rangle = \frac{1}{\sqrt{2}} \left[ \psi_1^\uparrow(\vec{r}_{e_1}) \psi_2^\downarrow(\vec{r}_{e_2}) - \psi_2^\downarrow(\vec{r}_{e_1}) \psi_1^\uparrow(\vec{r}_{e_2}) \right], \quad (2.80)$$

where  $\vec{r}_{e_1}$  and  $\vec{r}_{e_2}$  denote the coordinates of the two electrons  $e_1$  and  $e_2$ .

A schematic overview of all 15 configurations is provided in Fig. 2.3. These 15 configurations span the complete Hilbert space of the two-electron system. In the CI framework, the many-body eigenstates are approximated as linear combinations of these basis configurations:

$$|\Psi_n\rangle = \sum_{\alpha=1}^{15} C_\alpha^{(n)} |\Phi_\alpha\rangle, \quad (2.81)$$

where  $C_\alpha^{(n)}$  are the CI coefficients, obtained by diagonalizing the Hamiltonian in the chosen configuration basis. This allows the method to include electron correlation by mixing configurations with different electron arrangements.

The matrix representation of the Hamiltonian  $\hat{H}_C$  in the CI basis consists of both diagonal and off-diagonal elements. Each matrix element captures contributions from the single-particle kinetic energies and the two-particle Coulomb interactions, including both direct and exchange terms.

For a given configuration  $|\Phi_\alpha\rangle$ , the diagonal elements include the sum of the single-particle energies  $\epsilon_i$  of the occupied orbitals, as well as the expectation value of the Coulomb interaction within the same configuration. The Coulomb contribution consists of two parts: the direct term  $\langle ij|V|ji\rangle$ , which describes the classical electrostatic repulsion between electrons occupying orbitals  $\psi_i$  and  $\psi_j$ , thus contributing positively to the total energy, and the exchange term  $\langle ij|V|ij\rangle$ , which arises from the antisymmetry of the fermionic wavefunction and typically lowers the energy by enforcing the Pauli exclusion principle. The exchange term can be viewed as an effective attractive interaction between electrons with parallel spins. The diagonal matrix elements are thus given by:

$$H_{\alpha\alpha} = \sum_{i \in \text{occ.}} \epsilon_i + \frac{1}{2} \sum_{i,j \in \text{occ.}} (\langle ij|V|ji\rangle - \langle ij|V|ij\rangle), \quad (2.82)$$

where the factor 1/2 avoids double-counting electron pairs. The CMEs appearing above are defined as:

$$\langle ij|V|ji\rangle = \iint \psi_i^*(\vec{r}_1)\psi_j^*(\vec{r}_2) \frac{e^2}{4\pi\epsilon_0|\vec{r}_1 - \vec{r}_2|} \psi_j(\vec{r}_2)\psi_i(\vec{r}_1) d\vec{r}_1 d\vec{r}_2, \quad (2.83)$$

$$\langle ij|V|ij\rangle = \iint \psi_i^*(\vec{r}_1)\psi_j^*(\vec{r}_2) \frac{e^2}{4\pi\epsilon_0|\vec{r}_1 - \vec{r}_2|} \psi_i(\vec{r}_2)\psi_j(\vec{r}_1) d\vec{r}_1 d\vec{r}_2. \quad (2.84)$$

The off-diagonal matrix elements arise purely from the Coulomb interaction, which can couple different configurations. In particular, nonzero off-diagonal elements occur when two configurations  $|\Phi_\alpha\rangle$  and  $|\Phi_\beta\rangle$  differ by the occupation of one or two single-particle states. Such matrix elements incorporate both direct and exchange Coulomb contributions and are essential for capturing electron-electron correlations beyond the mean-field level. Configurations that differ by more than two orbitals are not connected by the two-body interaction operator and thus yield zero matrix elements.

The full CI basis grows exponentially with the number of particles and orbitals, making a complete treatment impractical. To address this, the basis is truncated to a subset of  $M$  configurations, typically selected based on the lowest kinetic energy or other physically motivated criteria. Once the basis is defined, the Hamiltonian matrix is constructed by computing all relevant diagonal and off-diagonal elements. Numerical diagonalization of this matrix (e.g., using LAPACK [440]) yields the eigenvalues and the eigenvectors of the many-body problem written in a general form as  $|\Psi_n\rangle = \sum_\alpha C_\alpha^{(n)} |\Phi_\alpha\rangle$ . The resulting eigenstates, including the GS and excited states, are expressed as superpositions of the selected configurations, with the CI coefficients  $C_\alpha^{(n)}$  reflecting the degree of configuration mixing induced by electron-electron interactions. Accurate evaluation of the CMEs is thus central to determining the interaction-induced structure of the many-body states. The next section focuses on the computation of these two-body integrals.

## 2.2.2 Coulomb Matrix Elements in Atomistic Basis

In this Section, we present the methodology for computing the Coulomb matrix elements (CMEs) [95, 98], which quantify electron-electron interaction strengths in many-body systems. Accurate evaluation of CMEs is needed for describing electronic structure and interaction energies, especially in simulations involving large particle numbers or multiple orbitals. We introduce an atomistic approach for calculating CMEs that strikes a balance between computational efficiency and the accuracy required for large-scale systems, enabling feasible calculations without compromising essential physical details.

To compute the CMEs, we first express the wavefunction  $\psi_i$  as a sum over atomic orbitals. This is done by expanding  $\psi_i$  in terms of the atomic orbitals  $\zeta_j$  centered at various atomic sites  $\vec{R}_j$ , with expansion coefficients  $D_j^{(i)}$ :

$$\psi_i = \sum_j D_j^{(i)} \zeta_j(\vec{r} - \vec{R}_j). \quad (2.85)$$

In this expression, the index  $j$  is a composite index that includes both the atomic site index  $n$  and the orbital index  $\mu$  associated with that site. The coefficients  $D_j^{(i)}$  are the properly normalized expansion coefficients of the wavefunction. The functions  $\zeta_j(\vec{r} - \vec{R}_j)$  are Slater-type orbitals, such as  $p_z$  orbitals in graphene.

With the wavefunction expressed in this form, we can now write the CMEs explicitly. The interaction between different electron states is given by the following expression:

$$\begin{aligned} \langle i, j | V_C | k, l \rangle &= \sum_p \left( D_p^{(i)} \right)^* \sum_q \left( D_q^{(j)} \right)^* \sum_r D_r^{(k)} \sum_s D_s^{(l)} \\ &\times \int \zeta_p^*(\vec{r}_1 - \vec{R}_p) \zeta_s(\vec{r}_1 - \vec{R}_s) d\vec{r}_1 \int \zeta_q^*(\vec{r}_2 - \vec{R}_q) \zeta_r(\vec{r}_2 - \vec{R}_r) d\vec{r}_2 \frac{2}{|\vec{r}_1 - \vec{r}_2|}. \end{aligned} \quad (2.86)$$

Since atomic orbitals are tightly localized around their atomic sites, significant overlap occurs only when atoms  $p$  and  $s$  (as well as  $q$  and  $r$ ) are spatially close. Otherwise, the overlap integrals vanish, significantly reducing computational effort. By leveraging this property, we extract the site-orbital-defined Coulomb operator  $\langle p, q | V_C | r, s \rangle$  from Eq. (2.86):

$$\langle p, q | V_C | r, s \rangle = \int \zeta_p^*(\vec{r}_1 - \vec{R}_p) \zeta_s(\vec{r}_1 - \vec{R}_s) d\vec{r}_1 \int \zeta_q^*(\vec{r}_2 - \vec{R}_q) \zeta_r(\vec{r}_2 - \vec{R}_r) d\vec{r}_2 \frac{2}{|\vec{r}_1 - \vec{r}_2|}. \quad (2.87)$$

These matrix elements are required for many-body physics simulations, but computing them directly can be highly computationally expensive. The complexity of calculating these interactions scales as  $O(N^4)$ , where  $N$  represents the number of basis functions used to describe the electron states. This scaling arises from the structure of the Coulomb integrals, which take the form  $\langle p, q | V_C | r, s \rangle$ , where  $p, q, r, s$  label atomic orbitals. Each of these indices runs over all  $N$  orbitals, leading to  $N^4$  combinations that must be considered. These integrals involve evaluating the electron-electron interaction between all possible pairs of orbital products, typically through spatial integrals over the Coulomb kernel.

To emphasize the computational challenge, consider a system with  $N = 10^6$  atomic orbitals. Even if evaluating a single Coulomb integral  $\langle p, q | V_C | r, s \rangle$  took just one CPU cycle (approximately 1 nanosecond), computing all  $N^4$  integrals would require on the order of  $10^{24}$  operations, corresponding to  $10^{15}$  seconds, or roughly the age of the universe ( $\sim 435 \times 10^{15}$  seconds). Clearly, brute-force evaluation is not feasible for large systems.

To address this bottleneck, efficient numerical techniques are required to approximate or reduce the cost of computing CMEs, such as exploiting sparsity, using localized basis functions, or applying resolution-of-identity and multipole expansions.

In the next step, we classify the site-orbital-defined Coulomb kernel  $\langle p, q | V_C | r, s \rangle$  into two interaction types: long-range and short-range interactions.

For long-range interactions, we consider only terms where  $\vec{R}_p = \vec{R}_s$  and  $\vec{R}_q = \vec{R}_r$ , as these provide the dominant contribution. When the atomic separation  $|\vec{R}_p - \vec{R}_q|$  is significantly larger than the extent of the charge distribution (typically beyond second NN), the charge density can be approximated as point charges. Under this approximation, the Coulomb denominator in Eq. (2.87)

simplifies to atomic positions, leading to:

$$\langle p, q | V_{LD} | r, s \rangle = \int \zeta_p^* (\vec{r}_1 - \vec{R}_p) \zeta_s (\vec{r}_1 - \vec{R}_p) dr_1 \int \zeta_q^* (\vec{r}_2 - \vec{R}_q) \zeta_r (\vec{r}_2 - \vec{R}_q) dr_2 \frac{2}{|\vec{R}_p - \vec{R}_q|}. \quad (2.88)$$

For identical orbitals, the integrals over  $\vec{r}_1$  and  $\vec{r}_2$  reduce to simple overlap integrals that normalize to 1. In contrast, if the orbitals differ (e.g. in TMDC layers within TB models where Molybdenum atoms possess five distinct  $d$  orbitals), the integrals vanish. For nonzero overlaps, the long-range interaction simplifies to a classical Coulomb form:

$$\langle p, q | V_{LD} | q, p \rangle = \frac{2}{|\vec{R}_p - \vec{R}_q|}. \quad (2.89)$$

This simplification reduces the computational complexity from  $O(N^4)$  to  $O(N^2)$ .

In contrast, short-range interactions occur when  $\vec{R}_p$ ,  $\vec{R}_s$ ,  $\vec{R}_q$ , and  $\vec{R}_r$  are in close proximity (typically within second NN). In these cases, the integrals in Eq. (2.87) must be computed explicitly, incorporating Slater-type orbital approximations:

$$\langle p, q | V_{SD} | r, s \rangle = \int \zeta_p^* (\vec{r}_1 - \vec{R}_p) \zeta_s (\vec{r}_1 - \vec{R}_s) dr_1 \int \zeta_q^* (\vec{r}_2 - \vec{R}_q) \zeta_r (\vec{r}_2 - \vec{R}_r) dr_2 \frac{2}{|\vec{r}_1 - \vec{r}_2|}. \quad (2.90)$$

By distinguishing between long- and short-range Coulomb interactions, this methodology provides an efficient and physically meaningful framework for calculating CMEs in atomistic models. While specific numerical implementations may vary depending on the material, the principles outlined here serve as a foundation for incorporating electron-electron interactions in a computationally feasible manner.

While we outline the core principles and methods here, the specific numerical techniques for efficiently calculating these matrix elements must be tailored to the material under consideration. Such techniques may involve various approximations or optimizations (e.g., truncating distant interactions or using advanced methods for orbital overlap integration), which depend on the specific characteristics of the material or system being modeled. These strategies are not described in detail here, as they require adaptation to the particular case at hand.

### 2.2.3 Electron-Electron Scattering Matrix Elements in an External Magnetic Field

In Sec. 2.1.4, we introduced the mDF Hamiltonian for a single electron in an external magnetic field. In this section, we extend our analysis to systems containing multiple electrons by focusing on two-body interactions between electron pairs in the presence of the magnetic field. Specifically, we compute the electron-electron Coulomb scattering matrix elements, which characterize these pairwise interactions. These matrix elements can be computed analytically [441–444].

To facilitate these calculations, we adopt effective atomic units defined by the effective Bohr radius  $a_B$  and the effective Rydberg energy  $Ry$ , given by:

$$a_B = \frac{\varepsilon \hbar^2}{m^* e^2}, \quad Ry = \frac{e^2}{2\varepsilon a_B} = \frac{\hbar^2}{2m^* a_B^2}, \quad (2.91)$$

where  $\varepsilon$  is the dielectric constant and  $m^*$  is the electron's effective mass. With the effective units introduced above, the Coulomb interaction potential takes the form:

$$V_C (|\vec{r}_1 - \vec{r}_2|) = \frac{2}{|\vec{r}_1 - \vec{r}_2|}, \quad (2.92)$$

where distances are measured in units of the effective Bohr radius  $a_B$ , and energies are in effective Rydbergs  $Ry$ . In second quantization, the electron-electron Coulomb interaction Hamiltonian is written as:

$$\hat{H}_C = \frac{1}{2} \sum_{i,j,k,l} \langle i, j | V_C | k, l \rangle \hat{c}_i^\dagger \hat{c}_j^\dagger \hat{c}_k \hat{c}_l, \quad (2.93)$$

where the indices  $i, j, k, l$  label single-particle states. Each index is a composite of the harmonic oscillator quantum numbers  $n$  and  $m$ :

$$i = (n'_1, m'_1), \quad j = (n'_2, m'_2), \quad k = (n_2, m_2), \quad l = (n_1, m_1). \quad (2.94)$$

To proceed with the analysis, we express the position coordinates of each particle in terms of the raising and lowering operators [438] as follows:

$$x = \frac{l_B}{\sqrt{2}} (\hat{a} + \hat{a}^\dagger + \hat{b} + \hat{b}^\dagger), \quad y = \frac{il_B}{\sqrt{2}} (\hat{a} - \hat{a}^\dagger - \hat{b} + \hat{b}^\dagger), \quad (2.95)$$

where  $l_B$  is the magnetic length, and  $\hat{a}$  and  $\hat{b}$  are the respective lowering operators for the  $x$  and  $y$  coordinates.

We start by unfolding the Coulomb interaction into the plane waves' basis:

$$\langle i, j | V_C | k, l \rangle = \langle i, j | \sum_q V_C^q e^{i\vec{q}(\vec{r}_1 - \vec{r}_2)} | k, l \rangle = \sum_q V_C^q \langle i | e^{i\vec{q}\vec{r}_1} | l \rangle \langle j | e^{-i\vec{q}\vec{r}_2} | k \rangle, \quad (2.96)$$

where  $V_C^q = \frac{4\pi}{q}$  is the Fourier transform of the 2D Coulomb potential  $V_C$ . We focus on calculating the first term in the above equation,  $e^{i\vec{q}\vec{r}_1}$ . With the use of the Cartesian coordinates operators, as defined in Eq. (2.95), we obtain:

$$e^{i\vec{q}\vec{r}_1} = e^{iQ^* \hat{a}_1^\dagger + iQ \hat{a}_1 + iQ \hat{b}_1^\dagger + iQ^* \hat{b}_1}, \quad (2.97)$$

with  $Q = \frac{l_B}{\sqrt{2}}(q_x + iq_y)$ . Using the Trotter-Suzuki formula  $e^{\hat{A} + \hat{B}} = e^{\hat{A}} e^{\hat{B}} e^{-\frac{1}{2}[\hat{A}, \hat{B}]}$  we can rewrite Eq. (2.97) as:

$$e^{i\vec{q}\vec{r}_1} = e^{-|Q|^2} e^{iQ^* \hat{a}_1^\dagger} e^{iQ \hat{a}_1} e^{iQ \hat{b}_1^\dagger} e^{iQ^* \hat{b}_1}, \quad (2.98)$$

and analogously:

$$e^{-i\vec{q}\vec{r}_2} = e^{-|Q|^2} e^{-iQ^* \hat{a}_2^\dagger} e^{-iQ \hat{a}_2} e^{-iQ \hat{b}_2^\dagger} e^{-iQ^* \hat{b}_2}. \quad (2.99)$$

Having the terms  $e^{i\vec{q}\vec{r}_1}$  and  $e^{-i\vec{q}\vec{r}_2}$  defined by Eq. (2.98) and (2.99), we can now calculate the matrix elements for both particles. The procedure will be presented on the example of the first particle, while the matrix element for the second particle can be calculated analogously. We calculate the matrix element  $\langle i | e^{i\vec{q}\vec{r}_1} | l \rangle$ :

$$M_1 = \langle i | e^{i\vec{q}\vec{r}_1} | l \rangle = \langle i | e^{-|Q|^2} e^{iQ^* \hat{a}_1^\dagger} e^{iQ \hat{a}_1} e^{iQ \hat{b}_1^\dagger} e^{iQ^* \hat{b}_1} | l \rangle = \frac{1}{\sqrt{n'_1! m'_1! n_1! m_1!}} \langle 0, 0 | (\hat{b}_1)^{m'_1} (\hat{a}_1)^{n'_1} e^{-|Q|^2} e^{iQ^* \hat{a}_1^\dagger} e^{iQ \hat{b}_1^\dagger} \hat{1} e^{iQ \hat{a}_1} e^{iQ^* \hat{b}_1} (\hat{a}_1^\dagger)^{n_1} (\hat{b}_1^\dagger)^{m_1} | 0, 0 \rangle. \quad (2.100)$$

We introduced here the operator

$$\hat{1} = \sum_{p_1=0}^{\infty} \sum_{p_2=0}^{\infty} |p_1, p_2\rangle \langle p_2, p_1| = \frac{1}{p_1! p_2!} \sum_{p_1=0}^{\infty} \sum_{p_2=0}^{\infty} (\hat{a}_1^\dagger)^{p_1} (\hat{b}_1^\dagger)^{p_2} |0, 0\rangle \langle 0, 0| (\hat{b}_1)^{p_2} (\hat{a}_1)^{p_1}. \quad (2.101)$$

The exponential operators can be unfolded now in Taylor series, e.g.  $e^{iQ \hat{a}_1} = \sum_{s=0}^{\infty} \frac{(iQ)^s}{s!} (\hat{a}_1)^s$ . It turns out now that the indices  $p_1$  and  $p_2$  can only change from 0 to  $\min(n_1, n'_1)$  and from 0 to

$\min(m_1, m'_1)$ , respectively. Furthermore, the matrix element is nonzero only for certain powers of lowering and raising operators. As a result we obtain the matrix element in the following form:

$$M_1 = \frac{e^{-|Q|^2}}{\sqrt{n_1! m'_1! n_1! m_1!}} \sum_{p_1=0}^{\min(n_1, n'_1)} \sum_{p_2=0}^{\min(m_1, m'_1)} p_1! p_2! \binom{n'_1}{p_1} \binom{n_1}{p_1} \binom{m'_1}{p_1} \binom{m_1}{p_1} \quad (2.102)$$

$$\times (iQ^*)^{n'_1-p_1} (iQ)^{m'_1-p_2} (iQ)^{n_1-p_1} (iQ^*)^{m_1-p_2}.$$

Calculating the matrix element for the second particle  $M_2$  analogously and combining the two terms we get:

$$\langle n_1, m_1; n_2, m_2 | V_C | n_3, m_3; n_4, m_4 \rangle = \frac{1}{4\pi^2} \int_0^{2\pi} q dq \int_0^{2\pi} \frac{4\pi}{q} M_1 M_2 d\phi_q =$$

$$\frac{1}{\sqrt{n_1! m_1! n_2! m_2! n_3! m_3! n_4! m_4!}} \sum_{p_1=0}^{\min(n_1, n_4)} p_1! \binom{n_1}{p_1} \binom{n_4}{p_1} \sum_{p_2=0}^{\min(m_1, m_4)} p_2! \binom{m_1}{p_2} \binom{m_4}{p_2} \quad (2.103)$$

$$\times \sum_{p_3=0}^{\min(n_2, n_3)} p_3! \binom{n_2}{p_3} \binom{n_3}{p_3} \sum_{p_4=0}^{\min(m_2, m_3)} p_4! \binom{m_2}{p_4} \binom{m_3}{p_4} \frac{1}{\pi} I_{p_1 p_2 p_3 p_4},$$

where the integral is defined as:

$$I_{p_1 p_2 p_3 p_4} = \int_0^\infty dq \int_0^{2\pi} d\phi_q e^{-2|Q|^2} (iQ^*)^{n'_1-p_1} (iQ)^{m'_1-p_2} (iQ)^{n_1-p_1} (iQ^*)^{m_1-p_2} \quad (2.104)$$

$$\times (-iQ^*)^{n'_2-p_3} (-iQ)^{m'_2-p_4} (-iQ)^{n_2-p_3} (-iQ^*)^{m_2-p_4}.$$

In order to unfold the integral  $I_{p_1 p_2 p_3 p_4}$  we change the variables. We write  $Q$  in the exponential form  $Q = |Q| e^{i\phi_q} = \frac{l_B}{\sqrt{2}} q e^{i\phi_q}$ , where we set  $|Q| = \frac{l_B}{\sqrt{2}} q$ , so that  $dq = d|Q| \frac{\sqrt{2}}{l_B}$ . Collecting carefully the modulus of  $Q$ , the phases of  $Q$ , the imaginary parts  $i$  and the  $(-1)$  appearing for the second particle, we can finally separate the integral  $I_{p_1 p_2 p_3 p_4}$  into two integrals: the one over  $Q$  and the one over  $\phi_q$ , respectively. We start by analyzing the integral over  $\phi_q$ :

$$\int_0^{2\pi} d\phi_q e^{i\phi_q(-n'_1+m'_1+n_1-m_1-n'_2+m'_2+n_2-m_2)} = 2\pi \delta_{R_L, R_R}, \quad (2.105)$$

where  $R_L = (m'_1 + m'_2) - (n'_1 + n'_2)$  defines the angular momentum of the pair of particles on the left hand side of the matrix element, and  $R_R = (m_1 + m_2) - (n_1 + n_2)$  - on the right hand side, respectively, hence  $\delta_{R_L, R_R}$  corresponds to the angular momentum conservation rule. From  $R_L = R_R$  we obtain  $n'_1 + n'_2 + m'_1 + m'_2 + n_1 + n_2 + m_1 + m_2 - 2p_1 - 2p_2 - 2p_3 - 2p_4 = 2p$ , hence the integral  $I_{p_1 p_2 p_3 p_4}$  defined in Eq. (2.104) can be rewritten as:

$$I_{p_1 p_2 p_3 p_4} = \frac{2\pi\sqrt{2}}{l_B} \int_0^\infty dQ e^{-2Q^2} (2Q)^{2p} \left(-\frac{1}{2}\right)^p (-1)^{n'_2+m'_2+n_2+m_2}, \quad (2.106)$$

where  $Q \equiv |Q|$ . We change the variables once again, defining  $x = 2Q^2$ , so that  $dx = 4QdQ$  and  $dQ = \frac{dx\sqrt{2}}{4\sqrt{x}}$ , and we get:

$$I_{p_1 p_2 p_3 p_4} = \frac{\pi}{l_B} \left(-\frac{1}{2}\right)^p (-1)^{n'_2+m'_2+n_2+m_2} \int_0^\infty dx e^{-x} x^{\frac{p+1}{2}} =$$

$$\frac{\pi}{l_B} \left(-\frac{1}{2}\right)^p (-1)^{n'_2+m'_2+n_2+m_2} \Gamma\left(p + \frac{1}{2}\right). \quad (2.107)$$

Collecting all the calculated terms together we obtain the final form of the Coulomb interaction

matrix element:

$$\begin{aligned}
\langle n'_1, m'_1; n'_2, m'_2 | V_C | n_1, m_1; n_2, m_2 \rangle &= \frac{1}{l_B} \frac{\delta_{R_L, R_R} (-1)^{n'_2 + m'_2 + n_2 + m_2}}{\sqrt{n'_1! m'_1! n'_2! m'_2! n_1! m_1! n_2! m_2!}} \left(-\frac{1}{2}\right)^p \Gamma\left(p + \frac{1}{2}\right) \\
&\times \sum_{p_1=0}^{\min(n_1, n'_1)} p_1! \binom{n'_1}{p_1} \binom{n_1}{p_1} \sum_{p_2=0}^{\min(m_1, m'_1)} p_2! \binom{m'_1}{p_2} \binom{m_1}{p_2} \\
&\times \sum_{p_3=0}^{\min(n_2, n'_2)} p_3! \binom{n'_2}{p_3} \binom{n_2}{p_3} \sum_{p_4=0}^{\min(m_2, m'_2)} p_4! \binom{m'_2}{p_4} \binom{m_2}{p_4}.
\end{aligned} \tag{2.108}$$

We developed the framework for calculating the Coulomb interaction matrix elements for interacting electrons in a magnetic field. Using effective atomic units defined by the effective Bohr radius  $a_B$  and the effective Rydberg energy  $Ry$ , we expressed the Coulomb interaction in terms of CMEs for effective-mass electrons in 2D in a magnetic field, which enabled us to unfold the Hamiltonian in terms of plane waves and compute the matrix elements.

We focused on how the matrix elements depend on the LL indices and the quantum numbers of the electrons, such as the angular momenta and the specific quantum states involved. The matrix elements include angular momentum conservation and show how the Coulomb interaction takes a specific form based on these quantum numbers.

The final expression for the Coulomb interaction matrix element, derived in Eq. (2.108), captures the full complexity of the electron-electron interactions under the influence of a magnetic field. This formalism enables further studies into many-body effects in systems under magnetic fields, with applications in understanding quantum Hall systems and related phenomena.

## 2.2.4 Effective Coulomb Interaction in Low-Dimensional Systems

In many-body physics, screening refers to the phenomenon where the presence of other charges reduces the effective interaction between two electrons [36, 217, 445, 446]. In a solid, electrons do not interact in isolation; instead, the surrounding electron cloud and ionic lattice rearrange in response to their presence, thereby partially “screening” the Coulomb interaction. This effect plays an important role in accurately describing electron-electron interactions, as it modifies the bare Coulomb potential, often weakening it significantly.

To model this screening effect, several approaches can be employed. A simplified treatment, known as static screening, approximates the effect by using a constant screening length. However, for a more nuanced and distance-dependent description, the Rytova-Keldysh approach [447, 448] provides a more detailed treatment of the screened Coulomb interaction. These methods allow for a more precise understanding of how screening influences the effective interactions in 2D systems, which is important for capturing many-body effects in such materials.

### 2.2.4.1 Static Screening

In the static screening model, electron-electron interactions are approximated by scaling the bare Coulomb potential with a dielectric constant  $\epsilon_r$ . This is based on the assumption that the surrounding medium’s response to electron-electron interactions is averaged and uniform, which simplifies the interaction between the charges. The scaled interaction is represented by the following screened Coulomb potential:

$$V_{\text{screened}}(r) = \frac{e^2}{4\pi\epsilon_r r}, \tag{2.109}$$

where  $e$  is the elementary charge,  $\varepsilon_r$  is the effective dielectric constant of the material, and  $r$  is the separation between two charges. This model uses a constant dielectric constant which does not vary with position or time. As such, it assumes a mean-field-like approximation, where the material is treated as homogeneous, and the dielectric properties do not change significantly throughout the system.

The static screening model is a scaled version of the bare Coulomb potential. This model is particularly effective in bulk materials or systems where the dielectric environment remains relatively stable and uniform. It provides a good first approximation in many cases, especially when more complex, spatially dependent models are not required. Despite its inability to capture spatial variations in the screening, static screening remains a valuable reference model in both theoretical and computational studies. It is often employed as a starting point for more refined approaches or when the computational cost of more sophisticated treatments becomes prohibitive.

### 2.2.4.2 Rytova-Keldysh Screening Model

In low-dimensional systems, the static screening model often falls short, as the dielectric constant can vary significantly, especially near boundaries or interfaces with a substrate or vacuum. In materials such as 2D semiconductors or graphene, screening is strongly influenced by the reduced dimensionality and environmental factors, leading to a spatially dependent dielectric response [217]. This limitation arises because static screening assumes a uniform dielectric environment, which does not accurately reflect the behavior of extended 2D systems. To address this, the Rytova-Keldysh model [447, 448] was introduced by solving the electrostatics problem for a dielectric sheet embedded between different media, capturing the non-local nature of screening. In this framework, the Coulomb interaction between charges depends on their separation, with the spatial dependence encoded through the wavevector  $q$ . The model incorporates the thickness of the dielectric sheet and the permittivities of the surrounding environments, providing a more accurate description of electron-electron interactions in 2D materials.

We aim to derive the Rytova-Keldysh potential [447, 448] in the context of a 2D material surrounded by different media, taking into account dielectric response and screening effects [36, 216, 446, 449]. We begin by solving the Poisson equation for the electrostatic potential  $\Phi(\vec{r})$  in the 3D real space. The Poisson equation in the CGS system of units is given by:

$$\nabla^2 \Phi(\vec{r}) = -4\pi\rho(\vec{r}), \quad (2.110)$$

where  $\rho(\vec{r})$  is the charge density, and  $\Phi(\vec{r})$  is the electrostatic potential at position  $\vec{r}$ . To simplify the problem, we take the Fourier transform of both sides of the Poisson equation. The Fourier transform of a function  $f(\vec{r})$  is defined as:

$$\tilde{f}(\vec{q}) = \int d^3r f(\vec{r}) e^{-i\vec{q}\cdot\vec{r}}, \quad (2.111)$$

where  $\tilde{f}(\vec{q})$  is the Fourier transform of  $f(\vec{r})$ , and  $\vec{q}$  is the wavevector. Now, applying the Fourier transform to both sides of the Poisson equation:

$$\mathcal{F}[\nabla^2 \Phi(\vec{r})] = \mathcal{F}[-4\pi\rho(\vec{r})], \quad (2.112)$$

For the left-hand side, we need to apply the Fourier transform to  $\nabla^2 \Phi(\vec{r})$ . The Laplacian operator in real space corresponds to multiplication by  $-q^2$  in Fourier space. Thus, we have:

$$\mathcal{F}[\nabla^2 \Phi(\vec{r})] = -q^2 \tilde{\Phi}(\vec{q}), \quad (2.113)$$

where  $q = |\vec{q}|$  is the magnitude of the wavevector. The Fourier transform of  $\rho(\vec{r})$  is simply:

$$\mathcal{F}[\rho(\vec{r})] = \tilde{\rho}(\vec{q}), \quad (2.114)$$

so the Fourier transform of the right-hand side becomes:

$$\mathcal{F}[-4\pi\rho(\vec{r})] = -4\pi\tilde{\rho}(\vec{q}). \quad (2.115)$$

Thus, in Fourier space:

$$-q^2\tilde{\Phi}(\vec{q}) = -4\pi\tilde{\rho}(\vec{q}), \quad (2.116)$$

which simplifies to:

$$q^2\tilde{\Phi}(\vec{q}) = 4\pi\tilde{\rho}(\vec{q}). \quad (2.117)$$

Solving for  $\tilde{\Phi}(\vec{q})$  gives:

$$\tilde{\Phi}(\vec{q}) = \frac{4\pi\tilde{\rho}(\vec{q})}{q^2}. \quad (2.118)$$

The prefactor  $\frac{4\pi}{q^2}$  is the Fourier representation of the Green's function in vacuum, and is recognized as the bare Coulomb interaction in momentum space:

$$\tilde{\Phi}_{\text{bare}}(q) = \frac{4\pi e}{q^2}. \quad (2.119)$$

This shows that the electrostatic potential can be interpreted as the product:

$$\tilde{\Phi}(\vec{q}) = \frac{\tilde{\Phi}_{\text{bare}}(q)\tilde{\rho}(\vec{q})}{e}, \quad (2.120)$$

which emphasizes that the potential is a response to the charge density, mediated by the bare Coulomb interaction.

We now derive the form of the Coulomb interaction when the system is confined to a 2D plane. We model a 2D charge distribution localized in the  $z = 0$  plane:

$$\rho(\vec{r}) = \sigma(\vec{r}_{\parallel})\delta(z), \quad (2.121)$$

where  $q^2 = q_{\parallel}^2 + q_z^2$  and  $\sigma(\vec{r}_{\parallel})$  is the 2D charge density. The Fourier transform of  $\rho(\vec{r})$  becomes:

$$\tilde{\rho}(\vec{q}) = \int d^2r_{\parallel} \sigma(\vec{r}_{\parallel}) e^{-i\vec{q}_{\parallel} \cdot \vec{r}_{\parallel}} \int dz \delta(z) e^{-iq_z z}, \quad (2.122)$$

which evaluates to:

$$\tilde{\rho}(\vec{q}) = \tilde{\sigma}(\vec{q}_{\parallel}), \quad (2.123)$$

because  $\int dz \delta(z) e^{-iq_z z} = 1$ . Thus, the electrostatic potential in momentum space reads:

$$\tilde{\Phi}(\vec{q}_{\parallel}, q_z) = \frac{4\pi}{q_{\parallel}^2 + q_z^2} \tilde{\sigma}(\vec{q}_{\parallel}). \quad (2.124)$$

To obtain the effective potential in 2D, we integrate out the  $q_z$  dependence and performing the partial inverse Fourier transform we get:

$$\tilde{\Phi}_{2D}(\vec{q}_{\parallel}) = \int \frac{dq_z}{2\pi} e^{iq_z z} \tilde{\Phi}(\vec{q}_{\parallel}, q_z) \Big|_{z=0} = \int \frac{dq_z}{2\pi} \tilde{\Phi}(\vec{q}_{\parallel}, q_z), \quad (2.125)$$

leading to:

$$\tilde{\Phi}_{2D}(\vec{q}_{\parallel}) = \tilde{\sigma}(\vec{q}_{\parallel}) \int \frac{dq_z}{2\pi} \frac{4\pi}{q_{\parallel}^2 + q_z^2}. \quad (2.126)$$

The integral evaluates to:

$$\int \frac{dq_z}{2\pi} \frac{4\pi}{q_{\parallel}^2 + q_z^2} = \frac{2\pi}{q_{\parallel}}, \quad (2.127)$$

where we used the standard result  $\int_{-\infty}^{\infty} \frac{dq_z}{q_{\parallel}^2 + q_z^2} = \frac{\pi}{q_{\parallel}}$ . Thus, the final expression for the electrostatic potential in 2D is:

$$\tilde{\Phi}_{2D}(\vec{q}_{\parallel}) = \frac{2\pi}{q_{\parallel}} \tilde{\sigma}(\vec{q}_{\parallel}). \quad (2.128)$$

Therefore, the bare Coulomb interaction in 2D is:

$$\tilde{\Phi}_{\text{bare}}(q_{\parallel}) = \frac{2\pi e}{q_{\parallel}}, \quad (2.129)$$

and hence we get the Coulomb potential energy:

$$V_{\text{bare}}(q_{\parallel}) = \frac{2\pi e^2}{q_{\parallel}}, \quad (2.130)$$

In the following part we will drop the subscript  $\parallel$  for simplicity.

To account for the material's dielectric response, we introduce the dielectric function  $\varepsilon(q)$ , which modifies the Coulomb interaction in momentum space. The dielectric function reflects how the material screens the electrostatic interaction.

The screened Coulomb potential energy in momentum space,  $\tilde{V}(q)$ , is related to the bare Coulomb potential energy,  $V_{\text{bare}}(q)$ , by:

$$\tilde{V}(q) = \frac{V_{\text{bare}}(q)}{\varepsilon(q)}. \quad (2.131)$$

The bare Coulomb potential energy in 2D is given in Eq. (2.130). Thus, the screened potential becomes:

$$\tilde{V}(q) = \frac{\frac{2\pi e^2}{q}}{\varepsilon(q)} = \frac{2\pi e^2}{q\varepsilon(q)}. \quad (2.132)$$

Next, we express the dielectric function  $\varepsilon(q)$  in terms of the material's polarizability  $\alpha$ . The dielectric function  $\varepsilon(q)$  describes how a material responds to an external electric field, including contributions from various physical processes. Its general form can be written as:

$$\varepsilon(q, \omega) = \varepsilon_{\infty} + (\text{e-e int.}) + (\text{e-ph int.}) + \dots \quad (2.133)$$

where  $\varepsilon_{\infty}$  is the high-frequency background dielectric constant (it describes how tightly bound electrons in the material respond almost instantaneously to an external electric field, without involving slower processes like lattice vibrations or low-energy excitations), and the other terms account for dynamic screening effects from electron-electron and electron-phonon interactions.

In the static limit ( $\omega \rightarrow 0$ ), and focusing on electron-electron interactions within the random phase approximation (RPA), the dielectric function simplifies to [36]:

$$\varepsilon(q) = 1 + V_{\text{bare}}(q)\Pi(q), \quad (2.134)$$

where  $V_{\text{bare}}(q)$  is the bare Coulomb interaction and  $\Pi(q)$  is the polarization function describing the density response of the material. For a 2D material, the bare Coulomb interaction takes the form given in Eq. (2.130) and, at small wavevectors  $q$ , the polarization function  $\Pi(q)$  behaves as [36]:

$$\Pi(q) \approx \frac{\alpha}{e^2} q^2, \quad (2.135)$$

where  $\alpha$  is the 2D polarizability of the material, which is related to its ability to respond to an external electric field. Substituting these expressions into the RPA formula Eq. (2.134) yields the dielectric function for a 2D material:

$$\varepsilon(q) = 1 + \frac{2\pi e^2}{q} \cdot \frac{\alpha}{e^2} q^2 = 1 + 2\pi\alpha q. \quad (2.136)$$

This expression shows that, in 2D, the dielectric screening grows linearly with  $q$  for small  $q$  values. Substituting this expression for  $\varepsilon(q)$  into the equation for the screened potential energy, Eq. (2.132), we get:

$$\tilde{V}(q) = \frac{2\pi e^2}{q \cdot (1 + 2\pi\alpha q)}. \quad (2.137)$$

and thus the screened potential can be written as [446]:

$$\tilde{\Phi}(q) = \frac{2\pi e}{q \cdot (1 + 2\pi\alpha q)}. \quad (2.138)$$

This is the screened Coulomb potential in momentum space, considering the dielectric response of the material. It accurately describes the long-range Coulomb interaction in 2D materials, where the dielectric response varies spatially. The modification of the Coulomb interaction by this non-local screening term is essential for correctly modeling the electron-electron interactions in systems like graphene and TMDCs, where the screening effects are highly dependent on the material's structure and environment.

The screened potential energy in real space can be obtained by performing the inverse Fourier transform of the product  $\tilde{V}(q)$ , and takes the following analytical form [216, 446–448]:

$$V_{\text{RK}}(r) = \frac{e^2}{4\alpha} \left( H_0 \left( \frac{r}{r_0} \right) - Y_0 \left( \frac{r}{r_0} \right) \right), \quad (2.139)$$

where  $r$  is the radial coordinate in 2D real space, and  $r_0 = 2\pi\alpha$  is a characteristic screening length determined by the 2D polarizability  $\alpha$  of the material and the effective background dielectric constant  $\varepsilon_r$ . The functions  $H_0$  and  $Y_0$  denote, respectively, the Struve function and the Bessel function of the second kind, both of order zero. This form of the potential, often referred to as the Rytova–Keldysh potential, captures the non-local screening effects specific to 2D materials.

The formula describes the effective Rytova-Keldysh potential  $V_{\text{RK}}(r)$  felt by an electron in a 2D material, incorporating the dielectric response of the material. The term  $\frac{e^2}{\alpha}$  scales the potential based on the material's polarizability  $\alpha$ .

The Rytova-Keldysh model is especially relevant for systems where the dielectric response is spatially varying, such as in monolayers or heterostructures of 2D materials like graphene and TMDCs, where the screening effects cannot be described by a simple constant dielectric constant. For these materials, the Rytova-Keldysh model provides a more accurate description of long-range Coulomb interactions, which are critical for understanding the material's electronic and optical properties. This model is particularly important when studying excitonic effects in 2D materials, as the long-range Coulomb interaction and spatially varying screening play a crucial role in the formation of excitons.

However, there are cases where the Rytova-Keldysh model is not applicable. In systems like BLG QDs or TMDCs in strong magnetic fields, the static screening model is often preferred. In these cases, the screening is dominated by a uniform background, such as the substrate or vacuum, rather than spatially varying effects. For QDs, the confinement of the electron wavefunction significantly reduces the influence of non-local screening effects, and the static model is usually

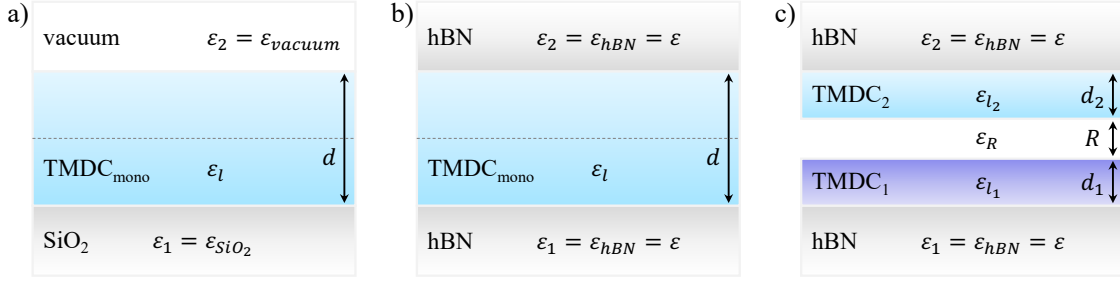


**Figure 2.4:** Schematic picture of the dielectric environment of (a) the TMDC monolayer on the SiO<sub>2</sub> substrate, (b) the TMDC monolayer encapsulated by hBN, and (c) TMDC heterostructure encapsulated by hBN, with potential finite separation  $R$  between layers.

sufficient to describe the electron-electron interactions. Similarly, in TMDCs under a strong magnetic field, the variation in screening is minimal compared to the effects of the magnetic field or electron correlations, making the static screening model a better approximation.

In contrast, the Rytova-Keldysh model becomes essential when dealing with more complex systems like 2D heterostructures, such as the MoSe<sub>2</sub>/WSe<sub>2</sub> system. These materials exhibit significant spatial variations in their dielectric response, and the Rytova-Keldysh model is necessary for accurately describing electron-electron interactions. This will be particularly relevant in future work, where the Rytova-Keldysh model will be employed to study optical properties, excitons, and other quantum phenomena in these materials.

We can see that the description of Coulomb electron-hole interactions in realistic systems becomes complicated due to screening by other carriers. In 2D materials, electron-electron interaction screening behaves differently compared to 3D systems, requiring a more detailed screening model. The Rytova-Keldysh model, developed in the previous Section, is the simplest model that captures the essential linear dependence of screening in  $k$ -space [447, 448]. As shown, this model approximates the Coulomb interaction by dividing it by a dielectric function as follows:

$$V_{R-K}(q) = \frac{V_{bare}(q)}{\epsilon_r^{R-K} (1 + 2\pi\alpha |\vec{q}|)}. \quad (2.140)$$

Interestingly, the static screening part  $\epsilon_r$  depends on the dielectric properties of the environment surrounding the 2D material, not those of the material itself. Specifically,  $\epsilon_r^{R-K}$  is given by the average of the dielectric constants of the media above and below the 2D crystal,  $\epsilon_r^{R-K} = (\epsilon_1 + \epsilon_2) / 2$ . This expression arises from the theory of dielectric slabs with finite thickness  $d$ , surrounded by two semi-infinite dielectric materials with electric permittivities  $\epsilon_1$  and  $\epsilon_2$ .

For the purpose of modeling screening effects in monolayer TMDCs, two typical dielectric environments are often considered in the literature, as illustrated in Fig. 2.4. The first configuration, shown in panel (a), consists of a monolayer TMDC with effective thickness  $d$  placed on a bulk SiO<sub>2</sub> substrate and exposed to vacuum from above. The second, depicted in panel (b), involves a monolayer encapsulated between hBN layers. These two setups represent commonly studied limiting cases of weak and strong dielectric screening, respectively [175, 223, 450].

The Coulomb interaction in TMDC heterostructures is considerably more complex than in monolayers due to the presence of multiple layers and surrounding dielectric materials. Both intralayer and interlayer interactions must be taken into account, each associated with a distinct screening behavior and corresponding dielectric function [302, 449]. In this section, we follow the formalism introduced by Simon Ovesen and Ermin Malic [449], which provides a generalized

Rytova-Keldysh model in reciprocal space suitable for describing the dielectric screening in TMDC heterostructures.

The screened Coulomb potential in the  $k$ -space formulation reads:

$$V_k^{l_2 l_2} = \frac{e_0^2}{k \varepsilon_0 \varepsilon^{l_2 l_2}(k)}, \quad (2.141)$$

where  $\varepsilon^{l_2 l_2}(k)$  is the dielectric function of the system, depending on the type of interaction (intra- or interlayer). It incorporates the specific electrostatic environment and geometry of the system. Here,  $l_1$  and  $l_2$  refer to the two constituent layers of the heterostructure.

To describe the full system, the dielectric functions for both intra- and interlayer interactions are required. These can be derived by solving Poisson's equation for a stratified dielectric environment that includes two TMDC monolayers of finite thickness, possibly separated by an insulating slab and encapsulated in an external dielectric, as schematically shown in Fig. 2.4(c).

The general expressions for the dielectric function, as derived in Ref. [449], read:

(1) intralayer dielectric function:

$$\varepsilon^{l_1 l_1}(k) = \varepsilon^{l_2 l_2}(k) = \frac{\cosh(kd_2) f(k)}{\cosh^2(k \frac{d_2}{2}) \left(1 + \tanh(k \frac{d_2}{2}) \frac{\varepsilon_2}{\varepsilon_{l_2}}\right)} \times \frac{1}{\left[ \left(1 + \frac{\varepsilon_1}{\varepsilon_R} \tanh(kR)\right) + \left(\frac{\varepsilon_{l_1}}{\varepsilon_{l_2}} + \frac{\varepsilon_{l_1} \varepsilon_R}{\varepsilon_{l_1} \varepsilon_{l_2}} \tanh(kR)\right) \tanh(kd_1) \tanh(k \frac{d_2}{2}) \right] + \left[\left(\frac{\varepsilon_1}{\varepsilon_{l_1}} + \frac{\varepsilon_{l_2}}{\varepsilon_R} \tanh(kR)\right) \tanh(kd_1) + \left(\frac{\varepsilon_1}{\varepsilon_{l_2}} + \frac{\varepsilon_R}{\varepsilon_{l_2}} \tanh(kR)\right) \tanh(kd_2)\right]}, \quad (2.142)$$

(2) interlayer dielectric function:

$$\varepsilon^{l_1 l_2}(k) = \cosh(kR) \frac{\cosh(kd_1) \cosh(kd_2)}{\cosh(k \frac{d_1}{2}) \cosh(k \frac{d_2}{2}) \left(1 + \frac{\varepsilon_1}{\varepsilon_{l_1}} \tanh(k \frac{d_1}{2})\right) \left(1 + \frac{\varepsilon_2}{\varepsilon_{l_2}} \tanh(k \frac{d_2}{2})\right)} f(k).$$

The function  $f(k)$  is defined as:

$$\begin{aligned} f(k) = & \left[ (\varepsilon_1 + \varepsilon_2) + \left( \frac{\varepsilon_1 \varepsilon_2}{\varepsilon_R} + \varepsilon_R \right) \tanh(kR) \right] \\ & + \left[ \left( \frac{\varepsilon_{l_2}}{\varepsilon_{l_1}} \varepsilon_1 + \frac{\varepsilon_{l_1}}{\varepsilon_{l_2}} \varepsilon_2 \right) + \left( \frac{\varepsilon_{l_1} \varepsilon_{l_2}}{\varepsilon_R} + \frac{\varepsilon_1 \varepsilon_2}{\varepsilon_R} \right) \tanh(kR) \right] \tanh(kd_2) \tanh(kd_2) \\ & + \left[ \left( \varepsilon_{l_1} + \frac{\varepsilon_1 \varepsilon_2}{\varepsilon_{l_1}} \right) + \left( \frac{\varepsilon_{l_1} \varepsilon_2}{\varepsilon_R} + \frac{\varepsilon_1 \varepsilon_R}{\varepsilon_{l_1}} \right) \tanh(kR) \right] \tanh(kd_1) \\ & + \left[ \left( \varepsilon_{l_2} + \frac{\varepsilon_1 \varepsilon_2}{\varepsilon_{l_2}} \right) + \left( \frac{\varepsilon_{l_2} \varepsilon_1}{\varepsilon_R} + \frac{\varepsilon_2 \varepsilon_R}{\varepsilon_{l_2}} \right) \tanh(kR) \right] \tanh(kd_2) \end{aligned} \quad (2.143)$$

To reduce the complexity of these expressions, we first consider the limit where the TMDC layers are in direct contact, i.e., there is no spacer slab ( $R = 0$ ). In this case, terms involving  $\tanh(kR)$  vanish and  $\cosh(kR) = 1$ . The dielectric functions simplify accordingly, leading to more tractable forms:

$$\begin{aligned} \varepsilon^{l_1 l_1}(k) = \varepsilon^{l_2 l_2}(k) = & \frac{\frac{\cosh(kd_2)}{\cosh^2(k \frac{d_2}{2}) \left(1 + \tanh(k \frac{d_2}{2}) \frac{\varepsilon_2}{\varepsilon_{l_2}}\right)} f(k)}{1 + \frac{\varepsilon_{l_1}}{\varepsilon_{l_2}} \tanh(kd_1) \tanh(k \frac{d_2}{2}) + \frac{\varepsilon_1}{\varepsilon_{l_1}} \tanh(kd_1) + \frac{\varepsilon_1}{\varepsilon_{l_2}} \tanh(kd_2)}, \quad (2.144) \\ \varepsilon^{l_1 l_2}(k) = & \frac{\cosh(kd_1) \cosh(kd_2)}{\cosh(k \frac{d_1}{2}) \cosh(k \frac{d_2}{2}) \left(1 + \frac{\varepsilon_1}{\varepsilon_{l_1}} \tanh(k \frac{d_1}{2})\right) \left(1 + \frac{\varepsilon_2}{\varepsilon_{l_2}} \tanh(k \frac{d_2}{2})\right)} f(k) \end{aligned}$$

and

$$f(k) = (\varepsilon_1 + \varepsilon_2) + \left( \frac{\varepsilon_{l_2}}{\varepsilon_{l_1}} \varepsilon_1 + \frac{\varepsilon_{l_1}}{\varepsilon_{l_2}} \varepsilon_2 \right) \tanh(kd_2) \tanh(kd_2) + \left( \varepsilon_{l_1} + \frac{\varepsilon_1 \varepsilon_2}{\varepsilon_{l_1}} \right) \tanh(kd_1) + \left( \varepsilon_{l_2} + \frac{\varepsilon_1 \varepsilon_2}{\varepsilon_{l_2}} \right) \tanh(kd_2) \quad (2.145)$$

Further simplification is achieved by assuming identical layer thicknesses ( $d_1 = d_2 = d$ ) and uniform encapsulation by hBN, for which  $\varepsilon_1 = \varepsilon_2 = \varepsilon$ . These assumptions yield the following compact forms for the intra- and interlayer dielectric functions:

$$\begin{aligned} \varepsilon^{l_1 l_1}(k) = \varepsilon^{l_2 l_2}(k) = & \frac{\cosh(kd) f(k)}{\cosh^2(k \frac{d}{2}) \left( 1 + \tanh(k \frac{d}{2}) \frac{\varepsilon}{\varepsilon_{l_2}} \right) \left( 1 + \frac{\varepsilon_{l_1}}{\varepsilon_{l_2}} \tanh(kd) \tanh(k \frac{d}{2}) + \frac{\varepsilon}{\varepsilon_{l_1}} \tanh(kd) + \frac{\varepsilon}{\varepsilon_{l_2}} \tanh(kd) \right)}, \\ \varepsilon^{l_1 l_2}(k) = & \frac{\cosh^2(kd)}{\cosh^2(k \frac{d}{2}) \left( 1 + \frac{\varepsilon}{\varepsilon_{l_1}} \tanh(k \frac{d}{2}) \right) \left( 1 + \frac{\varepsilon}{\varepsilon_{l_2}} \tanh(k \frac{d}{2}) \right)} f(k), \end{aligned} \quad (2.146)$$

and the  $f(k)$  function:

$$f(k) = 2\varepsilon + \left( \varepsilon_{l_1} + \frac{\varepsilon^2}{\varepsilon_{l_1}} + \varepsilon_{l_2} + \frac{\varepsilon^2}{\varepsilon_{l_2}} \right) \tanh(kd) + \varepsilon \left( \frac{\varepsilon_{l_2}}{\varepsilon_{l_1}} + \frac{\varepsilon_{l_1}}{\varepsilon_{l_2}} \right) \tanh^2(kd). \quad (2.147)$$

In the further notation we will keep  $\varepsilon \rightarrow \varepsilon_r^{R-K}$ . In the small-momentum limit ( $qd \ll 1$ ), relevant for excitonic binding and optical transitions, the dielectric functions can be approximated linearly in  $q$ :

$$\begin{aligned} \varepsilon^{l_1 l_1}(k) = \varepsilon^{l_2 l_2}(k) & \approx \varepsilon_r^{R-K} - \frac{(\varepsilon_{l_1} + \varepsilon_{l_2})(\varepsilon^2 - \varepsilon_{l_1} \varepsilon_{l_2})}{2\varepsilon_{l_1} \varepsilon_{l_2}} q \cdot d = \varepsilon_r^{R-K} \left( 1 - \frac{(\varepsilon_{l_1} + \varepsilon_{l_2})(\varepsilon^2 - \varepsilon_{l_1} \varepsilon_{l_2})}{2\varepsilon_{l_1} \varepsilon_{l_2}} q \cdot d \right) \\ \varepsilon^{l_1 l_2}(k) & \approx \varepsilon_r^{R-K} - \frac{1}{2}(\varepsilon_{l_1} + \varepsilon_{l_2}) q \cdot d = \varepsilon_r^{R-K} \left( 1 - \frac{\varepsilon_{l_1} + \varepsilon_{l_2}}{2\varepsilon_r^{R-K}} q \cdot d \right). \end{aligned} \quad (2.148)$$

These lead naturally to the Rytova-Keldysh form of the dielectric function, characterized by effective background permittivity  $\varepsilon_r^{R-K}$  and interaction-specific polarizabilities  $\alpha_{RK}^{intra}$  and  $\alpha_{RK}^{inter}$ :

$$\begin{aligned} \varepsilon^{l_1 l_1}(k) = \varepsilon^{l_2 l_2}(k) & \approx \varepsilon_r^{RK} [1 + \alpha_{RK}^{intra} \cdot q], \\ \varepsilon^{l_1, l_2}(q) & \approx \varepsilon_r^{RK} [1 + \alpha_{RK}^{inter} \cdot q]. \end{aligned} \quad (2.149)$$

The parameters  $\alpha_{RK}^{intra}$  and  $\alpha_{RK}^{inter}$  encapsulate the response of the dielectric environment to external fields and can be extracted from the binding energies of the  $1s$  excitonic states. As pointed out in Ref. [449], the Rytova-Keldysh model is particularly well-suited to describing interlayer screening, often yielding better agreement with experimental exciton spectra than its monolayer counterpart.

This framework forms the basis for computing the excitonic structure of TMDC heterostructures, such as the MoSe<sub>2</sub>/WSe<sub>2</sub> heterostructure [175] discussed in Chapter 5.

## 2.3 Theory of Correlated Electrons in 2D Crystals

The study of electronic correlations is essential for understanding the behavior of electrons in low-dimensional materials. In 2D crystals, reduced screening and enhanced Coulomb interactions lead to strong correlation effects that significantly modify electronic and optical properties compared to bulk systems. Capturing these phenomena requires theoretical approaches that go beyond the independent-particle approximation and account for many-body interactions explicitly.

One powerful framework for describing correlated electron-hole pairs in solids is the Bethe-Salpeter equation (BSE). Originally developed in the context of quantum electrodynamics (QED) to describe two-particle bound states, the concept was introduced by Yoichiro Nambu in 1950 [451] and formally derived by Hans Bethe and Edwin Salpeter in 1951 [452] to account for relativistic effects such as the Coulomb interaction between electron-positron pairs. In this framework, the BSE can be derived from the Dyson-Schwinger equations, which describe two-particle propagators in QED [453, 454]. Later, the BSE was adapted to condensed matter physics to capture excitonic effects and electron-hole interactions, providing a robust approach for studying many-body phenomena beyond the independent-particle approximation.

The BSE has since been adapted for condensed matter systems, where it is used to describe electron-hole correlations and excitonic effects. In this context, quasiparticle energies are often refined using the GW approximation [455–460], and the BSE is then solved to capture the interaction between optically created electrons and holes. This combined approach allows for the accurate prediction of optical spectra and excitonic states, particularly in low-dimensional materials where Coulomb interactions are strongly enhanced.

In the following sections, we apply the Bethe-Salpeter framework to study many-body excitations in 2D crystals. Understanding excitons, trions, and other optical complexes is essential for describing the optical response and carrier dynamics in two-dimensional semiconductors, such as TMDC. The BSE enables a description of these correlated states beyond the independent-particle approximation by incorporating both exchange and correlation effects.

### 2.3.1 Single Electron-Hole Excitations. Bethe-Salpeter Equation

To provide a clear and illustrative presentation of the Bethe-Salpeter theory, we focus on the derivation of the BSE for a neutral exciton—an electron-hole pair bound by Coulomb interaction—as a representative case. The neutral exciton is a simple yet important excitation that captures the key aspects of electron-hole interactions in many-body physics. This derivation introduces the main steps and approximations that form the foundation of the Bethe-Salpeter approach, including the role of electron-hole interactions and the formulation of the excitonic Hamiltonian.

While we present the details for a neutral exciton, the same formalism can be adapted to describe other complexes, such as trions, biexcitons, or even excitons interacting with filled LLs in 2D crystals under a magnetic field. These additional cases generally follow similar steps but require modifications to account for the specific interactions and symmetries of each complex. The neutral exciton example provides a basis for understanding the Bethe-Salpeter framework, which can be extended to a variety of optical many-body complexes in 2D materials.

We begin by modeling the many-body Hamiltonian for a single electron-hole pair excitation, derived from the  $N$ -electron GS. The GS is approximated as a single Slater determinant,  $|\text{GS}\rangle = \prod_i \hat{c}_i^\dagger |0\rangle$ , where  $\hat{c}_i^\dagger$  creates an electron in state  $i$ . In this formalism, a hole refers to the absence of an electron in an otherwise fully occupied VB, while an electron refers to a promoted carrier in the CB. Initially, the ground state consists of a fully occupied VB and an empty CB, as shown in Fig. 2.5(a). Exciting the system involves promoting a single electron from the VB to the CB, which results in the creation of electron-hole pairs, as shown in Fig. 2.5(b). By accounting for the interactions between the electron and hole, we obtain the exciton, a bound state where the electron and hole are correlated due to their mutual Coulomb interaction, as shown in Fig. 2.5(c). The spectrum of these excitons reflects the nature of these bound states.

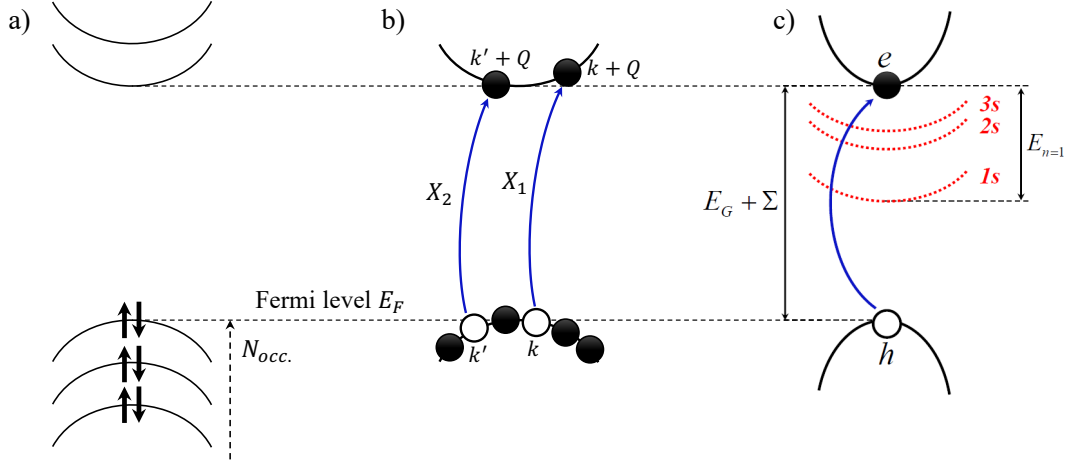


**Figure 2.5:** One-pair excitation scheme. (a)  $N$ -electron ground state configuration with the fully occupied VB and empty CB. (b) Possible single excitations from the top VB to the bottom CB mixed by Coulomb interactions, resulting in the creation of an electron-hole pair. (c) Exciton spectrum obtained by solving the eigenproblem for the exciton.

The many-body Hamiltonian describing the correlated electron-hole state is expressed as:

$$\begin{aligned} \hat{H}_{MB} &= \sum_m \epsilon_m \hat{c}_m^\dagger \hat{c}_m + \frac{1}{2} \sum_{\substack{m_1, m_2 \\ m_3, m_4}} \langle m_1, m_2 | V_C | m_3, m_4 \rangle \hat{c}_{m_1}^\dagger \hat{c}_{m_2}^\dagger \hat{c}_{m_3} \hat{c}_{m_4} - \sum_{m_1, m_2} V_{m_1, m_2}^P \hat{c}_{m_1}^\dagger \hat{c}_{m_2} \\ &= \hat{H}^{(1)} + \hat{H}^{(2)} - \hat{H}^{(3)}. \end{aligned} \quad (2.150)$$

Here,  $\hat{H}^{(1)}$  accounts for the single-particle energies  $\epsilon_m$ , where  $\hat{c}_m^\dagger$  and  $\hat{c}_m$  are the creation and annihilation operators for the electronic states labeled by index  $m$ . The second term,  $\hat{H}^{(2)}$ , describes the electron-electron Coulomb interaction, with matrix elements  $\langle m_1, m_2 | V_C | m_3, m_4 \rangle$  representing the interaction between pairs of electronic states, as explained in Sec. 2.2. The third term,  $\hat{H}^{(3)}$ , accounts for the interaction with the uniform positive background charge that ensures overall charge neutrality of the system. This background physically represents the ionic cores fixed in the crystal lattice, which balance the negative charge of electrons in the GS. In first-principles methods such as DFT, this ionic potential is included microscopically, typically through pseudopotentials, but only for the GS calculation. When modeling excited states or many-body effects beyond the GS, the distribution of charge carriers changes, requiring a re-evaluation of the positive background contribution to maintain neutrality. Additionally, in doped or gated systems, an extra positive background charge may be introduced to compensate for the added free carriers, allowing for the formation of homogeneous electron (or hole) gases with preserved translational invariance. Neglecting this background would result in a net charged system, causing electrons to repel and accumulate at the system edges, which is unphysical. Therefore, the positive background term is essential to ensure well-defined, finite interaction energies and physically meaningful many-body states.

To describe excitonic states, we write the excited state  $|\psi^\mu\rangle$  as a linear combination of single electron-hole pair excitations, depicted schematically in Fig. 2.5(b):

$$|\psi^\mu\rangle = \sum_{i,f} A_{i,f}^\mu \hat{c}_f^\dagger \hat{c}_i |\text{GS}\rangle. \quad (2.151)$$

Here,  $A_{i,f}^\mu$  represents the amplitude of the electron-hole pair configuration. The operator  $\hat{c}_i$  removes

an electron from the VB state  $i$ , leaving a hole, while  $\hat{c}_f^\dagger$  creates the electron in the unoccupied CB state  $f$ . The indices  $i$  and  $f$  run over all VB and CB states, respectively.

The electron-hole pair excitations are coupled through the electron-electron interaction  $V_C$ , which introduces many-body effects that go beyond the independent-particle picture. These interactions modify the exciton's energy levels and lead to a spectrum that reflects both the underlying band structure and the influence of Coulomb correlations.

Let us consider two different electron-hole excitations,  $X_1$  and  $X_2$ , schematically depicted in Fig. 2.5(c). These excitations are defined as:

$$|X_1\rangle = \hat{c}_{f_1}^\dagger \hat{c}_{i_1} |GS\rangle, \quad \text{and} \quad |X_2\rangle = \hat{c}_{f_2}^\dagger \hat{c}_{i_2} |GS\rangle. \quad (2.152)$$

To derive the BSE for the exciton amplitude  $A_{i,f}^\mu$ , we calculate the matrix elements of the many-body Hamiltonian between these states:

$$\langle X_2 | \hat{H}_{MB} | X_1 \rangle = \langle X_2 | \hat{H}^{(1)} | X_1 \rangle + \langle X_2 | \hat{H}^{(2)} | X_1 \rangle - \langle X_2 | \hat{H}^{(3)} | X_1 \rangle. \quad (2.153)$$

We now evaluate each term in the matrix element  $\langle X_2 | \hat{H}_{MB} | X_1 \rangle$  separately, beginning with the single-particle term. This contribution reads:

$$\langle X_2 | \hat{H}^{(1)} | X_1 \rangle = \langle X_2 | \sum_m \epsilon_m \hat{c}_m^\dagger \hat{c}_m | X_1 \rangle = \sum_m \epsilon_m \langle GS | \hat{c}_{i_2}^\dagger \hat{c}_{f_2} \hat{c}_m^\dagger \hat{c}_m \hat{c}_{f_1}^\dagger \hat{c}_{i_1} | GS \rangle. \quad (2.154)$$

To evaluate the above expectation value, we apply Wick's theorem [461]. We retain only non-vanishing contractions, as all terms involving pairs of creation or annihilation operators vanish when acting on the GS. This yields:

$$\langle GS | \hat{c}_{f_2} \hat{c}_{i_2}^\dagger \hat{c}_m^\dagger \hat{c}_m \hat{c}_{f_1}^\dagger \hat{c}_{i_1} | GS \rangle = \delta_{m,i_2} \langle GS | \hat{c}_{f_2} \hat{c}_m^\dagger \hat{c}_{f_1}^\dagger \hat{c}_{i_1} | GS \rangle + \delta_{i_1,i_2} \langle GS | \hat{c}_{f_2} \hat{c}_m^\dagger \hat{c}_m \hat{c}_{f_1}^\dagger | GS \rangle. \quad (2.155)$$

Using this result, we expand the remaining four-operator terms:

$$\langle GS | \hat{c}_{f_2} \hat{c}_m^\dagger \hat{c}_{f_1}^\dagger \hat{c}_{i_1} | GS \rangle = -\delta_{f_1,f_2} \delta_{i_1,m}, \quad (2.156)$$

$$\langle GS | \hat{c}_{f_2} \hat{c}_m^\dagger \hat{c}_m \hat{c}_{f_1}^\dagger | GS \rangle = \delta_{m,f_2} \delta_{f_1,m} + \delta_{f_1,f_2} \theta(m \leq N_{\text{occ.}}), \quad (2.157)$$

where  $\theta(m \leq N_{\text{occ.}})$  is 1 if  $m$  is an occupied state and 0 otherwise. Substituting back into Eq. (2.154), we obtain:

$$\begin{aligned} \langle X_2 | \hat{H}^{(1)} | X_1 \rangle &= \sum_m \epsilon_m [-\delta_{m,i_2} \delta_{f_1,f_2} \delta_{i_1,m} + \delta_{i_1,i_2} (\delta_{m,f_2} \delta_{f_1,m} + \delta_{f_1,f_2} \theta(m \leq N_{\text{occ.}}))] = \\ &\delta_{i_1,i_2} \delta_{f_1,f_2} \left[ \epsilon_{f_1} - \epsilon_{i_1} + \sum_{m=1}^{N_{\text{occ.}}} \epsilon_m \right]. \end{aligned} \quad (2.158)$$

This expression reveals the diagonal contribution of single-particle energies to the Bethe-Salpeter matrix, incorporating both the energies of the excited electron and the VB hole ( $\epsilon_{f_1}, \epsilon_{i_1}$ ), and the contribution from the fully occupied VB.

The same procedure can be used to derive the formula for the Coulomb interaction scattering of an electron-hole pair  $X_1$  to  $X_2$ . In the first step, we obtain:

$$\langle X_2 | \hat{H}^{(2)} | X_1 \rangle = \frac{1}{2} \sum_{\substack{m_1, m_2, \\ m_3, m_4}} \langle m_1, m_2 | V_C | m_3, m_4 \rangle \langle X_2 | c_{m_1}^\dagger c_{m_2}^\dagger c_{m_3} c_{m_4} | X_1 \rangle. \quad (2.159)$$

To evaluate the expectation value  $\langle X_2 | c_{m_1}^\dagger c_{m_2}^\dagger c_{m_3} c_{m_4} | X_1 \rangle$ , we again apply Wick's theorem [461], retaining only non-vanishing contractions. This yields:

$$\begin{aligned} \langle X_2 | c_{m_1}^\dagger c_{m_2}^\dagger c_{m_3} c_{m_4} | X_1 \rangle &= \langle GS | c_{i_2}^\dagger c_{f_2} c_{m_1}^\dagger c_{m_2}^\dagger c_{m_3} c_{m_4} c_{f_1}^\dagger c_{i_1} | X_1 \rangle = \\ &= -\delta_{m_3, i_2} \langle GS | c_{f_2} c_{m_1}^\dagger c_{m_2}^\dagger c_{m_4} c_{f_1}^\dagger c_{i_1} | X_1 \rangle + \delta_{m_4, i_2} \langle GS | c_{f_2} c_{m_1}^\dagger c_{m_2}^\dagger c_{m_3} c_{f_1}^\dagger c_{i_1} | X_1 \rangle \\ &+ \delta_{i_1, i_2} \langle GS | c_{f_2} c_{m_1}^\dagger c_{m_2}^\dagger c_{m_3} c_{m_4} c_{f_1}^\dagger | X_1 \rangle. \end{aligned} \quad (2.160)$$

In the above result, we expand the remaining six-operator terms in the following way:

$$\begin{aligned} \langle GS | c_{f_2} c_{m_1}^\dagger c_{m_2}^\dagger c_{m_4} c_{f_1}^\dagger c_{i_1} | X_1 \rangle &= \delta_{m_1, f_2} \langle GS | c_{m_2}^\dagger c_{m_4} c_{f_1}^\dagger c_{i_1} | X_1 \rangle \\ &- \delta_{m_2, f_2} \langle GS | c_{m_1}^\dagger c_{m_4} c_{f_1}^\dagger c_{i_1} | X_1 \rangle - \delta_{f_1, f_2} \langle GS | c_{m_1}^\dagger c_{m_2}^\dagger c_{m_4} c_{i_1} | X_1 \rangle. \end{aligned} \quad (2.161)$$

Following this procedure for the other two matrix elements, we are left with nine four-operator terms to be evaluated accordingly. Following this procedure for all the matrix elements, we finally arrive at the following expression for the Coulomb interaction scattering of the electron-hole configurations:

$$\begin{aligned} \langle X_2 | \hat{H}^{(2)} | X_1 \rangle &= \\ &= \underbrace{\langle i_1, f_2 | V | i_2, f_1 \rangle}_{\text{e-h exchange interaction}} - \underbrace{\langle i_1, f_2 | V | f_1, i_2 \rangle}_{\text{e-h direct interaction}} \\ &- \underbrace{\delta(f_1, f_2) \sum_m^{N_{\text{occ.}}} \langle i_1, m | V | m, i_2 \rangle + \delta(i_1, i_2) \sum_m^{N_{\text{occ.}}} \langle f_2, m | V | m, f_1 \rangle}_{\text{direct electron and hole self-energy}} \\ &+ \underbrace{\delta(f_1, f_2) \sum_m^{N_{\text{occ.}}} \delta_{\sigma_{i_1}, \sigma_{i_2}} \langle i_1, m | V | i_2, m \rangle - \delta(i_1, i_2) \sum_m^{N_{\text{occ.}}} \delta_{\sigma_{f_1}, \sigma_{f_2}} \langle m, f_2 | V | m, f_1 \rangle}_{\text{exchange self-energy corrections for electrons and holes}} \\ &+ \underbrace{\delta(i_1, i_2) \delta(f_1, f_2) \sum_{m_1 < m_2}^{N_{\text{occ.}}} (\langle m_1, m_2 | V | m_2, m_1 \rangle - \delta_{\sigma_{m_1}, \sigma_{m_2}} \langle m_1, m_2 | V | m_1, m_2 \rangle)}_{\text{GS energy}}. \end{aligned} \quad (2.162)$$

Each term in Eq. (2.162) represents a distinct physical contribution. The first line includes the electron-hole exchange and direct Coulomb interactions: the direct interaction appears with a negative sign, reflecting the attractive force between the electron and hole, while the exchange interaction has a positive sign, indicating repulsion. This negative sign in the second term arises from the nature of the Coulomb interaction (see Sec. 2.2.1) and is consistent with the Ward identity [462]. It enforces total charge conservation and captures the antisymmetric exchange process, which effectively swaps particle positions and momenta during interaction. The second and third lines account for electron and hole self-energy-like corrections due to interactions with the fully occupied GS, including both direct and exchange effects. Finally, the last line represents a constant correction to the GS energy.

Applying the same methodology for the positive background term, we get the following matrix elements:

$$\begin{aligned} \langle X_2 | \hat{H}^{(3)} | X_1 \rangle &= -\delta(f_1, f_2) \sum_{m=1}^{N_{\text{occ.}}} \langle i_1, m | V | m, i_2 \rangle + \delta(i_1, i_2) \sum_{m=1}^{N_{\text{occ.}}} \langle f_2, m | V | m, f_1 \rangle \\ &+ \delta(i_1, i_2) \delta(f_1, f_2) \sum_{m_1 < m_2}^{N_{\text{occ.}}} \langle m_1, m_2 | V | m_2, m_1 \rangle. \end{aligned} \quad (2.163)$$

In this case, the terms above resemble the direct self-energy corrections and GS energy from the  $\langle X_2 | \hat{H}^{(2)} | X_1 \rangle$  matrix elements but with opposite signs. The first two terms describe electron-hole interactions that are similar to the direct electron and hole self-energy terms, but with negative signs due to the positive background. The third term represents the GS energy, which is also similar to the one from the  $\langle X_2 | \hat{H}^{(2)} | X_1 \rangle$  matrix, with a sign reversal. These terms are important for maintaining charge neutrality and accounting for the overall Coulomb interaction within the system, and they will influence the excitonic states through their contribution to the full Bethe-Salpeter equation.

Now that we have derived the matrix elements for the single-particle energies and the interaction terms, we can combine them to obtain the full Bethe-Salpeter matrix. In the first step, we will focus on analyzing its diagonal part, which can be written (relative to the GS energy) as:

$$\langle X | \hat{H}^{MB} | X \rangle = \underbrace{(\varepsilon_f - \varepsilon_i)}_{\text{single-particle energies}} + \underbrace{(\langle i, f | V | i, f \rangle - \langle i, f | V | f, i \rangle)}_{\text{vertex correction}} + \underbrace{\sum_m^{N_{\text{occ.}}} \langle m, i | V | m, i \rangle}_{\text{hole self-energy}} - \underbrace{\sum_m^{N_{\text{occ.}}} \langle m, f | V | m, f \rangle}_{\text{electron self-energy}}. \quad (2.164)$$

The first term in the above expression accounts for the single-particle energy difference between the initial (hole) and final (electron) states of the electron-hole pair. The second term corresponds to the vertex correction, which includes both the diagonal exchange and direct electron-hole interaction. Finally, the third term represents the self-energy corrections, as both the electron and the hole states are renormalized by the Coulomb interaction with the ground state.

In the next step, we include the off-diagonal contributions. The off-diagonal part of the Bethe-Salpeter matrix corresponds to the interaction between different electron-hole pair configurations. These interactions include both the off-diagonal exchange and direct Coulomb interactions, which account for the correlation effects between different electron-hole pair states. The full Bethe-Salpeter matrix can thus be written (relative to the GS energy) as:

$$\begin{aligned} \langle X_2 | \hat{H}^{MB} | X_1 \rangle &= \delta(i_1, i_2) \delta(f_1, f_2) [\varepsilon_{f_1} - \varepsilon_{i_1}] + \langle i_1, f_2 | V | i_2, f_1 \rangle - \langle i_1, f_2 | V | f_1, i_2 \rangle \\ &+ \delta(f_1, f_2) \sum_m^{N_{\text{occ.}}} \delta(\sigma, \sigma') \langle m, i_1 | V | m, i_2 \rangle - \delta(i_1, i_2) \sum_m^{N_{\text{occ.}}} \delta(\sigma, \sigma') \langle m, f_2 | V | m, f_1 \rangle. \end{aligned} \quad (2.165)$$

Using matrix elements for the scattering of electron-hole pairs  $X_1$  and  $X_2$ , we can write the BSE for the exciton amplitudes  $A_{i,f}^\mu$  as:

$$\sum_{f', i'} [(E_{f'} + \Sigma_{f'}) - (E_{i'} + \Sigma_{i'})] \delta_{i, i'} \delta_{f, f'} A_{i', f'}^\mu + \sum_{f', i'} [\langle i, f' | V_C | i', f \rangle - \langle i, f' | V_C | f, i' \rangle] A_{i', f'}^\mu = E_\mu A_{i, f}^\mu. \quad (2.166)$$

Here, the energy of each electron-hole pair is renormalized by the self-energies of both the electron and the hole,  $\Sigma_m = -\sum_n \langle n, m | V_C | n, m \rangle$ , which accounts for the Coulomb interaction between electrons and holes with electrons in the filled VB. This interaction describes the scattering of electron-hole pairs, with an attractive (negative) direct term and a repulsive (positive) exchange term.

The BSE given in Eq. (2.166) can be adapted for use in different types of solids, such as monolayer materials or QDs. It can also be extended to explicitly include spin or valley degrees of freedom. By adjusting the form of the interaction  $V_C$  and incorporating the material-specific characteristics such as electron-hole interaction, electronic band structure, and dimensionality, the BSE can provide a reliable tool for modeling and predicting excitonic states in various materials.

This methodology plays a key role in the study of optical properties of both bulk crystals and nanostructures.

### 2.3.2 Charged Excitons

Building on our discussion of excitons, we now extend our analysis to trions, which are charged excitonic complexes formed by the binding of an additional electron or hole to an exciton. The inclusion of this extra charge carrier introduces additional electron-electron (or electron-hole) interactions, requiring a careful treatment within the many-body formalism.

To study charged excitons, we approximate the many-electron GS at half-filling as a single Slater determinant of all occupied VB states and a free electron in the CB. Next, we construct the negatively charged trion states,  $\psi_-^n$ , as linear combinations of 3-body states that involve one electron-hole pair excitation and an additional electron in the CB. These states are written as:

$$|\alpha, \sigma'; \beta, \sigma; i, \sigma\rangle = c_{\alpha, \sigma'}^\dagger c_{\beta, \sigma}^\dagger c_{i, \sigma} |GS\rangle, \quad (2.167)$$

where the hole is defined as the absence of an electron in the VB, i.e.,  $c_{i, \sigma} |GS\rangle$ . In this formulation, Greek letters denote electrons in the CB, while Latin letters refer to holes in the VB. The spin indices  $\sigma$  and  $\sigma'$  label the spin states of the electrons and hole.

The trion wavefunction is a linear combination of all possible trion configurations, which can be expressed as:

$$|\psi_-^n\rangle = \sum_{\alpha, \beta, i, \sigma, \sigma'} \sum_{\sigma'} A_{\alpha, \beta, i, \sigma, \sigma'}^n c_{\alpha, \sigma'}^\dagger c_{\beta, \sigma}^\dagger c_{i, \sigma} |GS\rangle. \quad (2.168)$$

In this equation,  $A_{\alpha, \beta, i, \sigma, \sigma'}^n$  represents the amplitude of the 3-body configuration for the trion state  $n$ . When  $\sigma = \sigma'$ , we only need to consider the configurations where  $\alpha > \beta$  to avoid double counting of states. For simplicity, we will omit the spin indices in the subsequent analysis, integrating them into the notation for the Greek and Latin indices.

The many-body Hamiltonian incorporates electron-electron interactions, which renormalize the energies of the quasi-particles (quasi-electrons and quasi-holes) and mix different trion configurations. As a consequence, the amplitudes  $A_{\alpha, \beta, i}^n$  of the trion wavefunctions satisfy a BSE for the trion states. This equation can be derived analogously to the methodology presented on the example of an exciton in Sec. 2.3.1, and it takes the following form:

$$\begin{aligned} E^n A_{\alpha, \beta, i}^n &= (\epsilon_\alpha + \epsilon_\beta - \epsilon_i) A_{\alpha, \beta, i}^n + \sum_{\mu, \lambda, j} \left( \begin{array}{l} +\Sigma_{\mu, \alpha} \delta_{i, j} \delta_{\beta, \lambda} - \Sigma_{\lambda, \alpha} \delta_{i, j} \delta_{\beta, \mu} \\ +\Sigma_{\lambda, \beta} \delta_{i, j} \delta_{\alpha, \mu} - \Sigma_{\mu, \beta} \delta_{i, j} \delta_{\alpha, \lambda} \\ -\Sigma_{i, j} \delta_{\alpha, \mu} \delta_{\beta, \lambda} \end{array} \right) A_{\mu, \lambda, j}^n \\ &+ \sum_{\mu, \lambda, j} \left[ \begin{array}{l} + (V_{i, \lambda, j, \beta} - V_{i, \lambda, \beta, j}) \delta_{\alpha, \mu} + (V_{i, \mu, j, \alpha} - V_{i, \mu, \alpha, j}) \delta_{\beta, \lambda} \\ - (V_{i, \lambda, j, \alpha} - V_{i, \lambda, \alpha, j}) \delta_{\beta, \mu} - (V_{i, \mu, j, \beta} - V_{i, \mu, \beta, j}) \delta_{\alpha, \lambda} \\ - (V_{\mu, \lambda, \alpha, \beta} - V_{\mu, \lambda, \beta, \alpha}) \delta_{i, j} \end{array} \right] A_{\mu, \lambda, j}^n, \end{aligned} \quad (2.169)$$

where  $\epsilon_p$  denotes the QD single-particle energies,  $\Sigma_{p, q} = -\sum_m^{N_{occ.}} \langle m, p | V_C | m, q \rangle$  defines the scatterings containing the self-energy terms  $\Sigma_{p, p}$ ,  $V_{p, q, r, s} = \langle p, q | V_C | r, s \rangle$  corresponds to the CME, and  $N_{occ.}$  corresponds to the number of occupied states.

Let us now focus on the energy of trion configurations, which corresponds to the diagonal part of the Bethe-Salpeter matrix. The diagonal matrix element is given by:

$$\begin{aligned} \langle i, \beta, \alpha | \hat{H}_{MB} | \alpha, \beta, i \rangle &= (\epsilon_\alpha + \Sigma_{\alpha, \alpha}) + (\epsilon_\beta + \Sigma_{\beta, \beta}) - (\epsilon_i + \Sigma_{i, i}) \\ &- V_{i, \alpha, \alpha, i} + V_{i, \alpha, i, \alpha} - V_{i, \beta, \beta, i} + V_{i, \beta, i, \beta} + V_{\alpha, \beta, \beta, \alpha} - V_{\alpha, \beta, \alpha, \beta}. \end{aligned} \quad (2.170)$$

This expression contains 12 terms in total. The first part,  $(\epsilon_\alpha + \Sigma_{\alpha,\alpha}) + (\epsilon_\beta + \Sigma_{\beta,\beta}) - (\epsilon_i + \Sigma_{i,i})$ , represents the contribution from the three QD single-particle energies  $\epsilon_p$  (one for the hole in the VB and two for the electrons in the CB), which are corrected by their corresponding exchange self-energies  $\Sigma_{p,p}$ . These self-energy terms account for the effects of electron-electron interactions on the single-particle energies of the hole and electrons. The second part,  $-V_{i,\alpha,\alpha,i} + V_{i,\alpha,i,\alpha} - V_{i,\beta,\beta,i} + V_{i,\beta,i,\beta} + V_{\alpha,\beta,\beta,\alpha} - V_{\alpha,\beta,\alpha,\beta}$ , contains six Coulomb terms, three of which are direct Coulomb interactions ( $V_{p,q,q,p}$ ) and three are exchange interactions ( $V_{p,q,p,q}$ ). The terms  $V_{i,\alpha,\alpha,i}$  and  $V_{i,\alpha,i,\alpha}$  describe the direct and exchange interactions, respectively, between electron  $\alpha$  and hole  $i$ . Similarly,  $V_{i,\beta,\beta,i}$  and  $V_{i,\beta,i,\beta}$  correspond to the direct and exchange interactions between electron  $\beta$  and hole  $i$ . These terms account for the Coulomb interactions between the hole and the electrons in the trion configuration. The last two Coulomb matrix elements,  $V_{\alpha,\beta,\beta,\alpha}$  and  $V_{\alpha,\beta,\alpha,\beta}$ , represent the direct and exchange interactions, respectively, between the two CB electrons,  $\alpha$  and  $\beta$ . These interactions play an important role in the overall trion configuration and its energy.

## 2.4 Optical Response of 2D Crystals

The optical response of 2D materials plays an important role in determining their electronic properties and potential applications in optoelectronics, quantum technologies, and nanophotonics. Due to their reduced dimensionality and unique band structure, 2D crystals exhibit strong light-matter interactions, giving rise to phenomena such as enhanced optical absorption, valley-selective transitions, and excitonic effects. Understanding these interactions requires a theoretical framework that captures the mechanisms governing optical transitions, including both selection rules and dipole coupling, as well as the excitonic processes involved in absorption and emission.

In this section, we distinguish between two complementary approaches to describing light-matter interaction. The  $\vec{p} \cdot \vec{A}$  formalism is typically used for extended or periodic systems, where electronic states are described by Bloch wavefunctions. The  $\vec{E} \cdot \vec{r}$  (dipole moment) formalism, on the other hand, is more appropriate for finite or confined systems, such as quantum dots, where transitions occur between discrete, spatially localized states. This second approach enables direct computation of dipole matrix elements (DMEs) and transition probabilities in such systems. Additionally, we describe how the  $\vec{p} \cdot \vec{A}$  framework can be extended to include magnetic fields, which is essential for analyzing magneto-optical phenomena.

The following subsections begin by outlining the optical selection rules for hexagonal lattices, including the underlying assumptions of the  $\vec{p} \cdot \vec{A}$  method. We then present the dipole moment formalism used in confined systems and explain its relationship to the  $\vec{E} \cdot \vec{r}$  approach. Finally, we describe the computation of absorption and emission spectra using Fermi's golden rule, which serves as the foundation for analyzing the optical response of specific systems, such as BLG QDs or TMDCs, in later chapters.

### 2.4.1 Optical Selection Rules in Hexagonal Crystals via the $\vec{p} \cdot \vec{A}$ Formalism. Inclusion of a magnetic field

This section discusses the optical selection rules for the hexagonal crystals, such as graphene or a monolayer of TMDCs, within the mDF model. These materials exhibit valley-dependent optical activity due to their honeycomb lattice symmetry and spin-orbit interactions. To analyze light-matter interactions in such extended systems, we employ the  $\vec{p} \cdot \vec{A}$  formalism, which captures

the coupling between the electronic momentum and the vector potential of the electromagnetic field. This approach is well suited to derive selection rules for interband transitions under linearly or circularly polarized light and reveals how crystal symmetry and polarization determine valley selectivity in optical transitions.

Furthermore, we extend the methodology to include the presence of a magnetic field, which modifies the electronic states through Landau quantization. This allows for the investigation of magneto-optical effects, including valley Zeeman splitting and magnetic field-dependent selection rules, which are especially relevant in high-mobility 2D systems.

### 2.4.1.1 Excitation with Circularly Polarized Light

We begin by considering the excitation of the massive DF using circularly polarized light, where the polarization is denoted as  $\sigma^\pm$ . The electric field components are described as:

$$E_x = \pm E_0 \sin \omega t, \quad E_y = E_0 \cos \omega t, \quad (2.171)$$

where  $E_0$  represents the electric field strength, and  $\omega$  is the light frequency. The corresponding vector potential  $\vec{A} = -\int \vec{E} dt$  is given by:

$$A_x = \pm \frac{E_0}{\omega} \cos(\omega t), \quad A_y = -\frac{E_0}{\omega} \sin(\omega t). \quad (2.172)$$

We start with the mDF Hamiltonian in the absence of a magnetic field, as expressed in Eq. (2.56). By replacing  $\vec{q} \rightarrow \vec{q} + |e|\vec{A}$  in the Hamiltonian (we took  $c = 1$  for simplicity), we obtain the perturbed Hamiltonian:

$$\hat{H}_{\text{light}}(\nu K) = \begin{bmatrix} \frac{\Delta}{2} & v_F(\nu(q_x + eA_x) - i(q_y + eA_y)) \\ v_F(\nu(q_x + eA_x) + i(q_y + eA_y)) & -\frac{\Delta}{2} \end{bmatrix} = \underbrace{\begin{bmatrix} \frac{\Delta}{2} & v_F(\nu q_x - i q_y) \\ v_F(\nu q_x + i q_y) & -\frac{\Delta}{2} \end{bmatrix}}_{\text{unperturbed part}} \pm \nu g \underbrace{\begin{bmatrix} 0 & e^{\pm i \nu \omega t} \\ e^{\mp i \nu \omega t} & 0 \end{bmatrix}}_{\text{perturbation}} = \hat{H}_{\text{mDF}} + \hat{H}'(\sigma^\pm). \quad (2.173)$$

In the above equation, using the definition given in Eq. (2.172), we introduced  $A_x - iA_y = \pm e^{\pm i \omega t}$  and  $A_x + iA_y = \pm e^{\mp i \omega t}$ . Furthermore, we defined  $g = \frac{\nu F e E_0}{\omega}$ , where  $E_0$  is the strength of electric field, and  $\omega$  is the frequency of light. The signs  $\pm$  in the time-dependent perturbation term correspond to the handedness of circularly polarized light, where the upper (lower) sign represents right-handed,  $\sigma^+$  [left-handed,  $\sigma^-$ ] polarization. With the added perturbation  $\hat{H}'(\sigma^\pm)$ , we seek a time-dependent wavefunction of the form:

$$|\psi(t)\rangle = C_{\vec{q}}^{\text{VB}}(t) e^{-\frac{i}{\hbar} E^{\text{VB}} t} |\psi_{\vec{q}}^{\text{VB}}\rangle + C_{\vec{q}}^{\text{CB}}(t) e^{-\frac{i}{\hbar} E^{\text{CB}} t} |\psi_{\vec{q}}^{\text{CB}}\rangle. \quad (2.174)$$

Here,  $C_{\vec{q}}^{\text{VB}}$  and  $C_{\vec{q}}^{\text{CB}}$  are the time-dependent coefficients for the VB and CB components for each  $\vec{q}$ , respectively, expressed in the basis of the unperturbed states defined in Eq. (2.58). From now on we will drop the subscript  $\vec{q}$  for simplicity. The time-dependent Schrödinger equation (TDSE) is then given by:

$$i\hbar \frac{\partial}{\partial t} |\psi(t)\rangle = \left( \hat{H}_{\text{mDF}} + \hat{H}'(\sigma^\pm) \right) |\psi(t)\rangle. \quad (2.175)$$

Substituting the wavefunction (2.174) into the TDSE (2.175) we obtain:

$$\begin{aligned} i\hbar \left( \frac{\partial C^{\text{VB}}}{\partial t} e^{-\frac{i}{\hbar} E^{\text{VB}} t} |\psi^{\text{VB}}\rangle + \frac{\partial C^{\text{CB}}}{\partial t} e^{-\frac{i}{\hbar} E^{\text{CB}} t} |\psi^{\text{CB}}\rangle \right) \\ = \hat{H}'(\sigma^\pm) \left( C^{\text{VB}}(t) e^{-\frac{i}{\hbar} E^{\text{VB}} t} |\psi^{\text{VB}}\rangle + C^{\text{CB}}(t) e^{-\frac{i}{\hbar} E^{\text{CB}} t} |\psi^{\text{CB}}\rangle \right). \end{aligned} \quad (2.176)$$

Projecting onto the unperturbed states  $|\psi^{\text{VB}}\rangle$  and  $|\psi^{\text{CB}}\rangle$ , we obtain a system of equations for the coefficients  $C^{\text{VB}}(t)$  and  $C^{\text{CB}}(t)$ :

$$\begin{cases} i\hbar \frac{\partial}{\partial t} C^{\text{VB}}(t) = C^{\text{VB}}(t) \langle \psi^{\text{VB}} | \hat{H}' | \psi^{\text{VB}} \rangle + C^{\text{CB}}(t) e^{-\frac{i}{\hbar} \Delta E t} \langle \psi^{\text{VB}} | \hat{H}' | \psi^{\text{CB}} \rangle, \\ i\hbar \frac{\partial}{\partial t} C^{\text{CB}}(t) = C^{\text{CB}}(t) e^{\frac{i}{\hbar} \Delta E t} \langle \psi^{\text{CB}} | \hat{H}' | \psi^{\text{CB}} \rangle + C^{\text{VB}}(t) \langle \psi^{\text{CB}} | \hat{H}' | \psi^{\text{VB}} \rangle. \end{cases} \quad (2.177)$$

where  $\Delta E = E^{\text{CB}} - E^{\text{VB}}$  represents the energy difference between the conduction and valence bands (the magnitude of the energy gap  $\Delta = |\Delta E|$ ). The matrix elements of the perturbation are analyzed in the unperturbed basis for both valleys, as defined in Eq. (2.58). For the circular polarization  $\sigma^\pm$ , the matrix elements of the perturbation are computed as:

$$\begin{aligned} \hat{H}'_{\text{VV}}(t) &= \langle \psi^{\text{VB}} | \hat{H}' | \psi^{\text{VB}} \rangle = \mp \frac{g v_F |\vec{q}|}{|E|} \cos(\omega t \pm \theta), \\ \hat{H}'_{\text{CC}}(t) &= \langle \psi^{\text{CB}} | \hat{H}' | \psi^{\text{CB}} \rangle = -\hat{H}'_{\text{VV}}(t), \\ \hat{H}'_{\text{VC}}(t) &= \langle \psi^{\text{VB}} | \hat{H}' | \psi^{\text{CB}} \rangle = \frac{g}{|E|} e^{i\nu\theta} \left[ \pm \nu \frac{\Delta}{2} \cos(\omega t \pm \theta) - i|E| \sin(\omega t \pm \theta) \right], \\ \hat{H}'_{\text{CV}}(t) &= \langle \psi^{\text{CB}} | \hat{H}' | \psi^{\text{VB}} \rangle = \left( \hat{H}'_{\text{VC}}(t) \right)^*. \end{aligned} \quad (2.178)$$

We now solve the following set of equations:

$$\begin{cases} i\hbar \frac{\partial}{\partial t} C^{\text{VB}}(t) = C^{\text{VB}}(t) \hat{H}'_{\text{VV}}(t) + C^{\text{CB}}(t) e^{-\frac{i}{\hbar} \Delta E t} \hat{H}'_{\text{VC}}(t), \\ i\hbar \frac{\partial}{\partial t} C^{\text{CB}}(t) = C^{\text{VB}}(t) e^{\frac{i}{\hbar} \Delta E t} \hat{H}'_{\text{CV}}(t) + C^{\text{CB}}(t) \hat{H}'_{\text{CC}}(t). \end{cases} \quad (2.179)$$

Defining:

$$C^{\text{VB}}(t) = \exp\left(-\frac{i}{\hbar} \int_0^t \hat{H}'_{\text{VV}}(t') dt'\right) \tilde{C}^{\text{VB}}(t), \quad (2.180)$$

$$C^{\text{CB}}(t) = \exp\left(-\frac{i}{\hbar} \int_0^t \hat{H}'_{\text{CC}}(t') dt'\right) \tilde{C}^{\text{CB}}(t), \quad (2.181)$$

and using perturbation theory we get:

$$i\hbar \frac{\partial}{\partial t} \tilde{C}^{\text{CB}}(t) = -\frac{i}{\hbar} \frac{g}{2|E|} e^{-\nu i\theta} \left[ \left( \pm \nu \frac{\Delta}{2} + |E| \right) e^{i(\omega t + \frac{\Delta E}{\hbar} t \pm \theta)} + \left( \pm \nu \frac{\Delta}{2} - |E| \right) e^{-i(\omega t + \frac{\Delta E}{\hbar} t \pm \theta)} \right], \quad (2.182)$$

where  $E \equiv E^{\vec{q}} = \pm \sqrt{v_F^2 |\vec{q}|^2 + \frac{\Delta^2}{4}}$ . We finally substitute the matrix elements  $\hat{H}'_{\text{VV}}(t)$ ,  $\hat{H}'_{\text{CC}}(t)$ ,  $\hat{H}'_{\text{VC}}(t)$ , and  $\hat{H}'_{\text{CV}}(t)$  into Eq. (2.179) and obtain the equations for time evolution of the coefficients  $\tilde{C}$ :

$$\begin{aligned} \sigma^+, \vec{K} : \frac{\partial}{\partial t} \tilde{C}^{\text{CB}}(t) &= -\frac{i}{\hbar} \frac{g}{2|E|} \left[ \left( \frac{\Delta}{2} + |E| \right) e^{i(\omega + \frac{\Delta E}{\hbar})t} + \left( \frac{\Delta}{2} - |E| \right) e^{-i(\omega t - \frac{\Delta E}{\hbar} t + 2\theta)} \right] \\ \sigma^+, \vec{K}' : \frac{\partial}{\partial t} \tilde{C}^{\text{CB}}(t) &= -\frac{i}{\hbar} \frac{g}{2|E|} \left[ \left( -\frac{\Delta}{2} + |E| \right) e^{i(\omega t + \frac{\Delta E}{\hbar} t + 2\theta)} - \left( \frac{\Delta}{2} + |E| \right) e^{-i(\omega - \frac{\Delta E}{\hbar})t} \right] \\ \sigma^-, \vec{K}' : \frac{\partial}{\partial t} \tilde{C}^{\text{CB}}(t) &= -\frac{i}{\hbar} \frac{g}{2|E|} \left[ \left( \frac{\Delta}{2} + |E| \right) e^{i(\omega + \frac{\Delta E}{\hbar})t} + \left( \frac{\Delta}{2} - |E| \right) e^{-i(\omega t - \frac{\Delta E}{\hbar} t - 2\theta)} \right] \\ \sigma^-, \vec{K} : \frac{\partial}{\partial t} \tilde{C}^{\text{CB}}(t) &= -\frac{i}{\hbar} \frac{g}{2|E|} \left[ \underbrace{\left( -\frac{\Delta}{2} + |E| \right) e^{i(\omega t + \frac{\Delta E}{\hbar} t - 2\theta)}}_{\text{quickly oscillating}} - \underbrace{\left( \frac{\Delta}{2} + |E| \right) e^{-i(\omega - \frac{\Delta E}{\hbar})t}}_{\text{slowly oscillating}} \right] \end{aligned} \quad (2.183)$$

### 2.4.1.2 Transition Rates and Fermi's Golden Rule

To derive the selection rules for the optical excitation of the material with circularly polarized light, we consider the time evolution of the amplitude  $\tilde{C}^{CB}(t)$ , described by the set of equations in Eq. (2.183). Here, we focus on the particular example:

$$\frac{\partial}{\partial t} \tilde{C}^{CB}(t) = -\frac{i}{\hbar} \frac{g}{2|E|} \left[ \left( -\frac{\Delta}{2} + |E| \right) e^{i(\omega t + \frac{\Delta E}{\hbar} t + 2\theta)} - \left( \frac{\Delta}{2} + |E| \right) e^{-i(\omega - \frac{\Delta E}{\hbar})t} \right]. \quad (2.184)$$

To find the time evolution of  $\tilde{C}^{CB}(t)$ , we integrate Eq. (2.184) assuming the conduction band is initially empty,  $\tilde{C}^{CB}(0) = 0$ :

$$\tilde{C}^{CB}(t) = -\frac{ig}{\hbar 2|E|} \left( -\frac{\Delta}{2} + |E| \right) \int_0^t e^{i(\omega + \frac{\Delta E}{\hbar} + 2\theta)t'} dt' + \frac{ig}{\hbar 2|E|} \left( \frac{\Delta}{2} + |E| \right) \int_0^t e^{-i(\omega - \frac{\Delta E}{\hbar})t'} dt'. \quad (2.185)$$

In the following analysis, we consider the limit  $t \rightarrow \infty$ . Thus, in the spirit of the rotating wave approximation, the quickly oscillating term integrates to zero and is neglected. We focus, therefore, on the slowly oscillating term:

$$\begin{aligned} \tilde{C}^{CB}(t) &= \frac{ig}{\hbar 2|E|} \left( \frac{\Delta}{2} + |E| \right) \int_0^t e^{-i(\omega - \frac{\Delta E}{\hbar})t'} dt' \\ &= \frac{ig}{\hbar 2|E|} \left( \frac{\Delta}{2} + |E| \right) \frac{1}{-i(\omega - \frac{\Delta E}{\hbar})} \left[ e^{-i(\omega - \frac{\Delta E}{\hbar})t} - 1 \right] \\ &= -\frac{g}{2\hbar|E|} \cdot \frac{1}{\omega - \frac{\Delta E}{\hbar}} \left( \frac{\Delta}{2} + |E| \right) \left[ e^{-i(\omega - \frac{\Delta E}{\hbar})t} - 1 \right]. \end{aligned} \quad (2.186)$$

Introducing  $\omega - \frac{\Delta E}{\hbar} = \Omega$  we get:

$$\tilde{C}^{CB}(t) = \frac{g}{2\hbar|E|} \cdot \frac{1}{\Omega} \left( \frac{\Delta}{2} + |E| \right) e^{-i\frac{\Omega}{2}t} \left[ e^{-i\frac{\Omega}{2}t} - e^{i\frac{\Omega}{2}t} \right] = i \frac{g}{\hbar|E|} \cdot \frac{1}{\Omega} \left( \frac{\Delta}{2} + |E| \right) e^{-i\frac{\Omega}{2}t} \sin\left(\frac{\Omega}{2}t\right). \quad (2.187)$$

Taking the squared modulus to get the transition probability rate we obtain:

$$|\tilde{C}^{CB}(t)|^2 = \frac{g^2}{\hbar^2|E|^2\Omega^2} \left( \frac{\Delta}{2} + |E| \right)^2 \sin^2\left(\frac{\Omega}{2}t\right). \quad (2.188)$$

and hence the time-independent transition probability rate  $\gamma$ :

$$\begin{aligned} \gamma &= \frac{d}{dt} |\tilde{C}^{CB}(t)|^2 = \frac{d}{dt} \left[ \frac{g^2}{\hbar^2|E|^2\Omega^2} \left( \frac{\Delta}{2} + |E| \right)^2 \sin^2\left(\frac{\Omega}{2}t\right) \right] = \\ &= \frac{g^2}{\hbar^2|E|^2\Omega^2} \left( \frac{\Delta}{2} + |E| \right)^2 \frac{d}{dt} \left[ \sin^2\left(\frac{\Omega}{2}t\right) \right] = \\ &= \frac{g^2}{\hbar^2|E|^2\Omega^2} \left( \frac{\Delta}{2} + |E| \right)^2 \cdot \frac{\Omega}{2} \cdot \sin(\Omega t) = \frac{g^2}{2\hbar^2|E|^2} \left( \frac{\Delta}{2} + |E| \right)^2 \cdot \frac{\sin(\Omega t)}{\Omega}. \end{aligned} \quad (2.189)$$

In the long-time limit, we use the identity:

$$\frac{\sin(ax)}{x} \xrightarrow{a \rightarrow \infty} \pi \delta(x), \quad (2.190)$$

which for  $t \rightarrow \infty$  leads us to:

$$\gamma = \frac{g^2}{2\hbar^2|E|^2} \left( \frac{\Delta}{2} + |E| \right)^2 \pi \delta\left(\omega - \frac{\Delta E}{\hbar}\right) \quad (2.191)$$

The transition rate  $\gamma$  represents the probability per unit time of an electron transitioning between energy states in the material under circularly polarized light. It is calculated from one of the four

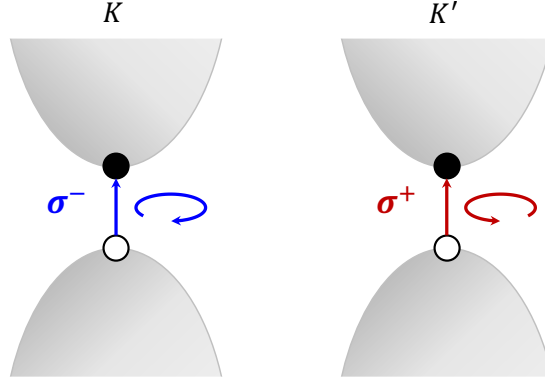


**Figure 2.6:** A schematic representation of optical selection rules for a TMDC monolayer presented for the  $K$  and  $K'$  valleys. The polarization of light  $\sigma^\pm$  and the allowed transitions are denoted in both panels.

equations given in Eq. (2.183) and corresponds to the Fermi's Golden Rule expression for transition probabilities. This rate is governed by energy conservation, expressed by the Dirac delta function, which enforces that the photon energy matches the energy difference between the initial and final states. The expression for  $\gamma$  depends on the factor  $g = \frac{v_F \epsilon E_0}{\omega}$ , the energy  $|E|$ , and the material's band gap  $\Delta$ . The transition rate is resonantly enhanced when the photon energy equals the band gap, enabling efficient electronic transitions.

This concludes the derivation of the time evolution for circularly polarized light. Similar expressions can be derived for the other three equations in Eq. (2.183). However, in two of these cases the resonance condition leads to a zero transition amplitude. Thus, only two transition rates remain nonzero, corresponding to the  $\sigma^-$  for valley  $K$ , and  $\sigma^+$  for valley  $K'$ , respectively. This result demonstrates the possibility of selectively exciting valleys using light with opposite circular polarization, as schematically illustrated in Fig. 2.6. This highlights the role of polarization in addressing specific valley states, offering a pathway for controlled manipulation of these states in potential applications.

### 2.4.1.3 Optical Selection Rules for TMDC Monolayers at High Magnetic Fields

Building on the methodology presented above, we perform an analogous analysis for the TMDC monolayer within the mDF model, now considering the inclusion of a magnetic field aligned with the  $z$  axis, and employing the symmetric gauge for the vector potential. The Hamiltonian for both valleys is defined in Eq. (2.65). For the wavefunctions in the LL basis, we refer to Eq. (2.193). With this setup, we calculate the matrix elements of the perturbation  $\hat{H}'(t)$  in the basis of LL orbitals [435].

To describe the time evolution of the system, we express the time-dependent wavefunction as a superposition of states in the conduction and valence bands at wavevector  $\vec{q}$ . This is done by expanding the total wavefunction  $|\psi^B(t)\rangle$  in terms of the LL eigenstates, which correspond to the energy eigenstates in the presence of a magnetic field. The expansion reads as:

$$|\psi^B(t)\rangle = C_{\vec{q},n,m}^{\text{VB}}(t) e^{-\frac{i}{\hbar} E_n^{\text{VB}} t} |\psi_{\vec{q},n,m}^{\text{VB}}\rangle + C_{\vec{q},n,m}^{\text{CB}}(t) e^{-\frac{i}{\hbar} E_n^{\text{CB}} t} |\psi_{\vec{q},n,m}^{\text{CB}}\rangle, \quad (2.192)$$

where  $C_{\vec{q},n,m}^{\text{VB}}(t)$  and  $C_{\vec{q},n,m}^{\text{CB}}(t)$  are the time-dependent coefficients for the VB and CB states, respectively, and  $|\psi_{\vec{q},n,m}^{\text{VB}}\rangle$ ,  $|\psi_{\vec{q},n,m}^{\text{CB}}\rangle$  represent the eigenstates of the magnetic field-dependent Hamiltonian for the respective bands. As previously, from now on we will drop the subscript  $\vec{q}$  for simplicity.

These eigenstates are spinors, which are the solutions to the Dirac equation in the presence of a magnetic field. The spinors are indexed by the LL quantum number  $n$  and the magnetic quantum number  $m$ . For both valleys, these wavefunctions, derived earlier, are written as:

$$|\psi_{n,m}^{\text{VB/CB}}(K)\rangle = \begin{pmatrix} \alpha_n^{\text{VB/CB}} |n-1, m\rangle \\ \beta_n^{\text{VB/CB}} |n, m\rangle \end{pmatrix} \quad \text{and} \quad |\psi_{n,m}^{\text{VB/CB}}(K')\rangle = \begin{pmatrix} \alpha_n^{\text{VB/CB}} |n, m\rangle \\ \beta_n^{\text{VB/CB}} |n-1, m\rangle \end{pmatrix}, \quad (2.193)$$

where  $\alpha_n^{\text{VB/CB}}$  and  $\beta_n^{\text{VB/CB}}$  are the components of the spinor wavefunction, and  $|n, m\rangle$  represent the LL eigenstates indexed by the LL quantum number  $n$  and the magnetic quantum number  $m$ . We then use the wavefunction (2.192) to solve the TDSE, which includes the perturbation due to the interaction with the light field:

$$i\hbar \frac{\partial}{\partial t} |\psi^{\text{B}}(t)\rangle = \left( \hat{H}_{\text{B}} + \hat{H}'(\sigma^{\pm}) \right) |\psi^{\text{B}}(t)\rangle. \quad (2.194)$$

Here,  $\hat{H}_{\text{B}}$  represents the unperturbed part of the Hamiltonian, while  $\hat{H}'(\sigma^{\pm})$  denotes the interaction part, where we consider the light field with circular polarization  $\sigma^{\pm}$ .

Similarly to the previous derivation, we calculate the matrix elements of  $\hat{H}'(\sigma^{\pm})$  in the basis of unperturbed LL states:

$$\langle \psi_{n,m}^{\text{VB/CB}} | \hat{H}'(\sigma^{\pm}) | \psi_{n',m'}^{\text{VB/CB}} \rangle = \pm \nu g \langle \psi_{n,m}^{\text{VB/CB}} | \begin{bmatrix} 0 & e^{\pm i\nu\omega t} \\ e^{\mp i\nu\omega t} & 0 \end{bmatrix} | \psi_{n',m'}^{\text{VB/CB}} \rangle \quad (2.195)$$

As before, we obtain the matrix elements for both valleys,  $K$  and  $K'$ , and both light polarizations,  $\sigma^+$  and  $\sigma^-$ :

$K$  valley :

$$\begin{aligned} \hat{H}'_{\text{VV}} &\equiv \hat{H}'_{\text{VV}}(t; n, m, n', m') = \langle \psi_{n,m}^{\text{VB}} | \hat{H}'(\sigma^{\pm}) | \psi_{n',m'}^{\text{VB}} \rangle = \\ &\pm g \left( e^{\mp i\omega t} \alpha_n^{\text{VB}} (\beta_n^{\text{VB}})^* \langle n, m | n' - 1, m' \rangle + e^{\pm i\omega t} (\alpha_n^{\text{VB}})^* \beta_n^{\text{VB}} \langle n - 1, m | n', m' \rangle \right), \\ \hat{H}'_{\text{CC}} &\equiv \hat{H}'_{\text{CC}}(t; n, m, n', m') = \langle \psi_{n,m}^{\text{CB}} | \hat{H}'(\sigma^{\pm}) | \psi_{n',m'}^{\text{CB}} \rangle = \\ &\pm g \left( e^{\mp i\omega t} \alpha_n^{\text{CB}} (\beta_n^{\text{CB}})^* \langle n, m | n' - 1, m' \rangle + e^{\pm i\omega t} (\alpha_n^{\text{CB}})^* \beta_n^{\text{CB}} \langle n - 1, m | n', m' \rangle \right), \\ \hat{H}'_{\text{VC}} &\equiv \hat{H}'_{\text{VC}}(t; n, m, n', m') = \langle \psi_{n,m}^{\text{VB}} | \hat{H}'(\sigma^{\pm}) | \psi_{n',m'}^{\text{CB}} \rangle = \\ &\pm g \left( e^{\mp i\omega t} \alpha_n^{\text{CB}} (\beta_n^{\text{VB}})^* \langle n, m | n' - 1, m' \rangle + e^{\pm i\omega t} (\alpha_n^{\text{VB}})^* \beta_n^{\text{CB}} \langle n - 1, m | n', m' \rangle \right), \\ \hat{H}'_{\text{CV}} &\equiv \hat{H}'_{\text{CV}}(t; n, m, n', m') = \langle \psi_{n,m}^{\text{CB}} | \hat{H}'(\sigma^{\pm}) | \psi_{n',m'}^{\text{VB}} \rangle = \\ &\pm g \left( e^{\mp i\omega t} \alpha_n^{\text{VB}} (\beta_n^{\text{CB}})^* \langle n, m | n' - 1, m' \rangle + e^{\pm i\omega t} (\alpha_n^{\text{CB}})^* \beta_n^{\text{VB}} \langle n - 1, m | n', m' \rangle \right), \end{aligned} \quad (2.196)$$

$K'$  valley :

$$\begin{aligned} \hat{H}'_{\text{VV}} &\equiv \hat{H}'_{\text{VV}}(t; n, m, n', m') = \langle \psi_{n,m}^{\text{VB}} | \hat{H}'(\sigma^{\pm}) | \psi_{n',m'}^{\text{VB}} \rangle = \\ &\mp g \left( e^{\pm i\omega t} \alpha_n^{\text{VB}} (\beta_n^{\text{VB}})^* \langle n - 1, m | n', m' \rangle + e^{\mp i\omega t} (\alpha_n^{\text{VB}})^* \beta_n^{\text{VB}} \langle n, m | n - 1, m' \rangle \right), \\ \hat{H}'_{\text{CC}} &\equiv \hat{H}'_{\text{CC}}(t; n, m, n', m') = \langle \psi_{n,m}^{\text{CB}} | \hat{H}'(\sigma^{\pm}) | \psi_{n',m'}^{\text{CB}} \rangle = \\ &\mp g \left( e^{\pm i\omega t} \alpha_n^{\text{CB}} (\beta_n^{\text{CB}})^* \langle n - 1, m | n', m' \rangle + e^{\mp i\omega t} (\alpha_n^{\text{CB}})^* \beta_n^{\text{CB}} \langle n, m | n' - 1, m' \rangle \right), \\ \hat{H}'_{\text{VC}} &\equiv \hat{H}'_{\text{VC}}(t; n, m, n', m') = \langle \psi_{n,m}^{\text{VB}} | \hat{H}'(\sigma^{\pm}) | \psi_{n',m'}^{\text{CB}} \rangle = \\ &\mp g \left( e^{\pm i\omega t} \alpha_n^{\text{CB}} (\beta_n^{\text{VB}})^* \langle n - 1, m | n', m' \rangle + e^{\mp i\omega t} (\alpha_n^{\text{VB}})^* \beta_n^{\text{CB}} \langle n, m | n' - 1, m' \rangle \right), \\ \hat{H}'_{\text{CV}} &\equiv \hat{H}'_{\text{CV}}(t; n, m, n', m') = \langle \psi_{n,m}^{\text{CB}} | \hat{H}'(\sigma^{\pm}) | \psi_{n',m'}^{\text{VB}} \rangle = \\ &\mp g \left( e^{\pm i\omega t} \alpha_n^{\text{VB}} (\beta_n^{\text{CB}})^* \langle n - 1, m | n', m' \rangle + e^{\mp i\omega t} (\alpha_n^{\text{CB}})^* \beta_n^{\text{VB}} \langle n, m | n' - 1, m' \rangle \right). \end{aligned} \quad (2.197)$$

In the following steps, we will drop the subscript  $n, m$  and retain it in the final expression.

Substituting the wavefunction (2.193) into the TDSE (2.175) follows the procedure presented in detail in Sec. 2.4.1.1 and finally leaves us with a system of equations for the coefficients  $C^{\text{VB}}(t)$  and  $C^{\text{CB}}(t)$ :

$$\begin{cases} i\hbar \frac{\partial}{\partial t} C^{\text{VB}}(t) = C^{\text{VB}}(t) \hat{H}'_{\text{VV}} + C^{\text{CB}}(t) e^{-\frac{i}{\hbar} \Delta E t} \hat{H}'_{\text{VC}}(t), \\ i\hbar \frac{\partial}{\partial t} C^{\text{CB}}(t) = C^{\text{VB}}(t) e^{\frac{i}{\hbar} \Delta E t} \hat{H}'_{\text{CV}} + C^{\text{CB}}(t) \hat{H}'_{\text{CC}}(t). \end{cases} \quad (2.198)$$

Defining as previously:

$$C^{\text{VB}}(t) = \exp\left(-\frac{i}{\hbar} \int_0^t \hat{H}'_{\text{VV}} dt'\right) \tilde{C}^{\text{VB}}(t), \quad (2.199)$$

$$C^{\text{CB}}(t) = \exp\left(-\frac{i}{\hbar} \int_0^t \hat{H}'_{\text{CC}}(t') dt'\right) \tilde{C}^{\text{CB}}(t), \quad (2.200)$$

and using the properties  $\hat{H}'_{\text{VV}} = -\hat{H}'_{\text{CC}}$  and  $\hat{H}'_{\text{VC}} = (\hat{H}'_{\text{CV}})^*$ , we obtain:

$$\begin{aligned} \frac{\partial}{\partial t} \tilde{C}^{\text{CB}}(t) &= \tilde{C}^{\text{VB}}(t) \hat{H}'_{\text{CV}} \exp\left(\frac{i}{\hbar} \int_0^t (\Delta E - 2\hat{H}'_{\text{VV}}) dt'\right) = \\ &= -\frac{i}{\hbar} \tilde{C}^{\text{VB}}(t) \frac{g}{2|E|} e^{-\nu i \theta} \left[ (\pm\nu \frac{\Delta}{2} + |E|) e^{i(\omega t \pm \theta)} + (\pm\nu \frac{\Delta}{2} - |E|) e^{-i(\omega t \pm \theta)} \right] \\ &\quad \times e^{\frac{i}{\hbar} \Delta E t} \exp\left(\pm 2 \frac{i}{\hbar} \frac{g v_F |\vec{q}|}{|E|} \frac{1}{\omega} (\sin(\omega t \pm \theta) - \sin(\pm \theta))\right). \end{aligned} \quad (2.201)$$

Here  $\Delta E = E_{n_1}^{\text{CB}} - E_{n_2}^{\text{VB}}$  denotes the energy difference between the conduction and valence LL states. Using the perturbation theory we expand  $\tilde{C}^{\text{CB}}(t)$  as:

$$\tilde{C}^{\text{CB}}(t) = \tilde{C}_0^{\text{CB}} + \frac{g}{E} \tilde{C}_1^{\text{CB}} + \left(\frac{g}{E}\right)^2 \tilde{C}_2^{\text{CB}} + \dots, \quad (2.202)$$

and taking only the first order in  $E_0$  ( $g = \frac{v_F e E_0}{\omega}$ ) we obtain the equations for the time evolution of the CB coefficients for each valley:

$$\begin{aligned} K : \quad \frac{\partial}{\partial t} \tilde{C}^{\text{CB}}(t) &= \mp \frac{ig}{\hbar} \begin{bmatrix} e^{i(\mp\omega + \frac{\Delta E}{\hbar})t} \alpha_{n'}^{\text{VB}} (\beta_n^{\text{CB}})^* \langle n, m | n' - 1, m' \rangle + \\ e^{i(\pm\omega + \frac{\Delta E}{\hbar})t} \beta_{n'}^{\text{VB}} (\alpha_n^{\text{CB}})^* \langle n - 1, m | n', m' \rangle \end{bmatrix} \\ K' : \quad \frac{\partial}{\partial t} \tilde{C}^{\text{CB}}(t) &= \pm \frac{ig}{\hbar} \begin{bmatrix} e^{i(\pm\omega + \frac{\Delta E}{\hbar})t} \alpha_{n'}^{\text{VB}} (\beta_n^{\text{CB}})^* \langle n - 1, m | n', m' \rangle + \\ e^{i(\mp\omega + \frac{\Delta E}{\hbar})t} \beta_{n'}^{\text{VB}} (\alpha_n^{\text{CB}})^* \langle n, m | n' - 1, m' \rangle \end{bmatrix}. \end{aligned} \quad (2.203)$$

Here  $\alpha$  and  $\beta$  are the coefficients of the non-perturbed single-particle LLs wavefunction. The terms inside the square brackets correspond to the different possible transitions between the LLs, involving the coupling between the valence and CB states, as well as the polarization of the light field. We now notice that in this system, the terms involving the products  $\alpha^{\text{VB}} \beta^{\text{CB}}$  are much smaller than those involving  $\alpha^{\text{CB}} \beta^{\text{VB}}$ , i.e.,  $\alpha^{\text{VB}} \beta^{\text{CB}} \ll \alpha^{\text{CB}} \beta^{\text{VB}}$ . This leads to the dominance of two specific transitions, with the other two being much weaker. As in the previous section, we apply the rotating wave approximation to neglect the rapidly oscillating terms. Consequently, we can retain only the slowly oscillating terms for the dominant transitions, simplifying the equations for each valley as follows:

$$\begin{aligned} \sigma^-, K : \quad \frac{\partial}{\partial t} \tilde{C}_{n,m,n',m'}^{\text{CB}}(t) &= \frac{ig}{\hbar} e^{i(-\omega + \frac{\Delta E}{\hbar})t} \beta_{n'}^{\text{VB}} (\alpha_n^{\text{CB}})^* \langle n - 1, m | n', m' \rangle \\ \sigma^+, K' : \quad \frac{\partial}{\partial t} \tilde{C}_{n,m,n',m'}^{\text{CB}}(t) &= \frac{ig}{\hbar} e^{i(-\omega + \frac{\Delta E}{\hbar})t} \beta_{n'}^{\text{VB}} (\alpha_n^{\text{CB}})^* \langle n, m | n' - 1, m' \rangle \end{aligned} \quad (2.204)$$

These equations allow to describe the time evolution of the CB coefficients in the presence of the light field for the  $\sigma^-$  and  $\sigma^+$  circular polarizations. As indicated by the equations, each valley has its own selection rules for the allowed transitions, determined by the polarization of the light.

### 2.4.1.4 Transition Rate with Magnetic Field

To calculate the transition rate in the presence of a magnetic field, we proceed similarly to the previous case, following the procedure described in Sec. 2.4.1.2. We begin by calculating the time-dependent coefficients  $\tilde{C}_{n,m,n',m'}^{\text{CB}}(t)$  for the CB states, where the interaction with the light field is present. The interaction Hamiltonian in this case is the same as previously defined,  $\hat{H}'(\sigma^\pm)$ , but now it takes into account the magnetic field and the corresponding selection rules derived in the previous subsection.

From the equations for the time evolution of the CB coefficients in the presence of a light field, we have:

$$\frac{\partial}{\partial t} \tilde{C}_{n,m,n',m'}^{\text{CB}}(t) = \frac{ig}{\hbar} e^{i(-\omega + \frac{\Delta E}{\hbar})t} \beta_{n'}^{\text{VB}} (\alpha_n^{\text{CB}})^* \langle n-1, m | n', m' \rangle. \quad (2.205)$$

This represents the interaction term for one of the dominant transitions (e.g.,  $\sigma^-$  polarization for valley  $K$ ). Similarly, for valley  $K'$  and  $\sigma^+$  polarization, we have the corresponding equation:

$$\frac{\partial}{\partial t} \tilde{C}_{n,m,n',m'}^{\text{CB}}(t) = \frac{ig}{\hbar} e^{i(-\omega + \frac{\Delta E}{\hbar})t} \beta_{n'}^{\text{VB}} (\alpha_n^{\text{CB}})^* \langle n, m | n'-1, m' \rangle. \quad (2.206)$$

Solving the differential equation gives the time evolution of the CB coefficients  $\tilde{C}^{\text{CB}}(t)$ .

As previously, the transition probability  $|\tilde{C}(t)|^2$  is the square of the magnitude of the coefficient  $\tilde{C}^{\text{CB}}(t)$ , which gives the probability of finding the system in the CB after interacting with the light field. The transition rate  $\gamma$  is the time derivative of the transition probability  $|\tilde{C}(t)|^2$ , which gives the rate at which transitions occur between the states. As  $t \rightarrow \infty$ , we arrive at the expression for the transition rate in the presence of the magnetic field:

$$\sigma^-, K : \quad \gamma_{n,m,n',m'} = \frac{2\pi g^2}{\hbar^2} |\beta_{n'}^{\text{VB}} (\alpha_n^{\text{CB}})^*|^2 \delta\left(\omega - \frac{\Delta E}{\hbar}\right) |\langle n, m | n'-1, m' \rangle|^2, \quad (2.207)$$

$$\sigma^+, K' : \quad \gamma_{n,m,n',m'} = \frac{2\pi g^2}{\hbar^2} |\beta_{n'}^{\text{VB}} (\alpha_n^{\text{CB}})^*|^2 \delta\left(\omega - \frac{\Delta E}{\hbar}\right) |\langle n, m | n'-1, m' \rangle|^2, \quad (2.208)$$

which describes the transition rate for optical processes between LLs in the presence of a magnetic field and light with circular polarization. In the above equation,  $\Delta E = E_{n_1}^{\text{CB}} - E_{n_2}^{\text{VB}} \equiv E_n^{\text{CB}} - E_{n'}^{\text{VB}}$ . This result is directly related to Fermi's Golden Rule, where the transition rate is governed by the matrix elements of the perturbation and the energy conservation condition, represented by the delta function.

This transition rate formula allows us to understand how light, in the form of circularly polarized radiation, induces transitions between LLs in the conduction and valence bands of the TMDC monolayer under the influence of a magnetic field.

The optical selection rules derived from these equations for the transitions between LLs from the valence band to the CB are as follows:

$$\begin{aligned} \sigma^-, K : \quad & n - n' = +1, \quad m = m' \\ \sigma^+, K' : \quad & n - n' = -1, \quad m = m' \end{aligned} \quad (2.209)$$

In these selection rules, it is evident that the magnetic quantum number  $m$  remains unchanged (i.e.,  $m = m'$ ), while the LL index  $n$  undergoes a shift of  $\pm 1$  for each valley. The  $\sigma^-$  polarization induces a transition where the LL index increases by one ( $n' = n + 1$ ), while the  $\sigma^+$  polarization causes a transition where the LL index decreases by one ( $n' = n - 1$ ).

Although the analysis is conducted without considering the SOC, it is straightforward to incorporate SOC into the model. The inclusion of SOC would not affect these selection rules significantly, as only optically active transitions, which do not flip the spin, are allowed. This makes the transitions between LLs spin-conserving.

### 2.4.2 Dipole Moments for Optical Transitions

In this section, we introduce the concept of dipole matrix elements (DMEs), which quantify the coupling between quantum states and an external electric field within the  $\vec{E} \cdot \vec{r}$  formalism. This approach is particularly suited for confined or finite systems, such as QDs or nanostructures, where transitions occur between discrete, spatially localized states.

The interaction of such systems with light is governed by the electric dipole Hamiltonian, where the perturbation due to the light is expressed as:

$$\hat{H} = -e \vec{E}_0^\pm \cdot \vec{r}, \quad (2.210)$$

with  $\vec{r}$  being the position operator, and  $\vec{E}_0^\pm$  denoting the electric field vector of circularly polarized light. The DMEs corresponding to this interaction are given by:

$$D_{p,q} = \langle \varphi_p | \vec{E}_0^\pm \cdot \vec{r} | \varphi_q \rangle, \quad (2.211)$$

where  $|\varphi_q\rangle$  and  $|\varphi_p\rangle$  represent the initial and final quantum states. These elements determine the strength and selection rules of optical transitions under the electric dipole approximation.

In general, the wavefunctions of confined systems can be expressed as linear combinations of localized basis states. A general expansion takes the form:

$$|\varphi^s\rangle = \sum_i C_i^s |\psi_i\rangle, \quad (2.212)$$

where  $C_i^s$  are expansion coefficients, and  $|\psi_i\rangle$  are basis functions, such as localized atomic orbitals. Using this expansion, the DME can be written as:

$$\vec{D}_{s,s'} = \langle s | \vec{r} | s' \rangle = \sum_{i,j} (C_i^s)^* C_j^{s'} \langle i | \vec{r} | j \rangle, \quad (2.213)$$

where  $\langle i | \vec{r} | j \rangle$  are the DMEs between individual basis states. These terms encapsulate the microscopic transition strengths and are essential for determining optical absorption and emission properties.

For systems with localized basis states, the matrix elements  $\langle i | \vec{r} | j \rangle$  can be approximated as [58, 95, 98, 130]:

$$\langle i | \vec{r} | j \rangle = D_{ij} (\hat{R}_j - \hat{R}_i) + \vec{R}_j \delta_{ij}, \quad (2.214)$$

where  $\hat{R}_i$  and  $\hat{R}_j$  denote the positions of the respective basis orbitals, and  $\delta_{ij}$  is the Kronecker delta. The coefficient  $D_{ij}$  quantifies the dipole coupling and is given by:

$$D_{ij} = \left| \int d\vec{r} \psi_i^* (\vec{r} - \vec{R}_i) \vec{r} \psi_j (\vec{r} - \vec{R}_j) \right|, \quad (2.215)$$

where  $\psi_i(\vec{r})$  and  $\psi_j(\vec{r})$  are localized orbitals centered at  $\vec{R}_i$  and  $\vec{R}_j$ , respectively. The value of  $D_{ij}$  reflects the spatial overlap and symmetry of the orbitals.

The  $\vec{E} \cdot \vec{r}$  formalism presented here provides a transparent and physically intuitive framework for computing transition probabilities in systems where electrons are spatially confined. In contrast to the  $\vec{p} \cdot \vec{A}$  formalism used in periodic systems, this dipole-based approach offers direct access to matrix elements without invoking the crystal momentum picture. It is thus ideally suited for the analysis of optically active quantum dots, heterostructures, and nanostructured 2D materials.

In subsequent sections, we will apply this formalism to specific systems, including BLG QDs and monolayer TMDCs, with an emphasis on how confinement, symmetry, and valley degrees of freedom influence the optical response.

### 2.4.3 Optical Absorption

Optical absorption is the process by which an incident photon promotes an electron from a lower-energy state to a higher-energy state, increasing the total energy of the system. In confined quantum systems, such as QDs or low-dimensional materials, the spatial quantization of electronic states leads to discrete absorption peaks, governed by the dipole selection rules and the symmetry of the system.

Within the electric dipole approximation, the absorption probability is given by Fermi's golden rule:

$$A(\omega) = \sum_{f,i} \left| \langle \psi_f | \hat{H} | \psi_i \rangle \right|^2 \delta(E_f - E_i - \hbar\omega), \quad (2.216)$$

where  $|\psi_i\rangle$  and  $|\psi_f\rangle$  denote the initial and final electronic states with energies  $E_i$  and  $E_f$ , respectively, and  $\omega$  is the frequency of the absorbed photon. The Hamiltonian in the  $\vec{E} \cdot \vec{r}$  formalism is given by:

$$\hat{H} = -e \vec{E}_0^\pm \cdot \vec{r}, \quad (2.217)$$

which leads to the matrix elements:

$$\langle \psi_f | \hat{H} | \psi_i \rangle = -e \vec{E}_0^\pm \cdot \vec{D}_{fi}, \quad (2.218)$$

with  $\vec{D}_{fi} = \langle \psi_f | \vec{r} | \psi_i \rangle$  representing the dipole matrix element between states  $i$  and  $f$ .

For example, to account for excitonic effects, the electronic states can be expressed as electron-hole pair excitations labeled by  $\mu$ . The absorption spectrum then becomes:

$$A(\omega) = \sum_{\mu} \left| \sum_{s,s',\sigma} \vec{E}_0^\pm \cdot \vec{D}_{s,s'} \left( A_{s,s',\sigma}^\mu \right)^* \right|^2 \delta(E_\mu - \hbar\omega), \quad (2.219)$$

where  $A_{s,s',\sigma}^\mu$  are the expansion coefficients of the excitonic eigenstate  $\mu$  in the basis of single-particle transitions between states  $s$  and  $s'$  (including spin  $\sigma$ ), and  $\vec{D}_{s,s'}$  denotes the dipole matrix element between those states. The  $\delta$ -function enforces energy conservation.

External fields, strain, or dielectric environments can modify the transition energies  $E_\mu$  and matrix elements  $\vec{D}_{s,s'}$ , resulting in shifts and intensity changes in the absorption spectrum. Additionally, when considering a larger number of electrons, many-body interactions will further influence these transition energies and matrix elements, leading to additional modifications in the absorption spectrum. These effects, including electron-electron interactions, screening, and the formation of excitons or other correlated states, will be addressed in later sections of the thesis. For now, we focus on the single-particle picture, which captures the primary optical response of the system. Nevertheless, these spectra are key to understanding the internal structure and interaction dynamics of the system.

### 2.4.4 Optical Emission

Optical emission describes the process by which an electron relaxes from an excited state to a lower-energy state, emitting a photon in the process. This can occur spontaneously or via stimulation by an external photon field. As in absorption, emission in confined quantum systems is governed by the dipole interaction and the energy spacing of the discrete quantum states.

The emission rate for a transition from an excited state  $|\psi_n\rangle$  to a lower-energy state  $|\psi_s\rangle$ , resulting in photon emission at energy  $\hbar\omega$ , is given by Fermi's golden rule:

$$A(\omega) = \sum_{n,s} W_n \left| \langle \psi_s | \hat{H} | \psi_n \rangle \right|^2 \delta(E_n - E_s - \hbar\omega), \quad (2.220)$$

where  $W_n$  is the thermal occupation probability of the excited state  $|\psi_n\rangle$ , and the Hamiltonian is again expressed in terms of the dipole operator.

The thermal occupation of the excited states follows a Boltzmann distribution:

$$W_n = \frac{e^{-E_n/k_B T}}{\sum_m e^{-E_m/k_B T}}, \quad (2.221)$$

where  $T$  is the system's effective temperature and  $k_B$  is Boltzmann's constant. This expression ensures that higher-energy states are less likely to be populated at lower temperatures.

The emitted intensity  $I(\omega)$  depends on both the thermal occupation of the excited states and the corresponding DMEs  $\vec{D}_{n,s} = \langle \psi_s | \vec{r} | \psi_n \rangle$ . As with absorption, the emission spectrum consists of discrete peaks, which carry information about energy level spacings, excitonic binding, and radiative recombination pathways.

The emission can also be tailored via system design, including the application of magnetic fields, changes in geometry or dielectric environment, or coupling to photonic cavities. This makes emission spectroscopy a powerful tool for characterizing and engineering optical processes in nanostructured materials.

Together, the absorption and emission spectra form the core of optical characterization in quantum systems, offering insight into energy structure, carrier dynamics, and many-body effects. In later sections, we apply this framework to the specific case of BLG QDs, where valley, spin, and spatial confinement strongly influence optical transitions.



## Chapter 3

# Optical Properties of Gated Bilayer Graphene Quantum Dots

There is growing interest in semiconductor quantum dots (QDs) as versatile platforms for quantum technologies [56, 64, 69, 70, 84, 85, 92, 93, 95–120]. Lateral gated QDs offer electrical tunability and are suitable for spin-based quantum computation [56, 145–147], while self-assembled QDs provide high optical quality and enable confinement of both electrons and holes, ideal for emitters and photon sources [124–129]. However, combining tunability with efficient optical response remains a major challenge.

A promising solution is offered by 2D materials, and in particular, bilayer graphene (BLG) [1]. In its natural form, BLG is gapless, but the application of a vertical electric field opens a tunable bandgap in the infrared regime, enabling new optoelectronic functionalities. This bandgap tunability makes BLG attractive for use in transistors [43, 65], as well as for creating voltage-controlled QDs that support confining both electrons and holes [57, 58, 103, 112, 113, 115, 130, 145].

Theoretical work by João Milton Pereira *et al.* [145] introduced a lateral confinement mechanism in BLG based on position-dependent doping, enabling ambipolar QDs and revealing unusual angular momentum selection rules due to the pseudospin winding number of 2. Subsequent experimental efforts successfully demonstrated lateral gated QDs in BLG [111, 112], paving the way for quantum devices based on these structures. Notably, two-electron complexes confined in BLG QDs revealed spin-triplet, valley-singlet ground states due to electron-electron interactions [56, 116].

At the same time, BLG's optical properties have garnered significant attention. Cheol-Hwan Park and Steven G. Louie [57] predicted the presence of strongly bound excitons in gated BLG, with optical selection rules dictated by Berry curvature and pseudospin winding. This was later confirmed experimentally by Long Ju *et al.* [48], who observed gate-tunable excitonic transitions in BLG, dominated by a bright  $2p$  state.

In this chapter, we provide a comprehensive study of QDs formed in gated Bernal-stacked BLG. Sec. 3.1 introduces the single-particle electronic structure of BLG QDs, highlighting the role of trigonal warping and the confinement potential. We also compute dipole matrix elements (DMEs) relevant for light-matter interaction. In Sec. 3.2, we analyze excitonic states confined in BLG QDs, emphasizing the impact of the electric field on their binding energies and optical selection rules. Sec. 3.3 is devoted to the study of trions in BLG QDs, focusing on their fine structure and temperature-dependent optical response. Finally, we discuss the implications of these findings for future quantum technologies, including electrically tunable single-photon emitters based on BLG.

### 3.1 Single-Particle Properties of Bilayer Graphene and Bilayer Graphene QDs

The study of non-interacting electrons in BLG QDs provides a foundation for understanding the electronic structure and behavior of these systems in the absence of many-body effects. In this section, we focus on the single-particle properties of BLG QDs, where the interactions between charge carriers are neglected. This simplified model allows us to investigate the effects of quantum confinement and the tunability of the energy gap, offering insights into the basic characteristics of BLG QDs that serve as a starting point for more complex, interacting systems.

#### 3.1.1 Tight-Binding Model for Bulk Bilayer Graphene

We begin by considering a Bernal-stacked BLG system, as shown schematically in Fig. 3.1(a). In this configuration, the sublattices of the two graphene layers are denoted as A and B for the first layer, and C and D for the second. The in-plane bond length is  $a = 0.143$  nm, while the distance between the two layers is  $h = 0.335$  nm. To describe the lattice geometry, we choose the unit cell vectors as:

$$\vec{a}_1 = a \left( 0, \sqrt{3} \right), \quad \vec{a}_2 = \frac{a}{2} \left( 3, \sqrt{3} \right). \quad (3.1)$$

The rhomboidal real-space computational box, depicted in Fig. 3.1(a), is defined by the vectors  $\vec{R}_{m,n} = m\vec{a}_1 + n\vec{a}_2$ , where the integer coefficients  $m = \left\{ -\frac{M-1}{2}, \dots, \frac{M-1}{2} \right\}$  and  $n = \left\{ -\frac{N-1}{2}, \dots, \frac{N-1}{2} \right\}$ , with  $M = N = 633$  representing the number of UCs along the directions of the lattice vectors. This configuration leads to a computational box that includes approximately 1.6 million carbon atoms, making the computational demands significant. To mitigate finite-size effects, periodic boundary conditions are applied, connecting the opposite edges of the rhomboid, which results in a set of allowed  $k$ -points [58, 59, 130].

The low-energy electronic structure of Bernal-stacked BLG can be described using a TB approach, considering both intralayer and interlayer hopping between the atomic orbitals of the carbon atoms. In BLG, each graphene layer consists of two sublattices:  $A$  and  $B$  for the top layer, and  $C$  and  $D$  for the bottom layer, as depicted in Fig. 3.1. The Hamiltonian for a single electron moving in the potential of  $A$ ,  $B$ ,  $C$  and  $D$  carbon atoms, including both the kinetic energy and potential terms, is given by:

$$\hat{H} = \frac{\hat{p}^2}{2m} + \sum_{\vec{R}^A} \hat{V}^A \left( \vec{r} - \vec{R}^A \right) + \sum_{\vec{R}^B} \hat{V}^B \left( \vec{r} - \vec{R}^B \right) + \sum_{\vec{R}^C} \hat{V}^C \left( \vec{r} - \vec{R}^C \right) + \sum_{\vec{R}^D} \hat{V}^D \left( \vec{r} - \vec{R}^D \right). \quad (3.2)$$

The vectors  $\vec{R}^l$  represent the positions of atomic sites. In graphene, each carbon atom has three NNs. The  $2s$ ,  $2p_x$ , and  $2p_y$  orbitals of these atoms hybridize to form  $sp^2$  hybridized orbitals, which result in strong  $\sigma$ -bonds that primarily determine graphene's remarkable mechanical properties. On the other hand, the unhybridized  $p_z$  orbitals, oriented perpendicular to the graphene plane, form  $\pi$ -bonds. These  $\pi$ -bonds are the main contributors to graphene's electronic and optical properties.

In the context of Bernal-stacked BLG, the electronic wave functions are constructed using the Bloch states associated with the four sublattices  $A$  and  $B$  in the top layer, and  $C$  and  $D$  in the bottom layer. The wave function of the system is described as a linear combination of the Bloch wave functions from each sublattice:

$$\Phi_{p,\vec{k}}(\vec{r}) = \sum_l \mu_{p,\vec{k}}^l \phi_{\vec{k}}^l(\vec{r}), \quad (3.3)$$

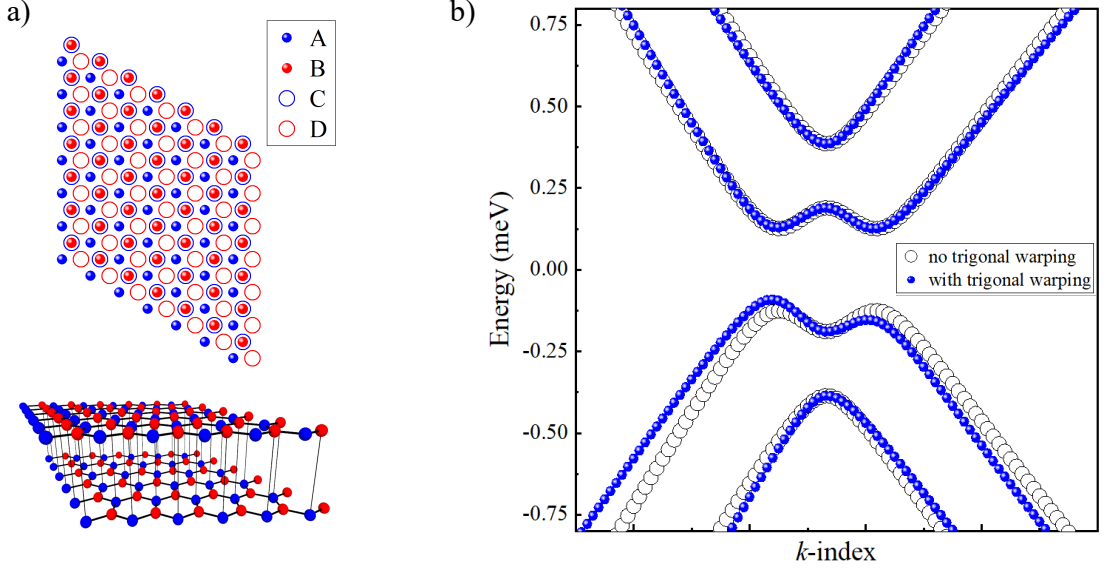


**Figure 3.1:** (a) The upper plot illustrates the rhomboidal computational box for BLG, depicted schematically to highlight the positions of sublattices  $A$  and  $B$  (layer 1, represented by filled symbols) and  $C$  and  $D$  (layer 2, represented by open circles). The lower diagram provides a 3D view of the BLG structure in its Bernal-stacked configuration. (b) The bulk electronic structure of BLG near the  $K$  point is shown, with a displacement voltage of  $V_E = 0.38$  eV. The data points are plotted without (black circles) and with (blue dots) the inclusion of trigonal warping (TW) effects. The variable  $k$  denotes the distance from the  $K$  point along the  $\vec{b}_1 + \vec{b}_2$  direction, where  $\vec{b}_1$  and  $\vec{b}_2$  are the reciprocal lattice vectors.

where  $\sum_l$  sums over the four sublattices  $A$ ,  $B$ ,  $C$ , and  $D$ ,  $\phi_k^l(\vec{r})$  are the atomic wave functions associated with the respective sublattices in real space, and  $\mu_{p,\vec{k}}^l$  are the coefficients representing the relative contributions of each sublattice to the overall wave function, determined by solving the Schrödinger equation for the Hamiltonian of the BLG system. Using the periodicity of the lattice, each atomic wave function associated with the respective sublattices in real space can be written explicitly as:

$$\phi_k^l(\vec{r}) = \frac{1}{\sqrt{N_{UC}}} e^{i\vec{k}\cdot\vec{R}^l} \varphi_{p_z}(\vec{r} - \vec{R}^l), \quad (3.4)$$

where  $e^{i\vec{k}\cdot\vec{r}}$  is the plane-wave factor capturing the translational symmetry of the crystal, and  $\varphi_{p_z}$  are the  $p_z$  orbitals localized on each sublattice  $l$ .  $N_{UC}$  denotes the number of UCs.

The TB Hamiltonian  $H(\vec{k})$  is constructed by evaluating the matrix elements  $H_{ij}(\vec{k}) = \langle \phi_i | \hat{H} | \phi_j \rangle$ , where  $\phi_i$  and  $\phi_j$  are the Bloch states localized on sublattices  $A, B, C$ , and  $D$ . These sublattices are associated with the top and bottom layers of BLG. The total Hamiltonian has contributions from intralayer hopping ( $\hat{H}_{\text{intra}}$ ) and interlayer hopping ( $\hat{H}_{\text{inter}}$ ).

The intralayer hopping occurs between NN atoms within the same graphene layer. For hopping within the top layer (between sublattices  $A$  and  $B$ ) and the bottom layer (between sublattices  $C$  and  $D$ ), the matrix elements of the intralayer Hamiltonian are:

$$\hat{H}_{\text{intra}}^{AB}(\vec{k}) = \langle \phi_A | \hat{H} | \phi_B \rangle, \quad (3.5)$$

$$\hat{H}_{\text{intra}}^{BA}(\vec{k}) = \langle \phi_B | \hat{H} | \phi_A \rangle = \langle \phi_A | \hat{H} | \phi_B \rangle^\dagger, \quad (3.6)$$

and similarly for the  $C$  and  $D$  sublattices in the bottom layer:

$$\hat{H}_{\text{intra}}^{CD}(\vec{k}) = \langle \phi_C | \hat{H} | \phi_D \rangle, \quad (3.7)$$

$$\hat{H}_{\text{intra}}^{DC}(\vec{k}) = \langle \phi_D | \hat{H} | \phi_C \rangle = \langle \phi_C | \hat{H} | \phi_D \rangle^\dagger. \quad (3.8)$$

We begin by calculating the matrix element  $\hat{H}_{\text{intra}}^{AB}(\vec{k}) = \langle \phi_A | \hat{H} | \phi_B \rangle$ . Substituting the explicit form of the wave functions given in Eq. (3.4) into the expression for the matrix element, we have:

$$\hat{H}_{\text{intra}}^{AB}(\vec{k}) = \langle \phi_A | \hat{H} | \phi_B \rangle = \frac{1}{N_{\text{UC}}} \sum_{\vec{R}^A, \vec{R}^B} e^{-i\vec{k} \cdot \vec{R}^A} e^{i\vec{k} \cdot \vec{R}^B} \int d^3r \varphi_{p_z}^*(\vec{r} - \vec{R}^A) \hat{H} \varphi_{p_z}(\vec{r} - \vec{R}^B). \quad (3.9)$$

Focusing on the NN hopping, we approximate the Hamiltonian contribution between sublattices A and B as the NN hopping parameter  $\gamma_0$ . This reduces the integral to the following form:

$$\int d^3r \varphi_{p_z}^*(\vec{r} - \vec{R}^A) \hat{H} \varphi_{p_z}(\vec{r} - \vec{R}^B) \approx \gamma_0, \quad (3.10)$$

where  $\gamma_0$  represents the strength of the intralayer hopping. Now, the summation over lattice positions captures the relative phases between neighboring sites. Each atom in sublattice A is surrounded by three NNs from sublattice B, located at specific relative positions within the UC. These relative positions introduce phase factors that contribute to the hopping amplitude. The relative positions of the three NNs of an atom in sublattice A (belonging to sublattice B) are given by:

$$\vec{\delta}_1 = \vec{\tau}, \quad \vec{\delta}_2 = \vec{\tau} - (\vec{a}_1 + \vec{a}_2), \quad \vec{\delta}_3 = \vec{\tau} - \vec{a}_2, \quad (3.11)$$

where  $\vec{\tau} = (a, 0)$  is the vector connecting the A and B sublattices within the same unit cell. The hopping amplitude between an atom in sublattice A and its NNs in sublattice B is described by the phase factor  $e^{i\vec{k} \cdot \vec{\delta}_j}$ , where  $\vec{\delta}_j$  is the relative position of the neighbor. The total contribution of the hopping is obtained by summing over the three NNs:

$$f(\vec{k}) = \sum_{j=1}^3 e^{i\vec{k} \cdot \vec{\delta}_j} = e^{i\vec{k} \cdot \vec{\tau}} \left( 1 + e^{-i\vec{k} \cdot (\vec{a}_1 + \vec{a}_2)} + e^{-i\vec{k} \cdot \vec{a}_2} \right). \quad (3.12)$$

This expression captures the total contribution of the NN hopping in the honeycomb lattice. The conjugate  $f^*(\vec{k})$ , needed for reverse hopping terms, is given by:

$$f^*(\vec{k}) = e^{-i\vec{k} \cdot \vec{\tau}} \left( 1 + e^{-i\vec{k} \cdot (\vec{a}_1 + \vec{a}_2)} + e^{-i\vec{k} \cdot \vec{a}_2} \right). \quad (3.13)$$

Substituting now  $\gamma_0$  and  $f(\vec{k})$  into the expression for  $\hat{H}_{\text{intra}}^{AB}$ , we obtain:

$$\hat{H}_{\text{intra}}^{AB}(\vec{k}) = \gamma_0 f(\vec{k}). \quad (3.14)$$

This result demonstrates how the intralayer hopping term arises from the overlap of  $p_z$ -orbitals and the lattice phase factors encoded in  $f(\vec{k})$ . Analogously, the remaining intralayer matrix elements can be calculated, giving:

$$\hat{H}_{\text{intra}}^{BA}(\vec{k}) = \langle \phi_B | \hat{H} | \phi_A \rangle = \gamma_0 f^*(\vec{k}), \quad (3.15)$$

and similarly for the  $C$  and  $D$  sublattices in the bottom layer:

$$\hat{H}_{\text{intra}}^{CD}(\vec{k}) = \gamma_0 f(\vec{k}), \quad (3.16)$$

$$\hat{H}_{\text{intra}}^{DC}(\vec{k}) = \gamma_0 f^*(\vec{k}). \quad (3.17)$$

The full intralayer Hamiltonian has the form:

$$\hat{H}_{\text{intra}}(\vec{k}) = \gamma_0 \begin{pmatrix} 0 & f(\vec{k}) & 0 & 0 \\ f^*(\vec{k}) & 0 & 0 & 0 \\ 0 & 0 & 0 & f(\vec{k}) \\ 0 & 0 & f^*(\vec{k}) & 0 \end{pmatrix}. \quad (3.18)$$

The interlayer hopping accounts for couplings between sublattices in the top and bottom graphene layers. This includes:  $\gamma_1$ , the vertical hopping between sublattices  $B$  (top) and  $C$  (bottom),  $\gamma_3$ , the slanted hopping between  $A$  (top) and  $D$  (bottom), and  $\gamma_4$ , the slanted hopping between  $A$  (top) and  $C$  (bottom), and  $B$  (top) and  $D$  (bottom). For the vertical hopping between  $B$  (top) and  $C$  (bottom), the matrix element is simply:

$$\hat{H}_{\text{inter}}^{BC} = \langle \phi_B | \hat{H} | \phi_C \rangle = \gamma_1, \quad (3.19)$$

and similarly for the reverse hopping:

$$\hat{H}_{\text{inter}}^{CB} = \langle \phi_C | \hat{H} | \phi_B \rangle = \gamma_1. \quad (3.20)$$

For slanted hopping between  $A$  (top) and  $C$  (bottom):

$$\hat{H}_{\text{inter}}^{AC} = \langle \phi_A | \hat{H} | \phi_C \rangle = \gamma_4 f(\vec{k}), \quad (3.21)$$

and the reverse hopping gives:

$$\hat{H}_{\text{inter}}^{CA} = \langle \phi_C | \hat{H} | \phi_A \rangle = \gamma_4 f^*(\vec{k}). \quad (3.22)$$

For the slanted hopping between  $A$  (top) and  $D$  (bottom), we obtain:

$$\hat{H}_{\text{inter}}^{AD} = \langle \phi_A | \hat{H} | \phi_D \rangle = \gamma_3 f^*(\vec{k}), \quad (3.23)$$

and for the reverse hopping:

$$\hat{H}_{\text{inter}}^{DA} = \langle \phi_D | \hat{H} | \phi_A \rangle = \gamma_3 f(\vec{k}). \quad (3.24)$$

Including all interlayer couplings ( $\gamma_1, \gamma_3, \gamma_4$ ), the interlayer Hamiltonian is:

$$\hat{H}_{\text{inter}}(\vec{k}) = \begin{pmatrix} 0 & 0 & \gamma_4 f(\vec{k}) & \gamma_3 f^*(\vec{k}) \\ 0 & 0 & \gamma_1 & \gamma_4 f(\vec{k}) \\ \gamma_4 f^*(\vec{k}) & \gamma_1 & 0 & 0 \\ \gamma_3 f(\vec{k}) & \gamma_4 f^*(\vec{k}) & 0 & 0 \end{pmatrix}. \quad (3.25)$$

Finally, combining the intralayer and interlayer contributions, the total Hamiltonian becomes:

$$H(\vec{k}) = \hat{H}_{\text{intra}}(\vec{k}) + \hat{H}_{\text{inter}}(\vec{k}), \quad (3.26)$$

which gives the complete TB Hamiltonian:

$$H(\vec{k}) = \begin{pmatrix} 0 & \gamma_0 f(\vec{k}) & \gamma_4 f(\vec{k}) & \gamma_3 f^*(\vec{k}) \\ \gamma_0 f^*(\vec{k}) & 0 & \gamma_1 & \gamma_4 f(\vec{k}) \\ \gamma_4 f^*(\vec{k}) & \gamma_1 & 0 & \gamma_0 f(\vec{k}) \\ \gamma_3 f(\vec{k}) & \gamma_4 f^*(\vec{k}) & \gamma_0 f^*(\vec{k}) & 0 \end{pmatrix}. \quad (3.27)$$

The interatomic interactions are governed by the following hopping parameters:  $\gamma_0$  describing the NN intralayer hopping within each graphene sheet,  $\gamma_1$  corresponding to the vertical interlayer

hopping between atoms in sublattices  $B$  (top layer) and  $C$  (bottom layer),  $\gamma_3$  for the interlayer hopping between atoms in sublattices  $A$  (top layer) and  $D$  (bottom layer), and  $\gamma_4$  capturing the interlayer hopping between atoms in sublattices  $A$  (top layer) and  $C$  (bottom layer), as well as  $B$  (top layer) and  $D$  (bottom layer). This Hamiltonian describes the electronic properties of Bernal-stacked BLG in the absence of external fields and serves as the foundation for further analysis of its band structure.

### 3.1.2 The Effect of Vertical Electric Field on the Electronic Structure of Bilayer Graphene

In the next step, we introduce an external electric field applied perpendicular to the BLG layers. The potential difference between the two layers is defined as  $V_E$ , with a potential of  $+V_E/2$  applied to layer 1 and  $-V_E/2$  to layer 2, respectively. This external field breaks the symmetry between the layers, leading to the opening of an energy gap in BLG. The BLG Hamiltonian defined in Eq. (3.27), expressed in the basis of the four sublattices ( $A$ ,  $B$ ,  $C$ , and  $D$ ), takes thus the following form:

$$H(\vec{k}) = \begin{pmatrix} \frac{V_E}{2} & \gamma_0 f(\vec{k}) & \gamma_4 f(\vec{k}) & \gamma_3 f^*(\vec{k}) \\ \gamma_0 f^*(\vec{k}) & \frac{V_E}{2} & \gamma_1 & \gamma_4 f(\vec{k}) \\ \gamma_4 f^*(\vec{k}) & \gamma_1 & -\frac{V_E}{2} & \gamma_0 f(\vec{k}) \\ \gamma_3 f(\vec{k}) & \gamma_4 f^*(\vec{k}) & \gamma_0 f^*(\vec{k}) & -\frac{V_E}{2} \end{pmatrix}, \quad (3.28)$$

where  $\gamma_0 = -2.5$  eV is the NN hopping parameter,  $\gamma_1 = 0.34$  eV represents the hopping between the AB-stacked atoms, and the interlayer hopping parameter is incorporated through  $\gamma_4$  and  $\gamma_3$ . The displacement voltage  $V_E$  is set to 0.38 eV. To account for the effects of trigonal warping (TW), we assume a finite matrix element  $\gamma_3 = 0.12|\gamma_0|$  eV [130, 147], and set  $\gamma_4 = \gamma_3$  [130].

The coefficients  $\mu_{p,\vec{k}}^l$  and energies  $\varepsilon_{p,\vec{k}}$  of the Bernal-stacked BLG with applied electric field are obtained by diagonalizing the Hamiltonian given in Eq. (3.28). The set of allowed  $k$  points is determined using the formulas:

$$k_x = \frac{\frac{2\pi m}{M} a_{1y} - \frac{2\pi n}{N} a_{2y}}{a_{2x} a_{1y} - a_{1x} a_{2y}}, \quad k_y = \frac{\frac{2\pi m}{M} a_{1x} - \frac{2\pi n}{N} a_{2x}}{a_{2y} a_{1x} - a_{1y} a_{2x}}. \quad (3.29)$$

Fig. 3.1(b) presents the obtained energy spectrum. The application of a vertical electric field induces the opening of an energy gap in BLG, transforming it into a tunable semiconductor. This effect arises as the electron-hole symmetry is broken due to the inclusion of non-zero matrix elements, such as  $\gamma_4$ , which introduces asymmetry between the layers. This breaking of symmetry results in distinct effective masses for the electron and hole around the  $K$  and  $K'$  valleys, as depicted in Fig. 3.1(b). The opening of the gap and the disparity in effective masses profoundly influence the transport and optical properties of the material.

Additionally, the inclusion of TW further modifies the electronic structure, reducing the symmetry of the system from  $C(\infty)$  to  $C(3)$ , as evidenced by the formation of three distinct energetic extrema in both the VB and CB. These extrema, visible in the insets of Fig. 3.1(b), arise due to the interplay of interlayer coupling and lattice asymmetry. Despite these changes, the electronic band structure retains the characteristic ‘‘Mexican hat’’-like dispersion near the  $K$  and  $K'$  points in the BZ, which is a hallmark of BLG in the electric field.

Near the  $K$  and  $K'$  points, the wave functions associated with the CB and VB exhibit a phase difference of  $2\phi_k$  between the two dominantly occupied sublattices ( $A$  and  $D$ ). This phase winding

is a consequence of the unique pseudospin texture of BLG and results in a pseudospin winding number of 2. This property, intrinsic to Bernal-stacked BLG, has significant implications for the topological and optical behavior of the system [145].

### 3.1.3 Laterally Gated Bilayer Graphene Quantum Dot Spectrum

In Ref. [130], it was shown that the application of a lateral potential, modeled through an *ab initio*-based screened Gaussian potential  $V^{QD}$ , allows for the confinement of both electrons and holes within a BLG QD. This potential facilitates the creation of a controllable environment to study localized electronic states in BLG. The Hamiltonian for the gated BLG QD can be written as:

$$\hat{H} = \hat{H}_{bulk} + \hat{V}_{QD}^{eff}. \quad (3.30)$$

The electronic states of the QD, labeled as  $\varphi_s(\vec{r})$ , can be represented as a linear combination of the bulk Bloch wave functions:

$$\varphi_s(\vec{r}) = \sum_p \sum_{\vec{k}} \nu_{p,\vec{k}}^s \Phi_{p,\vec{k}}(\vec{r}), \quad (3.31)$$

where the summation  $\sum_p$  runs over the four bands of BLG corresponding to sublattices  $A$ ,  $B$ ,  $C$ , and  $D$ , and  $\sum_{\vec{k}}$  sums over the  $\vec{k}$ -points defined within the computational rhombus introduced earlier.

To solve the problem efficiently, we employed a computational basis restricted to band states within an energy cutoff of  $E_{cut} = 600$  meV. This cutoff ensures the inclusion of states localized near the  $K$  and  $K'$  points, which dominate the low-energy electronic structure of BLG. This approach aligns with prior studies [58, 130], ensuring both accuracy and computational efficiency in describing the system.

To laterally confine electrons and holes at the center of the computational rhombus, we introduce a lateral potential at the center. This potential is attractive for electrons in the top layer (layer 1) and repulsive for electrons (but attractive for holes) in the bottom layer (layer 2). This can be achieved by removing a circular, disc-like region from both the top and bottom gates. The resulting confining potential due to the removed gates can be approximated by Gaussian potentials for the top ( $z = 0$ ) and bottom ( $z = -h$ ) layers, given by

$$V_{QD}(\rho) = \begin{cases} -\frac{V}{2} \exp\left(-\frac{\rho^2}{R_{QD}^2}\right) & z = 0, \\ +\frac{V}{2} \exp\left(-\frac{\rho^2}{R_{QD}^2}\right) & z = -h. \end{cases} \quad (3.32)$$

This form of potential was proposed in Refs. [145, 146]. Notably, the voltage drop of  $-V/2$  at the center of the top layer exactly cancels the applied bulk voltage of  $+V/2$ . A similar cancellation occurs at the bottom layer. As a result, the vertical electric field is zero at the center of the QD and gradually approaches the applied electric field at greater radial distances.

Given that the applied vertical electric field redistributes charges at each radius  $\rho$ , we seek to derive an effective potential  $V(\rho)$  that accounts for the screening effects in the gated system. This is achieved through *ab initio* calculations for biased bulk BLG, which yield a voltage drop  $V_{QD}(\rho)$  at radius  $\rho$ , from which we obtain a new screened voltage drop,  $V_{QD}^{eff}(\rho)$ . We then fit this effective potential using a sum of Gaussian functions. Two Gaussians are sufficient for an accurate

representation, leading to the effective potential:

$$V_{QD}^{eff}(\rho) = \begin{cases} -c_1 \exp\left(-\frac{\alpha_1 \rho^2}{r_{QD}^2}\right) - c_2 \exp\left(-\frac{\alpha_2 \rho^2}{r_{QD}^2}\right), & z = 0, \\ +c_1 \exp\left(-\frac{\alpha_1 \rho^2}{r_{QD}^2}\right) + c_2 \exp\left(-\frac{\alpha_2 \rho^2}{r_{QD}^2}\right), & z = -h, \end{cases} \quad (3.33)$$

Here,  $\rho$  represents the radial distance in the  $xy$ -plane, and  $r_{QD} = 20$  nm is the fixed radius of the QD. The parameters  $z = 0$  and  $z = -h$  correspond to the positions of the top and bottom graphene layers, respectively. The constants  $c_1 = -0.01763$  eV,  $c_2 = 0.20726$  eV,  $\alpha_1 = 6.128$ , and  $\alpha_2 = 1.0064$  control the strength and shape of the potential. These values were obtained from *ab initio* calculations. The Gaussian profile of the screened potential ensures spatial localization, effectively trapping charge carriers within a specific radial range. This confinement enables the study of well-defined quantum states in BLG QDs and serves as the foundation for analyzing the interaction and coupling effects of confined carriers within the bilayer system [130].

The Schrödinger equation governing the confined states within the QD can be expressed as follows:

$$\varepsilon_{p,\vec{k}} \nu_{p,\vec{k}}^s + \sum_{p',\vec{k}'} \langle \Phi_{p,\vec{k}} | \hat{V}^{QD} | \Phi_{p',\vec{k}'} \rangle \nu_{p',\vec{k}'}^s = \varepsilon_s \nu_{p,\vec{k}}^s, \quad (3.34)$$

where  $\varepsilon_{p,\vec{k}}$  are the eigenvalues of the bulk Hamiltonian described in Eq. (3.28). In this equation,  $\nu_{p,\vec{k}}^s$  represents the amplitude of the  $s$ -th QD state in the  $p$ -th band at the  $\vec{k}$ -point, and  $\varepsilon_s$  is the corresponding energy eigenvalue. The primary challenge here is solving this eigenequation to determine the coefficients  $\nu_{p,\vec{k}}^s$ , which describe the distribution of the QD state over the basis functions of the bulk Hamiltonian.

Assuming that  $V_{QD}^{eff}$  varies slowly in space, such that the potential within a unit cell is approximately constant, one obtains the following expression for the matrix elements:

$$\langle \Phi_{\vec{k}}^p | V_{QD}^{eff} | \Phi_{\vec{k}'}^{p'} \rangle = \sum_l A_{\vec{k},l}^{*p} A_{\vec{k}',l}^{p'} e^{i(\vec{k}' - \vec{k}) \cdot d_l} V_{\vec{k},\vec{k}',l}^{eff}. \quad (3.35)$$

Here, the term  $V_{\vec{k},\vec{k}',l}^{eff}$  is the Fourier transform of the confining potential, as given by equation (3.33), expressed in the basis of the band states labeled by the band index  $p$  and the wavevector  $\vec{k}$ :

$$V_{\vec{k},\vec{k}',l}^{eff} = \pm Q^2 R_{QD}^2 \left[ \frac{c_1}{\alpha_1} \exp\left(-\frac{R_{QD}^2 |\vec{k} - \vec{k}'|^2}{4\alpha_1}\right) + \frac{c_2}{\alpha_2} \exp\left(-\frac{R_{QD}^2 |\vec{k} - \vec{k}'|^2}{4\alpha_2}\right) \right], \quad (3.36)$$

where  $Q^2 = \frac{2\pi}{3\sqrt{3}Ma^2}$ . The + sign is used for the sublattices  $l = C, D$ , and the minus sign is used for  $l = A, B$ . We observe that the matrix elements of the confining potential are products of two contributions: (i) from the electrostatic confining potential and (ii) from the bulk wave functions, which carry information about the Berry curvature. To obtain the QD spectrum and wave functions, we solve the eigenvalue equation (3.34). If only the electrostatic confining potential were considered, we would obtain the spectrum of a 2D harmonic oscillator, as is typical in conventional semiconductor QDs. However, the additional contribution from the wave functions and Berry's phases significantly modifies the energy spectrum.

To solve Eq. (3.34) numerically, we employ full-matrix diagonalization techniques using a LAPACK routine [440], as implemented in Fortran, which yield the quantized energy spectrum of the QD. This spectrum reflects the localized electronic states induced by the lateral confinement potential, providing essential insight into the effects of confinement on the energy levels and the spatial distribution of the electronic states within the BLG QD.

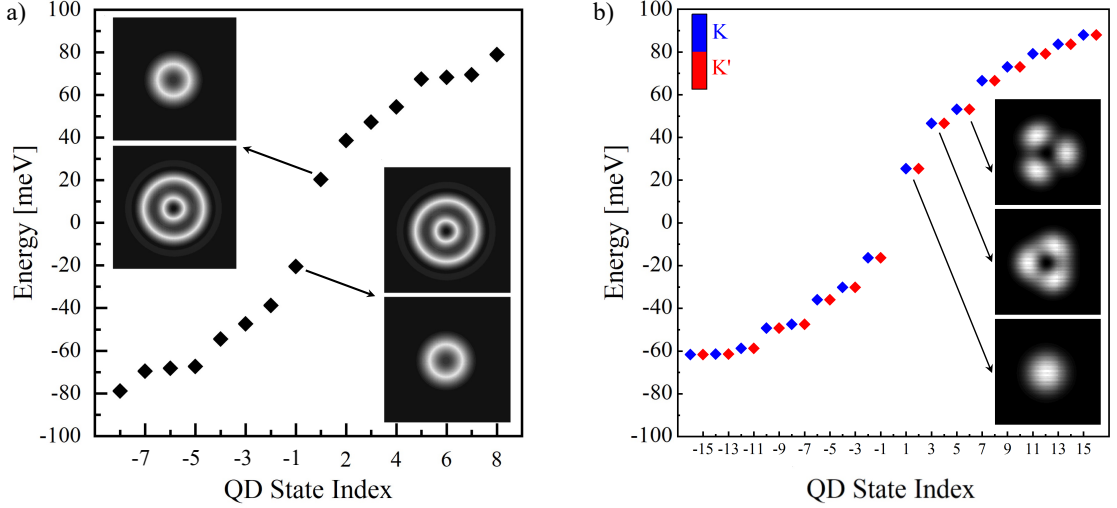


**Figure 3.2:** Single-particle energy spectrum of a gated BLG QD with a radius of  $r_{QD} = 20$  nm (a) without and (b) with the inclusion of the TW effects. The spectrum displays (a) 16 and (b) 32 (valley-resolved) QD states around the energy gap, with negative/positive indices corresponding to VB/CB states. The valley degree of freedom in panel (b) is indicated by color: blue/red represents the  $K/K'$  valley. Insets illustrate the charge density distributions for (a) top VB and bottom CB shells in the layer-resolved picture, and (b) the top layer CB, demonstrating the influence of TW effects, which reduces the symmetry of charge densities from  $C(\infty)$  to  $C(3)$ .

Fig. 3.2(a) and (b) show the momentum- and valley-resolved single-particle energy spectrum for a gated BLG QD with a radius of  $r_{QD} = 20$  nm. Panel (a) displays the spectrum without TW effects, while panel (b) includes the effects of TW. The spectrum in both cases is resolved around the energy gap, with panel (a) showing 16 QD states, and panel (b) showing 32 QD states. Negative indices correspond to VB states, while positive indices correspond to CB states. The valley degree of freedom is represented by color: blue for the  $K$  valley and red for the  $K'$  valley.

Insets in panel (a) display the charge density distributions for selected VB and CB shells, highlighting their spatial profiles. In panel (b), the charge density distribution for the top layer CB states is shown, emphasizing the influence of TW effects. The TW effects break the higher symmetry of the charge densities, reducing it from  $C(\infty)$  to  $C(3)$ , as reflected in the altered symmetry of the spatial distribution in the CB states.

### 3.1.4 Optical Transitions in a Bilayer Graphene Quantum Dot

In this section, we explore the electronic properties and optical transitions of a BLG QD, with a particular focus on the role of valley degrees of freedom and the effects of lateral confinement. A QD embedded in BLG provides a unique platform to investigate the interaction between the material's intrinsic band structure, spatial confinement of carriers, and the impact of external perturbations. As shown in previous sections, the electronic structure of the BLG QD differs significantly from that of QDs such as GaAs or self-assembled QDs, where the shell structure resembles that of a 2D harmonic oscillator. In particular, the presence of topological features and reduced symmetry in BLG leads to distinct electronic states and charge distributions. These differences can give rise to unique optical properties, including unconventional behavior of dipole matrix elements (DMEs), which govern interband transitions and shape the absorption spectrum. In the following sections,

we provide a detailed analysis of the DMEs corresponding to these optical transitions, and the resulting optical response of the system.

The BLG QD interacts with light via DMEs  $D_{p,q} = \langle \varphi_p | \mathcal{E}_0^\pm \cdot \vec{r} | \varphi_q \rangle$ , as described in Sec. 2.4.2, where  $\vec{r}$  is the position operator, and  $\mathcal{E}_0^\pm$  represents the electric field of circularly polarized light. These matrix elements describe the coupling between two QD states,  $p$  and  $q$ , mediated by the electric dipole operator associated with optical transitions. Furthermore, the QD wave functions can be expressed as linear combinations of atomic  $p_z$  orbitals, which can be rewritten from Eq. (3.31) as:

$$|\varphi^s\rangle = \sum_{\vec{R},l} c_{\vec{R},l}^s |\psi_{\vec{R},l}\rangle, \quad (3.37)$$

where the coefficients real space coefficients  $c_{\vec{R},l}^s$  are given by:

$$c_{\vec{R},l}^s = \frac{1}{\sqrt{N_{UC}}} \sum_{\vec{k},p} \nu_{p,\vec{k}}^s \mu_{p,\vec{k}}^l e^{i\vec{k} \cdot (\vec{R} + \vec{d}_l)}. \quad (3.38)$$

Here,  $\nu_{p,\vec{k}}^s$  and  $\mu_{p,\vec{k}}^l$  are components related to the wave function and  $\vec{d}_l$  is the sublattice vector for sublattice  $l$ . To calculate the DMEs  $\vec{D}_{s,s'}$  between these QD states, following the methodology described in Sec. 2.4.2, we use the expression:

$$\vec{D}_{s,s'} = \langle s | \vec{r} | s' \rangle = \sum_{i,j} (c_i^s)^* c_j^{s'} \langle i | \vec{r} | j \rangle. \quad (3.39)$$

The matrix elements  $\langle i | \vec{r} | j \rangle$ , which correspond to the DMEs between real-space orbitals, are given by:

$$\langle i | \vec{r} | j \rangle = D_{ij} \left( \hat{R}_j - \hat{R}_i \right) + \vec{R}_j \delta_{ij}, \quad (3.40)$$

where  $\hat{R}_i$  and  $\hat{R}_j$  are the positions of the  $i$ th and  $j$ th atoms, and  $\delta_{ij}$  is the Kronecker delta function. The quantity  $D_{ij}$  is defined as:

$$D_{ij} = \left| \int d\vec{r} \phi_{p_z}^* \left( \vec{r} - \vec{R}_i \right) \vec{r} \phi_{p_z} \left( \vec{r} - \vec{R}_j \right) \right|, \quad (3.41)$$

where  $\phi_{p_z}(\vec{r} - \vec{R}_i)$  is a Slater  $p_z$  orbital centered at position  $\vec{R}_i$  with a Slater parameter  $\xi = 3.25$ . For NN atoms, the value of  $D_{ij}$  is  $0.313763 a_B$ , where  $a_B$  is the Bohr radius. For next nearest neighbours (NNN), the DME is smaller,  $D_{ij} = 0.0711159 a_B$  [58, 59].

These DMEs play a role in determining the light-matter interaction in the BLG QD system, and are key to understanding the optical properties and transition rates between different electronic states.

Fig. 3.3 shows the energy spectra and DMEs for the BLG QD. Panels (a) and (c) display the QD energy spectra, corresponding to those in Fig. 3.2, with arrows indicating pairs of VB and CB states that are coupled by nonzero DMEs. These arrows highlight the transitions that will contribute to the absorption spectrum. In panel (a), we focus on the valence and conduction states connected by large DMEs in the case of TW effect being neglected, while in panel (c), we provide a solution for the TW effects included.

Panels (b) and (d) show the joint optical density of states (JDOS) for non-interacting electron-hole pairs in the BLG QD. Vertical arrows in these panels represent the magnitude (absolute value squared) of the corresponding DMEs calculated for states from the  $K'$  valley. These arrows indicate the strength of the optical transitions, and the peaks in the JDOS correspond to allowed transitions between VB and CB states. We label the peaks according to the transitions presented in the Fig. 3.3(a,c)

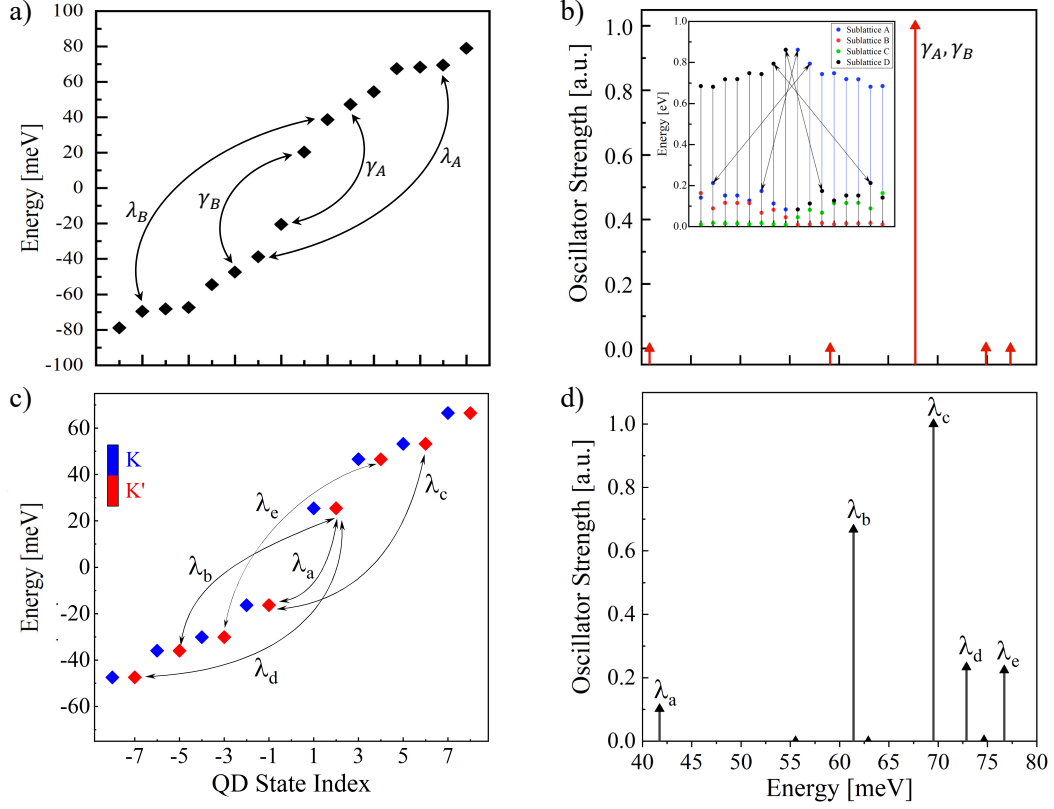


**Figure 3.3:** (a,c) QD energy spectra, corresponding to those in Fig. 3.2, shown (a) without and (c) with the inclusion of TW effects. Arrows indicate pairs of valence and conduction band states coupled by nonzero DMEs. (b,d) Joint optical density of states for non-interacting electrons and holes in the BLG QD. Vertical arrows represent the magnitude (absolute value squared) of the corresponding DMEs, calculated for states from the  $K'$  valley. The inset in panel (b) shows the charge density distribution of single-particle wave functions, decomposed into contributions from sublattices  $A$ ,  $B$ ,  $C$ , and  $D$ , represented by blue, red, green, and black lines and symbols, respectively. Black arrows highlight pairs of states connected by large DMEs.

The inset in panel (b) illustrates the charge density of the single-particle wave functions, decomposed into contributions from the sublattices of the BLG. For each state (labeled on the horizontal axis), the portion of the charge density coming from sublattices  $A$ ,  $B$ ,  $C$ , and  $D$  is represented by blue, red, green, and black lines and symbols, respectively. The black arrows in both panels (b) and (d) highlight pairs of states (one from the VB and one from the CB) that are strongly coupled by DMEs.

Starting with the case where the TW effects are neglected, depicted in Fig. 3.3(a,c), the analysis reveals that, unlike in self-assembled QDs, the top VB state (labeled by the QD index  $-1$ ) does not couple to the lowest-energy CB state ( $+1$ ), but instead to the third excited state in the CB ( $+3$ ), which we denote as transition  $\lambda_a$ . A symmetric transition,  $\lambda_b$ , connects the bottom CB state ( $+1$ ) to the third VB shell ( $-3$ ). The second-highest energy VB state ( $-2$ ) couples to a highly excited CB state ( $+7$ ). These transitions reflect the distinct optical selection rules in the BLG system, shaped by its unique electronic structure.

When the TW effects are included (Fig. 3.3(b,d)), we observe that, consistent with the previous case, the top VB state ( $-1$ ) does not couple strongly to the lowest-energy CB state ( $\lambda_a$ ), but instead

to the third conduction shell (+5) within the same valley—denoted as transition  $\lambda_c$ . A symmetric transition,  $\lambda_b$ , connects the bottom CB state (+1) to the third valence shell (−5). The most optically active transition, as presented in panel (d), is  $\lambda_c$ . Although the transition from the top valence state (−1) to the bottom conduction state (+1) is not strictly forbidden, it exhibits a very low oscillator strength. This complex light-matter coupling is further significantly influenced by electron-electron interactions.

It is also important to note that all intervalley transitions are characterized by very small DMEs, and, similar to monolayer TMDCs, only one valley is optically active for a given circular polarization of light [463].

## 3.2 Electrically Tunable Neutral Excitons

In this section, we explore the formation and properties of excitons in BLG QD under the influence of external electric fields. We begin by analyzing the evolution of the excitonic states as Coulomb interactions are progressively included. First, we examine the non-interacting electron-hole pair spectrum and subsequently account for the renormalization effects arising from self-energies and electron-hole attraction and repulsion. In the final part of this analysis, we solve the full BSE to determine the full excitonic spectrum, which includes all Coulomb interaction and correlations effects.

Following this, we turn our attention to the optical response of these excitonic states, specifically focusing on the absorption spectrum, which provides a direct probe of the exciton dynamics and their tunability under external perturbations.

### 3.2.1 Excitonic Spectrum and the Effect of Coulomb Interactions

In Sec. 2.3.1, we derived the BSE for a single electron-hole pair excitation. We now apply this formalism to calculate the excitonic states in a BLG QD. As before, we approximate the many-electron ground state as a single Slater determinant  $|GS\rangle = \prod_{p,\sigma} c_{p\sigma}^\dagger |0\rangle$ , where  $c_{p\sigma}^\dagger$  creates an electron in the  $p$ -th occupied VB state, as shown in Fig. 3.2.

The exciton states,  $|\psi^\mu\rangle$ , are written as linear combinations of electron-hole pair excitations, which conserve total spin  $S_z$ . These excitons are represented as:

$$|\psi^\mu\rangle = \sum_{p,q,\sigma} A_{p,q,\sigma}^\mu c_{q\sigma}^\dagger c_{p\sigma} |GS\rangle. \quad (3.42)$$

Here  $A_{p,q,\sigma}^\mu$  represents the amplitude for an electron-hole pair excitation, where  $c_{p\sigma}$  removes an electron with spin  $\sigma$  from the VB state  $p$ , and  $c_{q\sigma}^\dagger$  places it in the CB state  $q$ . The indices  $p$  and  $q$  span all the VB and CB states of the QD.

The Coulomb interaction  $V_C$  couples different electron-hole pairs, which renormalizes the exciton energy. The resulting amplitudes  $A_{p,q,\sigma}^\mu$  satisfy the BSE given in Eq. (2.166). This equation describes the interactions between electron-hole pairs, including terms for the single-particle energies, Coulomb interactions, and self-energy corrections. The exchange self-energy is given by  $\Sigma_{p,\sigma} = -\sum_{q,\sigma'} \delta_{\sigma,\sigma'} \langle q,p|V_C|q,p\rangle$ , where the sum over  $q$  runs over the VB states. For the QD system in question, the self-energies at the top of the VB and at the bottom of the CB converge after including 120 filled VB QD states.

The Coulomb interaction also leads to the scattering of electron-hole pairs, with an attractive (negative) direct term and a repulsive (positive) exchange term. This interaction plays a key role

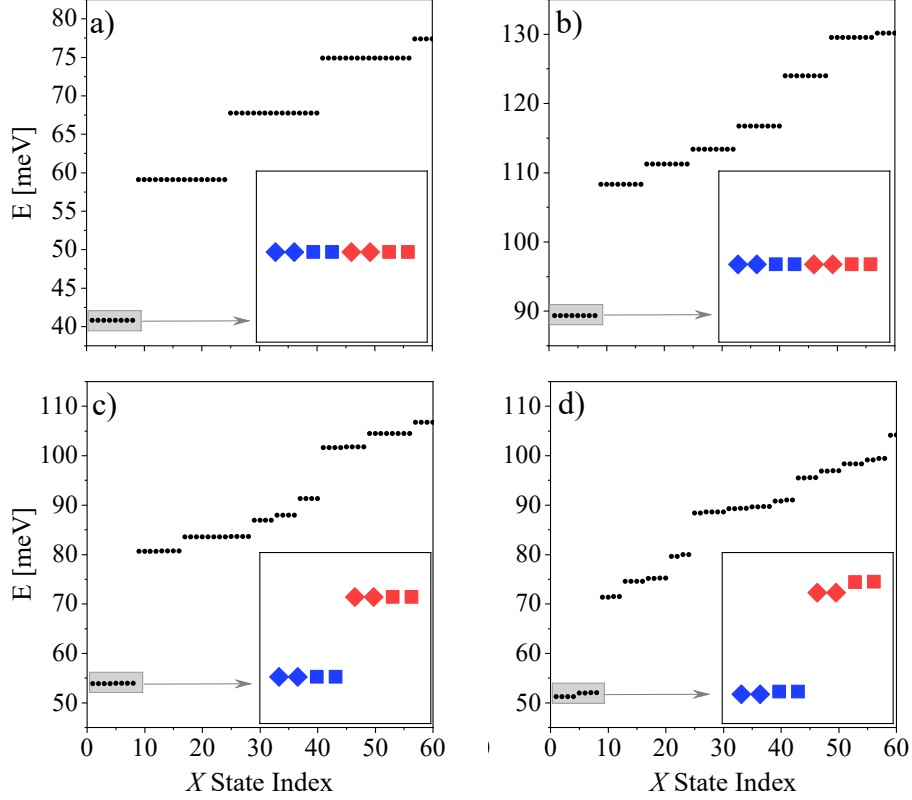


**Figure 3.4:** Excitonic energy spectra at different stages of including Coulomb interactions. (a) Energies of noninteracting electron-hole pairs. (b) Energy spectrum of the pairs renormalized by self-energies. (c) Energy spectrum of the pairs accounting for self-energies and vertex corrections (the electron-hole attraction) but without correlations. (d) Excitonic energy diagram accounting for all aspects of the electron-electron interaction. The boxes in the bottom right of each panel show the 8 lowest energy states zoomed in. The states are labeled as intervalley (blue), intravalley (red), singlet (squares), and triplet (diamonds).

in the calculation of exciton energies, with the BSE accounting for both the relative and center-of-mass motion of the electron-hole pairs.

To calculate the excitonic states, we solve the BSE in the subspace defined by 32 single-particle states near the Fermi level, which are shown for one valley in Fig. 3.2. These states contribute most significantly to the low-energy exciton spectrum. We begin by examining the spectrum of noninteracting electron-hole pairs, where the Coulomb interaction  $V_C \equiv 0$ , as illustrated in Fig. 3.4(a). In this case, we observe degenerate shells of electron-hole levels, which form either eight-fold or sixteen-fold degenerate manifolds. The eight-fold degeneracy can be understood by considering all possible electron-hole pairs with energy equal to the single-particle energy gap, while conserving total  $S_z$ . This corresponds to removing an electron from state  $-1$  and placing it in state  $+1$ , as depicted in Fig. 3.4(a). Both states  $-1$  and  $+1$  are degenerate with respect to spin and valley. Consequently, there are two electron-hole pairs for each valley (four total, including spin), and four additional pairs between valleys, yielding a total of eight possible electron-hole pairs at the energy of the single-particle gap.

Next, we consider the sixteen-fold degenerate manifold. This arises from the second-lowest-energy electron-hole pairs, which are formed by exciting electrons from state  $-1$  to state  $+2$ , and

from state  $-2$  to state  $+1$ , as shown in Fig. 3.2(a). The two electron-hole pair configurations resulting from the symmetry between valleys lead to a doubling of the degeneracy, giving a total of sixteen-fold degeneracy.

Next, we turn on the self-energy contribution to the electron-hole pair energies. The resulting spectrum is shown in Fig. 3.4(b). The self-energies result in a large blue shift of the electron-hole pair energies. Furthermore, the self-energies split the sixteen-fold degenerate manifolds into two subclasses because the values of the self-energy in the excitations involving states  $-1$  and  $+2$  are different from those involving states  $-2$  and  $+1$ .

We next calculate the energies of electron-hole pairs including self-energies and vertex corrections, i.e., the electron-hole attraction. These spectra are shown in Fig. 3.4(c). The direct electron-hole attraction is large and lowers the energy of the electron-hole complex, while the electron-hole exchange interaction is repulsive and raises the energy of the complex slightly. While the direct electron-hole interaction does not discriminate valleys, the exchange interaction is different within a valley and between valleys. This separates the energy of intervalley and intravalley electron-hole pairs. Indeed, the intervalley electron-hole pair has a lower energy due to its smaller repulsive exchange interaction. We also observe reordering of higher-energy electron-hole pairs due to large exchange values compared to the single-particle level spacing.

Finally, we include the Coulomb scattering connecting electron-hole pairs and solve the full BSE. The resulting excitonic spectrum is shown in Fig. 3.4(d). The single-particle gap is 40 meV, the gap renormalized by self-energies is 90 meV, and the exciton energy is 50 meV. Hence, the exciton binding energy is positive. The excitonic states can be categorized as inter/intra-valley singlets/triplets. The insets in Fig. 3.4 categorize the low-energy states accordingly. The intervalley excitons are at lower energies than their intravalley counterparts because the repulsive exchange interaction for intravalley excitons is stronger. Furthermore, each class of intravalley and intervalley excitons is further split into spin singlets and triplets. Triplets are at lower energies than their singlet counterparts, as the exchange interaction now favors triplets in energy. Focusing on the ground state, we see that it is approximately four-fold degenerate and corresponds to intervalley excitons formed from electron-hole pairs across the gap. The singlet-triplet splitting for these states is negligible, which is why it appears four-fold degenerate rather than two-fold degenerate.

### 3.2.2 Optical Absorption

Building on the methodology described in Sec. 2.4.3, we now proceed to calculate the absorption spectrum  $A(\omega)$  as a function of photon energy  $\omega$ :

$$A(\omega) = \sum_{\mu} \left| \sum_{s,s',\sigma} \mathcal{E}_0^{\pm} \cdot \vec{D}_{s,s'} \left( A_{s,s',\sigma}^{\mu} \right)^* \right|^2 \delta(E_{\mu} - \omega). \quad (3.43)$$

Here,  $\mathcal{E}_0^{\pm}$  represents the polarization vector of the incident photon, modeled by a circularly polarized electric field, and  $\vec{D}_{s,s'}$  denotes the DMEs. Figure 3.5 shows the absorption spectrum as a function of photon energy for our QD model. The vertical black lines correspond to the excitonic state energies  $E_{\mu}$ , while the red line represents the absorption spectrum resulting from the excitonic states.

In panel (a) of Fig. 3.5, we present the absorption spectrum assuming no interactions. We observe that the low-energy electron-hole pairs are dark, a consequence of the previously discussed vanishing DMEs for the two lowest-energy electron-hole complexes. The third dashed line indicates

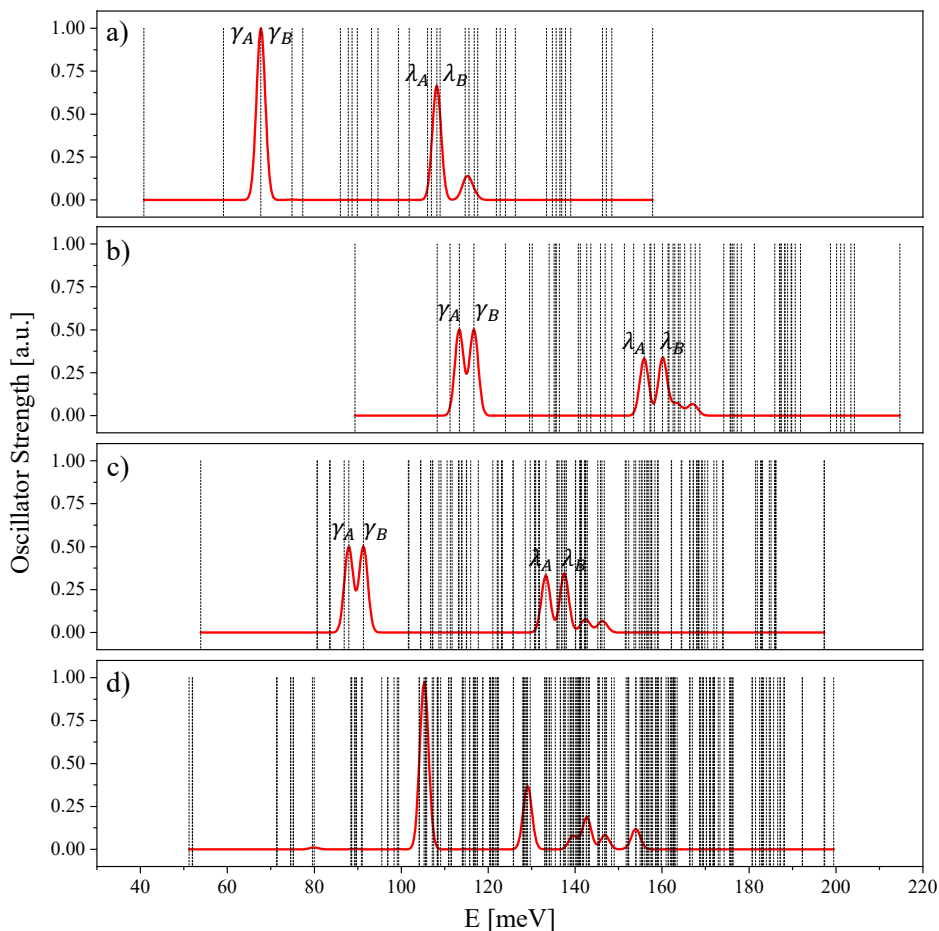


**Figure 3.5:** Optical absorption spectrum of the gated lateral BLG QD as a function of photon energy (horizontal axis) at various stages of incorporating Coulomb interactions. (a) Non-interacting electron-hole pairs. (b) Inclusion of self-energies. (c) Addition of self-energies and vertex corrections (electron-hole attraction). (d) Full inclusion of self-energies, vertex corrections, and correlation effects. Black dashed lines indicate the energies of the excitonic states, as shown in the corresponding panels of Fig. 3.4, while the red line represents the absorption spectrum computed using Fermi's Golden Rule.

the first bright peak at approximately 67 meV, corresponding to the energy of an electron-hole pair with a large DME, namely the sixteen-fold degenerate third manifold, as shown in Fig. 3.4(a). A second smaller peak is observed around 108 meV, which corresponds to the second bright DME transition.

Next, we include the effects of self-energies, as shown in Fig. 3.5(b). As discussed earlier, self-energies cause a splitting of the sixteen-fold degenerate manifold into two sub-manifolds. Consequently, the large peak, originally composed of transitions  $\gamma_A$  and  $\gamma_B$  (as labeled in Fig. 3.3), now splits into two distinct peaks. Additionally, the peaks shift to higher energies due to the blue shift introduced by the self-energy contributions.

The inclusion of the electron-hole attraction leads to a red shift, as shown in Fig. 3.5(c), bringing the absorption maxima closer to the non-interacting peaks. The vertex correction further breaks the degeneracy between intravalley and intervalley electron-hole pairs. This results in a reordering of levels due to the electron-hole exchange interaction, and new dark states appear at lower energies

compared to the bright states.

Finally, when scattering terms are included in the full BSE, the degenerate states split into triplets and singlets, with the triplets being dark, as shown in Fig. 3.5(d). The lowest exciton energy decreases to 50 meV due to correlation effects, but the bright exciton peak shifts to higher energy due to the singlet-triplet splitting. Many new dark states emerge at low energies as the dark triplets shift downward. Additional reordering of the levels occurs due to both singlet-triplet splitting and correlations. The bright peak is now blue-shifted to 110 meV ( $\sim 30$  THz). A second smaller peak appears at 130 meV, corresponding to the second optically active transition. This transition becomes smeared in the interacting system, as correlations spread the relevant optically active electron-hole pairs across multiple exciton states. The many dark low-energy excitonic states are primarily intervalley excitons, spin triplets, or states with vanishing DMEs. The presence of these low-energy dark states positions BLG QDs as promising candidates for photon storage.

### 3.3 Negatively Charged Excitons

In this section, we extend the analysis from excitons to negatively charged trions, which are three-body states formed by two electrons and one hole. Trions are of particular interest because they provide a more detailed understanding of many-body interactions determining exciton states interacting with free carriers in systems like BLG QDs. Building on the insights gained from excitons, we now focus on the effects of additional electron-electron interactions and how they determine the properties of these three-particle complexes. We begin by investigating the trion spectrum, including the fine structure of the different trion states, before moving on to explore their optical absorption and emission spectra.

#### 3.3.1 Fine Structure of Trions in Bilayer Graphene Quantum Dots

We begin by incorporating the effects of electron-electron interactions in the analysis of trions, following the methodology outlined in Sec. 2.3.2. The many-body Hamiltonian, which we have defined in Eq. (2.73), is now expressed in the basis of QD single-particle states and takes the following form:

$$\hat{H}_{MB} = \sum_{p,\sigma} \epsilon_p c_{p,\sigma}^\dagger c_{p,\sigma} + \frac{1}{2} \sum_{p,q,r,s} \sum_{\sigma,\sigma'} \langle p, q | V_C | r, s \rangle c_{p,\sigma}^\dagger c_{q,\sigma'}^\dagger c_{r,\sigma'} c_{s,\sigma} - \sum_{p,s,\sigma} V_{p,s}^P c_{p,\sigma}^\dagger c_{s,\sigma}, \quad (3.44)$$

where  $c_{p,\sigma}^\dagger$  and  $c_{p,\sigma}$  are the creation and annihilation operators for electrons with spin  $\sigma$  in state  $p$  of the QD, respectively. The indices  $p, q, r, s$  represent all possible QD states. The electron-electron interactions  $V_C$  are modeled as Coulomb interactions screened by the dielectric constant  $\kappa$ , with the form  $V_C = \frac{e^2}{\kappa|\vec{r}_1 - \vec{r}_2|}$ , where  $\kappa = 3.9$  [146, 464]. The Coulomb matrix elements  $\langle p, q | V_C | r, s \rangle$  are computed numerically using Slater-like  $p_z$  orbitals (for further computational details, see Ref. [130]). The last term in Eq. (3.44) accounts for the positive background charge of the QD, which ensures overall charge neutrality. This term is defined as  $V_{p,s}^P = 2 \sum_m^{N_{occ.}} \langle p, m | V_C | m, s \rangle$ .

To study many-body effects, we approximate the many-electron ground state at half-filling as a single Slater determinant of all occupied VB states. Next, we construct the negatively charged trion states,  $\psi_-^n$ , as linear combinations of 3-body states that involve one electron-hole pair excitation and an additional electron in the CB. Thanks to the two non-equivalent valleys in BLG QDs, we can construct ten low-energy trion configurations with  $S_z = \frac{1}{2}$ , based on states near the top of the VB and the bottom of the CB. Fig. 3.6 illustrates five of these configurations, with the

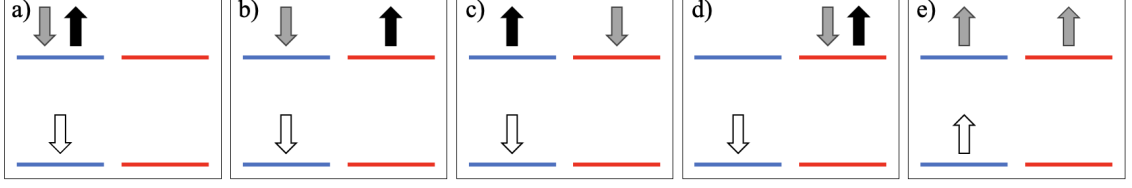


**Figure 3.6:** Diagram representing the low-energy trion configurations. Vertical arrows indicate carriers, where filled and empty arrows denote electrons and holes, respectively, with the direction of the arrow indicating spin (up or down). The states are constructed with a hole located at the bottom of the VB and two electrons at the bottom of the CB. The grey arrow represents an electron with the same spin as the hole. The horizontal lines are color-coded to indicate the valley (blue for the  $K$  valley and red for the  $K'$  valley).

remaining five corresponding to moving the hole from the  $K$  valley (blue) to the  $K'$  valley (red). The simplest configuration consists of an intravalley trion, where both CB electrons and the hole reside in the same valley (either  $K$  or  $K'$ ), and the spins of the electrons are opposite (Fig. 3.6(a)). Other configurations involve an exciton in one valley and an additional electron in the opposite valley, leading to configurations shown in Figs. 3.6(b) and (c). These correspond to intravalley excitons correlated with an extra electron in the opposite valley. A more complex configuration places both electrons in the same valley while the hole resides in the opposite valley, as shown in Fig. 3.6(d). Finally, we also consider a configuration where all carriers have the same spin, depicted in Fig. 3.6(e). The trion wave function is a linear combination of all possible trion configurations, as expressed in Eq. (2.168).

The many-body Hamiltonian incorporates electron-electron interactions, which renormalize the energies of the quasi-particles (quasi-electrons and quasi-holes) and mix different trion configurations. As a consequence, the amplitudes  $A_{\alpha,\beta,i}^n$  of the trion wave functions satisfy the BSE for the trion states, as described in Sec. 2.3.2.

We obtain the trion spectrum by solving the BSE within a subspace of 32 single-particle states around the Fermi level, as shown in Fig. 3.2. We restrict the trion states to the  $S_z = +\frac{1}{2}$  subspace. The self-energies  $\Sigma_{p,p}$  have converged for  $N_{occ.} = 120$  filled VB QD states [58].

We now move to a detailed description of the calculated trion spectrum, where we analyze the evolution of the spectrum as we include different types of Coulomb interactions. It is important to note that each state is at least doubly degenerate due to valley symmetry. For simplicity, we restrict our analysis to states in which the hole resides in the  $K$  valley, as depicted in Fig. 3.6. Fig. 3.7 shows the spectra obtained by solving the BSE for the trion states, as given in Eq. 2.169 and repeated here for clarity:

$$\begin{aligned}
 E^n A_{\alpha,\beta,i}^n &= (\epsilon_\alpha + \epsilon_\beta - \epsilon_i) A_{\alpha,\beta,i}^n + \sum_{\mu,\lambda,j} \left( \begin{array}{l} +\Sigma_{\mu,\alpha}\delta_{i,j}\delta_{\beta,\lambda} - \Sigma_{\lambda,\alpha}\delta_{i,j}\delta_{\beta,\mu} \\ +\Sigma_{\lambda,\beta}\delta_{i,j}\delta_{\alpha,\mu} - \Sigma_{\mu,\beta}\delta_{i,j}\delta_{\alpha,\lambda} \\ -\Sigma_{i,j}\delta_{\alpha,\mu}\delta_{\beta,\lambda} \end{array} \right) A_{\mu,\lambda,j}^n \\
 &+ \sum_{\mu,\lambda,j} \left[ \begin{array}{l} +(V_{i,\lambda,j,\beta} - V_{i,\lambda,\beta,j})\delta_{\alpha,\mu} + (V_{i,\mu,j,\alpha} - V_{i,\mu,\alpha,j})\delta_{\beta,\lambda} \\ -(V_{i,\lambda,j,\alpha} - V_{i,\lambda,\alpha,j})\delta_{\beta,\mu} - (V_{i,\mu,j,\beta} - V_{i,\mu,\beta,j})\delta_{\alpha,\lambda} \\ -(V_{\mu,\lambda,\alpha,\beta} - V_{\mu,\lambda,\beta,\alpha})\delta_{i,j} \end{array} \right] A_{\mu,\lambda,j}^n,
 \end{aligned} \tag{3.45}$$

with  $\epsilon_p$  denoting the QD single-particle energies,  $\Sigma_{p,q} = -\sum_m^{N_{occ.}} \langle m,p|V_C|m,q\rangle$  defining the scatterings containing the self-energy terms  $\Sigma_{p,p}$ ,  $V_{p,q,r,s} = \langle p,q|V_C|r,s\rangle$  corresponding to the

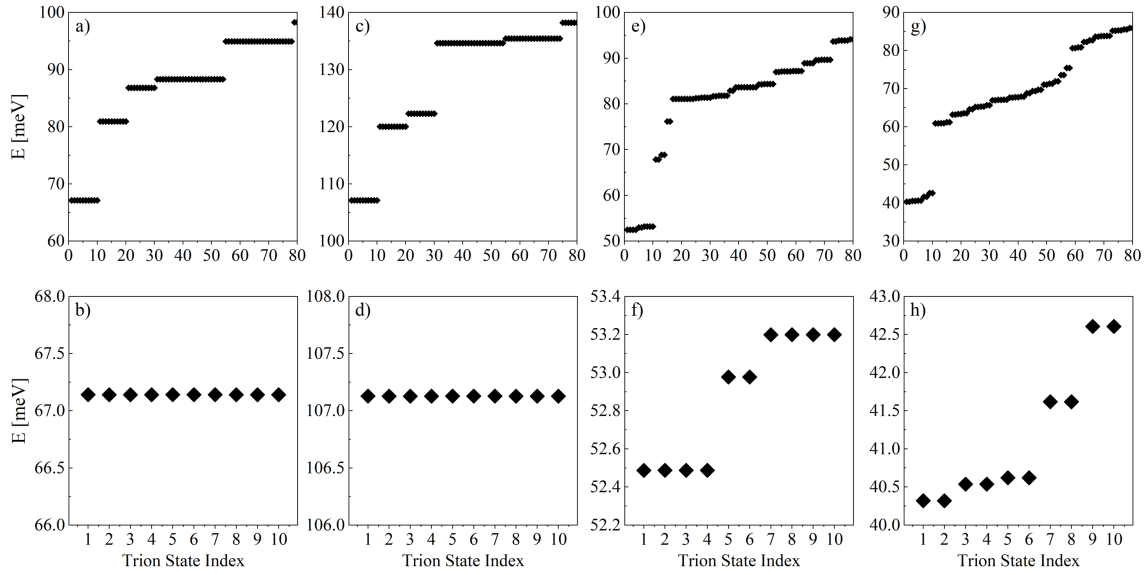


**Figure 3.7:** Trion energy spectra presented at different stages of including Coulomb interactions. (a,b) Energy levels for non-interacting trion states. (c,d) Trion spectrum renormalized by self-energies. (e,f) Energy spectrum accounting for the self-energies and the electron-hole direct and exchange interaction. (g,h) Spectrum obtained as a full BSE solution. The top row, (a,c,e,g), presents energy levels for the first 80 trion states obtained as a solution of the BSE. The bottom row, (b,d,f,h), shows zooms on the low-energy manifold (first 10 trion energy states), presenting the trion fine structure.

CME, and  $N_{occ.}$  representing to the number of occupied states.

The number of possible trion configurations for a given number of single-particle states  $N_{sp}$ , within the  $S_z = +\frac{1}{2}$  subspace, is given by the formula:

$$N_{conf.} = \left(\frac{N_{sp}}{2}\right)^3 + \left(\frac{N_{sp}}{2}\right) \cdot \frac{N_{sp}}{2}, \quad (3.46)$$

where we assume an equal number of VB and CB states. For  $N_{sp} = 32$  single-particle levels, this results in 6016 possible trion configurations. Each column in Fig. 3.7 corresponds to a different stage in the inclusion of Coulomb interactions. The bottom row of the figure shows zoomed-in views of the low-energy manifold of trion states.

We begin our analysis by considering only the non-interacting trion spectrum, when  $V_C \equiv 0$ . The result is presented in Fig. 3.7(a,b). In this case, we observe a degenerate low-energy manifold of 10 trion states, which correspond to the 5 negatively charged exciton configurations shown schematically in Fig. 3.6 and their valley-symmetric counterparts. These states are constructed solely from a hole residing in the top of the VB and two electrons in the bottom of the CB. The higher-energy part of the trion spectrum is more complex, as it reflects the large number of possible trion configurations and the breaking of electron-hole symmetry.

Next, we include the self-energy corrections to the electron and hole energies,  $\Sigma_{p,q}$ . The resulting trion spectrum is shown in Fig. 3.7(c,d). A significant blueshift of the trion energies is observed due to strong interactions. Additionally, the self-energies cause a reordering of the high-energy manifolds. This effect originates from the difference between the electron and hole self-energies.

In Fig. 3.7(e,f), we present the trion spectrum obtained by including both the self-energy terms  $\Sigma_{p,q}$  and the diagonal parts of the Coulomb direct and exchange interactions,  $V_{p,q,q,p} =$

$\langle p, q | V_C | q, p \rangle$  and  $V_{p,q,p,q} = \langle p, q | V_C | p, q \rangle$ , respectively. The direct electron-electron and electron-hole interactions do not depend on the valley and contribute only to a large overall redshift of the energy. However, the exchange interaction differs within the same valley and between different valleys. Moreover, the electron-electron interaction is stronger than the electron-hole interaction. The intravalley electron-hole exchange interaction is particularly large,  $\sim O(10^{-1})$  meV, and raises the energy of the electron-electron-hole complex. In contrast, the electron-electron exchange interaction,  $\sim O(10^{-2})$  meV, is attractive and thus lowers the trion energy. The smallest exchange interaction is the electron-hole intervalley exchange, which also increases the energy of the negatively charged exciton. This intervalley exchange interaction is of the order  $\sim O(10^{-3})$  meV in this case, and can be neglected in the analysis of the low-energy manifold. These Coulomb interactions result in splittings within the low-energy manifold. The first group of states is four-fold degenerate, corresponding to the configurations (a), (b), and (e) in Fig. 3.6. These configurations allow intravalley electron-hole exchange and have the highest energy within this manifold. The two “valley-unique” states, corresponding to the configurations (c) and (d), do not permit intravalley electron-hole exchange, making them the lowest energy states in the manifold. Next, we find a doublet corresponding to the spin ( $\uparrow\uparrow$ ) configurations, shown in Fig. 3.6(e). These configurations allow electron-electron exchange and thus have a lower energy than the previous four-fold degenerate states. The last low-energy shell is again four-fold degenerate, where both the electron and hole with the same spin belong to the same valley. This corresponds to the configurations (a) and (b) in Fig. 3.6. These configurations exhibit intravalley electron-hole exchange, but the energy is not lowered by electron-electron exchange, placing them at the highest energy within the low-energy manifold of 10 states. Higher-energy states also exhibit reordering due to large exchange splittings compared to the single-particle level spacing, as presented in Fig. 3.7(e).

Finally, we account for the effects of correlations. The resulting trion spectrum is presented in Fig. 3.7(g,h). In Fig. 3.7(g), we show the first 80 correlated trion states. A clear gap separates the 10 low-energy trion states from the higher-energy states. Each trion state appears as a doublet due to valley degeneracy, and these states are primarily built from the 10 possible low-energy 3-body configurations, with the hole occupying the top of the VB and the electrons located in the bottom of the CB. A zoom into the first 10 trion states is shown in Fig. 3.7(h). Unlike in gated lateral QDs in GaAs or self-assembled QDs, where trions do not exhibit any fine structure beyond spin [465–467], we observe a rich low-energy manifold of trion states [468, 469]. In the absence of Coulomb interactions, the low-energy trion states are exactly degenerate. Upon inclusion of electron-hole and electron-electron exchange interactions, the states split into three groups. Further inclusion of correlation effects results in the formation of five groups of doublets in the low-energy manifold. The splittings are proportional to intravalley and intervalley exchange interactions between the electron-hole and electron-electron complexes. These splittings are further corrected by the correlations. The lowest energy doublet is a spin  $\frac{3}{2}$  state, one formed in the  $K$  valley and the other in  $K'$ . The 8 higher energy states are spin  $\frac{1}{2}$  states.

Finally, we determine the binding energy of the trion. We define the binding energy of a negatively charged exciton as [470]:

$$E_b^T = E^T - E^{el} - E^X, \quad (3.47)$$

where  $E^T$  is the energy of the first bright trion state. From the trion spectrum, we find this energy to be  $E^T = 40.6$  meV, as shown in Fig. 3.7(b). The quantity  $E^{el}$  represents the energy of a free electron corrected by the self-energy, corresponding to the single-particle energy of an electron in

the bottom CB state of the BLG QD, renormalized by its self-energy. From our calculations, we determine this value to be  $E^{el} = -6.4$  meV. The difference  $E^T - E^{el} = 47.03$  meV represents the energy of a photon emitted from the first bright trion state. This value corresponds to the third vertical dashed line (first emission peak) in Fig. 3.9, indicating the energy of the photon emitted during trion recombination. The final term in Eq. (3.47),  $E^X$ , represents the energy of the first bright exciton state. This quantity is determined using the methodology described in our previous work [58], but with the inclusion of the non-zero matrix elements  $\gamma_3$  and  $\gamma_4$  in the bulk Hamiltonian (Eq. (3.28)), along with a screening constant  $\kappa = 3.9$ . We find that the energy of the first exciton state is  $E^X = 53.2$  meV.

Using this analysis, we can now calculate the trion binding energy as:

$$E_b^T = E^T - E^{el} - E^X = 40.6 \text{ meV} - (-6.4 \text{ meV}) - 53.2 \text{ meV} = -6.4 \text{ meV}. \quad (3.48)$$

Thus, we find that the trion binding energy is  $E_b^T = -6.4$  meV, indicating that the trion is bound.

### 3.3.2 Optical Absorption

In this section, we investigate the interaction of the trion with light in BLG QD systems, specifically examining how the presence of the additional charge carrier (electron) influences the absorption spectra. As with excitons, we calculate the absorption of light by a negatively charged exciton, or trion, using Fermi's golden rule to determine the photon absorption probability. This analysis parallels the approach for excitons in BLG QDs, where we previously described the absorption process involving a single electron and a hole [58]. In the case of trions, the initial state involves an additional electron, while the final state is a negatively charged exciton (trion). The probability of absorbing a photon is given by Fermi's golden rule, expressed as:

$$A(\omega) = \sum_{n,s} W_s \left| \langle \psi_-^n | \hat{P}^\dagger | \psi^s \rangle \right|^2 \delta(E^n - E^s - \omega), \quad (3.49)$$

where  $\psi^s$  represents the initial state, and a photon with energy  $\omega$  is absorbed, promoting an electron from the VB to the CB, thus creating the trion complex in state  $\psi_-^n$ .  $W_s$  indicates the probability of the initial state  $s$  being occupied at temperature  $T$ . The polarization operator  $\hat{P}^\dagger = \sum_{\alpha,i} D_{\alpha,i} c_\alpha^\dagger c_i$  creates an electron-hole pair excitation and annihilates a photon, with the excitation weighted by the DME  $D_{\alpha,i}$ . Following our previous work on excitons in BLG QDs [58], we approximate the initial state  $\psi^s$  as a single Slater determinant  $\psi^s \approx \psi^{s_q}$  (a fully occupied VB plus a single electron), where  $q$  indexes the specific QD state, as shown in Fig. 3.2(a). Since photon absorption conserves the  $S_z$  quantum number, we restrict our analysis to Slater determinants with  $S_z = \frac{1}{2}$ , specifically:

$$\psi^{s_q} = c_{q,\uparrow}^\dagger |GS\rangle. \quad (3.50)$$

At zero temperature, only two states are occupied by a single electron, corresponding to  $\psi^{s_1} = c_{1,\uparrow}^\dagger |GS\rangle$  and  $\psi^{s_2} = c_{2,\uparrow}^\dagger |GS\rangle$ , where 1 and 2 represent the states at the bottom of the CB in the two non-equivalent valleys. The transition energy is calculated as  $\omega = E^n - \epsilon_q - \Sigma_{q,q}$ , where  $\epsilon_q + \Sigma_{q,q}$  is the self-energy-corrected single-particle energy of QD state  $q$ .

In Fig. 3.8(a), we present the trion absorption spectrum obtained from Eq. (3.49). Analogous to the excitons in BLG QD systems [58], we observe a large absorption peak associated with the optically dominant transitions  $\gamma_b$  and  $\gamma_c$ , as shown in Fig. 3.3. This peak appears at a higher energy compared to the exciton absorption peaks. However, the trion absorption is significantly

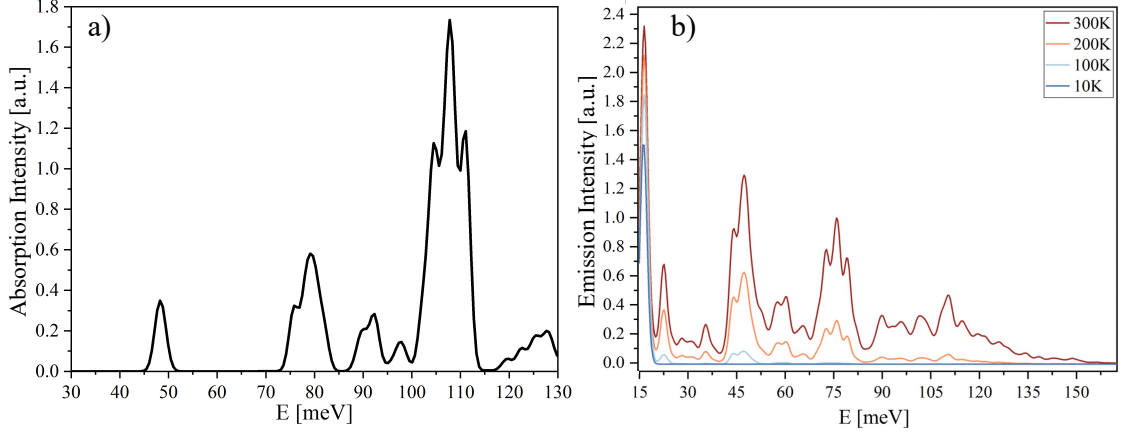


**Figure 3.8:** Trion (a) absorption and (b) temperature-dependent emission spectra. The solid lines represents the Gaussian-broadened absorption spectra. (b) Different colors represent different temperatures: blue for low temperatures, red for room temperature, where the temperature is given in Kelvin.

broadened, reflecting the increased complexity of trion states, which are more strongly correlated and involve many more configurations than exciton states.

We also note that, unlike simple excitonic states, the low-energy trion states are not entirely dark. The inclusion of trigonal warping terms,  $\gamma_3$  and  $\gamma_4$ , in the bulk Hamiltonian (Eq. (3.28)) results in optically active low-energy trion states, effectively "brightening" them. This phenomenon is reminiscent of the brightening of the  $1s$  exciton in gated BLG systems, as observed in earlier studies [79]. These results underscore the complexity introduced by the additional charge carrier in the trion and its impact on the optical properties of BLG QDs, further distinguishing the behavior of trions from that of neutral excitons.

### 3.3.3 Emission Spectrum

We now turn to the reverse process, where the initial state is a trion  $\psi_-^n$ , and a photon is emitted as one of the electrons in the CB recombines with the hole. As in the absorption case, the emission process is governed by Fermi's golden rule, which now describes the probability of photon emission due to carrier recombination in the QD system. While the emission spectrum is evaluated within the same theoretical framework as absorption, the key difference lies in the initial states being trions rather than the GS. As a result, statistical weights now reflect the occupancy of the excited trion states at finite temperature, and the transitions lead to final states with an extra electron in the CB.

The emission probability for a photon of energy  $\omega$  is given by:

$$A(\omega) = \sum_{n,s} W_n \left| \langle \psi^s | \hat{P} | \psi_-^n \rangle \right|^2 \delta(E^s + \omega - E^n), \quad (3.51)$$

where  $W_n$  represents the statistical weight of the trion state  $\psi_-^n$  at effective temperature  $T$ , given by:

$$W_n = \frac{e^{-E_n/k_B T}}{\sum_m e^{-E_m/k_B T}}. \quad (3.52)$$

We assume that the final state  $\psi^s$  corresponds to a single Slater determinant, describing an extra electron left behind after recombination in any of the excited QD states. The transition energy

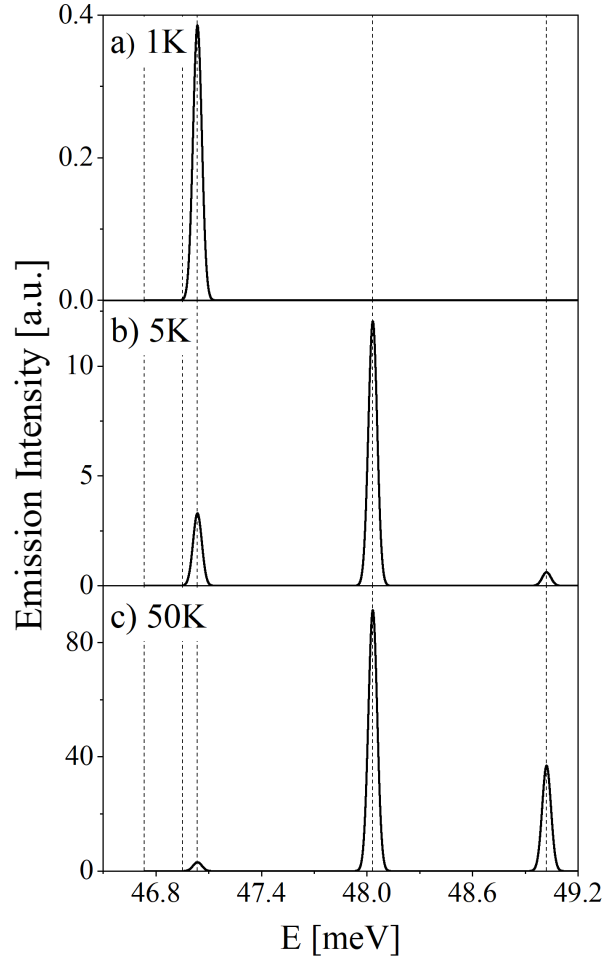


**Figure 3.9:** The emission spectrum of the 10 lowest-energy trion states is shown for three different temperatures: (a)  $T = 1$  K, (b)  $T = 5$  K, and (c)  $T = 50$  K. The solid lines represent the broadened emission spectra, while the dashed vertical lines indicate the possible recombination energies of the low-energy trion states.

for this process, similar to the case of absorption, is given by the energy difference between the initial and the final state.

Fig. 3.8(b) shows the trion emission spectrum for various temperatures. Unlike the absorption spectrum, where the higher-energy trion states dominate the absorption process, the emission spectrum reveals that low-energy trions are optically active and dominate the emission, especially at low temperatures. This can be attributed to the large energy gap separating the low-energy trion states from the higher-energy trions, which remain thermally unoccupied at low temperatures, thus making the low-energy trion states the primary contributors to the emission spectrum. Moreover, these low-energy trion states are tunable via an electric field, positioning QDs as promising candidates for single-photon emitters.

To further analyze the low-energy emission spectrum, we consider the shell of  $N = 10$  low-energy trion states, as presented in Fig. 3.7(b). Fig. 3.9 shows the emission spectra for temperatures of 1 K, 5 K, and 50 K, respectively. The dashed vertical lines represent the 5 doublets corresponding to the initial trion states in the emission process. The first doublet, which corresponds to the lowest energy state, is dark at all temperatures. This is because this state has a total spin  $S = \frac{3}{2}$ ,

while the final states have total spin  $S = \frac{1}{2}$ , as described by Eq. (3.50). Since total spin  $S$  is not conserved in this process, the emission from this state is spin-forbidden.

The second doublet corresponds to a trion state where the only recombination pathway is an intervalley recombination. However, because the intervalley DMEs are very small, this state is also dark. The third doublet, however, is optically active and leads to the brightest emission peak at 1 K, as shown in Fig. 3.9(a). This state allows for recombination of the electron-hole pair within the same valley, making it optically bright and dominant in the emission spectrum at low temperatures.

At higher energies, the trion states still support intravalley recombination, but these states remain dark at 1 K due to the energy gap ( $\sim 0.086$  meV), which prevents thermal occupation of these states at low temperatures. The energy gap between the third doublet and these higher states is sufficiently large that these higher-energy states are not thermally populated at 1 K. Consequently, the emission at low temperatures predominantly originates from the third doublet.

As the temperature increases to 5 K, we observe that the emission shifts to the fourth doublet in the low-energy manifold, as shown in Fig. 3.9(b). Concurrently, the intensity of the emission from the third doublet decreases due to thermal population effects, which make the higher-energy states more accessible. At even higher temperatures, such as 50 K (Fig. 3.9(c)), the fifth doublet begins to contribute to the emission, although with a lower intensity compared to the fourth doublet. This temperature dependence of the emission spectra illustrates how the fine structure of the trion states can be partially resolved, especially by shifting the emission peaks as a function of temperature.

In summary, while the absorption spectra reveal the optically active trion states involved in the creation of the trion complex, the emission spectra provide detailed insight into the recombination processes and the thermal occupation of trion states. This interplay of valley and spin effects, combined with the thermal occupation at different temperatures, allows for a detailed study of the trion fine structure in BLG QDs. Furthermore, the temperature-dependent shifting of the emission peaks highlights the potential of BLG QDs as efficient, tunable light emitters, with applications ranging from quantum optics to valleytronics.

### 3.4 Conclusions

This chapter explored the excitonic and trionic properties of BLG QDs, emphasizing the effects of bulk band structure, electric fields, quantum confinement, and many-body interactions. The study demonstrated the potential of BLG QDs for applications in nanoscale light sources and single-photon emitters.

Bulk BLG was modeled using a low-energy TB Hamiltonian, including TW effects and interlayer asymmetry, which significantly modified the electronic structure by breaking rotational symmetry and introducing more complex band profiles. The application of a perpendicular electric field further tuned the electronic properties by opening a band gap, turning BLG into a tunable semiconductor. The BLG QD was then modeled by introducing a screened Gaussian potential to confine both electrons and holes, generating discrete QD states in both the CBs and VBs. We observed that the single-particle states in the QD confinement have unique features distinct from conventional QDs. The inclusion of TW effects further modified the energy levels of the BLG QD. These QD states are quite different from those in conventional self-assembled semiconductor QDs, as BLG allows for both electron and hole confinement simultaneously, while still being tunable via external voltages.

Next, we analyzed the excitonic properties of BLG QDs by solving the BSE, which accounted for Coulomb interactions and hole-electron correlation effects. This revealed the formation of tightly bound excitons, with binding energies and fine structure that sensitively depended on the bulk BLG energy gap and the QD parameters [152]. The TW parameters were found to induce weak optical activity in otherwise dark exciton states. The excitons in BLG QDs differ significantly from those in conventional semiconductor QDs. In particular, the conservation of spin, valley, and orbital angular momentum leads to the formation of a band of dark low-energy states, making these systems promising candidates for photon storage, detection, and emission in the THz range. Additionally, the energy and optical spectrum of these excitons can be tuned electrically, offering a range of control from the THz to FIR. This tunability, combined with strong electron-hole interactions, gives BLG QDs unique properties for various quantum applications.

We then examined the negatively charged excitons (trions), focusing on their formation, binding energy, and interaction with light. We found that a trion formed in the BLG QDs, revealing a fine structure, an effect not observed in conventional QDs. The absorption spectrum displayed a prominent peak at energies around 110 meV, attributed to optically dominant transitions with large DMEs, similar to neutral excitons. We also analyzed the emission spectrum from trion states as a temperature-dependent process, where the lowest-energy trion states were bright at low temperatures, making BLG QDs strong candidates for tunable single-photon emitters. We proposed a method to extract the trion fine structure from the temperature dependence of the emission spectra. Finally, we calculated the trion binding energy, which was found to be  $-6.4$  meV, confirming that trions are stable and bound.

Altogether, this chapter provided a detailed theoretical framework for understanding the electronic and optical properties of BLG QDs. By incorporating the effects of bulk band structure, electric field tuning, quantum confinement, and many-body interactions, we uncovered the intricate behavior of excitons and trions, paving the way for future advancements in graphene-based quantum technologies.

## Chapter 4

# Optical Response of Transition Metal Dichalcogenide Monolayers in High Magnetic Fields

Atomically thin transition metal dichalcogenides (TMDCs) [168] have emerged as a novel platform for exploring both fundamental physics and practical applications in the realm of 2D materials [5, 169, 170]. As direct-gap semiconductors with strong optical response and pronounced spin-orbit coupling (SOC), TMDC monolayers exhibit distinctive electronic [5, 169, 173–175] and optical [6, 182–222] properties. These features arise from broken inversion symmetry and the presence of direct bandgaps in the visible range [7, 178–180], positioning them at the forefront of condensed matter research. Their complex excitonic properties, tunable via external perturbations, makes them ideal for studying quantum phenomena and developing next-generation optoelectronic devices.

The application of strong external magnetic fields introduces modifications to the electronic structure and optical response of TMDC monolayers, leading to the phenomena such as formation of Landau levels (LLs), Zeeman splitting, and magnetoexcitonic effects [220–222]. These effects enable the study of massive Dirac-like quasiparticles, characteristic of the TMDC low-energy band structure, as well as of bound excitonic states that can be modified by finite charge density. In particular, the formation of LLs in both conduction and valence bands leads to discrete energy levels that profoundly affect the optical spectra.

Spin-valley coupling, intrinsic to TMDCs, introduces an additional degree of freedom in the form of valley polarization, allowing selective optical excitation in different valleys. External magnetic fields can lift valley degeneracy through the valley Zeeman effect, thereby influencing valley polarization and enabling potential applications in spintronic and valleytronic devices [471, 472]. This valley-selective behavior, together with unique optical selection rules, further underscores the potential of TMDCs for next-generation optoelectronic devices that exploit the interplay of spin, valley, and charge.

This chapter presents a comprehensive theoretical investigation of the optical properties of monolayer TMDCs in strong magnetic fields, focusing on the formation and evolution of magnetoexciton states in both neutral and doped regimes. We begin in Sec. 4.1 with a first-principles analysis of the electronic structure and, in Sec. 4.2, we extract the effective low-energy massive

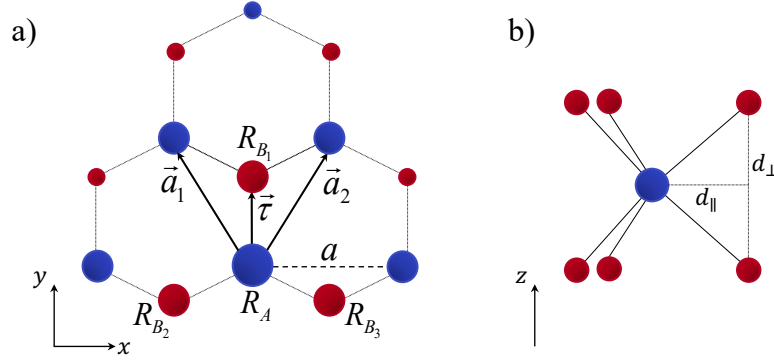


**Figure 4.1:** Geometry of the TMDC monolayer in (a) top view and (b) side view. Metal atoms are depicted in dark blue, while chalcogen atoms are shown in red. The in-plane lattice constant is labeled as  $a$ . The distance between chalcogen atoms is defined as  $d_{XX} \equiv 2d_{\perp}$ , the metal-chalcogen bond length is represented as  $d_{\parallel}$ , where  $\vec{\tau} = (0, d_{\parallel})$ , and the total metal-chalcogen distance is given by  $\sqrt{d_{\perp}^2 + d_{\parallel}^2}$ .

Dirac Fermion (mDF) model parameters by fitting the electronic structure to the *ab initio* results, capturing that captures the essential band features near the non-equivalent  $K$  and  $K'$  valleys. In the next step, we examine Coulomb interaction effects and self-energy corrections in Sec. 4.3. Sec. 4.4 explores the formation and optical response of magnetoexcitons at varying charge densities. We begin with a study of the magnetic-field-induced evolution of neutral excitons in Sec. 4.4.1. The impact of a finite electron filling factor,  $\nu = 1$ , on the exciton spectrum is addressed in Sec. 4.4.2. Sec. 4.4.3 then presents a single-valley analysis of negatively charged magnetoexcitons (trions), including trionic states interacting with a filled LL. For each of these optical complexes, we compute the corresponding emission spectra, highlighting the many-body features that emerge in the strong-field regime. Together, these sections establish a unified framework for interpreting the magneto-optical behavior of TMDC monolayers, as summarized in Sec. 4.5, and offer theoretical predictions directly relevant to ongoing experimental efforts [473–475].

## 4.1 First Principles Electronic Structure

We begin by examining the electronic and microscopic properties of TMDC monolayers using first-principles calculations. We analyze a single layer of TMDC in the  $2H$  phase, presented in Fig. 4.1. The crystal exhibits a honeycomb lattice structure, as shown in Fig. 4.1(a). Within this structure, the transition metal atom ( $R_A$ ) is surrounded by three NN chalcogen atoms in the plane ( $R_{B_1}$ ,  $R_{B_2}$ ,  $R_{B_3}$ ). The bond length is denoted as  $d_{\parallel}$ , as shown in the side view in Fig. 4.1(b).

The primitive lattice vectors in real space are defined as  $\vec{a}_1 = a \left(-\frac{1}{2}, \frac{\sqrt{3}}{2}\right)$  and  $\vec{a}_2 = a \left(\frac{1}{2}, \frac{\sqrt{3}}{2}\right)$ , where  $a$  represents the lattice constant, as marked in the figure. For the prototypical case of  $\text{MoS}_2$ , the lattice constant  $a$  has been calculated to be  $a = 3.16 \text{ \AA}$ . Furthermore, the separation of the chalcogen atoms is  $2d_{\perp} = 3.17 \text{ \AA}$ , and the distance between the metal and the chalcogen atoms is  $\sqrt{d_{\perp}^2 + d_{\parallel}^2} = 2.42 \text{ \AA}$ . Fig. 4.1(b) provides a side view of the monolayer structure, highlighting the three-plane arrangement of the UC, with a central metal atom layer sandwiched between top and bottom planes of chalcogen atoms.

The electronic energies and wave functions are computed *ab initio* using the DFT package ABINIT [406–408]. We employ the PBE parametrization of the GGA for the XC potentials [420],

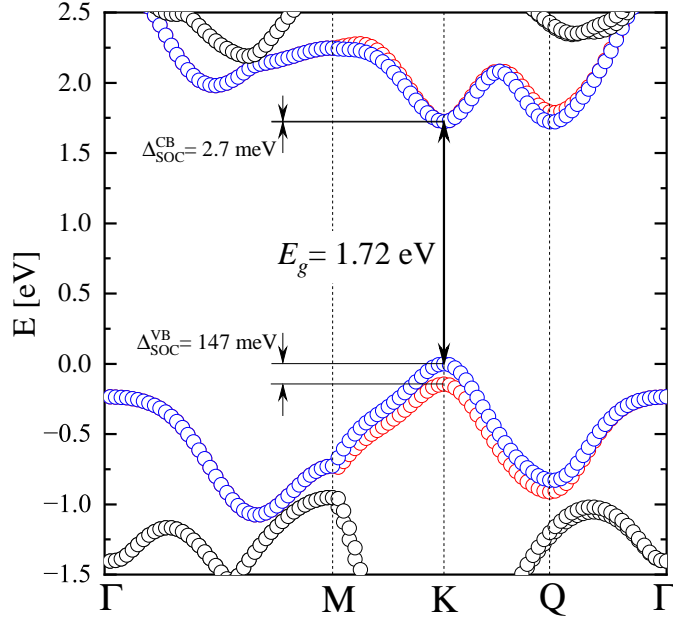


**Figure 4.2:** Electronic structure of the MoS<sub>2</sub> monolayer presented as the DFT energy spectrum along the high-symmetry path  $\Gamma$ -M-K-Q- $\Gamma$ , with the Fermi energy set at  $E_F = 0$ . The simplified spin-resolved band structure is shown for the 4 low-energy band, where spin orientation is indicated by color (blue for spin-up and red for spin-down). The values of SOC splittings and the energy gap are denoted on the figure.

alongside the PAW method [418]. Both the intrinsic SOC and vdW interactions are accounted for in the calculations. The vdW interactions are included through the DFT-D3 functional [476]. The computational parameters are set to ensure convergence and accuracy. A plane-wave cutoff energy of 160 Ha is used, with an additional energy cutoff of 80 Ha for the augmentation charge. The Brillouin zone is sampled with a  $16 \times 16 \times 1$  Monkhorst-Pack  $k$ -point grid. To simulate an isolated monolayer, a vacuum layer of 40 Å is included along the  $z$ -direction to eliminate interlayer vdW interactions.

The resulting electronic structure of the MoS<sub>2</sub> monolayer is presented in Fig. 4.2. In line with our previous findings [175], the MoS<sub>2</sub> monolayer exhibits two CB minima located at the K and Q points of the BZ, and a VB maximum at the K point, as shown in Fig. 4.2. Unlike its bulk counterpart, the monolayer features a direct bandgap at the K point (K-K transition). In Fig. 4.2, the eigenenergies are shifted such that the Fermi energy is set to  $E_F = 0$ , and the direct K-K gap is found to be  $E_g = 1.72$  eV.

To further resolve the electronic structure, we extract the spin-resolved Kohn-Sham wave functions,  $\Psi_{n,k}^{\uparrow,\downarrow}$ , and compute the corresponding in-plane integrated real-space densities  $\rho_{n,k}^{\uparrow,\downarrow}(z)$ , as described in Sec. 2.1.2. A simplified spin-resolved representation of the four low-energy bands is shown in Fig. 4.2, where red and blue colors denote spin-up and spin-down states, respectively. While spin mixing becomes increasingly relevant away from the K point—particularly due to SOC and orbital hybridization—this figure assumes a dominant spin character inherited from the K point throughout the band. This approximation is justified by the focus of our subsequent analysis on the mDF model, where such spin mixing effects are effectively averaged out and not explicitly retained.

The orbital character of the bands is analyzed via projection onto atom-centered Slater-type

orbitals, described in detail in Sec. 2.1.2, with metal atoms described by  $d$  orbitals with  $L = 2$ ,  $\mu = 0, \pm 2$ , and chalcogen atoms by  $p$  orbitals with  $L = 1$ ,  $\mu = 0, \pm 1$ . This decomposition confirms that the CB near the  $K$  point is predominantly composed of  $d_{m=0}$  orbitals localized on the metal atom, while the VB derives mainly from  $d_{m=\pm 2}$  orbitals. These findings are consistent with the observed dispersion and symmetry properties near high-symmetry points [175].

The chalcogen  $p$  orbitals, particularly  $p_x$  and  $p_y$ , play a supporting role through hybridization, which enhances band dispersion and influences state localization near  $K$  and  $Q$ . This orbital makeup, together with the intrinsic SOC, leads to significant spin splittings in both CB and VB, with values of  $\Delta_{\text{SOC}}^{\text{CB}} = 2.7$  meV and  $\Delta_{\text{SOC}}^{\text{VB}} = 147$  meV, respectively. The resulting spin-valley locking—observed for both electrons and holes in the  $K$  valley—highlights the intertwined nature of spin, valley, and orbital degrees of freedom in monolayer TMDCs.

These microscopic insights into orbital composition and symmetry form the basis for effective low-energy models, such as the mDF framework discussed in the following Sec. 4.2, and are essential for understanding the optical and magneto-optical phenomena addressed in later sections.

## 4.2 *Ab Initio*-Based Massive Dirac Fermion Model

The crystallographic structure of TMDC monolayers inherently breaks the inversion symmetry, which has profound implications for the electronic structure and optical properties of the material. This lack of inversion symmetry results in valley-dependent optical selection rules, allowing for the optical addressing of individual valleys, namely the  $K$  and  $K'$  valleys. As a result, one can selectively excite and probe electronic states associated with either of the valleys, as described in Sec. 2.4.1.1.

To accurately describe the low-energy spectrum of a single TMDC monolayer near these valleys, we turn to the *ab initio*-based mDF model. This model captures the essential features of the electronic band structure near the  $K$  and  $K'$  points of the BZ, while also incorporating the effects of strong SOC, which leads to spin-valley coupling [180, 463, 477]. The mDF model offers a convenient framework for understanding valley dynamics and optical behavior, particularly under external perturbations, such as magnetic fields.

### 4.2.1 Massive Dirac Fermion Model for MoS<sub>2</sub> Monolayer

The detailed description of the mDF model derivation has been presented in Sec. 2.1.4.2. To describe the electronic structure of a TMDC monolayer, we start with the mDF Hamiltonian, which captures the low-energy states of the conduction and valence bands near the  $K$  and  $K'$  valleys, given in Eq. (2.55), with its matrix form defined by Eq. (2.56). For a MoS<sub>2</sub> monolayer, we use the lattice constant  $a = 3.160$  Å, the hopping integral  $t = -1.4677$  eV, and the energy gap  $\Delta = 1.72$  eV. The eigenenergies and eigenstates are determined by diagonalizing the Hamiltonian, as defined in Eq. (2.57) and Eq. (2.58), respectively.

We then incorporate SOC into the mDF model, extending the Hamiltonian to include the spin degrees of freedom. This results in a four-band model, defined in Eq. (2.59), which describes both spin-up and spin-down states for the conduction and valence bands. The inclusion of SOC modifies the electronic structure by splitting the spin-up and spin-down bands at both the  $K$  and  $K'$  valleys. This spin splitting is crucial for understanding valley- and spin-dependent phenomena in TMDC monolayers, such as the valley Zeeman effect and spin-polarized optical transitions.

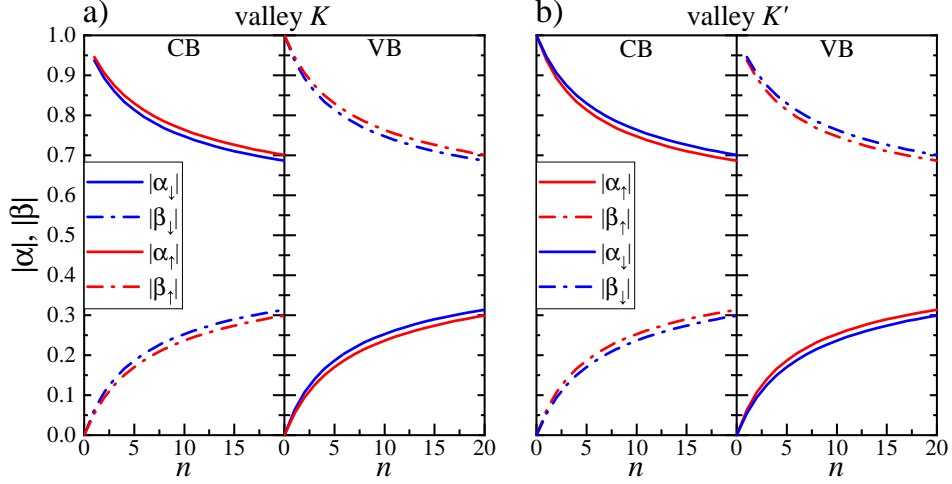


**Figure 4.3:** Absolute values of wave functions coefficients for a TMDC monolayer in vertical magnetic field as a function of the LL index  $n$  with the inclusion of SOC presented for the valley (a)  $K$  and (b)  $K'$ .

While the DFT results offer a more detailed picture of the full electronic structure, including the higher-energy bands, the mDF model provides a simplified yet accurate description of the low-energy behavior near the  $K$  and  $K'$  valleys. In the following part of this section, we apply the mDF approximation to the monolayer MoS<sub>2</sub> crystal, focusing specifically on the properties of the LLs that arise when a magnetic field is applied. We analyze the LL structure in the two non-equivalent valleys,  $K$  and  $K'$ , with special attention to the valley-dependent Zeeman effects induced by SOC. We also discuss the influence of an external magnetic field on optical transitions between the bands for the single-layer TMDC.

#### 4.2.2 The Effect of an External Magnetic Field

As described in Sec. 2.1.4.3, we now introduce a magnetic field  $B$  by substituting the canonical momentum as  $\vec{p} \rightarrow \vec{p} + e\vec{A}$ , where  $\vec{A}$  is introduced in the symmetric gauge (see Eq. (2.62)). This yields the Hamiltonian given in Eq. (2.63), which reflects the presence of a finite band gap  $\Delta \equiv E_g$ . Diagonalization using ladder operators defined in Eqs. (2.64) and (2.65) produces discrete LL energies (Eq. (2.66)) that scale with both the magnetic field and the gap. The corresponding wave functions (Eq. (2.193)) are spinors built from 2D harmonic oscillator states  $|n, m\rangle$ , indexed by harmonic oscillator quantum numbers  $n$  (labeling LLs) and  $m$  (indexing the degenerate orbitals within each LL).

The inclusion of SOC effects further enriches this structure by lifting spin degeneracy and introducing valley-dependent energy shifts. The spin-resolved Hamiltonian, given in Eq. (2.71), includes SOC contributions in both the conduction and valence bands, resulting in an LL spectrum that depends on spin  $s$ , valley index  $\nu$ , and the LL index  $n$ .

Figure 4.3 shows the spin-resolved absolute values of the wave function coefficients for a TMDC monolayer in a magnetic field as a function of the LL index  $n$ , both (a) in valley  $K$  and (b) in valley  $K'$ , where the inclusion of SOC is responsible for lifting the spin degeneracy. The wave function structure (see Eq. (2.193)) reveals that in valley  $K$ , the CB state with  $n = 0$  is absent, while the corresponding VB state is present. The reversed situation occurs in valley  $K'$ , reflecting

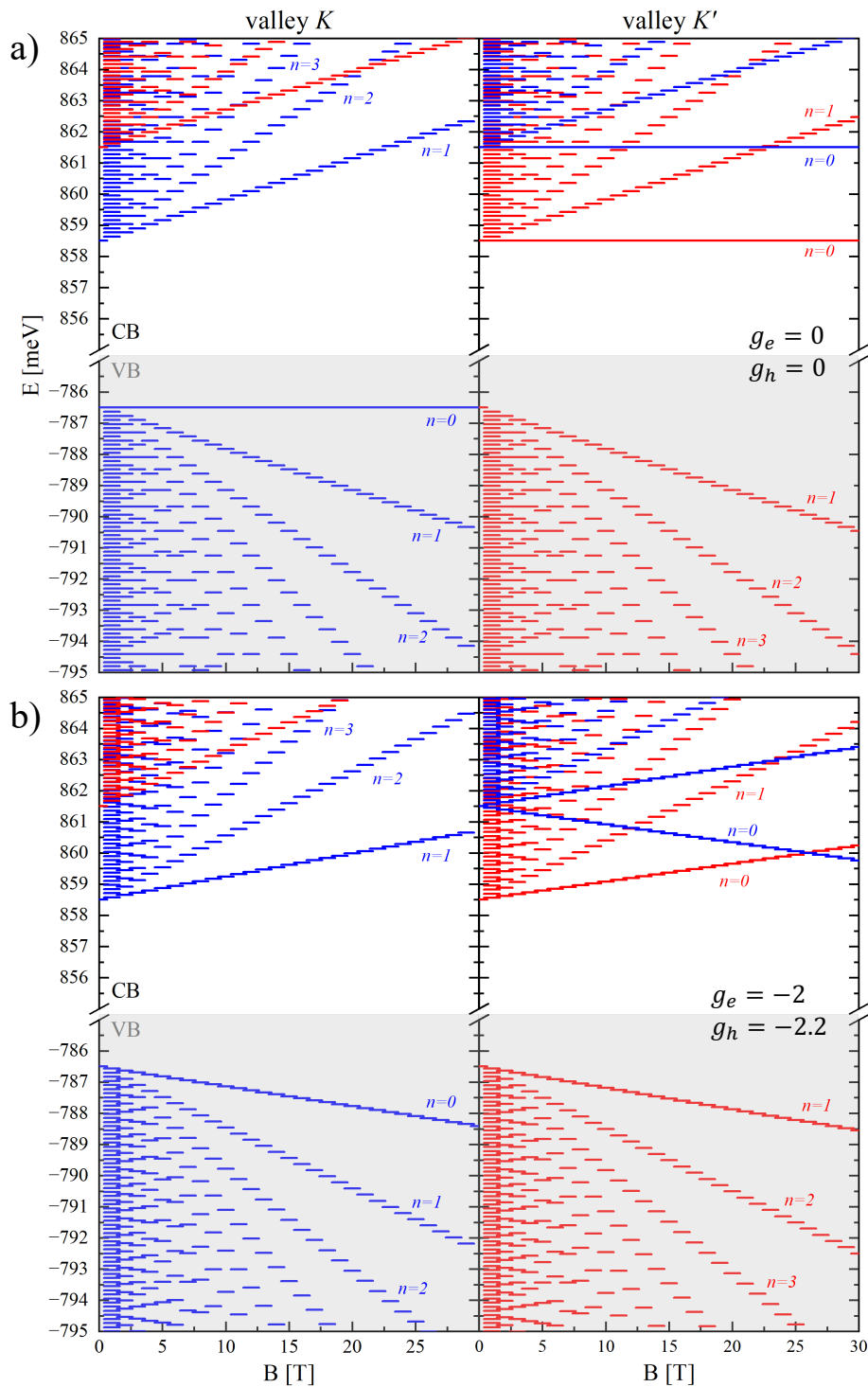


**Figure 4.4:** Spin-resolved LLs spectrum as a function of the vertical magnetic field for a  $\text{MoS}_2$  monolayer (a) with the  $g$ -factors set to zero and (b) with the non-zero  $g$  factors, as given in the figure.

the intrinsic valley asymmetry of the system.

The spin-resolved LL spectrum as a function of the applied magnetic field is presented for both valleys in Fig. 4.4. As expected from the wave function structure, the CB state with  $n = 0$  is missing in valley  $K$ , whereas the VB state with  $n = 0$  is missing in valley  $K'$ . This asymmetry results in a valley-dependent energy offset known as valley Zeeman splitting, where the first accessible conduction LL in valley  $K$  lies higher in energy than in valley  $K'$ . Panel (a) of Fig. 4.4 displays the LL fan diagram in the absence of the spin Zeeman effects, with all Landé  $g$ -factors set to zero. In this case, the levels for  $n > 0$  show an approximately linear dependence on  $B$ , consistent with expected LL scaling, while the  $n = 0$  level remains fixed in energy, reflecting the unique behavior of the lowest LL. In contrast, panel (b) incorporates finite  $g$ -factors—specifically  $g_e = -2$  for electrons and  $g_h = -2.2$  for holes—leading to noticeable spectral modifications. These Zeeman contributions introduce additional spin-dependent energy shifts, tilting the levels and amplifying the valley asymmetry. This effect becomes increasingly significant at higher magnetic fields, further altering the LL alignment and influencing excitonic transitions in the system.

Additionally, the LL energy spectrum at a fixed magnetic field of  $B = 10$  T, used throughout the subsequent calculations, is shown in Fig. 4.5, separately for the  $K$  and  $K'$  valleys. Grey semi-transparent curves represent the mDF band structure at  $B = 0$  without SOC, providing a baseline reference for the unperturbed conduction and valence bands. Red and blue curves indicate the  $B = 0$  mDF dispersion including SOC, revealing the spin-split band edges associated with each valley. Each panel presents three columns of states, progressively incorporating more physical effects. The LL indices  $n$  are labeled, highlighting the absence of the conduction band  $n = 0$  state in the  $K$  valley and the valence band  $n = 0$  state in the  $K'$  valley. The first column (black horizontal lines) shows the LL spectrum without SOC, capturing the fundamental magnetic quantization of the Dirac dispersion. Here, the valley Zeeman effect emerges naturally, breaking the time-reversal symmetry and causing distinct energy shifts between valleys even without spin splitting. In the second column, SOC is introduced, lifting spin degeneracy and leading to spin-split LLs, though spin Zeeman effects remain neglected. This reflects the intrinsic spin-valley coupling that is key to many TMDC phenomena. The third column shows the full model, including both SOC and finite electron and hole  $g$ -factors ( $g_e = -2$  and  $g_h = -2.2$ , respectively), resulting in the complete spin- and valley-resolved LL structure. This incorporates both spin and valley Zeeman splittings, further refining the spectral landscape and crucially influencing optical selection rules. Dashed lines connect the top valence and bottom conduction LLs across the three columns to illustrate how these levels evolve with increasing model complexity. Understanding this evolution is essential for interpreting the magnetic-field-dependent optical transitions and many-body effects discussed in later sections.

Furthermore, based on the light-matter coupling formalism introduced in Sec. 2.4.1.1, we analyze the selection rules governing optical transitions in this quantized LLs regime. The allowed transitions are schematically indicated in Fig. 4.5 by vertical arrows connecting specific LLs. These transitions conserve the LL number  $m$  and involve changes in the LL index  $n$  by  $\pm 1$ , consistent with angular momentum selection rules. In particular,  $\sigma^-$  polarized light couples states with  $n' = n + 1$ , while  $\sigma^+$  polarization couples states with  $n' = n - 1$ . These valley-resolved selection rules reflect the breaking of inversion and time-reversal symmetries in the presence of a magnetic field, illustrating how optical activity is distributed across the  $K$  and  $K'$  valleys in monolayer MoS<sub>2</sub>.

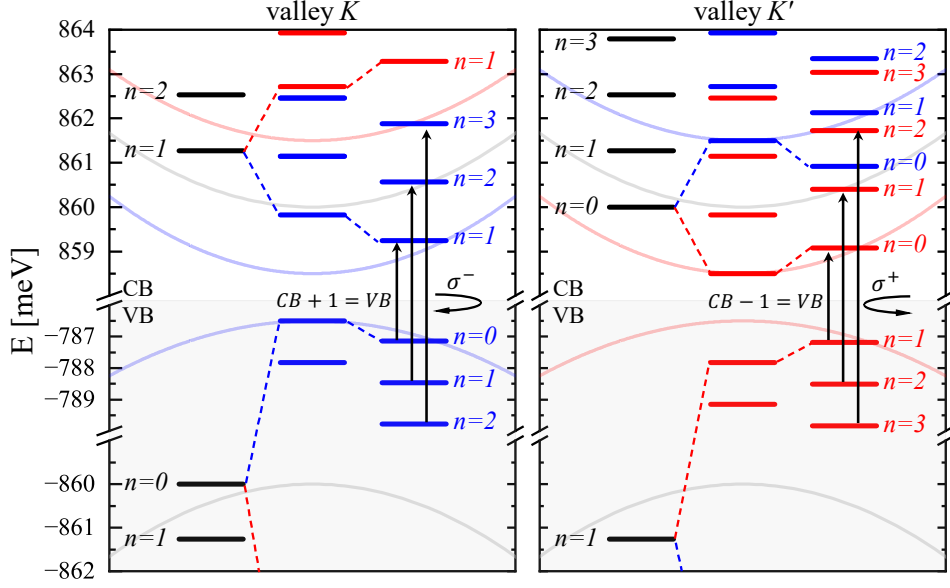


**Figure 4.5:** Schematic representation of optical selection rules for monolayer MoS<sub>2</sub> in the mDF model under an external magnetic field of  $B = 10$  T, shown separately for the  $K$  and  $K'$  valleys. Semi-transparent lines in the background depict the continuous-band mDF dispersion at  $B = 0$ : grey curves represent bands without SOC, while red and blue highlight the VB and CB edges with SOC. Each panel contains three columns illustrating the evolution of LLs with increasing model complexity. The first column shows the LL spectrum without SOC (black horizontal lines). The second includes SOC but assumes vanishing  $g$ -factors. The third shows the full model with  $g_e = -2$  and  $g_h = -2.2$ . Dashed lines connect selected LLs in the top VB and bottom CB to track their evolution. LL indices  $n$  are indicated explicitly in the Figure. Optically allowed interband transitions are indicated by vertical arrows, annotated with the circular polarization  $\sigma^\pm$  of light. Selection rules are explicitly stated for each valley, highlighting the role of magnetic field and valley asymmetry in determining optical activity.

### 4.3 Coulomb Interactions and Self-Energy Correction

In the previous section, we established that the low-energy spectrum of TMDC monolayers, such as MoS<sub>2</sub>, can be effectively described using the mDF framework. This analysis provided insights into the optical selection rules and the influence of an external magnetic field on the system's electronic properties. Building on these results, we now focus on how Coulomb interactions in the context of high magnetic fields influence the system.

We begin by discussing the electron-electron Coulomb scattering processes within the MoS<sub>2</sub> monolayer, which form the basis for understanding the many-body effects in the presence of strong magnetic fields. The Coulomb interaction in second quantization is described by the Hamiltonian presented in Eq. (2.93), which we now repeat for clarity:

$$\hat{H}_C = \frac{1}{2} \sum_{i,j,k,l} \langle i,j | V_C | k,l \rangle \hat{c}_i^\dagger \hat{c}_j^\dagger \hat{c}_k \hat{c}_l, \quad (4.1)$$

where  $V_C = \frac{e^2}{4\pi\epsilon_0\epsilon_r|\vec{r}-\vec{r}'|}$  describes the Coulomb potential in real space, and the indices  $i, j, k, l$  represent composite LLs indices  $i = (n_i, m_i)$ . The LL wave functions for electrons and holes in the

MoS<sub>2</sub> monolayer, as derived earlier in Eq. (2.193), are restated here in the following notation:

$$|\psi_{n,m,v}^{\text{VB/CB}}\rangle = \begin{pmatrix} \alpha_n^{\text{VB/CB}} w_{n,m,v}^A(\vec{r}) u^A(\vec{r}) \\ \beta_n^{\text{VB/CB}} w_{n,m,v}^B(\vec{r}) u^B(\vec{r}) \end{pmatrix} = \begin{pmatrix} A_{n,m,v}^{\text{VB/CB}}(\vec{r}) \\ B_{n,m,v}^{\text{VB/CB}}(\vec{r}) \end{pmatrix}, \quad (4.2)$$

where,  $w_{n,m,v}^{A/B}(\vec{r})$  represents the slowly varying envelope functions, and  $u^{A/B}(\vec{r})$  captures the fast oscillations due to the atomic-scale periodicity within the UC. Using these wave functions, the CME for electron-electron scattering can be expressed as:

$$\langle B_{n_1,m_1}^{\text{VB/CB}}(\vec{r}), A_{n_2,m_2}^{\text{VB/CB}}(\vec{r}) | V_C | A_{n_3,m_3}^{\text{VB/CB}}(\vec{r}), B_{n_4,m_4}^{\text{VB/CB}}(\vec{r}) \rangle = \iint d\vec{r} d\vec{r}' \left[ B_{n_1,m_1}^{\text{VB/CB}}(\vec{r}) \right]^* \left[ A_{n_2,m_2}^{\text{VB/CB}}(\vec{r}') \right]^* \frac{e^2}{4\pi\epsilon_0\epsilon_r|\vec{r}-\vec{r}'|} A_{n_3,m_3}^{\text{VB/CB}}(\vec{r}') B_{n_4,m_4}^{\text{VB/CB}}(\vec{r}). \quad (4.3)$$

To simplify the notation, we omit the valley index  $v$  in subsequent steps.

The evaluation of Coulomb scattering matrix elements benefits from the following simplification: the envelope function approximation. This assumes that the slow variation of  $w(\vec{r})$  can be decoupled from the fast oscillations of  $u(\vec{r})$ , as the latter occur on the scale of the UC. Specifically,  $\int d\vec{r} \rightarrow \sum_R \int_{\text{UC}} d\vec{r}$ , where  $R$  indexes the unit cells. Assuming that  $w(\vec{r})$  and  $V_C(|\vec{r}-\vec{r}'|)$  vary slowly on the scale of a single UC, the integration over the UC area can be performed independently. Thus, we obtain the transition  $\sum_R \int_{\text{UC}} d\vec{r} \rightarrow \sum_R \Omega \rightarrow \int d\vec{R}$ , where  $\Omega$  is the area of a single UC, and the integral over all UCs transforms into a continuous integral over the macroscopic coordinate  $\vec{R}$ . This leads to the following expression for the CMEs:

$$\langle B_{n_1,m_1}^{\text{VB/CB}}(\vec{r}), A_{n_2,m_2}^{\text{VB/CB}}(\vec{r}) | V_C | A_{n_3,m_3}^{\text{VB/CB}}(\vec{r}), B_{n_4,m_4}^{\text{VB/CB}}(\vec{r}) \rangle = \frac{e^2}{4\pi\epsilon_0\epsilon_r|\vec{r}-\vec{r}'|} \beta_{n_1}^{\text{VB/CB}} \alpha_{n_2}^{\text{VB/CB}} \alpha_{n_3}^{\text{VB/CB}} \beta_{n_4}^{\text{VB/CB}} \langle u^B, u^A | u^A, u^B \rangle \times \underbrace{\iint d\vec{R} d\vec{r}' \left[ w_{n_1,m_1}^B(\vec{R}) \right]^* \left[ w_{n_2,m_2}^A(\vec{r}') \right]^* \frac{1}{|\vec{R}-\vec{r}'|} w_{n_3,m_3}^A(\vec{r}') w_{n_4,m_4}^B(\vec{R})}_{\langle n_1,m_1;n_2,m_2 | V_C | n_3,m_3;n_4,m_4 \rangle}. \quad (4.4)$$

The term  $\langle u^B, u^A | u^A, u^B \rangle$  simplifies due to orthogonality and normalization conditions of the Bloch functions  $u^{A/B}(\vec{r})$ :

$$\langle u^A | u^A \rangle = \langle u^B | u^B \rangle = 1, \quad \text{and} \quad \langle u^A | u^B \rangle = \langle u^B | u^A \rangle = 0, \quad (4.5)$$

leading to:

$$V_{BAAB} = V_{BAAB} = V_{AAAA} = V_{BBBB} = 1 \quad \text{and} \quad V_{ABAB} = V_{BABA} \approx 0, \quad (4.6)$$

where  $\approx$  accounts for the approximation of separating the length scales.

Finally, the matrix elements derived from Eq. (2.108) are expressed in Rydberg units ( $Ry$ ) and scaled by the magnetic length  $l_B$ . For MoS<sub>2</sub>, the effective Rydberg ( $Ry^*$ ) and Bohr radius ( $a_B$ ) are defined as:

$$Ry^* = \frac{Ry \cdot m^*}{\epsilon_r^2 m_0}, \quad a_B = \frac{\epsilon_r m_0 a_0}{m^*}, \quad (4.7)$$

where  $m^* = 0.34m_0$  for MoS<sub>2</sub>.

In the next step, we proceed to analyze the self-energies and self-energy-like electron-electron scatterings, which describe the electron scattering by the positive background. To this end, we define the exchange scattering terms within the basis of LLs configurations, denoted as  $|a/b\rangle = |\psi_{a/b}^{\text{VB/CB}}\rangle$ , where  $a/b = (n, m, s, v)$  is a collective index that includes the LL indices  $n, m$ , spin  $s$ ,

and valley  $v = K/K'$ . The exchange terms are expressed as:

$$\begin{aligned}\Sigma_{a_1, a_2}^{\text{VB}} &= \sum_{\lambda < \lambda_F} \langle \psi_{a_1}^{\text{VB}}, \psi_{\lambda}^{\text{VB}} | V_C | \psi_{a_2}^{\text{VB}}, \psi_{\lambda}^{\text{VB}} \rangle, \\ \Sigma_{b_1, b_2}^{\text{CB}} &= \sum_{\lambda < \lambda_F} \langle \psi_{b_1}^{\text{CB}}, \psi_{\lambda}^{\text{VB}} | V_C | \psi_{b_2}^{\text{CB}}, \psi_{\lambda}^{\text{VB}} \rangle.\end{aligned}\quad (4.8)$$

Substituting the wave functions into the above definitions with  $\lambda = (n', m', s', v')$ , we apply the angular momentum conservation rule outlined in Sec. 2.2.3, namely,

$$(m_1 + m_2) - (n_1 + n_2) = (m_3 + m_4) - (n_3 + n_4). \quad (4.9)$$

Using the properties of the matrix elements in Eq. (4.6), the exchange scattering terms simplify to:

$$\Sigma_K^{\text{CB/VB}} = \sum_{n', m'} \left( \begin{aligned} & \left( \alpha_{n_1}^{\text{CB/VB}} \right)^* \alpha_{n_2}^{\text{CB/VB}} |\alpha_{n'}^{\text{VB}}|^2 \langle n_1 - 1, m_1; n' - 1, m' | V_C | n_2 - 1, m_2; n' - 1, m' \rangle \\ & + \left( \beta_{n_1}^{\text{CB/VB}} \right)^* \beta_{n_2}^{\text{CB/VB}} |\beta_{n'}^{\text{VB}}|^2 \langle n_1, m_1; n', m' | V_C | n_2, m_2; n', m' \rangle \\ & + \left( \alpha_{n_1}^{\text{CB/VB}} \right)^* \beta_{n_2}^{\text{CB/VB}} \alpha_{n'}^{\text{VB}} (\beta_{n'}^{\text{VB}})^* \langle n_1 - 1, m_1; n', m' | V_C | n_2, m_2; n' - 1, m' \rangle \\ & + \left( \beta_{n_1}^{\text{CB/VB}} \right)^* \alpha_{n_2}^{\text{CB/VB}} \beta_{n'}^{\text{VB}} (\alpha_{n'}^{\text{VB}})^* \langle n_1, m_1; n' - 1, m' | V_C | n_2 - 1, m_2; n', m' \rangle \end{aligned} \right), \quad (4.10)$$

$$\Sigma_{K'}^{\text{CB/VB}} = \sum_{n', m'} \left( \begin{aligned} & \left( \alpha_{n_1}^{\text{CB/VB}} \right)^* \alpha_{n_2}^{\text{CB/VB}} |\alpha_{n'}^{\text{VB}}|^2 \langle n_1, m_1; n', m' | V_C | n_2, m_2; n', m' \rangle \\ & + \left( \beta_{n_1}^{\text{CB/VB}} \right)^* \beta_{n_2}^{\text{CB/VB}} |\beta_{n'}^{\text{VB}}|^2 \langle n_1 - 1, m_1; n' - 1, m' | V_C | n_2 - 1, m_2; n' - 1, m' \rangle \\ & + \left( \alpha_{n_1}^{\text{CB/VB}} \right)^* \beta_{n_2}^{\text{CB/VB}} \alpha_{n'}^{\text{VB}} (\beta_{n'}^{\text{VB}})^* \langle n_1, m_1; n' - 1, m' | V_C | n_2 - 1, m_2; n', m' \rangle \\ & + \left( \beta_{n_1}^{\text{CB/VB}} \right)^* \alpha_{n_2}^{\text{CB/VB}} \beta_{n'}^{\text{VB}} (\alpha_{n'}^{\text{VB}})^* \langle n_1 - 1, m_1; n', m' | V_C | n_2, m_2; n' - 1, m' \rangle \end{aligned} \right). \quad (4.11)$$

Interestingly, the wave function coefficients  $\alpha$  and  $\beta$  have distinct properties:  $\alpha$  is purely imaginary, while  $\beta$  is purely real. As a result, the electron-electron scatterings defined above are purely real. The self-energy term can be extracted from Eqs. (4.10) and (4.11) as:

$$\Sigma_K^{\text{CB/VB}} = \sum_{n', m'} \left( \begin{aligned} & |\alpha_n^{\text{CB/VB}}|^2 |\alpha_{n'}^{\text{VB}}|^2 \langle n - 1, m; n' - 1, m' | V_C | n - 1, m; n' - 1, m' \rangle \\ & + |\beta_n^{\text{CB/VB}}|^2 |\beta_{n'}^{\text{VB}}|^2 \langle n, m; n', m' | V_C | n, m; n', m' \rangle \\ & - 2\text{Re} \left[ \left( \alpha_n^{\text{CB/VB}} \right)^* \beta_n^{\text{CB/VB}} \alpha_{n'}^{\text{VB}} (\beta_{n'}^{\text{VB}})^* \langle n - 1, m; n', m' | V_C | n, m; n' - 1, m' \rangle \right] \end{aligned} \right), \quad (4.12)$$

$$\Sigma_{K'}^{\text{CB/VB}} = \sum_{n', m'} \left( \begin{aligned} & |\alpha_n^{\text{CB/VB}}|^2 |\alpha_{n'}^{\text{VB}}|^2 \langle n, m; n', m' | V_C | n, m; n', m' \rangle \\ & + |\beta_n^{\text{CB/VB}}|^2 |\beta_{n'}^{\text{VB}}|^2 \langle n - 1, m; n' - 1, m' | V_C | n - 1, m; n' - 1, m' \rangle \\ & - 2\text{Re} \left[ \left( \alpha_n^{\text{CB/VB}} \right)^* \beta_n^{\text{CB/VB}} \alpha_{n'}^{\text{VB}} (\beta_{n'}^{\text{VB}})^* \langle n, m; n' - 1, m' | V_C | n - 1, m; n', m' \rangle \right] \end{aligned} \right). \quad (4.13)$$

It is important to consider the potential effects arising from the finite size of the system under study. We examine the difference between the CB and VB self-energies, denoted as  $\delta\Sigma_{n, n'} = \Sigma_n^{\text{CB}} - \Sigma_{n'}^{\text{VB}}$ . We find that  $\delta\Sigma_{1,0}$  for the  $K$  valley behaves such that the value of  $\delta\Sigma$  remains constant for LL index  $m < 15$  and decreases for  $m > 15$ . This behavior reflects the finite-size effects due to the truncation of the basis. To mitigate these effects in the subsequent analysis, we assume  $m = 0$  for the self-energies.

Furthermore, we perform a convergence study of the self-energies as functions of both the LL indices  $m'$  and  $n'$  for an electron in the first available LL state ( $n = 0, m = 0$ ), using a magnetic field of  $B = 10$  T. The self-energy,  $\Sigma^{\text{CB}}(m')$ , is found to primarily receive contributions from orbitals that are close in momentum space to the one occupied by the electron (or hole), specifically those characterized by the same angular momentum  $M = m' - n'$ . For an electron in the state with

$n = 0$  and  $m = 0$ , the dominant contribution to the self-energy comes from the orbital with  $M = 0$ , leading to an increase in the self-energy near  $m' = n'$ . Additionally, we study the self-energy as a function of  $n'$  for a fixed maximum value of  $m'$ . Since the exchange interaction is short-range, the convergence with respect to  $m'$  can be analyzed by considering a neighborhood around a given  $n'$ , rather than summing over all  $m'$  from 0 to  $m'_{\max}$ . This approach highlights the slow convergence of the self-energies with respect to  $n'$  when a large range of  $m'$  is included—an effect that parallels the slow convergence of the CME with increasing  $n'$ .

## 4.4 Optical Emission as a Function of Finite Charge Density

We have shown that the electronic properties and optical selection rules of TMDC monolayers in external magnetic fields can be accurately captured within the mDF framework. This approach also incorporates Coulomb interactions and self-energy corrections for electrons and holes, enabling a detailed treatment of many-body effects. Building on these results, this section investigates the behavior of interacting electrons and excitations in a MoS<sub>2</sub> monolayer under strong magnetic fields and finite charge density.

In this regime, magnetoexcitons—bound states of electrons and holes within LLs—play an important role in modifying the optical response. Finite carrier density further modifies excitonic interactions, providing a means to tune optical properties. The emission spectrum reveals these effects by capturing radiative transitions influenced by many-body interactions. Our goal is to elucidate how these competing interactions modify the excitonic spectrum and, consequently, the optical emission characteristics of the material. Understanding this interplay deepens insight into many-body phenomena in 2D materials.

Here, we analyze the combined influence of magnetic quantization, finite doping, and Coulomb interactions on the formation and properties of magnetoexcitons in a MoS<sub>2</sub> monolayer. Following the methodology outlined in Sec. 2.4.4, we compute emission spectra using Fermi's golden rule, as described in Eq. (2.220).

### 4.4.1 The Effect of the External Magnetic Field on the Spectrum of a Neutral Exciton

We begin by examining the optical properties of a single electron-hole excitation—a neutral exciton ( $X^0$ )—in a MoS<sub>2</sub> monolayer in an external magnetic field [463]. The field induces Landau quantization in both the CBs and VBs, altering the excitonic spectrum relative to the zero-field case [175, 223] (see Appendix A). The excitonic states are obtained by solving the BSE, following the methodology outlined in Sec. 2.3.1. We restrict the analysis to transitions between the top VB and the bottom CB only—the simplest case allowing to easily describe the effects of Coulomb interactions under magnetic quantization. The corresponding spin configurations of the resulting  $X^0$  states are illustrated in Fig. 4.6, where panel (a) shows spin-bright excitations and panels (b) and (c) correspond to spin-dark states.

In the first step, we analyze the effect of intervalley coupling on spin-bright excitonic configurations. We obtain the excitonic spectrum by solving the BSE, as given in Eq. (2.166). Based on the convergence of results and computational cost, we select  $m_{\max} = 30$  as the degeneracy cutoff for subsequent calculations. Initially, we neglect intervalley coupling, which in principle should be included for configurations sharing the same spin projection  $s_z$ . We then introduce coupling

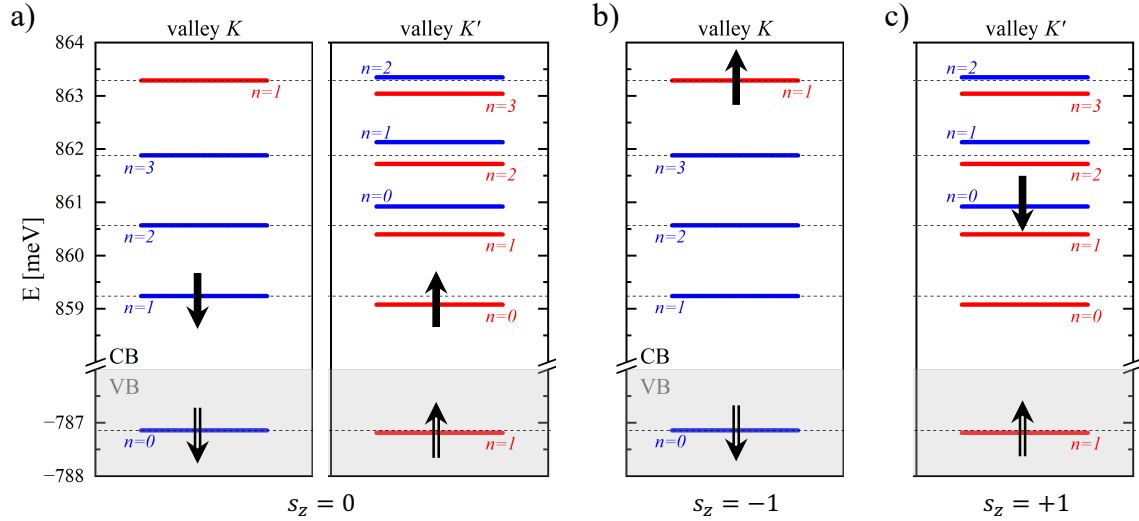


**Figure 4.6:** Schematic representation of the available (a) spin-bright and (b,c) spin-dark configurations of a neutral exciton for a MoS<sub>2</sub> monolayer at an external magnetic field. Different compound type of the arrows denotes the difference between electrons and holes, respectively. Furthermore, the index  $n$  is denoted for each LL, and the picture is presented with no degeneracy in  $m$ .

between the valleys via exchange interaction. The valley-resolved  $X^0$  spectrum, shown in Fig. 4.7, compares the results with (filled circles) and without (open circles) intervalley coupling. The negligible difference between the two spectra indicates that intervalley interactions are weak under the considered conditions.

The same figure presents also the spin-dark exciton spectrum (triangles), which is important for identifying the nature of the excitonic GS. A common expectation, supported by both theory and experiment [473], is that the lowest-energy excitonic state in MoS<sub>2</sub> should be spin triplet (spin-dark). In contrast, our results reveal that at  $B = 10$  T, the GS is spin-bright.

One might suspect this reversal is a magnetic-field effect. However, our calculations suggest that as  $B$  decreases, the bright-dark gap increases, reinforcing the bright state as the GS even at zero field. This indicates that the discrepancy originates in the model itself. A likely source is the treatment of electron-hole exchange interactions, which are challenging to capture accurately in effective mass or  $\vec{k} \cdot \vec{p}$  models. Similar limitations have been documented in studies of InAs/GaAs QDs [478, 479], where effective models failed to reproduce the correct dark-bright ordering. In our case, the mDF model includes only partial electron-hole exchange via the spinor structure of single-particle states. While this introduces a nonzero exchange contribution, it omits essential terms arising from the overlap of conduction and valence Bloch functions. As such, the electron-hole exchange interaction is likely underestimated, which may account for the incorrect GS ordering. Addressing this limitation is important for the reliability of future predictions. Improved modeling of electron-hole exchange—potentially through hybrid methods or empirical corrections—will be the object of future studies for a complete understanding of excitonic behavior in TMDCs under strong magnetic fields.

Next, we focus on spin-bright configurations and examine the impact of Coulomb interactions on the excitonic spectrum. The resulting evolution of the  $X^0$  spectrum as successive contributions from different types of Coulomb interactions are introduced is presented in Fig. 4.7. Each stage of approximation—ranging from single-particle states to the inclusion of self-energy corrections,

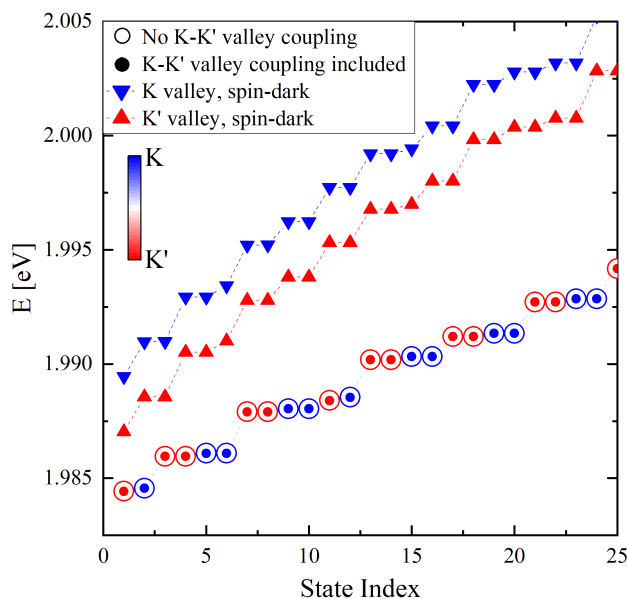


**Figure 4.7:**  $X^0$  spectrum in the basis of spin-bright and spin-dark configurations, as introduced in Fig. 4.6. Open and filled circles correspond to spin-bright excitons without and with inter-valley coupling, respectively, showing that the coupling has a negligible effect. Spin-dark excitons are represented by triangles. The data reveal that the lowest-energy state at  $B = 10$  T is spin-bright, in contrast to common expectations, highlighting a likely underestimation of electron-hole exchange interactions within the present model.

vertex corrections, and correlation effects—reveals the progressive restructuring of the excitonic structure due to many-body interactions. As a reference, the non-interacting single-particle transitions are shown in panel (a). These correspond to energy differences between the top valence and bottom conduction LL states, which are degenerate within each valley in the absence of interactions. Furthermore, the single-particle energy difference between electron-hole configurations from opposite valleys is negligibly small, so these states are shown in black. Including self-energy corrections, presented in panel (b), leads to a pronounced blue shift, reflecting the renormalization of quasiparticle energies due to interactions with the fully filled VB. This step also lifts the degeneracy of the LLs, revealing a clearer energy separation between  $K$  and  $K'$  valley configurations. In panel (c), vertex corrections are included to account for the attractive electron-hole interaction as well as the relatively weak repulsive exchange interaction. While the exchange slightly shifts energies upward, the dominant effect is a red shift of the spectrum. This stage also introduces further splitting and reorganization of the excitonic states. Finally, in panel (d), the full BSE is solved, incorporating all Coulomb scattering processes between different configurations. The resulting spectrum reflects the fully interacting spin-bright  $X^0$  response, with valley-specific character now made visible through color coding, in an applied magnetic field.

The detailed analysis of the excitonic wave functions allows us to determine that in all cases, the excitonic GS is predominantly formed by a configuration where the hole occupies the  $(n = 1, m = 0)$  LL and the electron resides in  $(n = 0, m = 0)$  state. This corresponds to an exciton localized near the center of the system.

Furthermore, we evaluate the exciton binding energy, which quantifies the energy required to separate the electron and hole comprising the exciton. It is defined as the difference between the

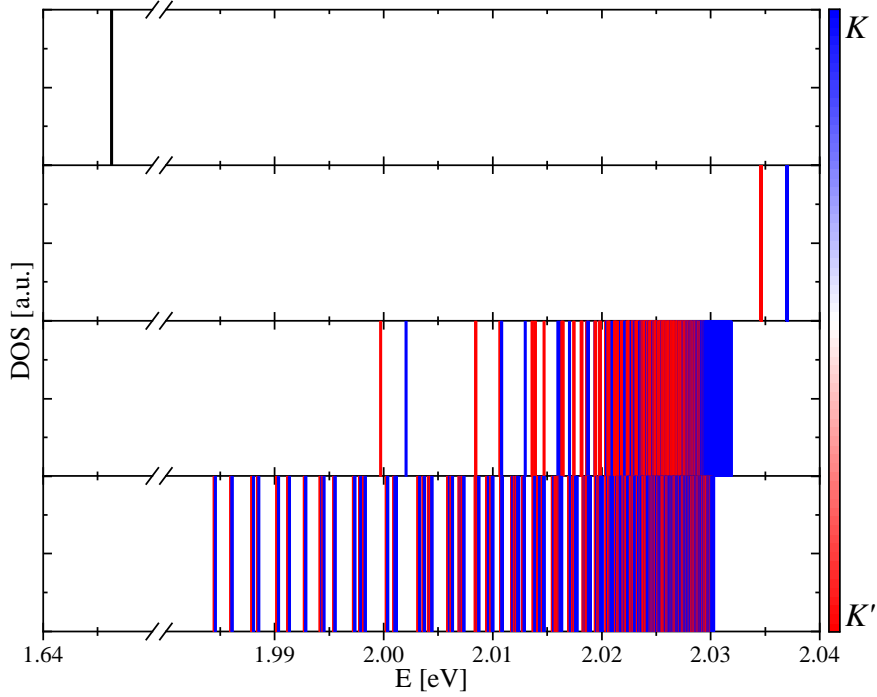


**Figure 4.8:** Evolution of the neutral exciton  $X^0$  spectrum in monolayer MoS<sub>2</sub> in a magnetic field, showing the sequential inclusion of Coulomb interactions within the mDF model. Only spin-bright states are shown; color denotes valley. Panels (a–d) display excitonic states as vertical lines at their energies. (a) Single-particle spectrum. (b) Inclusion of self-energy corrections. (c) Addition of vertex corrections. (d) Full interacting spectrum including correlation effects.

total energy of the non-interacting electron-hole pair (including self-energy corrections) and the GS energy of the bound exciton. This is expressed as:

$$E_b^{X^0} = [(E_e + \Sigma_e) - (E_h + \Sigma_h)] - E_0^{X^0}, \quad (4.14)$$

where  $E_e$  and  $E_h$  are the single-particle energies of the electron and hole,  $\Sigma_e$  and  $\Sigma_h$  are their respective self-energies, and  $E_0^{X^0}$  is the GS energy of the exciton. Using this definition, we obtain a binding energy of  $E_b^{X^0} = 47$  meV. This value reflects the stability of the exciton in the presence of both Coulomb interactions and an external magnetic field.

With this understanding of the excitonic spectra and binding energy, we next turn our attention to the optical emission spectrum, which provides insights into the material's optical properties. The emission spectrum reflects transitions between various energy states, revealing how the system recombines and emits light. This framework serves as the basis for understanding exciton recombination and the influence of many-body interactions on light emission in TMDC monolayers in a magnetic field.

Building on the methodology outlined in Sec. 2.4.4, we determine the emission spectra by applying Fermi's golden rule, as formulated in Eq. (2.220). To make it applicable to the current problem, we express it in the following form:

$$A(\hbar\omega) = \sum_{i,f} W_i \left| \langle \psi^{(f)} | \hat{P} | \psi^{(i)} \rangle \right|^2 \delta(E_f - E_i - \hbar\omega), \quad (4.15)$$

where  $A(\hbar\omega)$  denotes the emission intensity at energy  $\hbar\omega$ , and  $W_i$  is the thermal occupation probability of the initial state  $\psi^{(i)}$ . The interband polarization operator  $\hat{P} = \sum_{j,\alpha} D_{j,\alpha} \hat{c}_\alpha^\dagger \hat{c}_j$  describes

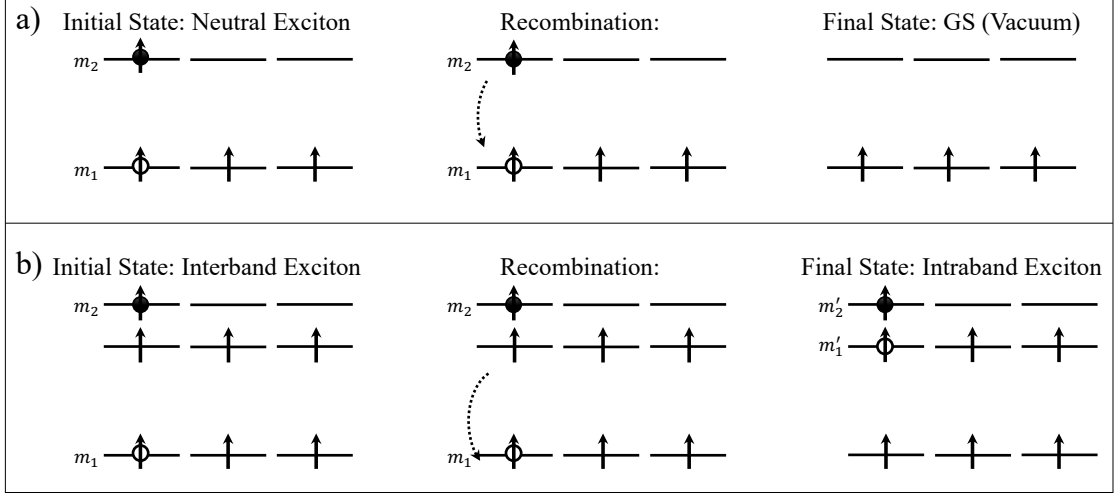


**Figure 4.9:** Schematic simplified representation of the recombination process for (a) a neutral exciton (first row) and (b) an exciton interacting with  $\nu = 1$  (second row).

the removal of an electron in a single-particle state  $j$  and its replacement onto a single-particle state  $\alpha$ , resulting in the creation of a photon with energy  $\omega$ . The transition DME  $D_{j,\alpha}$  weights this process and determines the strength of the optical transition. The occupation probability  $W_i$  for the initial state  $\psi^{(i)}$  at temperature  $T$  is given by the Boltzmann distribution,  $W_i = e^{\frac{-E_i}{k_B T}} / \sum_n e^{\frac{-E_n}{k_B T}}$  where  $E_i$  is the energy of the initial state,  $k_B$  is the Boltzmann constant, and the denominator normalizes the distribution over all states. This formalism incorporates the effects of temperature on the population distribution, with thermal occupation becoming sharply peaked around the GS at low temperatures and a broader distribution at higher temperatures.

The recombination process for the  $X^0$  is illustrated in a schematic form in Fig. 4.9(a), where the initial state is defined as  $|\psi^{(i)}\rangle = \sum_{m_1, m_2} A_{m_1, m_2}^{(i)} \hat{c}_{m_2}^\dagger \hat{c}_{m_1} |GS\rangle$ , corresponding to top left panel of the figure. The recombination connects only the electron and hole characterized by the same LL index  $m$ , as detailed in Sec. 2.4.1, and denoted in the middle panel. Consequently, the dipole moment can be written as  $D_{m, m'} = (\alpha_n^{CB})^* \beta_n^{VB} \delta_{m, m'}$ . The electron recombines, leaving the final state as the GS of the system,  $|\psi^{(f)}\rangle = |GS\rangle$ , shown in the top left panel of the figure. With these initial and final states, the formula for the emission spectrum takes the form:

$$A(\hbar\omega) = \sum_i W_i \left| (\alpha_n^{CB})^* \beta_n^{VB} \sum_{m_1} A_{m_1, m_1}^{(i)} \right|^2 \delta(E_i - \hbar\omega), \quad (4.16)$$

accounting for the fact that the GS energy is taken as a reference.

The emission spectrum from the exciton states is presented in Fig. 4.13. For a neutral exciton  $X^0$ , the emission occurs from states characterized by  $m_h - m_e = 0$ . At low temperatures ( $T = 1$  mK), we observe a single sharp emission line corresponding to the lowest-energy excitonic state. As the effective temperature increases to  $T = 5$  K, a second emission line, originating from the valley  $K$ , appears due to the thermal occupation of an almost-degenerate state. This temperature-induced effect highlights the role of valley polarization in magneto-optical responses.

#### 4.4.2 Magnetoexcitons in the Presence of $\nu = 1$ Charge Density

We now consider the case of an exciton  $X^0$  interacting with a fully filled  $n = 0$  CB LL, corresponding to a filling factor of  $\nu = 1$ . This interaction significantly alters the excitonic spectrum

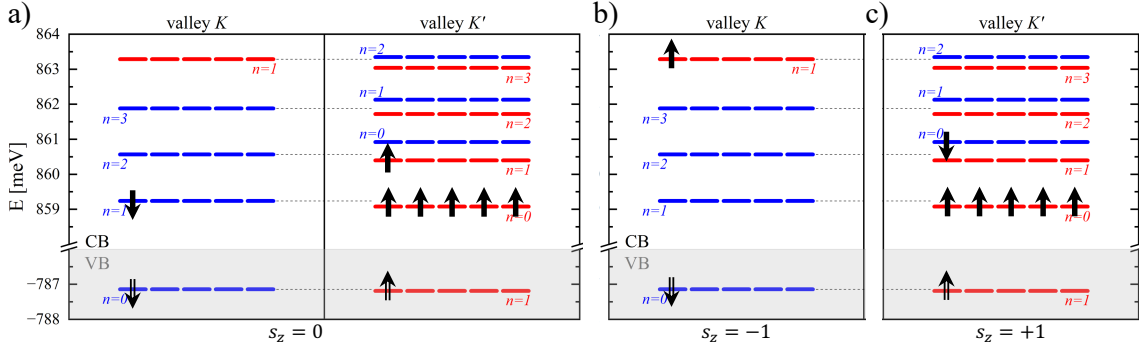


**Figure 4.10:** Schematic representation of the (a) spin-bright and (b,c) spin-dark configurations of a neutral exciton interacting with  $\nu = 1$ . Single arrows denote electrons, while double arrows correspond to holes, respectively. Furthermore, the index  $n$  is denoted for each LL, and the picture is presented for  $m = 0, \dots, 4$ .

due to the additional many-body effects resulting from the presence of CB electrons. To capture this, we build upon our prior studies of neutral excitons, extending the formalism to include the effects of a filled CB.

Fig. 4.10 summarizes the spin-bright and spin-dark excitonic configurations accessible when the  $n = 0$  CB is fully occupied in the  $K'$  valley, which hosts the energetically lowest conduction states. Panel (a) shows the spin-bright configuration, in which the photoexcited electron has the same spin orientation as the VB hole. This configuration enables optically allowed transitions and, in the  $K$  valley, reduces to the neutral exciton case described earlier, since the filled CB belongs to valley  $K'$ . In contrast, panels (b) and (c) depict spin-dark configurations, where the electron and hole have opposite spins. These lead to spin-forbidden transitions. We collectively refer to both  $K$  and  $K'$  valley excitons as interband excitons ( $X^{\text{inter}}$ ) and—guided by the neutral exciton analysis—we neglect the spin-dark configurations in the following discussion.

The recombination dynamics of the more complex case of the  $K'$  valley exciton in the presence of a fully occupied  $n = 0$  CB LL are schematically illustrated in Fig. 4.9(b). In this case, the system initially hosts a single electron-hole excitation on top of a completely filled  $n = 0$  CB LL, as depicted in the left panel. The recombination process is constrained by optical selection rules, which permit transitions only between LLs whose orbital quantum numbers differ by  $\Delta n = \pm 1$ , as shown in the middle panel. As the electron recombines with the hole in the VB, it leaves behind a vacancy—a hole—in the previously filled  $n = 0$  CB LL. The resulting state, shown in the right panel, is a neutral intraband excitation within the CB, formed by the remaining  $n = 0$  electron and the hole left behind. This excitation is referred to as an intraband exciton, or  $X^{\text{intra}}$ . This scenario contrasts sharply with the pristine neutral exciton case, where the emission process leads directly back to the GS. Here, both the initial and final states belong to a spectrum of many-body excitations. As a result, the emission involves a broader set of accessible transitions, significantly modifying the optical response. This highlights the essential role of finite carrier density in shaping the emission characteristics, as the interplay between excitonic recombination and the Fermi sea of electrons introduces new final states and redistributes spectral weight.

We approximate the many-body GS as a single Slater determinant and construct the  $X^{\text{inter}}$  states as linear combinations of two-body configurations. Specifically, we consider two arbitrary excitonic states, which may differ in their LL indices, spin states, or valley indices. These states

are written as:

$$|X_1^{\text{inter}}\rangle = \hat{c}_{f_1}^\dagger \hat{c}_{i_1} |GS\rangle, \quad |X_2^{\text{inter}}\rangle = \hat{c}_{f_2}^\dagger \hat{c}_{i_2} |GS\rangle, \quad (4.17)$$

where  $i_1$  and  $f_1$  correspond to the initial and final configurations of the first exciton, respectively, and  $i_2$  and  $f_2$  refer to the configurations of the second exciton. This formalism enables the inclusion of interactions between different excitonic configurations, which are evaluated using the BSE to determine the matrix elements of the many-body Hamiltonian. The BSE, which governs the scattering processes between excitonic states, is given by:

$$\begin{aligned} & \langle X_1^{\text{inter}} | \hat{H}_{MB} | X_2^{\text{inter}} \rangle - \langle GS | \hat{H}_{MB} | GS \rangle = \\ & = \delta_{i_1, i_2} \delta_{f_1, f_2} (\varepsilon_{f_1} - \varepsilon_{i_1}) + \left[ -\delta_{s_1, s_2} \delta_{v_1, v_2} \langle i_1, f_2 | V_C | i_2, f_1 \rangle \right] + \\ & + \left[ \delta_{f_1, f_2} \sum_m^{N_{\text{occ}}^{VB}} \langle m^{VB}, i_1 | V_C | m^{VB}, i_2 \rangle + \delta_{f_1, f_2} \sum_m^{N_{\text{occ}}^{CB}} \langle m^{CB}, i_1 | V_C | m^{CB}, i_2 \rangle \right] \\ & - \left[ -\delta_{i_1, i_2} \sum_m^{N_{\text{occ}}^{VB}} \langle m^{VB}, f_2 | V_C | m^{VB}, f_1 \rangle - \delta_{i_1, i_2} \sum_m^{N_{\text{occ}}^{CB}} \langle m^{CB}, f_2 | V_C | m^{CB}, f_1 \rangle \right], \end{aligned} \quad (4.18)$$

where  $\varepsilon_p$  denotes the single-particle energy associated with state  $p$ , and  $V_C$  represents the Coulomb interaction matrix elements. The sums over  $N_{\text{occ}}^{VB}$  and  $N_{\text{occ}}^{CB}$  account for the occupied VB and CB states, respectively. The modified BSE for the  $K'$  valley  $X^{\text{inter}}$  closely resembles the neutral exciton BSE, with the additional exchange self-energy-like terms arising from the interactions with the filled  $n = 0$  CB. These terms describe how the CB electrons influence the excitonic states, capturing the subtle interplay between the neutral exciton and the CB electrons.

Fig. 4.11 shows the resulting spectrum of  $X^{\text{inter}}$  in different stages of including the Coulomb interactions. As a reference, panel (a) presents the non-interacting single-particle transitions, which correspond to the sum of the energies of all particles in the top valence and bottom conduction LLs. Since the occupied  $n = 0$  CB is located in the  $K'$  valley, the energy of the intervalley  $K'$  exciton is initially higher than that of the interband exciton in the  $K$  valley. In panel (b), quasiparticle self-energy corrections arising from interactions with the filled VB are introduced, which reduce the energy splitting between the  $K$  and  $K'$  valley excitons. This step also results in a significant blue shift of the entire spectrum and lifts the degeneracy of the LLs, reflecting the renormalization of quasiparticle energies due to electron–electron and hole–hole interactions. In panel (c), additional self-energy-like effects due to the filled CB are included. These account for the presence of the  $\nu = 1$  electron population and lead to further energy shifts and a reordering of excitonic states. Notably, the energy of the  $K'$  exciton decreases significantly, while the  $K$  exciton remains largely unaffected, as it does not interact with the filled CB in the  $K'$  valley. This results in an inversion of the excitonic level ordering, with the  $K'$  exciton now becoming the lower-energy state. In the next step, shown in panel (d), vertex corrections are included to account for the attractive direct Coulomb interaction between the electron and hole, as well as the repulsive exchange interaction. These effects lead to a substantial red shift and introduce additional splittings and reorganization of the spectrum. However, the excitonic GS continues to be formed predominantly from  $K'$  valley configurations. Finally, in panel (e), the full BSE is solved, incorporating all Coulomb scattering processes and correlations. This results in a complex and richly structured spectrum that reflects the many-body character of the system.

Beyond interband excitons, Fig. 4.12 presents the spectrum of  $X^{\text{intra}}$  states, which corresponds to the final emission state. The spectrum reveals a remarkably flat energy distribution, with the first 500 states shown in panel (a) and a zoomed-in view of the lowest 20 states in panel (b). This near-degeneracy of the lowest-energy  $X^{\text{intra}}$  states has significant implications for the emission

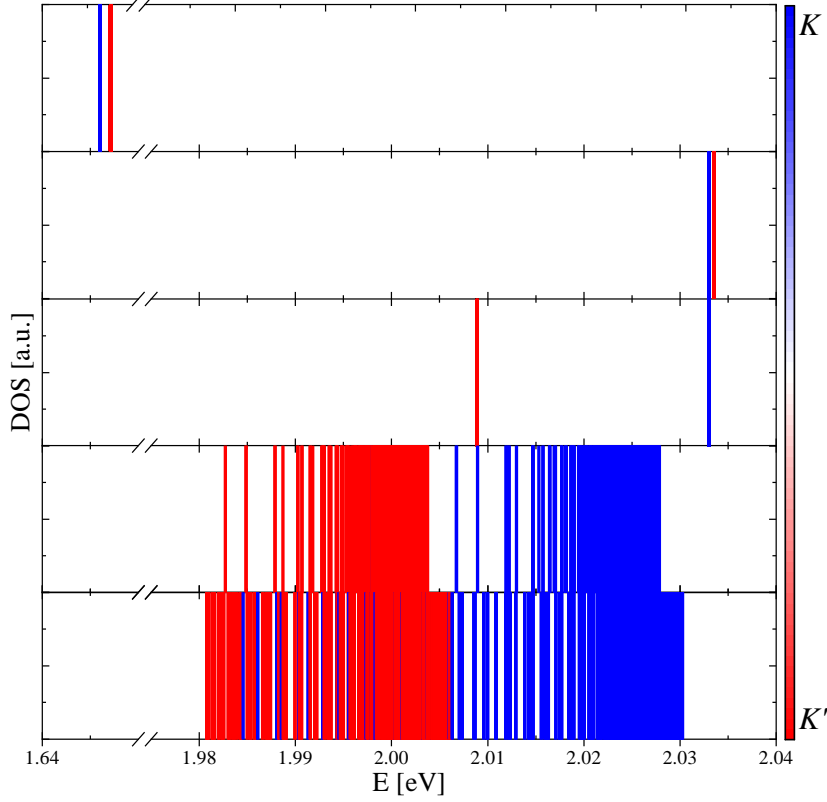


**Figure 4.11:** Evolution of the  $X^{\text{inter}}$  spectrum in the presence of a fully filled  $n = 0$  CB ( $\nu = 1$ ), showing the progressive inclusion of Coulomb interactions. Color indicates valley. Panels (a–e) show excitonic states as vertical lines. (a) Single-particle spectrum. (b) VB self-energy corrections. (c) CB self-energy-like effects from the filled  $n = 0$  LL. (d) Inclusion of vertex corrections. (e) Full interacting spectrum with the correlations effects.

process, as it leads to a broad recombination spectrum even at low temperatures. The subtle interplay between the initial and final states of emission—governed by the spectral structure of  $X^{\text{intra}}$ —further underscores the importance of many-body interactions in modifying the optical properties of the system.

In the next step, we present the emission formula for the exciton interacting with the filled  $n = 0$  CB. The initial  $X^{\text{inter}}$  configuration can be written as  $|1\text{VB}, m_1; 1\text{CB}, m_2\rangle = \hat{c}_{1\text{CB}, m_2}^\dagger \hat{c}_{1\text{VB}, m_1} |GS\rangle$ , where we introduced a shortened notation  $|1\text{VB}, m\rangle \equiv |n = 1, m, \text{VB}\rangle$  and analogously for CB. In this case, the electron recombines from the fully filled  $n = 0$  CB, leaving the intraband exciton in the CB (right panel of Fig. 4.9(b)). This state can be described as  $|0\text{CB}, m'_1; 1\text{CB}, m'_2\rangle = \hat{c}_{1\text{CB}, m'_2}^\dagger \hat{c}_{0\text{CB}, m'_1} |GS\rangle$ . We now calculate the matrix element  $\langle \psi^{(f)} | \hat{P} | \psi^{(i)} \rangle$ :

$$\begin{aligned} \langle 1\text{CB}, m'_2; 0\text{CB}, m'_1 | \hat{P} | 1\text{VB}, m_1; 1\text{CB}, m_2 \rangle = \\ \langle GS | \hat{c}_{1\text{CB}, m'_2}^\dagger \hat{c}_{0\text{CB}, m'_1}^\dagger \hat{c}_{1\text{VB}, m}^\dagger \hat{c}_{0\text{CB}, m} \hat{c}_{1\text{CB}, m_2}^\dagger \hat{c}_{1\text{VB}, m_1} | GS \rangle = \delta_{m, m_1} \delta_{m, m'_1} \delta_{m_2, m'_2}, \end{aligned} \quad (4.19)$$

which finally gives us the formula for emission as:

$$A(\hbar\omega) = \sum_{i, f} W_i (\alpha_n^{CB})^* \beta_n^{VB} \left| \sum_{m_1, m_2} \left( B_{m_1, m_2}^{(f)} \right)^* A_{m_1, m_2}^{(i)} \right|^2 \delta(E_i - E_f - \hbar\omega). \quad (4.20)$$

The resulting emission spectrum is presented in Fig. 4.13. When the exciton interacts with

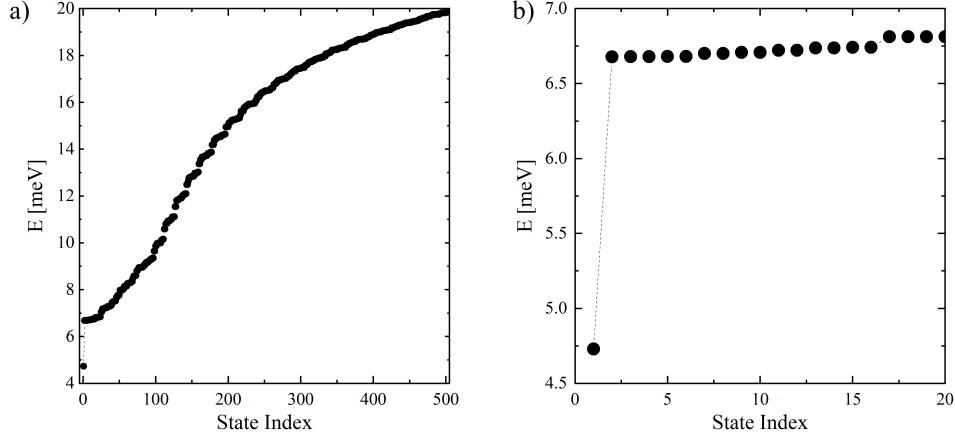


**Figure 4.12:** Spectrum of the intraband exciton  $X^{\text{intra}}$ , representing the final state of emission for  $X^{\text{inter}}$  recombination. (a) Full spectrum showing the first 500 states. (b) Zoom-in on the lowest 20 states, highlighting the separated GS and the nearly degenerate excited states.

a fully filled  $n = 0$  CB (corresponding to  $\nu = 1$ ), the emission spectrum undergoes significant broadening compared to the case of a neutral exciton  $X^0$ , even at very low temperatures. This broadening arises from two main factors. First, the initial state of the emission process consists of a shell of nearly degenerate low-energy states, as illustrated in Fig. 4.11. Second, the final state of emission is not the vacuum (as in the neutral exciton case) but an intraband exciton state, which has its own energy spectrum, presented in Fig. 4.12(a). Importantly, this spectrum is remarkably flat, with the lowest 20 states spread across only about 2 meV, as shown in Fig. 4.12(b). This intrinsic structure, along with many-body interactions, results in a broadened emission profile. As temperature increases, thermal population of excited initial and final states becomes more likely, further widening the emission through increased spectral overlap and enhanced recombination channels. The predicted spectrum stays in agreement with the experimental observations [473–475].

#### 4.4.3 Negatively Charged $K'$ -Valley Magnetoexcitons

Negatively charged excitons  $X^-$ —trions—are known to play an important role in the optical response of gated TMDC monolayers, particularly when the material is placed in strong magnetic fields, where Landau quantization strongly influences the few-body states [474]. While the full characterization of trions in the LL regime is a complex problem involving the two non-equivalent valleys and different spin configurations, we take a first step here by analyzing a simplified single-valley and single-spin model. Although this represents only an approximation to the full physics, it allows us to build qualitative intuition for the internal structure and optical signatures of trions in external magnetic field. Further generalizations will be required to capture the full richness of valley and spin configurations.

We model the negatively charged trion in the  $K'$  valley by constructing the  $X^-$  states as linear combinations of three-particle configurations, based on a Slater determinant GS,  $|GS\rangle = \prod_p c_p^\dagger |0\rangle$ . Each configuration includes one electron-hole pair and an additional CB electron:

$$|\alpha, \beta, i\rangle = c_\alpha^\dagger c_\beta^\dagger c_i |GS\rangle, \quad (4.21)$$

where Greek indices label CB electron states and Latin indices label holes in the VB. The many-

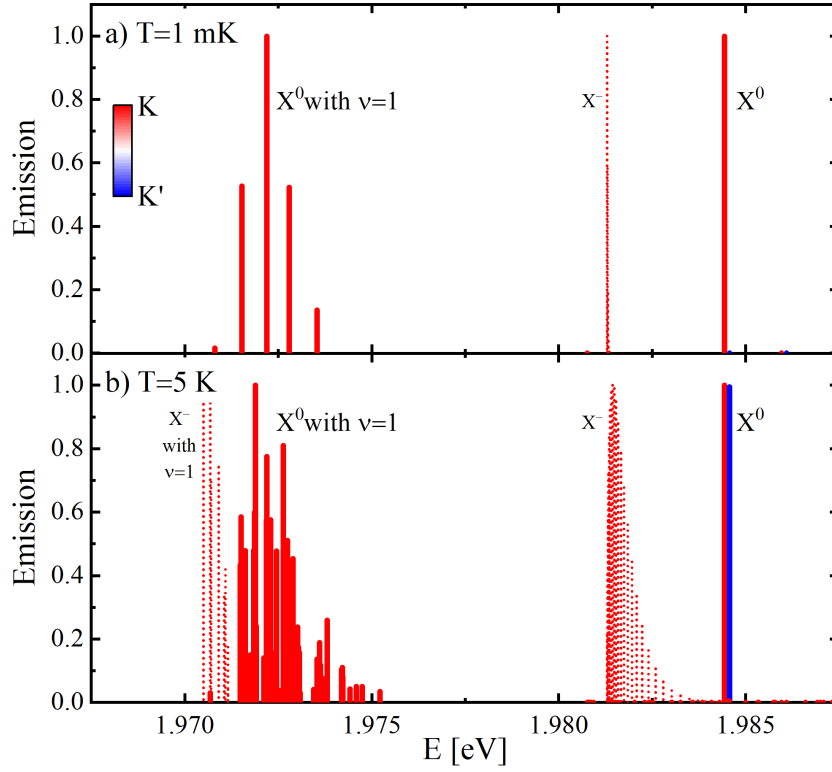


**Figure 4.13:** Optical response of a neutral exciton  $X^0$  and an exciton  $X^0$  interacting with  $\nu = 1$  for a MoS<sub>2</sub> monolayer in magnetic field  $B = 10$  T at the temperature (a)  $T = 1$  mK and (b)  $T = 5$  K. Additionally, the dotted lines correspond to the emission from the single-valley trion and trion interacting with  $\nu = 1$  states.

body trion states are then obtained by solving the corresponding BSE, given in Eq. (2.169) (see Sec. 2.3.2).

Fig. 4.14 presents the energy spectrum of a single-valley triplet trion. Panel (a) shows the  $X^-$  energies as a function of state index, revealing a step-like pattern in the spectrum. Panel (b) presents the generalized angular momentum  $m_\alpha + m_\beta - m_i$  of each state, providing a possible explanation of the step-like character of the trion spectrum. The piecewise-linear progression of this quantity, with periodic resets, mirrors the locations of energy steps, suggesting a reorganization of orbital momentum configurations in magnetic confinement. Vertical dashed lines in both panels connect corresponding step-features, highlighting how angular momentum quantization manifests in the energy landscape of trion states.

To evaluate the optical response, we compute the emission spectrum associated with trion recombination. The initial state is a bound trion of the form:

$$|\psi^{(i)}\rangle = \sum_{m_1, m_2, m_3} A_{m_3, m_2, m_1}^{(i)} \hat{c}_{m_3}^\dagger \hat{c}_{m_2}^\dagger \hat{c}_{m_1} |GS\rangle, \quad (4.22)$$

and the final state consists of a single electron left in the CB:

$$|\psi^{(f)}\rangle = \sum_{m'_2} B_{m'_2}^{(f)} \hat{c}_{m'_2}^\dagger |GS\rangle. \quad (4.23)$$

The number of potential final states is equal to the LL CB degeneracy. Each of these final states has the coefficient  $B_{m'_2}^{(f)} = 0$ , except for the orbital  $m'_2$  occupied by the single electron, where

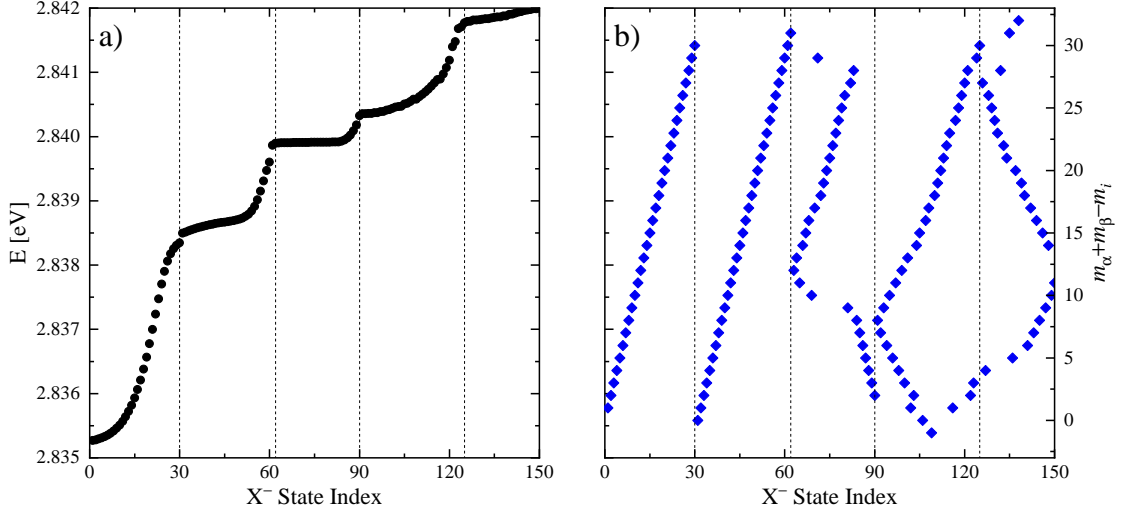


**Figure 4.14:** Trion spectrum in monolayer MoS<sub>2</sub> in a magnetic field within the  $K'$  valley. (a) Trion energies as a function of state index, revealing a step-like structure. (b) Generalized angular momentum  $m_\alpha + m_\beta - m_i$  of the same states, showing how momentum reorganization correlates with the spectral steps. Vertical dashed lines connect corresponding features in both panels.

$B_{m'_2}^{(f)} = 1$ . With the initial and final states defined as above, the matrix element  $\langle \psi^{(f)} | \hat{P}^- | \psi^{(i)} \rangle$  can be calculated as follows:

$$\begin{aligned}
 \langle \psi^{(f)} | \hat{P}^- | \psi^{(i)} \rangle &= \sum_{m_1, m_2, m_3} A_{m_3, m_2, m_1}^{(i)} \sum_{m'_2} B_{m'_2}^{(f)} \sum_{m, m'} D_{m, m'} \langle GS | c_{m'_2} c_m^\dagger c_{m'} c_{m_3}^\dagger c_{m_2}^\dagger c_{m_1} | GS \rangle \\
 &= (\alpha_{n=0}^{CB})^* \beta_{n'=1}^{VB} \sum_{m_1, m_2, m_3} A_{m_3, m_2, m_1}^{(i)} \sum_{m'_2} B_{m'_2}^{(f)} \sum_{m, m'} \delta_{m, m'} \delta_{m, m_1} \langle GS | c_{m'_2} c_{m'} c_{m_3}^\dagger c_{m_2}^\dagger | GS \rangle \\
 &= (\alpha_{n=0}^{CB})^* \beta_{n'=1}^{VB} \sum_{m_1, m_2, m_3} A_{m_3, m_2, m_1}^{(i)} \sum_{m'_2} B_{m'_2}^{(f)} \langle GS | c_{m'_2} c_{m_1} c_{m_3}^\dagger c_{m_2}^\dagger | GS \rangle \\
 &= (\alpha_{n=0}^{CB})^* \beta_{n'=1}^{VB} \sum_{m_1, m_2, m_3} A_{m_3, m_2, m_1}^{(i)} \sum_{m'_2} \underbrace{B_{m'_2}^{(f)}}_{=1} (\delta_{m_1, m_3} \delta_{m_2, m'_2} - \delta_{m_1, m_2} \delta_{m_3, m'_2})
 \end{aligned}$$

and thus the emission intensity is given by:

$$A(\hbar\omega) = \sum_{i, f} W_i \left| (\alpha_{n=0}^{CB})^* \beta_{n'=1}^{VB} \left( \sum_{m_1, m_2} A_{m_1, m_2, m_1}^{(i)} - \sum_{m_1, m_3} A_{m_3, m_1, m_1}^{(i)} \right) \right|^2 \delta(E_i - E_f - \hbar\omega), \quad (4.24)$$

where  $W_i$  is the thermal occupation factor of the initial trion state. As expected, the resulting emission signal appears energetically below the main exciton peak, consistent with the trion's binding energy. This can be observed directly in the full emission spectrum, presented in Fig. 4.13 with the dotted lines. At  $T = 0$  K, only the lowest-energy trion state contributes, resulting in a sharp, isolated line. However, at elevated temperature (e.g.,  $T = 5$  K), thermal occupation of higher trion states leads to a noticeable broadening of the low-energy side of the emission line, a hallmark of many-body bound states.

We also explore the formation of a negatively charged magnetoexciton,  $X^-$ , interacting with a fully filled  $n = 0$  CB ( $\nu = 1$ ), by adding an additional electron to the interband magnetoexciton discussed previously. The resulting emission spectrum, shown as dotted lines in Fig. 4.13, reveals peaks appearing just below those of the neutral  $X^0$  interacting with  $\nu = 1$ , consistent with the expected redshift due to increased electron density.

## 4.5 Conclusions

In this chapter, we explored the optical response of monolayer MoS<sub>2</sub> in strong magnetic fields as a function of additional carrier density  $n$ , ranging from the neutral exciton at  $n = 0$ , through the trion at low density ( $n = 1$ ), to finite carrier density at filling factor  $\nu = 1$ . Using the mDF model and incorporating many-body Coulomb interactions, we traced the evolution of excitonic spectra and analyzed how interaction and correlation effects influence both the excitonic structure at finite charge densities and the resulting emission.

Our results show that even the neutral exciton spectrum is strongly modified by magnetic confinement and many-body effects, including self-energy renormalization, vertex corrections, and the effects of correlations. When the bottom CB is filled with carriers, the emission spectrum broadens and redshifts significantly, reflecting the complex structure of both the initial interband and final intraband excitons. We also examined the simplified case of a single-valley negatively charged magnetoexciton,  $X^-$ , which displays a step-like energy structure tied to angular momentum quantization, and whose emission appears slightly redshifted compared to the neutral case. Notably, our theoretical predictions of the emission spectra as a function of charge density align well with experimental observations [473–475], supporting the validity of our approach.

These findings deepen our understanding of light–matter interactions in strongly correlated 2D materials and lay the groundwork for future studies of magnetoexciton and magnetotrion dynamics under more realistic conditions, including intervalley coupling, finite doping, and disorder.

## Chapter 5

# Electrically Tunable MoSe<sub>2</sub>/WSe<sub>2</sub> Heterostructure-Based Quantum Dots

Single TMDC monolayers are 2D semiconductors that host low-energy mDFs with controllable spin-valley pseudospin textures [180, 223, 480]. These materials serve as fundamental “building blocks” for designing tailored vdW heterostructures [45, 261]. TMDC heterostructures, exemplified by MoSe<sub>2</sub>/WSe<sub>2</sub>, offer tunable interlayer excitons and long-lived excitonic states with sustained valley coherence, making them promising platforms for excitonic transport and quantum device applications [299, 300, 481].

Precise quantum state manipulation—essential for quantum information processing—is often achieved through electrical means. While valley polarization can be initialized optically using circularly polarized light [482], electrical control over valley states is feasible in TMDCs via sharp confinement potentials [483, 484], lateral heterostructures [485], or intrinsic defects [486]. Although most efforts have focused on the *K*-valley states, their coupling by purely electrical means remains challenging. In contrast, the *Q*-valleys offer a promising alternative: they form a naturally triply degenerate subspace, making them suitable for qutrit implementation and potentially advantageous for fault-tolerant quantum operations [487, 488].

MoSe<sub>2</sub>/WSe<sub>2</sub> heterostructures, benefiting from nearly perfect lattice matching [489], have become a prominent platform for studies in optoelectronics, valleytronics, and emergent quantum technologies [291, 490]. Their type-II band alignment and strong interlayer interactions introduce new possibilities for device functionality. However, most prior theoretical studies rely on simplified TB or  $\vec{k} \cdot \vec{p}$  approaches [337, 491], leaving aspects of atomistic interlayer hybridization insufficiently explored.

In this chapter, we bridge this gap by constructing an atomistic interlayer coupling model that explicitly includes both metal and chalcogen orbitals. We analyze the MoSe<sub>2</sub>/WSe<sub>2</sub> electronic structure using first-principles DFT calculations and develop a corresponding TB model rooted in monolayer-based orbital representations. Leveraging this model, we propose a strategy for coherent control of *Q*-valley isospins using electrostatically defined quantum dots (QDs).

In this chapter, we begin with DFT calculations that highlight key features of the MoSe<sub>2</sub>/WSe<sub>2</sub> electronic structure in Sec. 5.1. Building on these results, we develop a TB model that incorpo-

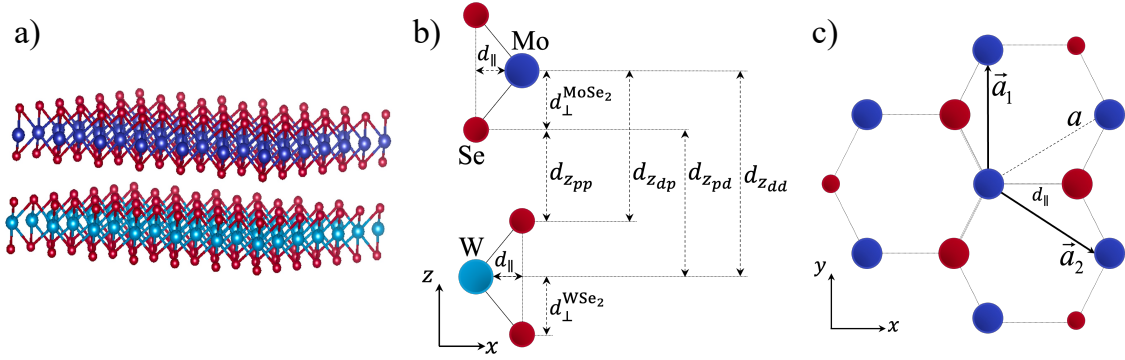


**Figure 5.1:** Geometry of the  $\text{MoSe}_2/\text{WSe}_2$  heterostructure in AB stacking: (a) 3D view, (b) side view, and (c) top view. The  $\text{MoSe}_2$  top layer and  $\text{WSe}_2$  bottom layer are shown with Mo (dark blue), W (light blue), and Se (red) atoms. The interlayer distance  $d_{zdd}$ , a key factor in interlayer interactions, is indicated in (b), which also marks the UC. Panel (c) shows the primitive lattice vectors  $\vec{a}_1$  and  $\vec{a}_2$ , defining in-plane symmetry. AB stacking offsets the layers to enhance chalcogen atom interactions.

rates monolayer orbital bases and interlayer coupling in Sec. 5.2. We then examine the effects of external electric fields on band alignment and valley ordering in Sec. 5.3. Finally, we explore how electrostatically defined QDs can enable tunable valley coupling and potential quantum control of  $Q$ -valley isospins in Sec. 5.4.

## 5.1 *Ab Initio* Band Structure of $\text{MoSe}_2/\text{WSe}_2$

In this section, we present the electronic properties of the  $\text{MoSe}_2/\text{WSe}_2$  heterostructure, as determined from first-principles DFT calculations. The 3D geometry of the system is shown in Fig. 5.1(a). Our study focuses on the energetically favorable AB stacking configuration [224], in which the metal atoms of one layer (Mo or W) are positioned directly beneath the chalcogen atoms (Se) of the other layer. This stacking arrangement results in optimal interlayer interactions, which are crucial for understanding the material's electronic properties.

In Fig. 5.1(b), we present a side view of the heterostructure, where the UC is shown to consist of six atoms—three from each of the  $\text{MoSe}_2$  and  $\text{WSe}_2$  layers. The UC is a fundamental building block in describing the material's periodicity. Panel (c) shows the top view of the heterostructure, revealing the honeycomb lattice structure characteristic of TMDCs, with distinct Mo and W atomic sites arranged in a periodic fashion. The primitive lattice vectors in real space, which define the periodicity of the system, are given by  $\vec{a}_1 = (0, a)$  and  $\vec{a}_2 = (a\sqrt{3}/2, -a/2)$ , where  $a$  is the in-plane lattice constant, related to the interlayer distance by  $a = d_{\parallel}\sqrt{3}$ .

The lattice mismatch between the  $\text{MoSe}_2$  and  $\text{WSe}_2$  layers in the heterostructure is extremely small, with a relative mismatch  $\Delta a < 0.001 \text{ \AA}$ , meaning that the heterostructure does not experience significant strain or deformation, a factor that ensures the stability of the system. We have set the lattice constant to  $a = 3.323 \text{ \AA}$ , consistent with experimental values for the monolayers. To determine the optimal interlayer distance,  $d_{zdd}$ , we systematically studied the total energy of the system as a function of layer separation [224]. The energy is minimized for an interlayer distance of  $d_{zdd} = 6.40 \text{ \AA}$ , which corresponds to the equilibrium configuration of the heterostructure. The metal-chalcogen bond lengths,  $d_{\perp}$ , between Mo (W) and Se atoms in the top and bottom layers

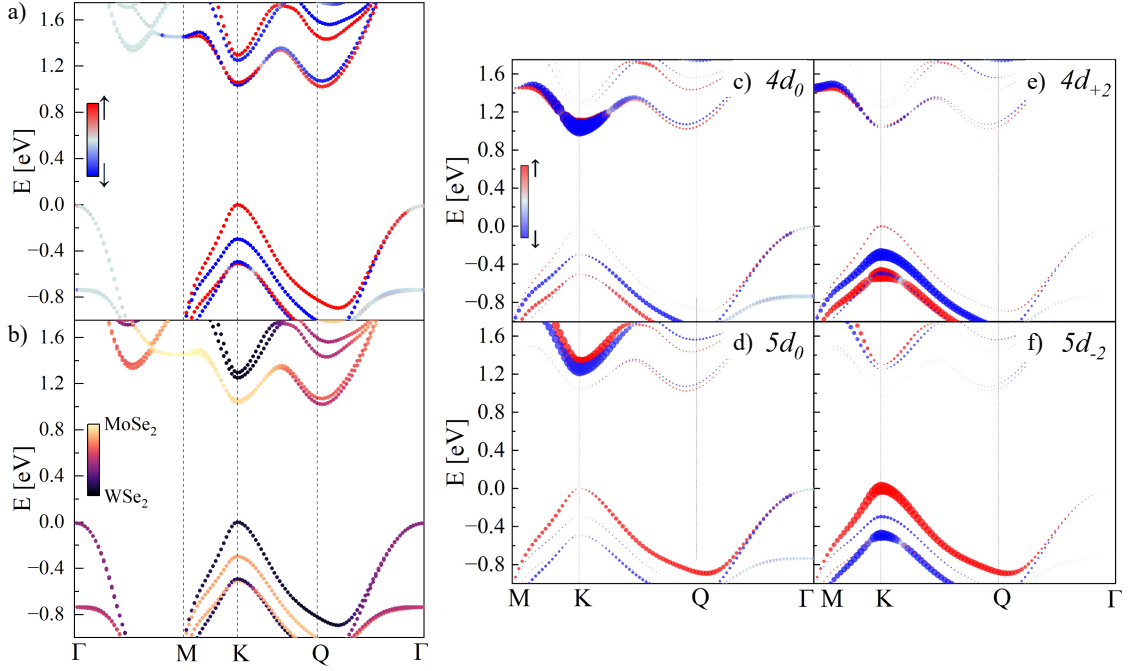


**Figure 5.2:** DFT electronic structure and orbital contribution for the leading orbitals from both layers of the MoSe<sub>2</sub>/WSe<sub>2</sub> heterostructure along the  $\Gamma$ - $M$ - $K$ - $Q$ - $\Gamma$  path in the BZ. Panel (a) shows the spin-resolved structure, with spin-up and spin-down states in red and blue, respectively. Panel (b) presents the layer-resolved structure, highlighting MoSe<sub>2</sub> and WSe<sub>2</sub> contributions in yellow and black. This dual view reveals the spin-layer coupling and the degenerate conduction band valleys at the  $K$  and  $Q$  points, key features of the heterostructure. (c-f) Orbital contribution: (c)  $4d_{m=0}$  and (d)  $4d_{m=+2}$  from molybdenum, and (e)  $5d_{m=0}$  and (f)  $5d_{m=-2}$  from tungsten. Color denotes spin.

are calculated to be 1.669 Å and 1.680 Å, respectively, which are typical of TMDCs.

The electronic energies and wave functions of the system were calculated following the methodology described in Sec. 4.1, using the *ab initio* software package Abinit [406–408], employing the PBE parametrization of the GGA for the XC functional [420]. The projector augmented wave (PAW) method [418] was used to model the interaction between the ions and electrons. Both SOC and vdW interactions were considered in the calculations. For the vdW interactions, we applied the DFT-D3 XC functional [476], which accurately captures long-range dispersion forces between the layers. The plane-wave basis set was truncated with an energy cutoff of 80 Ha, and the wave function was sampled using a  $16 \times 16 \times 1$  grid of  $k$ -points in the reciprocal space. A vacuum region of 40 Å was introduced along the  $z$ -direction to decouple the periodic images of the heterostructure and minimize interactions between adjacent supercells.

Next, we examine the properties of the Kohn-Sham wave functions,  $\Psi_{n,k}^{\uparrow,\downarrow}$ , which describe the electronic states in the heterostructure. Here,  $n$  denotes the band index and  $k$  represents the wavevector in reciprocal space. As in the monolayer case (see Sec. 4.1), the real-space charge density,  $\rho_{n,k}^{\uparrow,\downarrow}$ , quantifies the charge distribution in the UC. This density enables a detailed layer- and spin-resolved analysis of the electronic states, offering insights into the interlayer coupling and spin-valley interactions in the MoSe<sub>2</sub>/WSe<sub>2</sub> heterostructure.

The band structure of the heterostructure, shown in Fig. 5.2, reveals quasi-degenerate CB

minima at the  $K$  and  $Q$  points, with an energy separation of 1.8 meV, and VB maxima at the  $K$  and  $\Gamma$  points, separated by 35.5 meV. The direct  $K$ - $K$  bandgap,  $E_g = 1.04$  eV, is smaller than those of the individual monolayers ( $E_g^{\text{MoSe}_2} = 1.34$  eV and  $E_g^{\text{WSe}_2} = 1.24$  eV), highlighting the effect of interlayer coupling. Spin-orbit coupling (SOC) effects, consistent with isolated monolayers, yield spin splittings of  $\Delta_{\text{SOC}}^{CB} = 12$  meV and  $\Delta_{\text{SOC}}^{VB} = 211$  meV for MoSe<sub>2</sub>, and  $\Delta_{\text{SOC}}^{CB} = 30$  meV and  $\Delta_{\text{SOC}}^{VB} = 473$  meV for WSe<sub>2</sub>.

The heterostructure exhibits type-II band alignment, with conduction band electrons at  $K$  localized in the MoSe<sub>2</sub> layer and valence band holes in the WSe<sub>2</sub> layer. This layer separation is consistent with charge-transfer mechanisms observed in previous studies [175, 450]. Around the  $K$  valley, a strong spin-layer localization is evident, while at the  $Q$  valley, electrons are delocalized across both layers. Spin-resolved densities,  $\rho_{n,k}^{\uparrow,\downarrow}$ , further confirm these trends, showing spin mixing in the  $Q$  valley due to interlayer coupling.

Orbital-resolved decomposition of the Kohn-Sham wave functions, based on projections onto Slater orbitals, elucidates the atomic-like contributions to the electronic states. As in the monolayer case (see Sec. 4.1), these orbitals,  $\varphi_{\alpha,\mu}$ , are defined by radial functions and spherical harmonics. The decomposition, depicted in Fig. 5.2(b), highlights the dominant  $d$ - and  $p$ -orbital contributions from Mo, W, and Se atoms, reflecting the strong hybridization and bonding characteristic of the heterostructure.

As observed in the case of single layers of TMDCs [175, 223], the primary contributions to the bands near the Fermi level originate from the symmetric (even) atomic orbitals. The CB is predominantly composed of the metal orbitals:  $4d_{m=0}$  for the MoSe<sub>2</sub> layer and  $5d_{m=0}$  for the WSe<sub>2</sub> layer, as shown in Fig. 5.2(c,e). In contrast, the VB is primarily influenced by the  $4d_{m=\pm 2}$  orbitals for Mo and the  $5d_{m=\pm 2}$  orbitals for W, as depicted in Fig. 5.2(d,f). The AB-stacking arrangement of the layers leads to a dominant orbital contribution at the  $K$  valley in the VB, where the  $4d_{m=+2}$  orbital from the MoSe<sub>2</sub> layer and the  $5d_{m=-2}$  orbital from the WSe<sub>2</sub> layer are most significant. This behavior aligns with the simplistic view of opposite valleys being stacked on top of one another. However, it is important to note that this does not imply a simple valley-layer locking due to the strong localization effects of the layers.

In contrast, the orbital contributions around the  $Q$  valley are more intricate, reflecting the delocalization of electrons across the distinct layers. This delocalization significantly influences the orbital makeup at the  $Q$  valley, as detailed in Fig. 5.2(d,f). The complexity arises from the interlayer coupling, which modifies the electronic states and leads to a mixed character in the orbital contributions across the layers. The detailed orbital contributions to the energy bands at the high symmetry points of the BZ are provided in Tab. 5.1, offering a comprehensive view of the distribution of orbital character across the different layers and valleys.

## 5.2 Tight-Binding Model

In this section, we develop an *ab initio*-based TB model for a type-II TMDC heterostructure. This TB approach provides a powerful framework for understanding a range of phenomena, including interlayer interactions and the impact of external electric fields. Furthermore, it offers the possibility of studying heterobilayer-based nanostructures, which could have unique electronic properties due to the interaction between layers.

**Table 5.1:** Orbital contribution for the even subspace presented for the atomic orbitals with the main contribution to the top VB and bottom CB. Values are represented as percentages for each high symmetry point.

		K, VB	K, CB	Q, CB	$\Gamma$ , VB
		$\downarrow/\uparrow$	$\downarrow/\uparrow$	$\downarrow/\uparrow$	$\downarrow/\uparrow$
Se <sub>2</sub> <sup>(top)</sup>	4p <sub>-1</sub>	-	0%/20%	2%/1%	-
	4p <sub>0</sub>	-	-	4%/1%	7%/5%
	4p <sub>+1</sub>	4%/0%	-	7%/2%	-
Mo	4d <sub>-2</sub>	-	0%/20%	14%/4%	1%/0%
	4d <sub>0</sub>	-	0%/73%	8%/2%	12%/9%
	4d <sub>+2</sub>	8%/0%	-	4%/1%	0%/1%
Se <sub>2</sub> <sup>(bottom)</sup>	4p <sub>-1</sub>	27%/0%	-	7%/1%	-
	4p <sub>0</sub>	-	-	3%/1%	7%/5%
	4p <sub>+1</sub>	-	-	2%/1%	-
W	5d <sub>-2</sub>	53%/0%	-	2%/1%	-
	5d <sub>0</sub>	-	2%/0%	5%/1%	13%/10%
	5d <sub>+2</sub>	-	0%/1%	10%/1%	0%/1%

### 5.2.1 Orbital Basis

Building upon our previous work on monolayer TMDCs [175, 223, 483], we extend the tight-binding formalism to model a two-layer TMDCs heterostructure with AB-stacked layers. The model we construct is a 44 spinful even-odd orbital system, incorporating both inter- and intralayer hoppings within the next-nearest neighbor approximation. The electron wave function in this model is expressed as a linear combination of atomic orbitals  $\varphi_{\alpha,\mu}$ . Specifically, the wave function is given by the following expression [223]:

$$\Psi_n(\vec{k}, \vec{r}) = e^{i\vec{k}\cdot\vec{r}} u_n(\vec{k}, \vec{r}) = e^{i\vec{k}\cdot\vec{r}} \frac{1}{\sqrt{N_U}} \sum_{i=1}^{N_U} \sum_{\alpha=1}^{N_l} \sum_{\mu=1}^{N_o} e^{-i\vec{k}\cdot(\vec{r}-\vec{U}_{i,\alpha})} \nu_{\alpha,\mu} \varphi_{\alpha,\mu}(\vec{r}-\vec{U}_{i,\alpha}), \quad (5.1)$$

where  $n$  represents the band index,  $\vec{k}$  is the wavevector within the two-dimensional BZ, and  $u_n$  are the periodic Bloch functions. The number of UCs in the system is denoted as  $N_U$ , with  $N_l = 4$  representing the number of sublattices per UC (two per layer). Additionally,  $N_o$  denotes the number of orbitals per metal atom (5 orbitals) or per chalcogen dimer site (6 orbitals). The coefficients  $\nu_{\alpha,\mu}$  are determined by solving the TB Hamiltonian.

From our *ab initio* calculations, we take the  $d$ -orbitals of the metal atoms (Mo or W) with  $m = \{0, \pm 1, \pm 2\}$  and the  $p$ -orbitals of the chalcogen dimers, constructed from orbitals with  $m = \{0, \pm 1\}$ . The orbitals are localized at positions  $\vec{U}_{i,\alpha} = \vec{U}_i + \vec{\tau}_\alpha$ , where  $\vec{U}_i$  are the coordinates of the UC and  $\tau_\alpha$  represents the atomic positions within each UC.

For computational convenience, we separate the orbital sum into two distinct subspaces: the even subspace  $\mathcal{H}_{\text{even}}$  and the odd subspace  $\mathcal{H}_{\text{odd}}$ , defined relative to the metal planes of the monolayer TMDCs. The basis functions are ordered as follows: for the even subspace,  $\{m_d = -2, 0, 2, m_p = -1, 0, 1\}$ , and for the odd subspace,  $\{m_d = -1, 1, m_p = -1, 0, 1\}$ . The  $p$ -orbitals of

the chalcogen dimers, denoted  $X_2$ , are defined differently for each subspace. For the even subspace, the chalcogen dimer orbitals are expressed as:

$$\begin{aligned} m_{p+1} &= \frac{1}{\sqrt{2}} \left( |m_{p+1}^{X(1)}\rangle \pm |m_{p+1}^{X(2)}\rangle \right), \\ m_{p0} &= \frac{1}{\sqrt{2}} \left( |m_{p0}^{X(1)}\rangle \mp |m_{p0}^{X(2)}\rangle \right), \\ m_{p-1} &= \frac{1}{\sqrt{2}} \left( |m_{p-1}^{X(1)}\rangle \pm |m_{p-1}^{X(2)}\rangle \right), \end{aligned} \quad (5.2)$$

where the  $+/-$  signs correspond to the even/odd subspaces, and the indices 1/2 refer to the top and bottom atoms of the chalcogen dimer, respectively. Thus, the full spinless even-odd wave function for a monolayer TMDC heterostructure can be written as:

$$\Psi_n(\vec{k}, \vec{r}) = \left[ \Psi_n^{\text{ev}}(\vec{k}, \vec{r}), \Psi_n^{\text{odd}}(\vec{k}, \vec{r}) \right]^T. \quad (5.3)$$

Finally, in this chiral basis, it is necessary to use linear combinations of standard Slater-Koster hopping integrals [492] to model the inter- and intralayer hopping terms. These hopping integrals define the coupling between the various orbitals and help establish the electronic structure of the heterostructure.

## 5.2.2 Spinfull Monolayer Hamiltonian

In this section, we describe the monolayer Hamiltonians for MoSe<sub>2</sub> and WSe<sub>2</sub>, two commonly studied TMDCs, incorporating the effects of SOC. The general form of these Hamiltonians is derived following the methodology outlined in our previous works [175, 223, 483], which extend the TB approach to include the intrinsic spin-orbit interaction that is present in these materials. The Hamiltonian for a single monolayer of TMDCs is expressed in matrix form as:

$$H_{\text{MX}_2} = \begin{bmatrix} H_{\uparrow}^{\text{ev}} & 0 & 0 & H_{\uparrow\downarrow}^{\text{ev-odd}} \\ & H_{\uparrow}^{\text{odd}} & H_{\uparrow\downarrow}^{\text{odd-ev}} & 0 \\ & & H_{\downarrow}^{\text{ev}} & 0 \\ & & & H_{\downarrow}^{\text{odd}} \end{bmatrix}. \quad (5.4)$$

In this equation, the Hamiltonian is represented as a block matrix where each block corresponds to different components of the system. Specifically, the Hamiltonian is partitioned by spin ( $\uparrow$  and  $\downarrow$ ) and subspace (even and odd) indices. The even subspace (denoted as ev) and odd subspace (denoted as odd) represent the different electronic bands associated with the monolayer's atomic structure. The off-diagonal blocks, such as  $H_{\uparrow\downarrow}^{\text{ev-odd}}$  and  $H_{\uparrow\downarrow}^{\text{odd-ev}}$ , account for the coupling between the even and odd states of different spin orientations.

To understand the structure of this Hamiltonian, it is important to recognize that the Hilbert space is constructed from the direct sum of the even and odd subspaces, each of which is further tensorized with the spin space. Thus, the full Hilbert space for the system is given by:

$$\mathcal{H}_{\text{MX}_2} = (\mathcal{H}_{\text{even}} \oplus \mathcal{H}_{\text{odd}}) \otimes \mathcal{H}_{\text{spin}}. \quad (5.5)$$

This implies that the total dimension of the system is the sum of the dimensions of the even and odd subspaces (which are 6 and 5, respectively) multiplied by the spin degree of freedom, resulting in a  $22 \times 22$  matrix representation for the Hamiltonian. This formulation incorporates both the electron's spin and the symmetry properties of the monolayer's electronic structure, making it suitable for studying spin-dependent phenomena in TMDCs.

Furthermore, the atomic SOC is included in each layer's Hamiltonian. The SOC term is expressed as:

$$\hat{H}_{\text{SOC}} = \sum_a \frac{\lambda_a}{\hbar} \hat{\mathbf{L}}_a \cdot \hat{\mathbf{S}}_a, \quad (5.6)$$

where  $\lambda_a$  is the SOC strength specific to each atom  $a$ ,  $\hat{\mathbf{L}}_a$  is the atomic orbital angular momentum operator, and  $\hat{\mathbf{S}}_a$  is the spin operator. The strength of the SOC varies depending on the type of atom in the monolayer, influencing the magnitude of the spin splitting and, consequently, the electronic band structure of the material. The presence of SOC is essential for understanding many of the unique properties of TMDCs, such as spin-valley coupling, and contributes to the rich physics observed in these materials.

However, the construction of the Hamiltonian for a heterostructure consisting of two stacked monolayers requires additional considerations. In particular, the stacking arrangement, which is typically AB-stacked as shown in Fig. 5.1(b), introduces interlayer interactions that must be accounted for in the Hamiltonian. The AB-stacking corresponds to a relative rotation of  $180^\circ$  between the two monolayers, which makes the interlayer coupling different from that in AA stacking, where the metal and chalcogen atoms in one layer are aligned with the corresponding metal and chalcogen atoms in the other layer. Consequently, the TB Hamiltonian for each monolayer must be modified to capture the changes induced by the stacking geometry. This modification leads to different Hamiltonians for each monolayer in the heterostructure. The Hamiltonian for the MoSe<sub>2</sub> monolayer after accounting for the rotation is denoted as  $H_{\text{MoSe}_2}^{\text{rot}}$ , and for the WSe<sub>2</sub> monolayer, it is  $H_{\text{WSe}_2}$ . The distinction between these two Hamiltonians plays a key role in accurately describing the interlayer coupling. The next step in constructing the heterostructure Hamiltonian involves modifying the monolayer Hamiltonian to account for the interlayer interactions, which will be discussed in the following section.

In the case of a non-rotated layer (denoted by the superscript (0)), the monolayer NNN Hamiltonian can be expressed in a block form for both the even and odd subspaces. This representation ensures a structured separation of contributions from different atomic orbitals, as shown below [175, 223, 493]:

$$H^{(0)} = \begin{bmatrix} H_{M-M}^{(0),\text{ev}} & H_{M-X_2}^{(0),\text{ev}} & 0 & 0 \\ & H_{X_2-X_2}^{(0),\text{ev}} & 0 & 0 \\ & & H_{M-M}^{(0),\text{odd}} & H_{M-X_2}^{(0),\text{odd}} \\ & & & H_{X_2-X_2}^{(0),\text{odd}} \end{bmatrix}. \quad (5.7)$$

Here, the Hamiltonian incorporates different types of interactions between the metal and chalcogen atoms. The metal-metal interactions ( $H_{M-M}$ ), chalcogen-chalcogen interactions ( $H_{X_2-X_2}$ ), and metal-chalcogen interactions ( $H_{M-X_2}$ ) are further subdivided into contributions from the even and odd subspaces, as detailed below.

The matrix describing the metal-metal NNN interactions in the even subspace is:

$$H_{M-M}^{(0),\text{ev}} = \begin{bmatrix} E_{m_d=-2} & W_3 g_2(\vec{k}) & W_4 g_4(\vec{k}) \\ +W_1 g_0(\vec{k}) & E_{m_d=0} & W_3 g_2(\vec{k}) \\ & +W_2 g_0(\vec{k}) & E_{m_d=2} \\ & & +W_1 g_0(\vec{k}) \end{bmatrix}, \quad (5.8)$$

while for the odd subspace, it takes the form:

$$H_{M-M}^{(0),\text{odd}} = \begin{bmatrix} E_{m_d=-1} & -W_9 g_2(\vec{k}) \\ +W_8 g_0(\vec{k}) & E_{m_d=+1} \\ & +W_8 g_0(\vec{k}) \end{bmatrix}. \quad (5.9)$$

The corresponding matrix for the chalcogen-chalcogen ( $X_2$ - $X_2$ ) dimer interactions in the even subspace is:

$$H_{X_2-X_2}^{(0),\text{ev}} = \begin{bmatrix} E_{m_p=-1} & 0 & -W_7g_2(\vec{k}) \\ +W_5g_0(\vec{k}) & E_{m_p=0} & 0 \\ & +W_6g_0(\vec{k}) & E_{m_p=1} \\ & & +W_5g_0(\vec{k}) \end{bmatrix}, \quad (5.10)$$

and for the odd subspace:

$$H_{X_2-X_2}^{(0),\text{odd}} = \begin{bmatrix} E_{m_p=-1}^{\text{odd}} & 0 & -W_7g_2(\vec{k}) \\ +W_5g_0(\vec{k}) & E_{m_p=0}^{\text{odd}} & 0 \\ & +W_6g_0(\vec{k}) & E_{m_p=1}^{\text{odd}} \\ & & +W_5g_0(\vec{k}) \end{bmatrix}. \quad (5.11)$$

The metal-chalcogen tunneling interactions ( $H_{M-X_2}$ ) are described as follows. For the even subspace:

$$H_{M-X_2}^{(0),\text{ev}} = \begin{bmatrix} V_1f_{-1}(\vec{k}) & -V_2f_0(\vec{k}) & V_3f_1(\vec{k}) \\ -V_4f_0(\vec{k}) & -V_5f_1(\vec{k}) & V_4f_{-1}(\vec{k}) \\ -V_3f_1(\vec{k}) & -V_2f_{-1}(\vec{k}) & -V_1f_0(\vec{k}) \end{bmatrix}, \quad (5.12)$$

and for the odd subspace:

$$H_{M-X_2}^{(0),\text{odd}} = \begin{bmatrix} -V_6f_{+1}(\vec{k}) & -V_8f_{-1}(\vec{k}) & V_7f_0(\vec{k}) \\ V_7f_{-1}(\vec{k}) & V_8f_0(\vec{k}) & -V_6f_{+1}(\vec{k}) \end{bmatrix}. \quad (5.13)$$

In the monolayer Hamiltonian given by Eq. (5.7), the matrix elements corresponding to NN tunneling are characterized by parameters  $V_i$ . These parameters are expressed in terms of geometric factors and coupling constants as follows:

$$\begin{aligned} V_1 &= \frac{1}{\sqrt{2}} \frac{d_{\parallel}}{d} \left[ \frac{\sqrt{3}}{2} \left( \frac{d_{\perp}^2}{d^2} - 1 \right) V_{dp\sigma} - \left( \frac{d_{\perp}^2}{d^2} + 1 \right) V_{dp\pi} \right], \\ V_2 &= \frac{1}{2} \left( \frac{d_{\parallel}}{d} \right)^2 \frac{d_{\perp}}{d} \left[ \sqrt{3}V_{dp\sigma} - 2V_{dp\pi} \right], \\ V_3 &= \frac{1}{\sqrt{2}} \left( \frac{d_{\parallel}}{d} \right)^3 \left[ \frac{\sqrt{3}}{2} V_{dp\sigma} - V_{dp\pi} \right], \\ V_4 &= \frac{1}{2} \frac{d_{\parallel}}{d} \left[ \left( 3 \frac{d_{\perp}^2}{d^2} - 1 \right) V_{dp\sigma} - 2\sqrt{3} \frac{d_{\perp}^2}{d^2} V_{dp\pi} \right], \\ V_5 &= \frac{1}{\sqrt{2}} \frac{d_{\perp}}{d} \left[ \left( 3 \frac{d_{\perp}^2}{d^2} - 1 \right) V_{dp\sigma} - 2\sqrt{3} \left( \frac{d_{\perp}^2}{d^2} - 1 \right) V_{dp\pi} \right], \\ V_6 &= \frac{1}{\sqrt{2}} \frac{d_{\perp}}{d} \left[ \frac{d_{\parallel}^2}{d^3} \left( \sqrt{3}V_{dp\sigma} - 2V_{dp\pi} \right) + 2V_{dp\pi} \right], \\ V_7 &= \frac{1}{\sqrt{2}} \frac{d_{\perp}d_{\parallel}^2}{d^3} \left( \sqrt{3}V_{dp\sigma} - 2V_{dp\pi} \right), \\ V_8 &= \frac{d_{\parallel}}{d} \left[ \frac{d_{\perp}^2}{d^2} \left( \sqrt{3}V_{dp\sigma} - 2V_{dp\pi} \right) + V_{dp\pi} \right], \end{aligned} \quad (5.14)$$

where  $d_{\parallel}$  and  $d_{\perp}$  represent the in-plane and out-of-plane components of the interatomic distance  $d$ , and  $V_{dp\sigma}$  and  $V_{dp\pi}$  are the orbital coupling parameters. Additionally, the  $k$ -dependent functions  $f_i(\vec{k})$  describe the symmetry-adapted tunneling contributions for NN interactions and are given by:

$$f_{-1}(\vec{k}) = e^{ik_x d_{\parallel}} + e^{-ik_x d_{\parallel}/2} e^{i\sqrt{3}k_y d_{\parallel}/2} e^{i2\pi/3} + e^{-ik_x d_{\parallel}/2} e^{-i\sqrt{3}k_y d_{\parallel}/2} e^{-i2\pi/3},$$

$$\begin{aligned}
f_0(\vec{k}) &= e^{ik_x d_{\parallel}} + e^{-ik_x d_{\parallel}/2} e^{i\sqrt{3}k_y d_{\parallel}/2} e^{-i2\pi/3} + e^{-ik_x d_{\parallel}/2} e^{-i\sqrt{3}k_y d_{\parallel}/2} e^{i2\pi/3}, \\
f_{+1}(\vec{k}) &= e^{ik_x d_{\parallel}} + e^{-ik_x d_{\parallel}/2} e^{i\sqrt{3}k_y/2} + e^{-ik_x d_{\parallel}/2} e^{-i\sqrt{3}k_y/2}.
\end{aligned} \tag{5.15}$$

The NNN tunneling elements are similarly characterized by parameters  $W_i$ , which are expressed in terms of orbital coupling constants as follows:

$$\begin{aligned}
W_1 &= \frac{1}{8} (3V_{dd\sigma} + 4V_{dd\pi} + V_{dd\delta}), \\
W_2 &= \frac{1}{4} (V_{dd\sigma} + 3V_{dd\delta}), \\
W_3 &= -\frac{\sqrt{3}}{4\sqrt{2}} (V_{dd\sigma} - V_{dd\delta}), \\
W_4 &= \frac{1}{8} (3V_{dd\sigma} - 4V_{dd\pi} + V_{dd\delta}), \\
W_5 &= \frac{1}{2} (V_{pp\sigma} + V_{pp\pi}), \\
W_6 &= V_{pp\pi}, \\
W_7 &= \frac{1}{2} (V_{pp\sigma} - V_{pp\pi}), \\
W_8 &= \frac{1}{2} (V_{dd\pi} + V_{dd\delta}), \\
W_9 &= \frac{1}{2} (V_{dd\pi} - V_{dd\delta}),
\end{aligned} \tag{5.16}$$

where  $V_{dd\sigma}$ ,  $V_{dd\pi}$ ,  $V_{dd\delta}$ ,  $V_{pp\sigma}$ , and  $V_{pp\pi}$  denote the overlap integrals for different orbital combinations. Finally, the  $k$ -dependent functions  $g_i(\vec{k})$  for NNN tunneling are defined as:

$$\begin{aligned}
g_0(\vec{k}) &= 4 \cos(3k_x d_{\parallel}/2) \cos(\sqrt{3}k_y d_{\parallel}/2) + 2 \cos(\sqrt{3}k_y d_{\parallel}), \\
g_2(\vec{k}) &= 2 \cos(3k_x d_{\parallel}/2 + \sqrt{3}k_y d_{\parallel}/2) e^{i\pi/3} + 2 \cos(3k_x d_{\parallel}/2 - \sqrt{3}k_y d_{\parallel}/2) e^{-i\pi/3} \\
&\quad - 2 \cos(\sqrt{3}k_y d_{\parallel}), \\
g_4(\vec{k}) &= 2 \cos(3k_x d_{\parallel}/2 + \sqrt{3}k_y d_{\parallel}/2) e^{i2\pi/3} + 2 \cos(3k_x d_{\parallel}/2 - \sqrt{3}k_y d_{\parallel}/2) e^{-i2\pi/3} \\
&\quad + 2 \cos(\sqrt{3}k_y d_{\parallel}).
\end{aligned} \tag{5.17}$$

Having fully defined the non-rotated monolayer TMDC NNN TB model, we now describe the modifications in the Hamiltonian introduced by the in-plane rotation by  $180^\circ$  ( $180^\circ \equiv \pi$ ) of one layer relative to the other. Importantly, this rotation does not alter the functional forms of the  $\vec{k}$ -dependent functions  $f$  and  $g$ , nor does it affect the definitions of the amplitude parameters  $V$  and  $W$ . However, it does lead to specific changes in the NN couplings. These changes include a reversal of the sign in the  $\vec{k}$  coordinates for the metal-chalcogen dimer couplings, i.e.,  $\vec{k} \rightarrow -\vec{k}$ , and the introduction of a  $(-1)$  factor in front of particular NN Hamiltonian matrix elements associated with the metal-chalcogen dimer couplings. The full Hamiltonian for a rotated monolayer is then expressed as:

$$H^{(\pi)} = \begin{bmatrix} H_{M-M}^{(0),\text{ev}} & H_{M-X_2}^{(\pi),\text{ev}} & 0 & 0 \\ & H_{X_2-X_2}^{(0),\text{ev}} & 0 & 0 \\ & & H_{M-M}^{(0),\text{odd}} & H_{M-X_2}^{(\pi),\text{odd}} \\ & & & H_{X_2-X_2}^{(0),\text{odd}} \end{bmatrix}. \tag{5.18}$$

Here, the submatrices  $H_{M-M}$ ,  $H_{X_2-X_2}$ , and  $H_{M-X_2}$  represent the couplings between metal-metal atoms, chalcogen-chalcogen dimers, and metal atoms-chalcogen dimers, respectively. The superscripts ‘‘even’’ and ‘‘odd’’ denote the symmetry subspaces. The  $M-X_2$  matrix elements in the

rotated TMDC monolayer Hamiltonian components  $H^{(\pi)}$  are explicitly redefined below. In the even subspace, the matrix reads:

$$H_{M-X_2}^{(\pi),\text{ev}} = \begin{bmatrix} -V_1 f_{-1}(-\vec{k}) & -V_2 f_0(-\vec{k}) & -V_3 f_1(-\vec{k}) \\ V_4 f_0(-\vec{k}) & -V_5 f_1(-\vec{k}) & -V_4 f_{-1}(-\vec{k}) \\ V_3 f_1(-\vec{k}) & -V_2 f_{-1}(-\vec{k}) & V_1 f_0(-\vec{k}) \end{bmatrix}, \quad (5.19)$$

while in the odd subspace, it takes the form:

$$H_{M-X_2}^{(\pi),\text{odd}} = \begin{bmatrix} -V_6 f_{+1}(-\vec{k}) & V_8 f_{-1}(-\vec{k}) & V_7 f_0(-\vec{k}) \\ V_7 f_{-1}(-\vec{k}) & -V_8 f_0(-\vec{k}) & -V_6 f_{+1}(-\vec{k}) \end{bmatrix}. \quad (5.20)$$

These redefined matrices account for the changes in coupling symmetry and the reversal of  $\vec{k}$  caused by the in-plane rotation by 180° of one layer relative to the other.

Next, we turn our attention to the SOC Hamiltonian, as defined in Eq. 5.4. This Hamiltonian introduces distinct contributions within the even and odd subspaces, as well as coupling between them. The non-zero diagonal matrix elements of the  $H_{\uparrow}^{\text{ev}}$  block, corresponding to the spin-up subspace, are expressed as:

$$\text{diag} \left( -\lambda_M, 0, \lambda_M, -\frac{1}{2}\lambda_{X_2}, 0, \frac{1}{2}\lambda_{X_2} \right), \quad (5.21)$$

where  $\lambda_M$  and  $\lambda_{X_2}$  represent the SOC strengths for the metal and chalcogen atoms, respectively. Similarly, the diagonal elements of the  $H_{\uparrow}^{\text{odd}}$  block for the odd spin-up subspace are given by:

$$\text{diag} \left( -\frac{1}{2}\lambda_M, \frac{1}{2}\lambda_M, -\frac{1}{2}\lambda_{X_2}, 0, \frac{1}{2}\lambda_{X_2} \right). \quad (5.22)$$

For the spin-down subspaces, both even and odd blocks exhibit the same structure but with the opposite sign for their diagonal elements. This reflects the time-reversal symmetry of the system and ensures that the SOC contributions for opposite spins are symmetric but sign-reversed. In addition to these diagonal terms, the SOC Hamiltonian also couples the even and odd subspaces through the off-diagonal elements  $H_{\uparrow\downarrow}^{\text{ev-odd}}$  and  $H_{\uparrow\downarrow}^{\text{odd-ev}}$ . These coupling terms represent transitions between the even and odd states induced by SOC and are characterized by four non-zero matrix elements for each block. In the first coupling block,  $H_{\uparrow\downarrow}^{\text{ev-odd}}$ , the non-zero elements are as follows:

- $\langle m_d = -2 \uparrow, \text{ev} | \hat{H}_{\text{SOC}} | m_d = -1 \downarrow, \text{odd} \rangle = \lambda_M,$
- $\langle m_d = 0 \uparrow, \text{ev} | \hat{H}_{\text{SOC}} | m_d = 1 \downarrow, \text{odd} \rangle = \sqrt{\frac{3}{2}}\lambda_M,$
- $\langle m_p = -1 \uparrow, \text{ev} | \hat{H}_{\text{SOC}} | m_p = 0 \downarrow, \text{odd} \rangle = \frac{\sqrt{2}}{2}\lambda_{X_2},$
- $\langle m_p = 0 \uparrow, \text{ev} | \hat{H}_{\text{SOC}} | m_p = 1 \downarrow, \text{odd} \rangle = \frac{\sqrt{2}}{2}\lambda_{X_2}.$

For the second coupling block,  $H_{\uparrow\downarrow}^{\text{odd-ev}}$ , which corresponds to transitions in the reverse direction, the non-zero elements are given by:

- $\langle m_d = -1 \uparrow, \text{odd} | \hat{H}_{\text{SOC}} | m_d = 0 \downarrow, \text{ev} \rangle = \sqrt{\frac{3}{2}}\lambda_M,$
- $\langle m_d = 1 \uparrow, \text{odd} | \hat{H}_{\text{SOC}} | m_d = 2 \downarrow, \text{ev} \rangle = \lambda_M,$
- $\langle m_p = -1 \uparrow, \text{odd} | \hat{H}_{\text{SOC}} | m_p = 0 \downarrow, \text{ev} \rangle = \frac{\sqrt{2}}{2}\lambda_{X_2},$
- $\langle m_p = 0 \uparrow, \text{odd} | \hat{H}_{\text{SOC}} | m_p = 1 \downarrow, \text{ev} \rangle = \frac{\sqrt{2}}{2}\lambda_{X_2}.$

These coupling terms reveal the interplay between the spin, orbital angular momentum, and subspace parity, highlighting the intricate nature of SOC in this system. Together with the diagonal elements, they provide a complete description of the SOC effects within the monolayer.

### 5.2.3 Heterostructure Hamiltonian

The TB Hamiltonian for the MoSe<sub>2</sub>/WSe<sub>2</sub> heterostructure can be represented in a block matrix form, explicitly separating the contributions from the two monolayers and their interlayer coupling. This is given by:

$$\hat{H}_{\text{hetero}} = \begin{bmatrix} \hat{R}_z^\pi H_{\text{MoSe}_2} & H_{\text{inter}} \otimes \mathbf{1}_\sigma \\ & H_{\text{WSe}_2} \end{bmatrix}, \quad (5.23)$$

where  $\hat{R}_z^\pi H_{\text{MoSe}_2}$  denotes the Hamiltonian of the MoSe<sub>2</sub> monolayer, rotated by  $\pi$  about the  $z$ -axis to reflect the AB-stacking configuration of the heterostructure. This contrasts with the WSe<sub>2</sub> monolayer, whose Hamiltonian,  $H_{\text{WSe}_2}$ , remains in its standard orientation. The detailed derivation of these monolayer Hamiltonians, including the effects of rotation, has been presented in the previous Section.

The off-diagonal term,  $H_{\text{inter}}$ , represents the coupling between the two layers and is spin-independent, as indicated by the identity matrix  $\mathbf{1}_\sigma$  in the spin space. This term describes the interlayer interactions that play an important role in determining the electronic structure of the heterostructure. Its specific form depends on the overlap and hybridization between the orbitals of the two layers.

The overall Hilbert space of the heterostructure is the direct sum of the Hilbert spaces of the individual monolayers,  $\mathcal{H}_{\text{MoSe}_2} \oplus \mathcal{H}_{\text{WSe}_2}$ . Given that each monolayer contributes a Hilbert space of dimension 22, the total dimension of the heterostructure Hamiltonian is  $22 + 22 = 44$ . This block structure provides a clear framework for understanding the interplay between intralayer and interlayer interactions in the MoSe<sub>2</sub>/WSe<sub>2</sub> heterostructure.

### 5.2.4 Interlayer Coupling

In this section, we develop a TB framework to describe the interlayer interactions in the MoSe<sub>2</sub>/WSe<sub>2</sub> heterostructure. These interactions include contributions up to the NNN terms, which notably account for interlayer metal-metal couplings. The interlayer coupling Hamiltonian,  $H_{\text{inter}}$ , can be expressed in a block matrix form as follows:

$$H_{\text{inter}} = \begin{bmatrix} H_{dd}^{\text{ev-ev}} & H_{dp}^{\text{ev-ev}} & H_{dd}^{\text{ev-odd}} & H_{dp}^{\text{ev-odd}} \\ H_{pd}^{\text{ev-ev}} & H_{pp}^{\text{ev-ev}} & H_{pd}^{\text{ev-odd}} & H_{pp}^{\text{ev-odd}} \\ H_{dd}^{\text{odd-ev}} & H_{dp}^{\text{odd-ev}} & H_{dd}^{\text{odd-odd}} & H_{dp}^{\text{odd-odd}} \\ H_{pd}^{\text{odd-ev}} & H_{pp}^{\text{odd-ev}} & H_{pd}^{\text{odd-odd}} & H_{pp}^{\text{odd-odd}} \end{bmatrix}, \quad (5.24)$$

where the blocks correspond to the different types of orbital interactions between the layers. These include interactions between the  $d$  orbitals of Mo and W metal atoms ( $dd$ ), between the  $p$  orbitals of the chalcogen dimers ( $pp$ ), and mixed interactions between the metal  $d$  orbitals and chalcogen  $p$  orbitals ( $pd$  and  $dp$ ).

Each of these interaction blocks is further categorized based on the parity of the subspaces (even or odd) of the orbitals involved. For example,  $H_{dd}^{\text{ev-ev}}$  represents the coupling between the even-parity  $d$  orbitals in both layers, while  $H_{pd}^{\text{odd-ev}}$  describes the coupling between odd-parity  $p$  orbitals of one layer and even-parity  $d$  orbitals of the other. This structure provides a comprehensive description of the interlayer interactions, which are important for capturing the electronic properties of the heterostructure.

We define the interlayer Hamiltonian in both the even and odd subspaces, while also incorporating the mixing between them. Consequently, the interlayer coupling Hamiltonian,  $H_{\text{inter}}$ , can

be written in the form given by Eq. (5.24). However, several symmetries between the particular couplings can be identified, which allow us to simplify the Hamiltonian:

$$\begin{aligned}
H_{pp}^{\text{ev-ev}} &= H_{pp}^{\text{ev-odd}} = -H_{pp}^{\text{odd-odd}} = -H_{pp}^{\text{odd-ev}} = H_{pp}, \\
H_{pd}^{\text{ev-ev}} &= -H_{pd}^{\text{odd-odd}} = H_{pd}^{(1)}, \\
H_{pd}^{\text{ev-odd}} &= -H_{pd}^{\text{odd-ev}} = H_{pd}^{(2)}, \\
H_{dp}^{\text{ev-ev}} &= H_{dp}^{\text{ev-odd}} = H_{dp}^{(1)}, \\
H_{dp}^{\text{odd-odd}} &= H_{dp}^{\text{odd-ev}} = H_{dp}^{(2)},
\end{aligned} \tag{5.25}$$

These symmetries allow us to rewrite Eq. (5.24) in a simplified form as:

$$H_{\text{inter}} = \begin{bmatrix} H_{dd}^{(1)} & H_{dp}^{(1)} & H_{dd}^{(2)} & H_{dp}^{(1)} \\ H_{pd}^{(1)} & H_{pp} & H_{pd}^{(2)} & H_{pp} \\ H_{dd}^{(3)} & H_{dp}^{(2)} & H_{dd}^{(4)} & H_{dp}^{(2)} \\ -H_{pd}^{(1)} & -H_{pp} & -H_{pd}^{(2)} & -H_{pp} \end{bmatrix}. \tag{5.26}$$

Next, we define the blocks corresponding to the  $p$ - $p$  couplings, which take the form:

$$H_{pp} = \begin{bmatrix} T_1 f_{+1}(\vec{k}) & -T_2 f_{-1}(\vec{k}) & T_3 f_0(\vec{k}) \\ T_2 f_0(\vec{k}) & T_4 f_{+1}(\vec{k}) & -T_2 f_{-1}(\vec{k}) \\ T_3 f_{-1}(\vec{k}) & T_2 f_0(\vec{k}) & T_1 f_{+1}(\vec{k}) \end{bmatrix} \tag{5.27}$$

For the  $p$ - $d$  and  $d$ - $p$  couplings, we have the following matrix forms:

$$H_{pd}^{(1)} = \begin{bmatrix} 0 & 0 & 0 \\ 0 & T_5 & 0 \\ 0 & 0 & 0 \end{bmatrix}, \quad H_{dp}^{(1)} = \begin{bmatrix} 0 & 0 & 0 \\ 0 & T_7 & 0 \\ 0 & 0 & 0 \end{bmatrix}, \quad H_{pd}^{(2)} = \begin{bmatrix} T_6 & 0 \\ 0 & 0 \\ 0 & T_6 \end{bmatrix}, \quad H_{dp}^{(2)} = \begin{bmatrix} T_8 & 0 & 0 \\ 0 & 0 & T_8 \end{bmatrix}. \tag{5.28}$$

Lastly, for the couplings involving  $d$  orbitals on both layers (referred to as  $d$ - $d$  couplings), we derive the following expressions:

$$\begin{aligned}
H_{dd}^{(1)} &= \begin{bmatrix} T_9 f_{+1}(-\vec{k}) & T_{10} f_0(-\vec{k}) & T_{11} f_{-1}(-\vec{k}) \\ T_{10} f_{-1}(-\vec{k}) & T_{12} f_{+1}(-\vec{k}) & T_{10} f_0(-\vec{k}) \\ T_{11} f_0(-\vec{k}) & T_{10} f_{-1}(-\vec{k}) & T_9 f_{+1}(-\vec{k}) \end{bmatrix}, \\
H_{dd}^{(2)} &= \begin{bmatrix} T_{13} f_{-1}(-\vec{k}) & T_{14} f_{+1}(-\vec{k}) \\ T_{15} f_0(-\vec{k}) & -T_{15} f_{-1}(-\vec{k}) \\ -T_{14} f_{+1}(-\vec{k}) & -T_{13} f_0(-\vec{k}) \end{bmatrix}, \\
H_{dd}^{(3)} &= \begin{bmatrix} T_{13} f_0(-\vec{k}) & T_{15} f_{-1}(-\vec{k}) & -T_{14} f_{+1}(-\vec{k}) \\ T_{14} f_{+1}(-\vec{k}) & -T_{15} f_0(-\vec{k}) & -T_{13} f_{-1}(-\vec{k}) \end{bmatrix}, \\
H_{dd}^{(4)} &= \begin{bmatrix} T_{16} f_{+1}(-\vec{k}) & T_{17} f_0(-\vec{k}) \\ T_{17} f_{-1}(-\vec{k}) & T_{16} f_{+1}(-\vec{k}) \end{bmatrix}
\end{aligned} \tag{5.29}$$

In the equations presented above, the functions  $f$  represent  $\vec{k}$ -dependent terms that were defined in detail in the preceding section, while the amplitudes  $T$  are determined by the geometric configuration of the heterostructure and the associated Slater-Koster parameters.

The amplitudes  $T$  define the strength of the interlayer interactions, specifically characterizing the Mo-W interactions (denoted by the subscript  $dd$ ), Se<sub>2</sub>-Se<sub>2</sub> interactions (subscript  $pp$ ), and metal-chalcogen interactions (subscripts  $pd$  and  $dp$ ). These interactions depend on the geometric configuration of the heterostructure. All the relevant distances are depicted in Fig. 5.1(b).

To streamline the notation, we define the following composite distances based on the layer geometry:

$$d_{pp} = \sqrt{d_{zpp}^2 + d_{\parallel}^2}, \quad d_{dd} = \sqrt{d_{zdd}^2 + d_{\parallel}^2}, \quad d_{dp} = d_{zdp}, \quad d_{pd} = d_{zpd}, \quad (5.30)$$

where the vertical offsets  $d_{zdp}$ ,  $d_{zpd}$ , and  $d_{zpp}$  are expressed as:

$$d_{zdp} = d_{zdd} - d_{\perp}^{\text{WSe}_2}, \quad d_{zpd} = d_{zdd} - d_{\perp}^{\text{MoSe}_2}, \quad d_{zpp} = d_{zdd} - d_{\perp}^{\text{MoSe}_2} - d_{\perp}^{\text{WSe}_2}. \quad (5.31)$$

The parameter  $d_{\parallel}$  represents the lateral distance between interlayer atoms, and  $d_{zdd}$  denotes the overall vertical separation between the Mo and W atoms in the heterostructure. The numerical values assigned to these parameters were extracted from DFT calculations:

$$d_{\perp} = \frac{3.323}{\sqrt{3}} \text{ \AA}, \quad d_{\perp}^{\text{MoSe}_2} = 1.669 \text{ \AA}, \quad d_{\perp}^{\text{WSe}_2} = 1.680 \text{ \AA}, \quad d_{zdd} = 6.40 \text{ \AA}. \quad (5.32)$$

With these definitions, the specific expressions for the 17 amplitudes  $T$  that parameterize the interlayer couplings can be derived. For the  $p$ - $p$  couplings, the amplitudes are given as follows:

$$\begin{aligned} T_1 &= \frac{1}{4} \left( \left[ 1 - \left( \frac{d_{zpp}}{d_{pp}} \right)^2 \right] V_{pp\sigma} + \left[ 1 + \left( \frac{d_{zpp}}{d_{pp}} \right)^2 \right] V_{pp\pi} \right), \\ T_2 &= \frac{1}{2\sqrt{2}} \frac{d_{\parallel} d_{zpp}}{d_{pp}^2} (V_{pp\sigma} - V_{pp\pi}), \\ T_3 &= -\frac{1}{4} \left( \frac{d_{\parallel}}{d_{pp}} \right)^2 (V_{pp\sigma} - V_{pp\pi}), \\ T_4 &= -\frac{1}{2} \left( \left( \frac{d_{zpp}}{d_{pp}} \right)^2 V_{pp\sigma} + \left( 1 - \left( \frac{d_{zpp}}{d_{pp}} \right)^2 \right) V_{pp\pi} \right), \end{aligned} \quad (5.33)$$

Subsequently, we define the amplitudes for the  $p$ - $d$  and  $d$ - $p$  interlayer couplings as follows:

$$\begin{aligned} T_5 &= \frac{1}{\sqrt{2}} V_{pd\sigma}, \\ T_6 &= -\frac{1}{\sqrt{2}} V_{pd\pi}, \\ T_7 &= \frac{1}{\sqrt{2}} V_{dp\sigma}, \\ T_8 &= \frac{1}{\sqrt{2}} V_{dp\pi}. \end{aligned} \quad (5.34)$$

Lastly, for the  $d$ - $d$  interlayer couplings, the amplitudes are expressed as:

$$\begin{aligned} T_9 &= \frac{1}{8} \left[ \left( 3 - 6 \left( \frac{d_{zdd}}{d_{dd}} \right)^2 + 3 \left( \frac{d_{zdd}}{d_{dd}} \right)^4 \right) V_{dd\sigma} \right. \\ &\quad \left. + \left( 4 - 4 \left( \frac{d_{zdd}}{d_{dd}} \right)^4 \right) V_{dd\pi} + \left( 1 + 6 \left( \frac{d_{zdd}}{d_{dd}} \right)^2 + \left( \frac{d_{zdd}}{d_{dd}} \right)^4 \right) V_{dd\delta} \right], \\ T_{10} &= \frac{1}{4} \sqrt{\frac{3}{2}} \left( \frac{d_{\parallel}}{d_{dd}} \right)^2 \left[ \left( -1 + 3 \left( \frac{d_{zdd}}{d_{dd}} \right)^2 \right) V_{dd\sigma} - 4 \left( \frac{d_{zdd}}{d_{dd}} \right)^2 V_{dd\pi} + \left( 1 + \left( \frac{d_{zdd}}{d_{dd}} \right)^2 \right) V_{dd\delta} \right], \\ T_{11} &= \frac{1}{8} \left( \frac{d_{\parallel}}{d_{dd}} \right)^4 (3V_{dd\sigma} - 4V_{dd\pi} + V_{dd\delta}), \\ T_{12} &= \frac{1}{4} \left[ \left( 1 - 6 \left( \frac{d_{zdd}}{d_{dd}} \right)^2 + 9 \left( \frac{d_{zdd}}{d_{dd}} \right)^4 \right) V_{dd\sigma} + 12 \left( \left( \frac{d_{zdd}}{d_{dd}} \right)^2 - \left( \frac{d_{zdd}}{d_{dd}} \right)^4 \right) V_{dd\pi} \right. \\ &\quad \left. + \left( 3 - 6 \left( \frac{d_{zdd}}{d_{dd}} \right)^2 + 3 \left( \frac{d_{zdd}}{d_{dd}} \right)^4 \right) V_{dd\delta} \right], \end{aligned}$$

$$\begin{aligned}
T_{13} &= \frac{1}{4} \frac{d_{\parallel}}{d_{dd}} \frac{d_{zdd}}{d_{dd}} \left[ \left( 3 - 3 \left( \frac{d_{zdd}}{d_{dd}} \right)^2 \right) V_{dd\sigma} + 4 \left( \frac{d_{zdd}}{d_{dd}} \right)^2 V_{dd\pi} - \left( 3 + \left( \frac{d_{zdd}}{d_{dd}} \right)^2 \right) V_{dd\delta} \right], \\
T_{14} &= -\frac{1}{4} \left( \frac{d_{\parallel}}{d_{dd}} \right)^3 \frac{d_{zdd}}{d_{dd}} (3V_{dd\sigma} - 4V_{dd\pi} + V_{dd\delta}), \\
T_{15} &= \frac{1}{2} \sqrt{\frac{3}{2}} \frac{d_{\parallel}}{d_{dd}} \frac{d_{zdd}}{d_{dd}} \left[ \left( -1 + 3 \left( \frac{d_{zdd}}{d_{dd}} \right)^2 \right) V_{dd\sigma} + \left( 2 - 4 \left( \frac{d_{zdd}}{d_{dd}} \right)^2 \right) V_{dd\pi} \right. \\
&\quad \left. + \left( -1 + \left( \frac{d_{zdd}}{d_{dd}} \right)^2 \right) V_{dd\delta} \right], \\
T_{16} &= \frac{1}{2} \left[ 3 \left( \left( \frac{d_{zdd}}{d_{dd}} \right)^2 - \left( \frac{d_{zdd}}{d_{dd}} \right)^4 \right) V_{dd\sigma} + \left( 1 - 3 \left( \frac{d_{zdd}}{d_{dd}} \right)^2 + 4 \left( \frac{d_{zdd}}{d_{dd}} \right)^4 \right) V_{dd\pi} \right. \\
&\quad \left. + \left( 1 - \left( \frac{d_{zdd}}{d_{dd}} \right)^4 \right) V_{dd\delta} \right], \\
T_{17} &= -\frac{1}{2} \left( \frac{d_{\parallel}}{d_{dd}} \right)^2 \left[ 3 \left( \frac{d_{zdd}}{d_{dd}} \right)^2 V_{dd\sigma} + \left( 1 - 4 \left( \frac{d_{zdd}}{d_{dd}} \right)^2 \right) V_{dd\pi} + \left( -1 + \left( \frac{d_{zdd}}{d_{dd}} \right)^2 \right) V_{dd\delta} \right], \quad (5.35)
\end{aligned}$$

The parameters for the complete TB model of the MoSe<sub>2</sub>/WSe<sub>2</sub> heterostructure are listed in Tab. 5.2. This table outlines the Slater-Koster parameters, providing values for the MoSe<sub>2</sub> and WSe<sub>2</sub> monolayers as well as for the interlayer couplings. The parameters include on-site energies for different orbitals, spin-orbit coupling strengths, and hopping amplitudes for various orbital combinations. These values reflect the intricate interplay of geometric configuration, material properties, and interlayer interactions.

In addition to these parameters, Tab. 5.3 highlights the orbital contributions to the energy bands for the even subspace. Specifically, it provides a breakdown of the primary atomic orbitals contributing to the top of the VB and the bottom of the CB, illustrating the dominant roles of certain orbitals in shaping the electronic properties. This detailed parameterization serves as the foundation for accurately modeling the electronic structure and interlayer coupling effects in MoSe<sub>2</sub>/WSe<sub>2</sub> heterostructures.

### 5.2.5 Full Tight-Binding Model Dispersion and Spin-Layer-Orbital Properties

Next, we parameterize a total of 26 intralayer and 9 interlayer Slater-Koster parameters, as listed in Tab. 5.2. These parameters have been optimized to ensure an accurate fit of the TB model to the DFT results described in Sec. 5.1. The fitting process employs the differential evolution (DE) method [494], with specific emphasis on achieving degenerate CB minima at the *K* and *Q* valleys and reproducing the VB maxima at *K* and  $\Gamma$ . Additionally, to accurately capture the spin ordering of bands, an extra term is incorporated into the DE loss function.

The single-particle spectrum and corresponding wave functions within the TB framework are obtained by diagonalizing the heterostructure Hamiltonian given in Eq. (5.23). The resulting spin-resolved TB electronic structure is shown in Fig. 5.3. The model reproduces key microscopic features of spin and layer contributions in agreement with the *ab initio* results. Specifically, the conduction band exhibits degenerate minima at the *K* and *Q* valleys, while the valence band maxima at *K* and  $\Gamma$  show a slightly larger splitting compared to the DFT calculations. The direct energy gap at the *K* point (*K-K* transition) is approximately 1.03 eV. Importantly, the correct spin-layer ordering of bands around the *K*-point gap is successfully captured.

**Table 5.2:** Slater-Koster parameters for the MoSe<sub>2</sub>/WSe<sub>2</sub> heterostructure in the full/simplified TB model.

	MoSe <sub>2</sub>	WSe <sub>2</sub>	interlayer
$E_d$	-0.140/-0.240	-0.220/-0.210	-
$E_{p_1}$	-5.060/-5.258	-4.234/-4.419	-
$E_{p_0}$	-5.268/-5.620	-4.620/-4.890	-
$V_{dp\sigma}$	-2.980/-2.976	-3.251/-3.262	-0.044/ -
$V_{pd\sigma}$	-	-	-1.344/ -
$V_{dp\pi}$	1.073/1.175	1.060/1.020	0.411/ -
$V_{pd\pi}$	-	-	-1.780/ -
$V_{dd\sigma}$	-1.028/-0.923	-1.240/-1.223	0.196/-0.500
$V_{dd\pi}$	0.838/0.751	0.817/0.860	-0.480/2.000
$V_{dd\delta}$	0.229/0.225	0.255/0.238	0.091/-0.330
$V_{pp\sigma}$	1.490/1.397	1.258/1.079	1.393/-1.101
$V_{pp\pi}$	-0.550/-0.468	-0.350/-0.366	-0.012/-0.155
$E_{p_1}^{\text{odd}}$	-5.051/-5.398	-4.132/-4.559	-
$E_{p_0}^{\text{odd}}$	-5.236/-5.598	-4.554/-5.029	-
$E_d^{\text{odd}}$	-0.112/-0.380	-0.032/-0.350	-
$\lambda_M$	0.093/0.093	0.236/0.236	-
$\lambda_{X_2}$	0.175/0.100	-0.275/-0.195	-

Additionally, the spin-dependent nature of optical transitions is reproduced: the direct transition at  $K$ - $K$  between the top VB and bottom CB is spin-forbidden (dark), whereas the indirect  $K$ - $Q$  transition is spin-allowed (bright), as illustrated in Fig. 5.3(a). The band splittings due to SOC are also consistent with DFT. Furthermore, Fig. 5.3(b) highlights the layer-resolved contributions, confirming the type-II band alignment in the heterostructure. Notably, the TB model captures the interlayer electron delocalization effect at the  $Q$  valley in the conduction band.

To gain further insight, we decompose the wave functions in terms of orbital contributions, identifying the dominant orbitals for each band at high-symmetry  $k$ -points. Consistent with DFT (see Sec. 5.1), the low-energy states near  $K$  and  $Q$  primarily arise from symmetric (even) orbitals. Specifically, the VB is dominated by metal atom orbitals  $4d_{m=0}$  for Mo and  $5d_{m=0}$  for W, while the CB predominantly features  $4d_{m=\pm 2}$  orbitals for Mo and  $5d_{m=\pm 2}$  for W. A detailed breakdown of orbital contributions at  $K$  and  $Q$  is presented in Tab. 5.2.

### 5.2.6 Simplified Tight-Binding Model

We acknowledge that the full  $44 \times 44$  TB model is quite complex and may present significant challenges for practical implementation. Although we intend to address a systematic reduction of this model in future work, we present here a simplified analysis of the interlayer couplings, which only considers the coupling of the even blocks of orbitals within each monolayer. This approach allows us to focus on a more manageable even-only TB model, which consists of 6 orbitals per layer

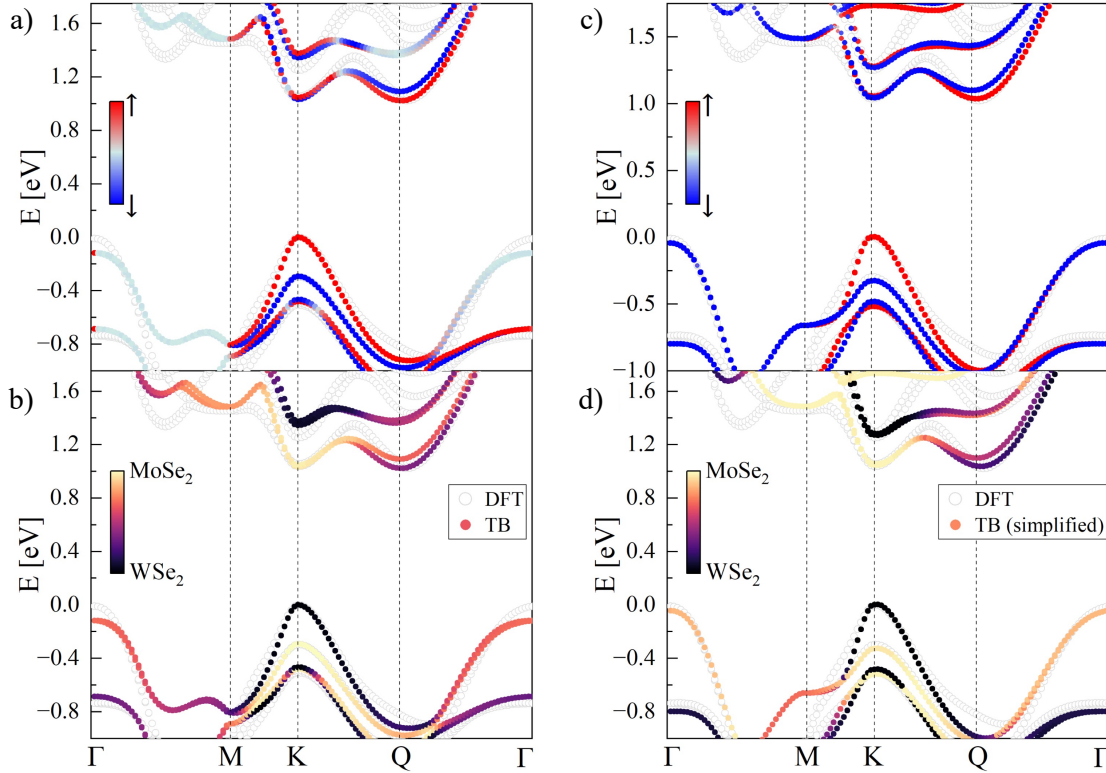


**Figure 5.3:** Electronic structure of the MoSe<sub>2</sub>/WSe<sub>2</sub> heterostructure as captured by the (a,b) full and (c,d) simplified TB model. The panels display: (a,c) spin-resolved band structure and (b,d) layer-resolved band structure. In both panels, the color coding provides insight into the respective properties: red and blue represent spin-up and spin-down states, while yellow and black correspond to contributions from the MoSe<sub>2</sub> and WSe<sub>2</sub> layers, respectively. For comparison, open circles indicate the results obtained from DFT calculations, serving as a benchmark for the TB model's accuracy. The parameter set used for these calculations is provided in Tab. 5.2.

per spin. Additionally, we have simplified the interlayer interactions to retain the most significant orbital couplings. In the following, we explore the details and behavior of this simplified TB model to better understand its implications.

Incorporating the full TB model that accounts for all interlayer orbital interactions, we now introduce a simplified approach that preserves the key features of the MoSe<sub>2</sub>/WSe<sub>2</sub> heterostructure, as revealed by DFT studies and captured by the full TB model described in Sec. 5.2.4. Guided by the primary orbital contributions to the valence and conduction bands at high symmetry points, which were identified in the DFT calculations, we modify the interlayer interaction Hamiltonian,  $H_{\text{inter}}$ , originally defined in Eq. (5.24). In this simplified version, we retain only the most significant interlayer couplings corresponding to the  $p_0$ - $p_0$ ,  $d_0$ - $d_0$ ,  $d_{-2}$ - $d_{+2}$ , and  $d_{+2}$ - $d_{-2}$  interactions, all of which arise from the even orbital subspace. As a result, we reduce  $H_{\text{inter}}$  to the following compact form:

$$H_{\text{inter}} = \begin{bmatrix} H_{dd} & 0 \\ 0 & H_{pp} \end{bmatrix}, \quad (5.36)$$

**Table 5.3:** Orbital contributions from the full TB model in the even subspace, highlighting the atomic orbitals that make the primary contributions to the top VB and the bottom CB. The contributions are expressed as percentages for each high symmetry point, providing a detailed breakdown of the orbital character at key points in the BZ.

		K, VB	K, CB	Q, CB	$\Gamma$ , VB
		$\downarrow/\uparrow$	$\downarrow/\uparrow$	$\downarrow/\uparrow$	$\downarrow/\uparrow$
Se <sub>2</sub> <sup>top</sup>	4p <sub>-1</sub>	-	0%/12%	2%/0%	-
	4p <sub>0</sub>	-	-	7%/1%	3%/3%
	4p <sub>+1</sub>	-	-	1%/0%	-
Mo	4d <sub>-2</sub>	-	-	13%/1%	-
	4d <sub>0</sub>	-	0%/83%	11%/1%	32%/32%
	4d <sub>+2</sub>	-	-	3%/0%	-
Se <sub>2</sub> <sup>bottom</sup>	4p <sub>-1</sub>	-	-	4%/0%	-
	4p <sub>0</sub>	-	-	9%/0%	-
	4p <sub>+1</sub>	-	-	1%/0%	-
W	5d <sub>-2</sub>	97%/0%	-	1%/0%	-
	5d <sub>0</sub>	-	1%/0%	17%/1%	15%/15%
	5d <sub>+2</sub>	-	0%/1%	24%/0%	-

where the individual coupling blocks  $H_{dd}$  and  $H_{pp}$  are defined as:

$$\begin{aligned}
 H_{dd} &= \\
 &= \begin{bmatrix} 0 & 0 & f_{-1}(-\vec{k})T_{11} \\ 0 & f_{+1}(-\vec{k})T_{12} & 0 \\ f_0(-\vec{k})T_{11} & 0 & 0 \end{bmatrix}, \tag{5.37}
 \end{aligned}$$

and

$$H_{pp} = \begin{bmatrix} 0 & 0 & 0 \\ 0 & f_{+1}(\vec{k})T_4 & 0 \\ 0 & 0 & 0 \end{bmatrix} \tag{5.38}$$

where the functions  $f$  and the amplitudes  $T$  are defined in the previous section. This simplification significantly reduces the complexity of the interlayer Hamiltonian while maintaining the essential features that define the electronic structure of the MoSe<sub>2</sub>/WSe<sub>2</sub> heterostructure, as observed in the DFT results. By focusing only on the most impactful couplings, we ensure that the model remains computationally tractable without losing the accuracy required to capture the essential physical behavior of the system.

This simplification results in a total of 5 interlayer Slater-Koster parameters, as compared to the 9 parameters in the full TB model, and 26 intralayer parameters (13 for each layer), yielding a subspace of 31 Slater-Koster parameters that must be parametrized. These parameters are summarized in Tab. 5.2, which presents the complete set of parameters for the simplified TB model of the MoSe<sub>2</sub>/WSe<sub>2</sub> heterostructure.

The electronic structure of the MoSe<sub>2</sub>/WSe<sub>2</sub> heterostructure, derived by diagonalizing the Hamiltonian in Eq. (5.23) with the simplified interlayer interactions as defined in Eqs. (5.37) and

(5.38), is shown in Fig. 5.3(c,d). The type-II band alignment is correctly captured, with a direct  $K$ - $K$  energy gap of approximately 1 eV. The band dispersion is characterized by degenerate minima in the CB at the  $K$  and  $Q$  points, as well as degenerate maxima in the VB at the  $K$  and  $\Gamma$  points, which are in nearly perfect agreement with the DFT results. The effective masses around the  $K$  valley are also consistent with DFT. Moreover, the spin-valley locking effect near the  $K$  valley is reproduced, as seen in Fig. 5.3(c).

The intralayer spin splittings due to spin-orbit coupling (SOC) at the  $K$  point are found to be  $\Delta_{\text{SOC}}^{CB} = 12$  meV and  $\Delta_{\text{SOC}}^{VB} = 189$  meV for MoSe<sub>2</sub>, and  $\Delta_{\text{SOC}}^{CB} = 30$  meV and  $\Delta_{\text{SOC}}^{VB} = 521$  meV for WSe<sub>2</sub>, all of which agree with the DFT results. However, the effects of spin mixing resulting from interactions between even and odd orbitals, particularly in the low-energy bands, are not captured by this simplified model. Additionally, Fig. 5.3(d) reveals that the electron in the  $Q$  valley is delocalized across the layers, though the extent of this interlayer delocalization is not quantitatively captured in the model.

To further investigate the electronic structure, we performed an analysis of the orbital contributions to the energy bands. The results for the orbital compositions at the  $K$  and  $Q$  points are presented in Tab. 5.3. These contributions show qualitative agreement with those obtained from the full TB model. Specifically, the low-energy bands are primarily composed of the even orbitals. At the  $K$  valley, the VB is predominantly composed of the  $4d_{m=\pm 2}$  orbitals from Mo and the  $5d_{m=\pm 2}$  orbitals from W, while the CB is mainly composed of the  $4d_{m=0}$  orbitals from Mo and the  $5d_{m=0}$  orbitals from W. Furthermore, the two lowest CB states around the  $Q$  valley are composed chiefly of orbitals with  $m = \pm 2$ .

## 5.3 Electric Field Effect

In this section, we investigate the effect of an applied vertical electric field on the energetic ordering of the valleys in the MoSe<sub>2</sub>/WSe<sub>2</sub> heterostructure. We demonstrate that this electric field can control the relative position of the valleys, which is an important feature for tuning the electronic properties of the system. The electric field is incorporated into the TB model by adding an additional Hamiltonian term,  $H_E$ , that accounts for the interaction between the system and the external field.

The applied electric field, denoted as  $E_z$ , corresponds to negative and positive voltages  $V_E(z) = E_z z$  at the lower and upper TMDC layers, respectively, e.g., generated by vertical gates placed above and below (substrate) the heterostructure. Specifically, the voltage at any point  $z$  in the heterostructure is given by  $V_E(z) = E_z z$ , where  $z$  represents the position within the heterostructure. The voltage distribution is such that the upper layer of the heterostructure (e.g., MoSe<sub>2</sub>) experiences a positive potential, while the bottom layer (e.g., WSe<sub>2</sub>) is subjected to a negative potential. This potential difference is induced by vertical gates placed above and below the heterostructure, with the voltage at the interface between the two layers set to zero. For simplicity, we assume that the voltage at the metal atoms in the upper layer is  $+\frac{1}{2}E_z d_{zdd}$  and at the metal atoms in the lower layer it is  $-\frac{1}{2}E_z d_{zdd}$ , where  $d_{zdd}$  is the interlayer distance.

### 5.3.1 Tight-Binding Model in Electric Field

To model the effect of the electric field within the TB framework, we follow a similar approach to our previous work [483], where the electric field term,  $H_E$ , is added to the Hamiltonian for

both layers of the heterostructure. The expression for the electric field Hamiltonian block,  $H_E$ , is written as:

$$\hat{H}_E = \begin{bmatrix} H_E^{\text{MoSe}_2} \otimes \mathbf{1}_\sigma & 0 \\ 0 & H_E^{\text{WSe}_2} \otimes \mathbf{1}_\sigma \end{bmatrix}, \quad (5.39)$$

where each of the individual blocks  $H_E^{\text{MoSe}_2}$  and  $H_E^{\text{WSe}_2}$  represents the electric field effect on the MoSe<sub>2</sub> and WSe<sub>2</sub> monolayers, respectively. These blocks are further divided into diagonal and off-diagonal terms that describe the impact of the electric field on both the even and odd orbital subspaces.

$$H_E^{\text{MoSe}_2} = \begin{bmatrix} \hat{V}_E^{\text{ev}} & \hat{V}_E^{\text{ev-odd}} \\ & \hat{V}_E^{\text{odd}} \end{bmatrix}, \quad H_E^{\text{WSe}_2} = \begin{bmatrix} -\hat{V}_E^{\text{ev}} & \hat{V}_E^{\text{ev-odd}} \\ & -\hat{V}_E^{\text{odd}} \end{bmatrix}. \quad (5.40)$$

The diagonal blocks,  $\hat{V}_E^{\text{ev}}$  and  $\hat{V}_E^{\text{odd}}$ , represent the voltage shifts in the even and odd orbital subspaces, respectively, and are given by:

$$\hat{V}_E^{\text{ev}} = E_z \frac{1}{2} d_{z_{dd}} \text{diag}(1, 1, 1, 1, 1, 1), \quad \hat{V}_E^{\text{odd}} = E_z \frac{1}{2} d_{z_{dd}} \text{diag}(1, 1, 1, 1, 1, 1), \quad (5.41)$$

where the voltage difference is proportional to the applied electric field  $E_z$  and the interlayer distance  $d_{z_{dd}}$ . The off-diagonal block,  $\hat{V}_E^{\text{ev-odd}}$ , couples the even and odd orbital subspaces and is given by the following matrix form:

$$\hat{V}_E^{\text{ev-odd}} = \begin{bmatrix} 0 & 0 & 0 & 0 & 0 \\ 0 & 0 & 0 & 0 & 0 \\ 0 & 0 & 0 & 0 & 0 \\ 0 & 0 & V_{X_2} & 0 & 0 \\ 0 & 0 & 0 & V_{X_2} & 0 \\ 0 & 0 & 0 & 0 & V_{X_2} \end{bmatrix}. \quad (5.42)$$

Here,  $V_{X_2}$  represents the potential difference between chalcogen atoms in the dimer, defined as  $V_{X_2} = \frac{1}{2}(V_{X^{(1)}} - V_{X^{(2)}})$ , where  $V_{X^{(1)}}$  and  $V_{X^{(2)}}$  are the potentials at the respective atoms in the dimer. This coupling term allows for the interaction between even and odd orbitals, modifying the energy levels accordingly.

To transform the Hamiltonian into a form suitable for diagonalization in the dimer basis, we begin with the single-atomic basis for each Se atom in the monolayer. The Hamiltonian for a single monolayer of TMDC crystals is expressed in the basis  $\{d_{-2}, d_0, d_2, p_{-1}^t, p_0^t, p_1^t, d_{-1}, d_1, p_{-1}^b, p_0^b, p_1^b\}$ , where  $p^t$  and  $p^b$  refer to  $p$ -orbitals on the top and bottom Se atoms, respectively. The electric field Hamiltonian for a single layer is then written as an  $11 \times 11$  diagonal matrix:

$$H_E^{\text{atom}} = \text{diag}(V_M, V_M, V_M, V_{X^t}, V_{X^t}, V_{X^t}, V_M, V_M, V_{X^b}, V_{X^b}, V_{X^b}), \quad (5.43)$$

where  $V_M$  represents the voltage at the metal atoms, and  $V_{X^t}$  and  $V_{X^b}$  are the voltages at the top and bottom chalcogen atoms, respectively.

To transform the Hamiltonian from the single-atomic basis to the dimer basis, we apply the

unitary transformation matrix  $\hat{U}_E$ , which relates the two bases:

$$\hat{U}_E = \frac{1}{\sqrt{2}} \begin{bmatrix} \sqrt{2} & 0 & 0 & 0 & 0 & 0 & 0 & 0 & 0 & 0 & 0 \\ 0 & \sqrt{2} & 0 & 0 & 0 & 0 & 0 & 0 & 0 & 0 & 0 \\ 0 & 0 & \sqrt{2} & 0 & 0 & 0 & 0 & 0 & 0 & 0 & 0 \\ 0 & 0 & 0 & 1 & 0 & 0 & 0 & 0 & 1 & 0 & 0 \\ 0 & 0 & 0 & 0 & 1 & 0 & 0 & 0 & 0 & -1 & 0 \\ 0 & 0 & 0 & 0 & 0 & 1 & 0 & 0 & 0 & 0 & 1 \\ 0 & 0 & 0 & 0 & 0 & 0 & \sqrt{2} & 0 & 0 & 0 & 0 \\ 0 & 0 & 0 & 0 & 0 & 0 & 0 & \sqrt{2} & 0 & 0 & 0 \\ 0 & 0 & 0 & 1 & 0 & 0 & 0 & 0 & -1 & 0 & 0 \\ 0 & 0 & 0 & 0 & 1 & 0 & 0 & 0 & 0 & 1 & 0 \\ 0 & 0 & 0 & 0 & 0 & 1 & 0 & 0 & 0 & 0 & -1 \end{bmatrix}. \quad (5.44)$$

By applying this unitary transformation, we can rewrite the electric field Hamiltonian in the dimer basis, resulting in the form given in Eqs. (5.39) and (5.40). This transformation allows us to fully capture the effects of the electric field on the heterostructure's electronic properties and make predictions regarding valley shifts, spin splittings, and other key aspects of the system's behavior in an applied electric field perpendicular to the layers.

### 5.3.2 Effect of an Electric Field on the TMDC Heterostructure: DFT and Full TB Comparison

The evolution of the  $K$ ,  $Q$ , and  $\Gamma$  valley states as a function of the vertical electric field  $E_z$  is shown in Fig. 5.4. We observe good agreement between the DFT results (Fig. 5.4(a)) and those obtained from the TB model (Fig. 5.4(b,c)), validating the effectiveness of the simplified TB model in capturing key features of the heterostructure's electronic properties. For reference, we set the top of the VB at the  $K$  point to zero energy for all values of the applied electric field.

In both the DFT and TB results, we observe clear trends in the evolution of both the VB and CB as  $E_z$  increases. At large negative values of  $E_z$ , both the VB maximum and the CB minimum occur at the  $K$  valley. As the electric field is increased, the CB minimum transitions from the  $K$  valley to the  $Q$  valley. A similar switching behavior is observed for the VB, where the maximum shifts from the  $K$  to the  $\Gamma$  valley. This suggests that the MoSe<sub>2</sub>/WSe<sub>2</sub> heterostructure behaves as a multi-valley system, in which the occupation of different valleys can be controlled using a moderate vertical electric field.

Turning our focus to the spin properties, we find that the applied electric field does not alter the spin orientation in the  $K$  valley for either the VB or CB, as shown in Fig. 5.4(b). In contrast, for negative  $E_z$ , spin-mixing effects become evident at the  $Q$  valley. The SOC splittings in the CB at the  $K$  valley remain nearly constant, whereas the SOC splittings in the VB are significantly influenced by the applied electric field. At the  $Q$  valley, the spin splitting between the two CB bands increases with increasing positive  $E_z$ . Moreover, we observe an intriguing spin-flip phenomenon across the gap: the lowest CB at the  $K$  valley, which initially exhibits a spin-dark, momentum-bright optical transition, undergoes a reversal, becoming spin-bright and momentum-dark as  $E_z$  increases.

Qualitatively, the TB model captures the essential features seen in the DFT results. However, there is one noticeable discrepancy: the TB model does not fully reproduce the strong anticrossing

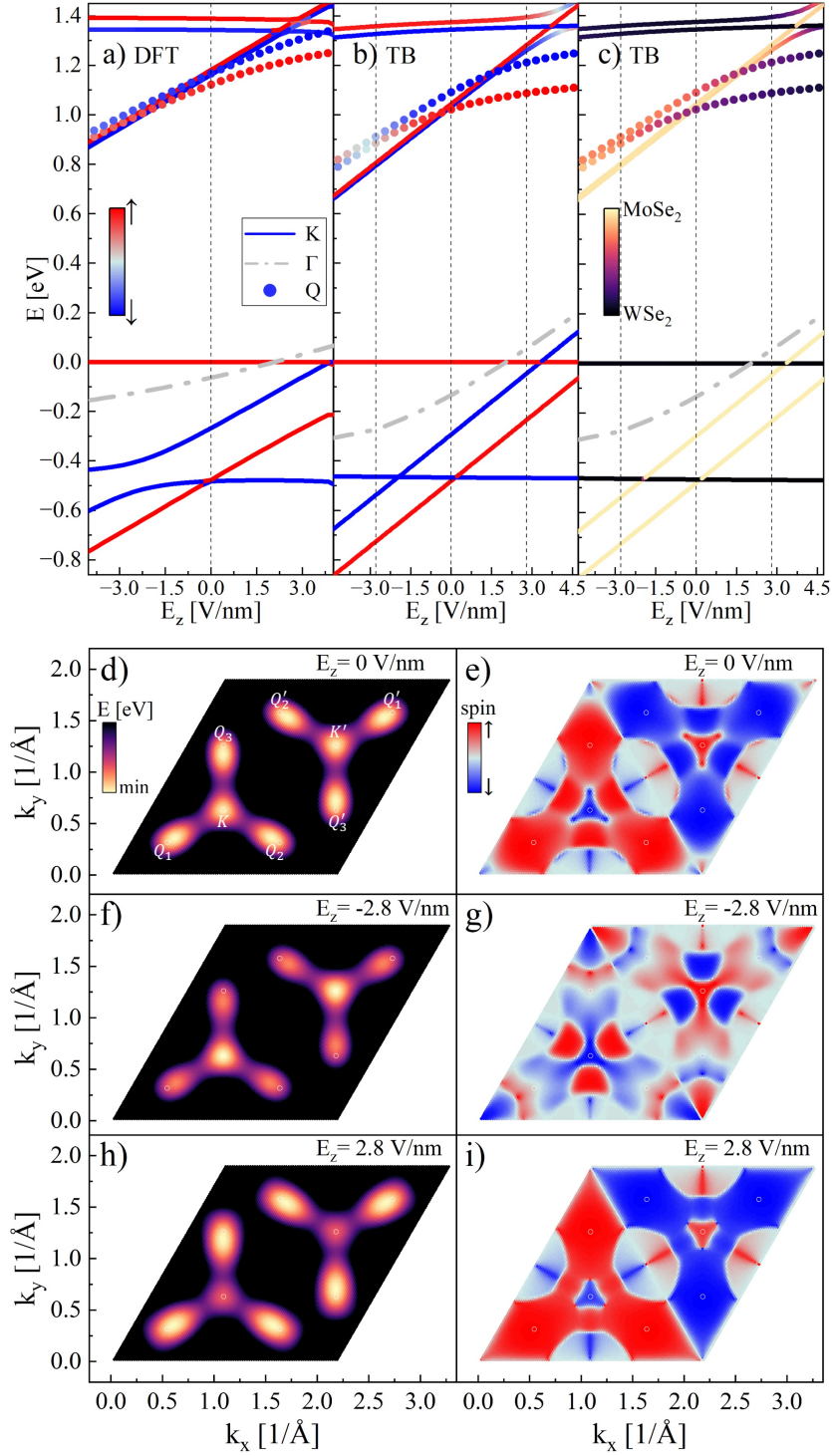


**Figure 5.4:** The effect of a vertical electric field on the electronic structure. (a-c) The energies of selected bands as a function of the applied vertical electric field  $E_z$ , adapted from Ref. [495], for the  $K$ ,  $Q$ , and  $\Gamma$  points. The results are presented for both (a) DFT and (b,c) TB calculations. Different line styles represent the  $K$ ,  $Q$ , and  $\Gamma$  valleys, with colors corresponding to (a,b) spin and (c) layer compositions. Due to the degeneracy of the VB at the  $\Gamma$  point, spin- and layer-resolved notation is omitted in this case. Vertical dashed lines indicate the electric field strengths of 0 and  $\pm 0.4$  V/nm. (d-f,h) Energy maps and (e,g,i) spin-resolved color maps of the lowest CB across the entire BZ for three different values of the applied electric field: (d,e)  $E_z = 0$  V/nm, (f,g)  $E_z = -2.8$  V/nm, and (h,i)  $E_z = 2.8$  V/nm. White circles mark the high-symmetry points selected for the plots.

observed in the VB at the  $K$  point. Nevertheless, it appears that the simplified model introduced in Sec. 5.2.6 can partially account for this mixing effect (see Fig. 5.5).

Next, we analyze the evolution of the layer contributions, which is directly accessible within the TB framework (Fig. 5.4(c)). We find that the electric field couples and mixes the CB much more strongly than the VB. In the case of the CB, the  $K$  valley primarily originates from the MoSe<sub>2</sub> layer, but for large values of  $E_z$ , it becomes increasingly mixed with the WSe<sub>2</sub> layer. For the  $Q$  valley, the layer contribution is already mixed at  $E_z = 0$ , and it continues to evolve continuously as the electric field is applied. This layer mixing not only facilitates valley switching between  $K$  and  $Q$  but also induces a transition from layer-localized to layer-delocalized bands in the CB. This suggests that the occupation of valleys in the CB involves not just a switching between valleys, but also a change in the nature of the electronic states from being primarily localized to one layer to being spread across both layers.

Now, we move on to the analysis of the CBs across the entire BZ as a function of the applied vertical electric field  $E_z$ , as summarized in Fig. 5.4(d-i). We begin by considering the system with no electric field applied, shown in Fig. 5.4(d,e). In agreement with spin-valley locking, the two non-equivalent valleys,  $K$  and  $K'$ , are distinguished by spin, as depicted in Fig. 5.4(e). In the CB, each of these valleys is surrounded by three  $Q$  points, forming a system of six non-equivalent  $Q$  points within the BZ. Additionally, the  $K$  and  $Q$  valleys are nearly degenerate in energy, as shown in Fig. 5.4(d).

Next, we apply a strong electric field of  $E_z = -0.4$  V/nm, as illustrated in Fig. 5.4(f,g). This results in the breaking of the degeneracy between the energy minima at the  $K$  and  $Q$  valleys. In particular, Fig. 5.4(g) reveals a change in the spin at the  $Q$  valleys, consistent with the flip of the two lowest CBs around the  $Q$  valley observed earlier in Fig. 5.4(b). Finally, when the electric field is increased to  $E_z = 0.4$  V/nm, as shown in Fig. 5.4(h,i), we observe a further breaking of the energetic degeneracy, this time in favor of the  $Q$  valleys. This results in an  $E_z$ -field-controlled contribution of  $Q$  valleys into the spectral content of the electronic states.

It is also worth noting that a similar CB structure, composed of three valleys near each  $K$ -point [496], appears in bilayer graphene subjected to a perpendicular electric field. This effect is driven by the interplay between trigonal warping and the  $E_z$ -field-induced interlayer asymmetry band gap [497]. These triple-degenerate states have been studied theoretically [147, 152] and experimentally [498–500], though no clear method for effectively manipulating these triply-degenerate states has been proposed. In the next section, we will attempt to address this question.

### 5.3.3 Simplified TB Approach with Vertical Electric Field

In the previous section, we explored the electronic structure and valley behavior of the vdW MoSe<sub>2</sub>/WSe<sub>2</sub> heterostructure in an external electric field  $E_z$  using the full TB model. While this approach provides a detailed description, the complexity of the full model makes it challenging to perform large-scale systematic studies. To overcome these limitations and gain a more intuitive understanding, we now turn to a simplified version of the TB model, which captures the essential physics with reduced computational effort.

In this next step, we apply the methodology outlined in Sec. 5.3 to study the evolution of the electronic structure under the influence of the vertical electric field. The spin and layer contributions to the energy bands around the gap, for the high-symmetry points  $K$ ,  $Q$ , and  $\Gamma$ , are presented in Fig. 5.5. In contrast to the full TB model, where the applied electric field influences

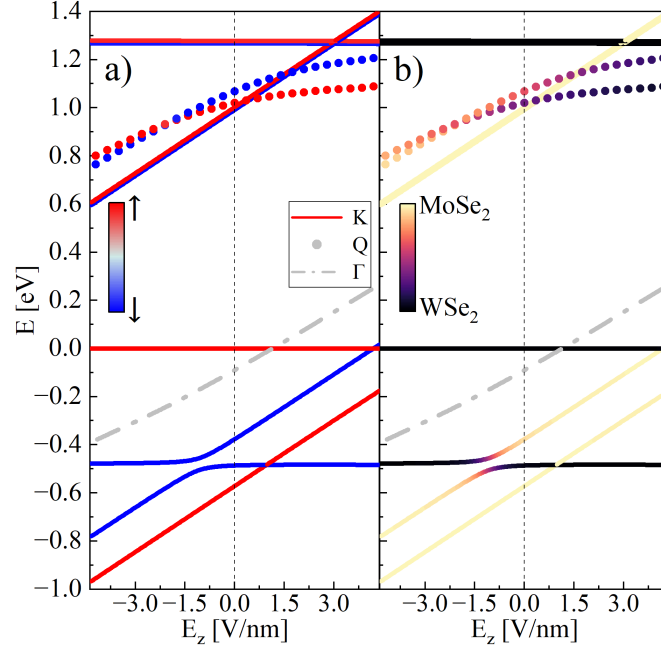


**Figure 5.5:** The effect of a vertical electric field on the electronic structure in the simplified TB model. Energies of selected bands are shown as a function of the applied  $E_z$  for the  $K$ ,  $Q$ , and  $\Gamma$  valleys. The top of the VB at the  $K$  point is set to  $E = 0$  eV. Different types of lines represent the following valleys:  $K$  (solid line),  $Q$  (dashed line), and  $\Gamma$  (dash-dotted line), as indicated in the figure. The colors correspond to (a) spin and (b) layer composition, with the color schemes provided in the plots. Due to the degeneracy of the VB at the  $\Gamma$  point, the spin- and layer-resolved notations are omitted for this valley.

both the spin and layer characteristics of the bands, the simplified model does not induce changes in the spin localization at the  $K$  and  $Q$  points. Specifically, in the simplified TB approach, the spin configuration remains unchanged in both the VB and CB at the  $K$  and  $Q$  valleys. The SOC splittings in the CB at the  $K$  point are unaffected by the electric field, while the VB splittings increase with negative  $E_z$ , in agreement with the full TB results. As also observed in the full TB and DFT models, the spin-splitting between the two lowest CBs at the  $Q$  point increases with positive  $E_z$  and decreases with negative  $E_z$ . In the simplified TB model, we observe the crossing of the CBs at the  $Q$  point as  $E_z$  becomes more negative, leading to a change in the nature of the  $K$ - $Q$  energy gap. However, it is important to note that the simplified model does not capture the spin mixing effect at the crossing points, which is observed in the full TB model.

The layer composition of the bands is shown in Fig. 5.5(b). The simplified TB model captures the key feature of the electric field's effect on the layer coupling, which is also observed in the full TB results. However, the simplified model provides a more straightforward representation of how the leading layer contribution changes. Specifically, it reveals that the layer contribution at the  $Q$  point for the CBs, as well as at the  $K$  point for the VBs, can switch depending on the applied electric field. This behavior aligns with the trends observed in the DFT calculations.

Another notable difference between the full and simplified TB models lies in the intralayer energy gaps. While the intralayer gap for  $WSe_2$  remains almost unchanged in the electric field in both models, the gap for  $MoSe_2$  changes due to the mixing of the layers in the VB. This effect is present in the simplified TB model but not captured by the full TB model. Additionally, the

direct interlayer energy gap decreases with increasing  $E_z$ , consistent with both the DFT and full TB results.

In summary, the simplified TB model successfully captures the main trends observed in both the DFT and full TB models, providing valuable insights into the field-induced modulation of the electronic structure with a reduced computational cost. The agreement between the three approaches strengthens the confidence in our understanding of the system's response to external electric fields.

## 5.4 Electrically Tunable Laterally Gated Quantum Dot

We have demonstrated how electric field perpendicular to the MoSe<sub>2</sub>/WSe<sub>2</sub> layers shifts the relative energies of different valleys. In this section, we leverage this effect in a lateral gate-defined QD. We investigate this system using the approach outlined in Refs. [58, 59, 130, 483, 487, 501, 502]. We begin with the MoSe<sub>2</sub>/WSe<sub>2</sub> computational rhombus, which serves as the basis for defining Bloch functions in  $k$ -space. These functions are subsequently employed to describe the states of the gated QD and to analyze the effect of the applied vertical electric field, presented in Fig. 5.6.

To describe the QD we start by creating the rhomboidal real-space computational box consisting of MoSe<sub>2</sub> and WSe<sub>2</sub> atoms, depicted in Fig. 5.6(a). We impose the periodic boundary conditions connecting the opposite edges of the rhombus, thus giving us a set of allowed  $\vec{k}$ -vectors. We expand the electron wave function in the basis of Bloch functions  $\varphi_{\vec{k}}^p(\vec{r})$ , see Eq. (5.1), built of WSe<sub>2</sub> and MoSe<sub>2</sub> atomic orbitals. For each  $\vec{k}$  wavevector we diagonalize the Hamiltonian given in Eq. (5.23) and obtain bulk electronic energies  $\varepsilon_{\vec{k}}^p$  and eigenvectors  $A_{\vec{k},l}^p$ . We confine electrons in a gate-defined lateral Gaussian potential  $V_{\text{QD}} = U_{\text{QD}}(1 - \exp(-r^2/\sigma_{\text{QD}}^2/2))$ , presented in Fig. 5.6(b). The basis of the band states of the bulk system are functions  $\varphi_{\vec{k}}^p(\vec{r}) = \sum_l A_{\vec{k},l}^p \phi_{\vec{k},l}(\vec{r})$ , where  $l$  denotes the orbital within a UC,  $p$  corresponds to the band index, and  $\phi_{\vec{k},l}(\vec{r})$  are the orbital Bloch functions build from the localized Slater orbitals. The QD states, expanded in the basis of low-energy band states  $\varphi_{\vec{k}}^p$ , are defined as:

$$\Phi^s(\vec{r}) = \sum_p \sum_{\vec{k}} B_{\vec{k}}^{s,p} \varphi_{\vec{k}}^p(\vec{r}), \quad (5.45)$$

where the summation is carried over the bands  $p$  and the wave vectors  $\vec{k}$  defined by the computational rhombus. The Schrödinger equation gives the integral equation for the amplitudes  $B_{\vec{k}}^{s,p}$ :

$$\varepsilon_{\vec{k}}^p B_{\vec{k}}^{s,p} + \sum_{p',\vec{k}'} \langle \varphi_{\vec{k}}^p | V_{\text{QD}} | \varphi_{\vec{k}'}^{p'} \rangle B_{\vec{k}'}^{s,p'} = \epsilon^s B_{\vec{k}}^{s,p}, \quad (5.46)$$

with  $\varepsilon_{\vec{k}}^p$  denoting the single-particle energies of the heterostructure Hamiltonian described by Eq. (5.23). The coupling between the band states due to the confinement potential  $V_{\text{QD}}$  is determined by the matrix elements given as:

$$\langle \varphi_{\vec{k}}^p | V_{\text{QD}} | \varphi_{\vec{k}'}^{p'} \rangle = \sum_l \left( A_{\vec{k},l}^p \right)^* A_{\vec{k}',l}^{p'} e^{i(\vec{k}' - \vec{k}) \cdot \vec{\tau}_l} V_{\vec{k},\vec{k}',l}. \quad (5.47)$$

Here  $\vec{\tau}_l$  corresponds to the position of orbitals  $l$  within a UC, while  $V_{\vec{k},\vec{k}',l}$  is the Fourier transform of the QD potential.

The eigenenergies and eigenstates of the QD, denoted as  $\epsilon^s$  and  $\Phi^s$ , respectively, are determined by solving Eq. (5.46). The QD potential is modeled as a Gaussian potential characterized by a width of  $\sigma_{\text{QD}} = 5$  nm and an depth of  $U_{\text{QD}} = 300$  mV. In our calculations, we restrict  $p, p'$  to the

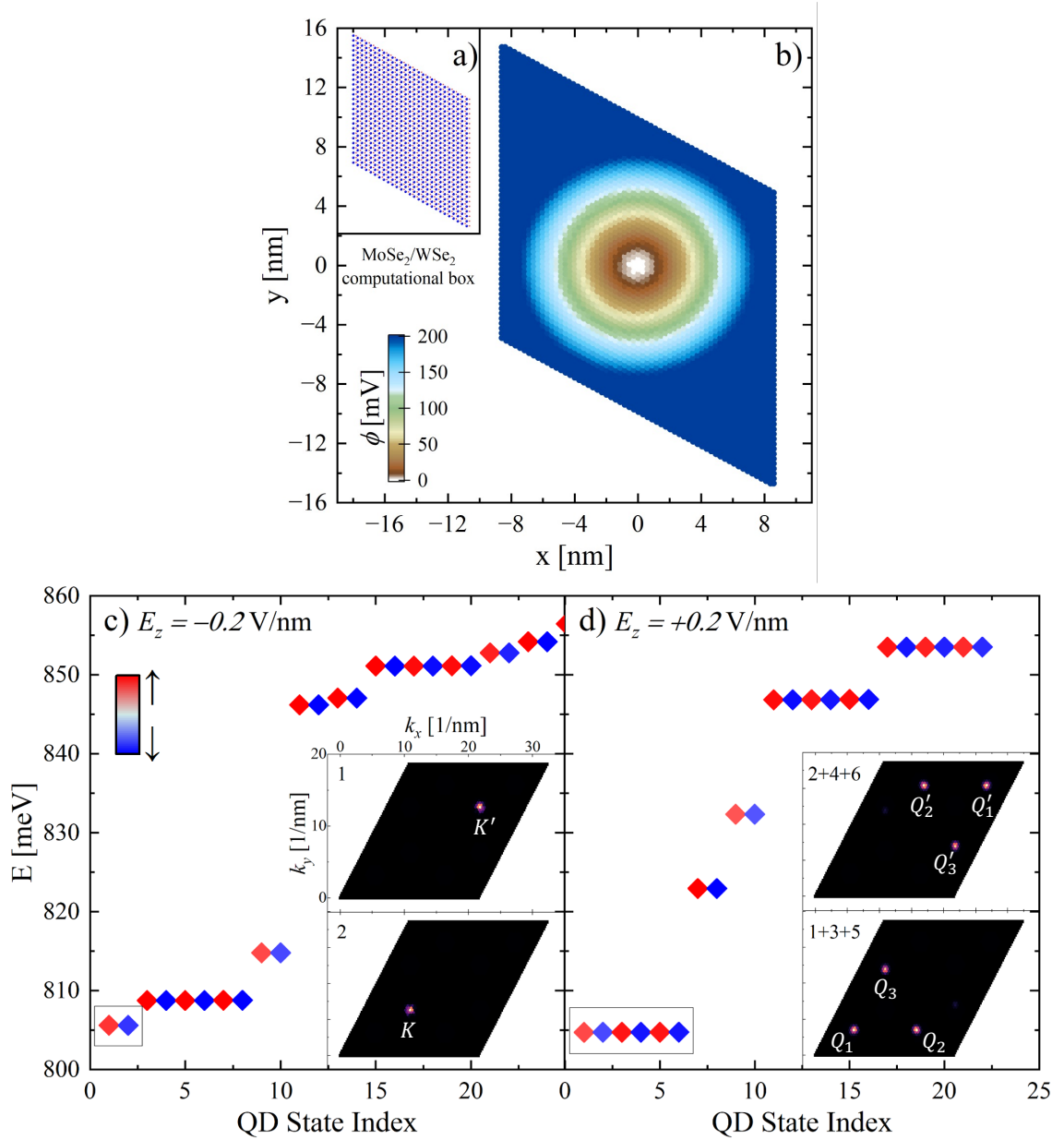


**Figure 5.6:** (a) Schematic illustration of the computational box in real space. (b) Electric potential  $\phi$  profile of a Gaussian QD. (c) Spin-resolved QD energy spectrum for vertical electric field  $E_z = -0.2$  V/nm and CB minimum located in the  $K$  valleys. (d) Analogous spectrum for  $E_z = +0.2$  V/nm, for which CB minima are in  $Q$  points. Spin is indicated by color. The insets in panel (c) show density for the first  $|\psi_1|^2$  and the second  $|\psi_2|^2$  state, and the insets in panel (d) present two sums over states in the lowest shell in a specific spin subspace ( $|\psi_1|^2 + |\psi_3|^2 + |\psi_5|^2$  and  $|\psi_2|^2 + |\psi_4|^2 + |\psi_6|^2$ , respectively).

two lowest CBs. Figure 5.6(c,d) illustrates the spin-resolved QD energy spectrum for two directions of an applied vertical electric field  $E_z$ . When a negative electric field is applied, electrons localize in the  $K$  and  $K'$  valleys, resulting in a doubly degenerate shell of lowest-energy states, as shown in Fig. 5.6(c). The wave functions for these states are confined within the  $K/K'$  valleys, as illustrated in the insets of Fig. 5.6(c). The second shell originates from the secondary (higher) CB minimum at the 6  $Q$  points. The third shell, also doubly degenerate, arises from the spin-split bands at the  $K$  points. The degeneracies of higher-energy shells can be understood in terms of the Fock-Darwin spectrum, including doubly degenerate  $2p$ - $2p$  states at the  $K$  points (four states in total) and  $2p$ - $2p$  states from the  $Q$  valleys ( $2 \times 6$  states in total), and further states following the same pattern.

Applying a positive electric field shifts electron localization from the  $K$  to the  $Q$  valleys, resulting in a 6-fold degenerate low-energy shell of QD states, as shown in Fig. 5.6(d). In this configuration, the wave functions for each spin subspace form a superposition across all three  $Q$  valleys, as illustrated in the insets of Fig. 5.6(d). The second and third shells are doubly degenerate, originating from spin-split bands around the  $K$  points. This behavior aligns with the reversal of valley character ( $Q$  vs.  $K$ ) in successive shells, which governs their degeneracy.

A shift in the conduction band minimum's valley type in an applied electric field can significantly influence the system's optical properties. In the case of extended states, the lowest-energy excitonic transition changes from a spin-forbidden ( $K$ - $K$ ) transition to a momentum-forbidden ( $K$ - $Q$ ) one, both remaining optically dark. However, in QDs, mixing of different  $k$ -space states relaxes the momentum conservation constraints for optically active excitons [58, 59, 503]. This introduces an energy competition between excitons formed by holes near the  $K$  valley—repelled by the confining potential—and electrons localized in either the  $K$  or  $Q$  valley.

The first energy scale defining this fine-structure splitting arises from spin-orbit coupling [223, 504], which is slightly reduced in QDs compared to its bulk counterpart [487]. Specifically, for  $K$ -like states, the splitting decreases from 12 meV in bulk to 9 meV in QDs, while for  $Q$ -like states, it drops from 74 meV to 42 meV. Assuming comparable electron-hole direct interactions for excitons in QDs, this spin-orbit-induced splitting leads to an interlayer dark ground state for  $K$ -derived excitons, whereas  $Q$ -derived excitons remain optically bright. However, exchange interactions between electrons and holes, typically stronger in confined systems than in extended states, may modify this scenario. In particular, for  $K$  states, the exchange interaction is expected to enhance the dark-bright splitting, whereas for  $Q$  states, it could override the spin-orbit effect and shift the dark exciton to the ground state. Additionally, the degeneracy of quantum dot excitons differs:  $K$ -like excitons form a single state, whereas  $Q$ -like excitons exhibit threefold degeneracy. Disentangling the contributions of direct and exchange Coulomb interactions—or, more broadly, full electron-hole correlations—between different valley states necessitates real-space computation of CMEs and scattering among different configurations, a nontrivial task [502, 505]. A detailed quantitative study of fine-structure splitting is beyond the present scope and will be addressed in future work.

## 5.5 Conclusions

In this chapter, we have explored the electronic properties of MoSe<sub>2</sub>/WSe<sub>2</sub> heterostructures. Beginning with DFT calculations, we identified a type-II band alignment characterized by closely spaced CB minima at the  $K$  and  $Q$  points, as well as VB maxima near the  $\Gamma$  and  $K$  points. Analysis of the Kohn-Sham wave functions provided insights into the layer, spin, and orbital contributions

to the electronic states.

Building upon these findings, we developed an *ab initio*-based TB model that captures the complexity of interlayer interactions. This model facilitated a deeper understanding of the electronic structure and allowed us to investigate the effects of external perturbations. Specifically, we examined the influence of a perpendicular electric field, demonstrating that vertical gating can modulate the energy landscape, enabling control over valley extrema.

Furthermore, we applied the TB model to study laterally gated QDs within the heterostructure. Our analysis revealed that tuning the electric field allows for selective localization of electronic states in either the  $K$  or  $Q$  valleys. This valley-specific confinement, evidenced by characteristic degeneracies and wave function distributions, underscores the potential of these QDs for valleytronic applications and quantum information processing.

Overall, our comprehensive approach combining DFT and TB methodologies provides a robust framework for understanding and manipulating the electronic properties of MoSe<sub>2</sub>/WSe<sub>2</sub> heterostructures, paving the way for future explorations of electrically tunable quantum devices.



# Conclusions

This dissertation presented a detailed theoretical study of many-body effects in 2D van der Waals materials, focusing on the optical response of excitonic and selected trionic complexes in a variety of material systems. The diversity of platforms investigated—ranging from BLG QDs, to TMDC monolayers in high magnetic fields, and heterostructure QDs—has allowed for detailed exploration of how external fields, reduced dimensionality, and interlayer coupling govern the behavior of electron-hole interactions.

In BLG QDs, we demonstrated that lateral gating combined with a perpendicular electric field allows for the confinement of both types of carriers—electrons and holes—as well as for the tuning of the electronic band gap. Our atomistic TB model combined with many-body calculations via the BSE revealed a complex excitonic structure with a broad tunability of optical transitions from THz to FIR regimes. Notably, we predicted that the fine structure of charged excitons (trions) arises in BLG QDs—a characteristic absent in conventional QD systems. Furthermore, the low-energy trion states appear to be bright; hence, we proposed a method to experimentally access the fine structure via temperature-dependent spectroscopy.

For monolayer TMDCs in strong magnetic fields, we explored how the interplay between charge carrier density, SOC, and the application of an external magnetic field leads to the formation of magnetoexcitons. Our approach, based on *ab initio*-informed models incorporating spin and valley Zeeman effects, allowed us to uncover the evolution of magnetoexcitonic spectra as a function of carrier doping. The analysis emphasized the role of many-body interactions in shaping the optical response in the quantum Hall regime.

Finally, our investigation of MoSe<sub>2</sub>/WSe<sub>2</sub> heterostructures and their lateral QDs provided insights into how vertical electric fields modulate interlayer coupling and valley-specific confinement. Through a combined framework of *ab initio* methods and a constructed TB model, we showed that the band alignment and valley occupancy in such heterostructures can be precisely tuned, offering control over the spatial and orbital character of quantum dot states. This tunability has important implications for valleytronic applications and for quantum light sources based on 2D heterostructures.

Across these distinct yet complementary projects, a central theme has emerged: the optical properties of 2D materials are highly sensitive to external fields, spatial confinement, and many-body interactions. This work has contributed new theoretical tools and predictions that deepen our understanding of excitonic complexes in low-dimensional systems. Crucially, the demonstrated ability to manipulate neutral and charged excitons—via electrostatic gating, magnetic fields, and interlayer engineering—opens pathways toward the design of next-generation optoelectronic and quantum devices, including tunable infrared emitters and valley-based qubits.



# Appendix

## A Topological Effects in Transition Metal Dichalcogenide Crystals

In this section, we describe topological effects in 2D TMDCs, focusing particularly on the manifestation of Berry curvature in the excitonic spectra [446]. The interplay between the valley-dependent Berry curvature and electron-hole interactions significantly influences the fine structure of excitonic states. Beyond the hydrogenic exciton model, several renormalization mechanisms shape the excitonic spectrum in TMDC monolayers. The electron-hole exchange interaction couples excitonic states and lifts degeneracies, significantly influencing the fine structure, especially for higher angular momentum states such as  $2p$  and  $3p$ . The Berry curvature acts as an effective valley-dependent magnetic field in momentum space, inducing valley-contrasting energy shifts that manifest as topological splittings of excitonic shells. Additionally, the dielectric environment, modeled by the Rytova-Keldysh potential, modulates the Coulomb interaction strength through the dielectric constant  $\epsilon_r$  of the surroundings, thus tuning exciton binding energies and inter-shell spacings. These mechanisms collectively necessitate a comprehensive treatment that combines TB electronic structure, electron-hole correlations, and band topology, as detailed in our previous work [175].

Here we present an analysis of the excitonic spectrum of the MoS<sub>2</sub> monolayer using a combination of the minimal TB model [175, 223, 493], the BSE (see Sec. 2.3.1), and a simplified Coulomb interaction model with form factors defined as [175]:

$$F^D(\vec{k}, \vec{k}', \vec{G}) = \sum_{\alpha, \alpha'=1}^2 \sum_{\mu, \mu'=1}^3 \left[ v_{\alpha\mu}^{VB}(\vec{k}') \right]^* v_{\alpha\mu}^{VB}(\vec{k}) \left[ v_{\alpha'\mu'}^{CB}(\vec{k}) \right]^* v_{\alpha'\mu'}^{CB}(\vec{k}') e^{i\vec{G}\cdot(-\vec{\tau}_\alpha + \vec{\tau}_{\alpha'})}, \quad (\text{A.1})$$

where  $\nu$  denote the single-particle TB wave function coefficients,  $\vec{G}$  represents reciprocal space vectors (see Sec. 2.1.2), and  $\vec{\tau}$  is the position vector within the UC. This expression captures the real-space localization and orbital composition of the electron and hole wave functions, essential for accurate form-factor modeling.

We present the exciton fine structure of the MoS<sub>2</sub> monolayer determined for two dielectric environments: (i) MoS<sub>2</sub> on a SiO<sub>2</sub> substrate, and (ii) MoS<sub>2</sub> encapsulated in hBN, as shown in Fig. 2.4(a,b). The static screening term  $\epsilon_r$ , governed by the surrounding environment rather than the monolayer itself, takes values of 2.5 for SiO<sub>2</sub> and 4.5 for hBN.

Figure A.1 presents the calculated excitonic spectra relative to the continuum. The diagrams are restricted to the first three excitonic shells ( $n = 1, 2, 3$ ). Notably, for both dielectric environments, the  $2s$  excitonic state exhibits a smaller energy compared to the  $2p$  states, illustrating the complex role of orbital angular momentum and screening effects in 2D excitons. The spectra further reveal

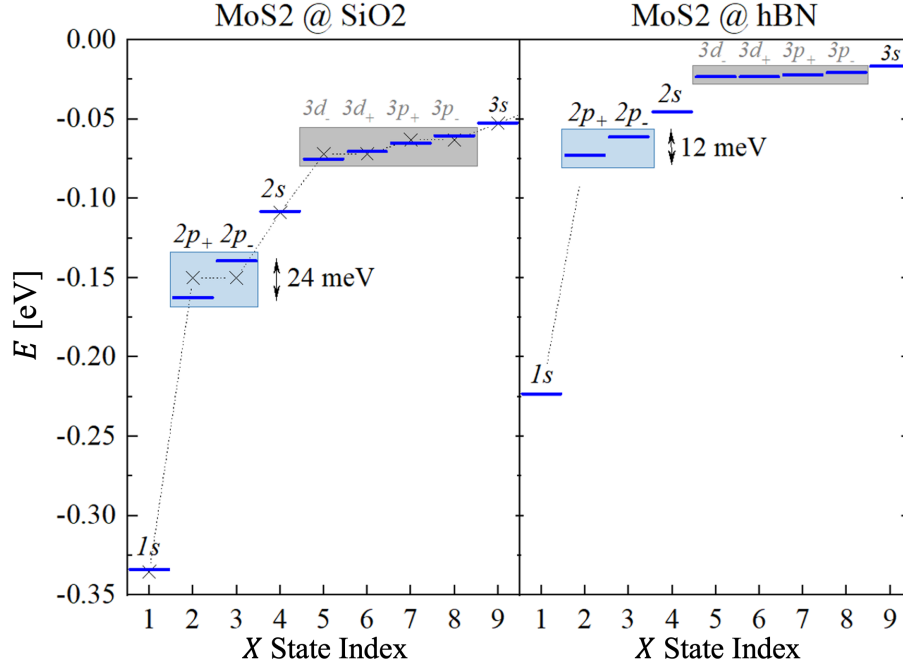


**Figure A.1:** Exciton fine structure for a MoS<sub>2</sub> monolayer (a) on a SiO<sub>2</sub> substrate and (b) encapsulated with hBN, computed within the full TB model incorporating complex electron-hole interactions. The results are restricted to the first three excitonic shells. The topological splitting of the  $2p$ ,  $3p$ , and  $3d$  excitonic states is clearly visible in the spectrum of the MoS<sub>2</sub> monolayer. In panel (a), the effect of neglecting the complex phase of the exciton wave function is also shown, indicated by the  $\times$  symbols [175].

characteristic topological splittings of the  $2p$ ,  $3p$ , and  $3d$  excitonic states, arising from the Berry curvature of the underlying electronic bands and the associated valley-contrasting physics [446].

For MoS<sub>2</sub> on SiO<sub>2</sub>, presented in panel (a), the exciton binding energy is  $E_b = 335$  meV, with an energy separation between the  $1s$  and  $2s$  states of  $E^{1s-2s} = 226$  meV. Encapsulation in hBN, shown in panel (b), reduces both the exciton binding energy to  $E_b = 223$  meV and the  $1s$ - $2s$  splitting to  $E^{1s-2s} = 176$  meV, consistent with enhanced dielectric screening.

The observed topological features in the excitonic spectrum highlight the importance of these effects, which are absent in simple effective-mass or hydrogenic models. Their inclusion enables a more accurate interpretation of experimental data. These results provide a foundation for engineering excitonic properties through dielectric and topological tuning in 2D materials. Future work will focus on applying the Rytova-Keldysh screening model to TMDC heterostructures.

# Bibliography

- [1] K. S. Novoselov, A. K. Geim, S. V. Morozov, D. Jiang, Y. Zhang, S. V. Dubonos, I. V. Grigorieva, and A. A. Firsov, *Electric Field Effect in Atomically Thin Carbon Films*, *Science* **306**, 666–669 (2004).
- [2] K. S. Novoselov, A. K. Geim, S. V. Morozov, D. Jiang, M. I. Katsnelson, I. V. Grigorieva, S. V. Dubonos, and A. A. Firsov, *Two-dimensional gas of massless Dirac fermions in graphene*, *Nature* **438**, 197–200 (2005).
- [3] A. K. Geim and K. S. Novoselov, *The rise of graphene*, *Nature Materials* **6**, 183–191 (2007).
- [4] E. McCann and M. Koshino, *The electronic properties of bilayer graphene*, *Reports on Progress in Physics* **76**, 056503 (2013).
- [5] S. Manzeli, D. Ovchinnikov, D. Pasquier, O. V. Yazyev, and A. Kis, *2D transition metal dichalcogenides*, *Nature Reviews Materials* **2**, 17033 (2017).
- [6] T. C. Berkelbach, M. S. Hybertsen, and D. R. Reichman, *Theory of neutral and charged excitons in monolayer transition metal dichalcogenides*, *Physical Review B* **88**, 045318 (2013).
- [7] G. Wang, A. Chernikov, M. M. Glazov, T. F. Heinz, X. Marie, T. Amand, and B. Urbaszek, *Colloquium: Excitons in atomically thin transition metal dichalcogenides*, *Reviews of Modern Physics* **90**, 021001 (2018).
- [8] A. Ramasubramaniam, D. Naveh, and E. Towe, *Tunable band gaps in bilayer transition-metal dichalcogenides*, *Physical Review B* **84**, 205325 (2011).
- [9] H. Terrones, F. López-Urías, and M. Terrones, *Novel hetero-layered materials with tunable direct band gaps by sandwiching different metal disulfides and diselenides*, *Scientific Reports* **3**, 1–7 (2013).
- [10] H. J. Conley, B. Wang, J. I. Ziegler, R. F. Haglund Jr, S. T. Pantelides, and K. I. Bolotin, *Bandgap engineering of strained monolayer and bilayer MoS<sub>2</sub>*, *Nano Letters* **13**, 3626–3630 (2013).
- [11] R. K. Defo, S. Fang, S. N. Shirodkar, G. A. Tritsarlis, A. Dimoulas, and E. Kaxiras, *Strain dependence of band gaps and exciton energies in pure and mixed transition-metal dichalcogenides*, *Physical Review B* **94**, 155310 (2016).
- [12] J. Gusakova, X. Wang, L. L. Shiao, A. Krivosheeva, V. Shaposhnikov, V. Borisenko, V. Gusakov, and B. K. Tay, *Electronic Properties of Bulk and Monolayer TMDs: Theoretical Study Within DFT Framework (GVJ-2e Method)*, *Physica Status Solidi A* **214**, 1700218 (2017).
- [13] A. Chaves, J. G. Azadani, H. Alsaman, D. R. da Costa, R. Frisenda, A. J. Chaves, S. H. Song, Y. D. Kim, D. He, J. Zhou, A. Castellanos-Gomez, F. M. Peeters, Z. Liu, C. L. Hinkle, S.-H. Oh, P. D. Ye, S. J. Koester, Y. H. Lee, P. Avouris, X. Wang, and T. Low, *Bandgap engineering of two-dimensional semiconductor materials*, *npj 2D Materials and Applications* **4**, 29 (2020).
- [14] A. Srivastava, M. Sidler, A. V. Allain, D. S. Lembke, A. Kis, and A. Imamoglu, *Optically active quantum dots in monolayer WSe<sub>2</sub>*, *Nature Nanotechnology* **10**, 491 (2015).
- [15] P. R. Wallace, *The Band Theory of Graphite*, *Physical Review* **71**, 622–634 (1947).
- [16] P. A. M. Dirac, *The quantum theory of the electron*, *Proceedings of the Royal Society of London. Series A, Containing Papers of a Mathematical and Physical Character* **117**, 610–624 (1928).
- [17] H. Weyl, *Gravitation and the electron*, *Proceedings of the National Academy of Sciences* **15**, 323–334 (1929).
- [18] S. Y. Zhou, G.-H. Gweon, J. Graf, A. V. Fedorov, C. D. Spataru, R. D. Diehl, Y. Kopelevich, D.-H. Lee, S. G. Louie, and A. Lanzara, *First direct observation of Dirac fermions in graphite*, *Nature Physics* **2**, 595–599 (2006).
- [19] H. Boehm, A. Clauss, G. Fischer, and U. Hofmann, *Anorg. Allg. Chem.* Anorganische und Allgemeine Chemie **316**, 119 (1962).

- [20] P. Hawrylak and K. R. Subbaswamy, *Kinetic model of stage transformation and intercalation in graphite*, [Physical Review Letters](#) **53**, 2098–2101 (1984).
- [21] V. Yu, E. Whiteway, J. Maassen, and M. Hilke, *Raman spectroscopy of the internal strain of a graphene layer grown on copper tuned by chemical vapor deposition*, [Physical Review B](#) **84**, 205407 (2011).
- [22] C. Berger, Z. Song, T. Li, X. Li, A. Y. Ogbazghi, R. Feng, Z. Dai, A. N. Marchenkov, E. H. Conrad, P. N. First, and W. A. de Heer, *Ultrathin epitaxial graphite: 2D electron gas properties and a route toward graphene-based nanoelectronics*, [The Journal of Physical Chemistry B](#) **108**, 19912–19916 (2004).
- [23] S. Stankovich, D. A. Dikin, G. H. B. Dommett, K. M. Kohlhaas, E. J. Zimney, E. A. Stach, R. D. Piner, S. T. Nguyen, and R. S. Ruoff, *Graphene-based composite materials*, [Nature](#) **442**, 282–286 (2006).
- [24] R. Saito, M. Fujita, G. Dresselhaus, and M. S. Dresselhaus, *Electronic structure of graphene tubules based on  $C_{60}$* , [Physical Review B](#) **46**, 1804–1811 (1992).
- [25] S. Iijima, *Helical microtubules of graphitic carbon*, [Nature](#) **354**, 56–58 (1991).
- [26] M. I. Katsnelson, K. S. Novoselov, and A. K. Geim, *Chiral tunnelling and the Klein paradox in graphene*, [Nature Physics](#) **2**, 620–625 (2006).
- [27] J. González, F. Guinea, and M. Vozmediano, *Non-Fermi liquid behavior of electrons in the half-filled honeycomb lattice (a renormalization group approach)*, [Nuclear Physics B](#) **424**, 595–618 (1994).
- [28] T. Ando, *Theory of electronic states and transport in carbon nanotubes*, [Journal of the Physical Society of Japan](#) **74**, 777–817 (2005).
- [29] A. H. C. Neto, F. Guinea, N. M. R. Peres, K. S. Novoselov, and A. K. Geim, *The electronic properties of graphene*, [Reviews of Modern Physics](#) **81**, 109–162 (2009).
- [30] A. A. Balandin, S. Ghosh, W. Bao, I. Calizo, D. Teweldebrhan, F. Miao, and C. N. Lau, *Superior Thermal Conductivity of Single-Layer Graphene*, [Nano Letters](#) **8**, 902–907 (2008).
- [31] K. S. Novoselov, Z. Jiang, Y. Zhang, S. V. Morozov, H. L. Stormer, U. Zeitler, J. C. Maan, G. S. Boebinger, P. Kim, and A. K. Geim, *Room-Temperature Quantum Hall Effect in Graphene*, [Science](#) **315**, 1379–1379 (2007).
- [32] A. F. Young and P. Kim, *Quantum interference and Klein tunnelling in graphene heterojunctions*, [Nature Physics](#) **5**, 222–226 (2009).
- [33] M. L. Sadowski, G. Martinez, M. Potemski, C. Berger, and W. A. de Heer, *Landau Level Spectroscopy of Ultrathin Graphite Layers*, [Physical Review Letters](#) **97**, 266405 (2006).
- [34] K. Bolotin, K. Sikes, Z. Jiang, M. Klima, G. Fudenberg, J. Hone, P. Kim, and H. Stormer, *Ultrahigh electron mobility in suspended graphene*, [Solid State Communications](#) **146**, 351–355 (2008).
- [35] S. V. Morozov, K. S. Novoselov, M. I. Katsnelson, F. Schedin, D. C. Elias, J. A. Jaszczak, and A. K. Geim, *Giant Intrinsic Carrier Mobilities in Graphene and Its Bilayer*, [Physical Review Letters](#) **100**, 016602 (2008).
- [36] E. H. Hwang and S. Das Sarma, *Dielectric function, screening, and plasmons in two-dimensional graphene*, [Physical Review B](#) **75**, 205418 (2007).
- [37] J.-W. Jiang, J.-S. Wang, and B. Li, *Young's modulus of graphene: A molecular dynamics study*, [Physical Review B](#) **80**, 113405 (2009).
- [38] C. Lee, X. Wei, J. W. Kysar, and J. Hone, *Measurement of the Elastic Properties and Intrinsic Strength of Monolayer Graphene*, [Science](#) **321**, 385–388 (2008).
- [39] E. Pop, V. Varshney, and A. K. Roy, *Thermal properties of graphene: Fundamentals and applications*, [MRS Bulletin](#) **37**, 1273–1281 (2012).
- [40] S. Bae, H. Kim, Y. Lee, X. Xu, J.-S. Park, Y. Zheng, J. Balakrishnan, T. Lei, H. Ri Kim, Y. I. Song, Y.-J. Kim, B. Özyilmaz, J.-H. Ahn, B. H. Hong, and S. Iijima, *Roll-to-roll production of 30-inch graphene films for transparent electrodes*, [Nature Nanotechnology](#) **5**, 574–578 (2010).
- [41] O. Akhavan, E. Ghaderi, and R. Rahighi, *Toward Single-DNA Electrochemical Biosensing by Graphene Nanowalls*, [ACS Nano](#) **6**, 2904–2916 (2012).
- [42] F. Yavari and N. Koratkar, *Graphene-Based Chemical Sensors*, [The Journal of Physical Chemistry Letters](#) **3**, 1746–1753 (2012).

- [43] C. Liu, L. Du, W. Tang, D. Wei, J. Li, L. Wang, G. Chen, X. Chen, and W. Lu, *Towards sensitive terahertz detection via thermoelectric manipulation using graphene transistors*, *NPG Asia Materials* **10**, 318–327 (2018).
- [44] D. A. Bandurin, D. Svintsov, I. Gayduchenko, S. G. Xu, A. Principi, M. Moskotin, I. Tret'yakov, D. Yagodkin, S. Zhukov, T. Taniguchi, K. Watanabe, I. V. Grigorieva, M. Polini, G. N. Goltsman, A. K. Geim, and G. Fedorov, *Resonant terahertz detection using graphene plasmons*, *Nature Communications* **9**, 5392 (2018).
- [45] A. K. Geim and I. V. Grigorieva, *Van der Waals heterostructures*, *Nature* **499**, 419–425 (2013).
- [46] T. Ohta, A. Bostwick, T. Seyller, K. Horn, and E. Rotenberg, *Controlling the Electronic Structure of Bilayer Graphene*, *Science* **313**, 951–954 (2006).
- [47] Y. Zhang, T.-T. Tang, C. Girit, Z. Hao, M. C. Martin, A. Zettl, M. F. Crommie, Y. R. Shen, and F. Wang, *Direct observation of a widely tunable bandgap in bilayer graphene*, *Nature* **459**, 820–823 (2009).
- [48] L. Ju, L. Wang, T. Cao, T. Taniguchi, K. Watanabe, S. G. Louie, F. Rana, J. Park, J. Hone, F. Wang, and P. L. McEuen, *Tunable excitons in bilayer graphene*, *Science* **358**, 907–910 (2017).
- [49] E. McCann and V. I. Fal'ko, *Landau-Level Degeneracy and Quantum Hall Effect in a Graphite Bilayer*, *Physical Review Letters* **96**, 086805 (2006).
- [50] E. McCann, D. S. Abergel, and V. I. Fal'ko, *Electrons in bilayer graphene*, *Solid State Communications* **143**, 110–115 (2007).
- [51] E. V. Castro, K. S. Novoselov, S. V. Morozov, N. M. R. Peres, J. M. B. L. dos Santos, J. Nilsson, F. Guinea, A. K. Geim, and A. H. C. Neto, *Biased Bilayer Graphene: Semiconductor with a Gap Tunable by the Electric Field Effect*, *Physical Review Letters* **99**, 216802 (2007).
- [52] J. B. Oostinga, H. B. Heersche, X. Liu, A. F. Morpurgo, and L. M. K. Vandersypen, *Gate-induced insulating state in bilayer graphene devices*, *Nature Materials* **7**, 151–157 (2008).
- [53] K. F. Mak, C. H. Lui, J. Shan, and T. F. Heinz, *Observation of an Electric-Field-Induced Band Gap in Bilayer Graphene by Infrared Spectroscopy*, *Physical Review Letters* **102**, 256405 (2009).
- [54] A. B. Kuzmenko, L. Benfatto, E. Cappelluti, I. Crassee, D. van der Marel, P. Blake, K. S. Novoselov, and A. K. Geim, *Gate Tunable Infrared Phonon Anomalies in Bilayer Graphene*, *Physical Review Letters* **103**, 116804 (2009).
- [55] L. M. Zhang, Z. Q. Li, D. N. Basov, M. M. Fogler, Z. Hao, and M. C. Martin, *Determination of the electronic structure of bilayer graphene from infrared spectroscopy*, *Physical Review B* **78**, 235408 (2008).
- [56] M. Eich, F. š. Herman, R. Pisoni, H. Overweg, A. Kurzman, Y. Lee, P. Rickhaus, K. Watanabe, T. Taniguchi, M. Sigrist, T. Ihn, and K. Ensslin, *Spin and Valley States in Gate-Defined Bilayer Graphene Quantum Dots*, *Physical Review X* **8**, 031023 (2018).
- [57] C.-H. Park and S. G. Louie, *Tunable Excitons in Biased Bilayer Graphene*, *Nano Letters* **10**, 426–431 (2010).
- [58] Y. Saleem, K. Sadecka, M. Korkusinski, D. Miravet, A. Dusko, and P. Hawrylak, *Theory of Excitons in Gated Bilayer Graphene Quantum Dots*, *Nano Letters* **23**, 2998–3004 (2023).
- [59] K. Sadecka, Y. Saleem, D. Miravet, M. Albert, M. Korkusinski, G. Bester, and P. Hawrylak, *Electrically tunable fine structure of negatively charged excitons in gated bilayer graphene quantum dots*, *Physical Review B* **109**, 085434 (2024).
- [60] Z. Fei, E. G. Iwinski, G. X. Ni, L. M. Zhang, W. Bao, A. S. Rodin, Y. Lee, M. Wagner, M. K. Liu, S. Dai, M. D. Goldflam, M. Thiemens, F. Keilmann, C. N. Lau, A. H. Castro-Neto, M. M. Fogler, and D. N. Basov, *Tunneling plasmonics in bilayer graphene*, *Nano Letters* **15**, 4973–4978 (2015).
- [61] A. Cortijo, A. G. Grushin, and M. A. H. Vozmediano, *Topological insulating phases in monolayer and bilayer graphene: an effective action approach*, *Physical Review B* **82**, 195438 (2010).
- [62] E. Prada, P. San-Jose, L. Brey, and H. Fertig, *Band topology and the quantum spin Hall effect in bilayer graphene*, *Solid State Communications* **151**, 1075–1083 (2011).
- [63] Y.-W. Son, M. L. Cohen, and S. G. Louie, *Energy Gaps in Graphene Nanoribbons*, *Physical Review Letters* **97**, 216803 (2006).
- [64] X. Yan, X. Cui, B. Li, and L.-s. Li, *Large, Solution-Processable Graphene Quantum Dots as Light Absorbers for Photovoltaics*, *Nano Letters* **10**, 1869–1873 (2010).

- [65] T. Ihn, J. Güttinger, F. Molitor, S. Schnez, E. Schurtenberger, A. Jacobsen, S. Hellmüller, T. Frey, S. Dröscher, C. Stampfer, and K. Ensslin, *Graphene single-electron transistors*, [Materials Today](#) **13**, 44–50 (2010).
- [66] L. Yang, J. Deslippe, C.-H. Park, M. L. Cohen, and S. G. Louie, *Excitonic Effects on the Optical Response of Graphene and Bilayer Graphene*, [Physical Review Letters](#) **103**, 186802 (2009).
- [67] F. H. L. Koppens, D. E. Chang, and F. J. García de Abajo, *Graphene Plasmonics: A Platform for Strong Light–Matter Interactions*, [Nano Letters](#) **11**, 3370–3377 (2011).
- [68] I. Ozfidan, M. Korkusinski, A. D. Güçlü, J. A. McGuire, and P. Hawrylak, *Microscopic theory of the optical properties of colloidal graphene quantum dots*, [Physical Review B](#) **89**, 085310 (2014).
- [69] C. Volk, C. Neumann, S. Kazarski, S. Fringes, S. Engels, F. Haupt, A. Müller, and C. Stampfer, *Probing relaxation times in graphene quantum dots*, [Nature Communications](#) **4**, 1753 (2013).
- [70] J. Güttinger, T. Frey, C. Stampfer, T. Ihn, and K. Ensslin, *Spin States in Graphene Quantum Dots*, [Physical Review Letters](#) **105**, 116801 (2010).
- [71] D. S. L. Abergel and V. I. Fal’ko, *Optical and magneto-optical far-infrared properties of bilayer graphene*, [Physical Review B](#) **75**, 155430 (2007).
- [72] W.-K. Tse and A. H. MacDonald, *Interaction effects in the optical conductivity of bilayer graphene: Drude-interband coupling and screening*, [Physical Review B](#) **80**, 195418 (2009).
- [73] L. Benfatto, S. G. Sharapov, and J. P. Carbotte, *Robustness of the optical conductivity sum rule in bilayer graphene*, [Physical Review B](#) **77**, 125422 (2008).
- [74] E. J. Nicol and J. P. Carbotte, *Optical conductivity of bilayer graphene with and without an asymmetry gap*, [Physical Review B](#) **77**, 155409 (2008).
- [75] C. L. Lu, C. P. Chang, Y. C. Huang, R. B. Chen, and M. L. Lin, *Influence of an electric field on the optical properties of few-layer graphene with AB stacking*, [Physical Review B](#) **73**, 144427 (2006).
- [76] F. Guinea, A. H. Castro Neto, and N. M. R. Peres, *Electronic states and Landau levels in graphene stacks*, [Physical Review B](#) **73**, 245426 (2006).
- [77] K. F. Mak, M. Y. Sfeir, Y. Wu, C. H. Lui, J. A. Misewich, and T. F. Heinz, *Measurement of the Optical Conductivity of Graphene*, [Physical Review Letters](#) **101**, 196405 (2008).
- [78] F. Kadi and E. Malic, *Optical properties of Bernal-stacked bilayer graphene: A theoretical study*, [Physical Review B](#) **89**, 045419 (2014).
- [79] J. Henriques, I. Epstein, and N. Peres, *Absorption and optical selection rules of tunable excitons in biased bilayer graphene*, [Physical Review B](#) **105**, 045411 (2022).
- [80] M. O. Sauer and T. G. Pedersen, *Exciton absorption, band structure, and optical emission in biased bilayer graphene*, [Physical Review B](#) **105**, 115416 (2022).
- [81] X. He, H. Htoon, S. Doorn, W. Pernice, F. Pyatkov, R. Krupke, A. Jeantet, Y. Chassagneux, and C. Voisin, *Carbon nanotubes as emerging quantum-light sources*, [Nature materials](#) **17**, 663–670 (2018).
- [82] E. D. Walsh, D. K. Efetov, G.-H. Lee, M. Heuck, J. Crossno, T. A. Ohki, P. Kim, D. Englund, and K. C. Fong, *Graphene-Based Josephson-Junction Single-Photon Detector*, [Physical Review Applied](#) **8**, 024022 (2017).
- [83] S. Luo, Y. Wang, X. Tong, and Z. Wang, *Graphene-based optical modulators*, [Nanoscale Research Letters](#) **10**, 1–11 (2015).
- [84] W.-d. Sheng, M. Korkusinski, A. D. Güçlü, M. Zielinski, P. Potasz, E. S. Kadantsev, O. Voznyy, and P. Hawrylak, *Electronic and optical properties of semiconductor and graphene quantum dots*, [Frontiers of Physics](#) **7**, 328–352 (2012).
- [85] A. D. Güçlü, P. Potasz, M. Korkusinski, and P. Hawrylak, *Graphene Quantum Dots*, [Springer](#) (2014).
- [86] F. Wang, Y. Zhang, C. Tian, C. Girit, A. Zettl, M. Crommie, and Y. R. Shen, *Gate-Variable Optical Transitions in Graphene*, [Science](#) **320**, 206–209 (2008).
- [87] K. S. Novoselov, E. McCann, S. V. Morozov, V. I. Fal’ko, M. I. Katsnelson, U. Zeitler, D. Jiang, F. Schedin, and A. K. Geim, *Unconventional quantum Hall effect and Berry’s phase of  $2\pi$  in bilayer graphene*, [Nature Physics](#) **2**, 177–180 (2006).
- [88] Y. B. Zhang, Y. W. Tan, H. L. Stormer, and P. Kim, *Experimental observation of the quantum Hall effect and Berry’s phase in graphene*, [Nature](#) **438**, 201 (2005).

- [89] M. Prada, *Angular momentum anisotropy of Dirac carriers: a new twist in graphene*, [Physical Review B](#) **103**, 115425 (2021).
- [90] F. Zhang, J. Jung, G. A. Fiete, Q. Niu, and A. H. MacDonald, *Spontaneous quantum Hall states in chirally stacked few-layer graphene systems*, [Physical Review Letters](#) **106**, 156801 (2011).
- [91] C.-H. Park and N. Marzari, *Berry phase and pseudospin winding number in bilayer graphene*, [Physical Review B](#) **84**, 205440 (2011).
- [92] L.-s. Li and X. Yan, *Colloidal Graphene Quantum Dots*, [The Journal of Physical Chemistry Letters](#) **1**, 2572–2576 (2010).
- [93] M. Bacon, S. J. Bradley, and T. Nann, *Graphene Quantum Dots*, [Particle & Particle Systems Characterization](#) **31**, 415–428 (2014).
- [94] L. Jacak, A. Wójs, and P. Hawrylak, *Quantum Dots*, [Springer Science & Business Media](#) (2013).
- [95] M. Cygorek, M. Korkusinski, and P. Hawrylak, *Atomistic theory of electronic and optical properties of InAsP/InP nanowire quantum dots*, [Physical Review B](#) **101**, 075307 (2020).
- [96] S. Raymond, S. Studenikin, A. Sachrajda, Z. Wasilewski, S. J. Cheng, W. Sheng, P. Hawrylak, A. Babinski, M. Potemski, G. Ortner, and M. Bayer, *Excitonic Energy Shell Structure of Self-Assembled InGaAs/GaAs Quantum Dots*, [Physical Review Letters](#) **92**, 187402 (2004).
- [97] M. Korkusinski and P. Hawrylak, *Atomistic theory of emission from dark excitons in self-assembled quantum dots*, [Physical Review B](#) **87**, 115310 (2013).
- [98] M. Zieliński, M. Korkusiński, and P. Hawrylak, *Atomistic tight-binding theory of multiexciton complexes in a self-assembled InAs quantum dot*, [Physical Review B](#) **81**, 085301 (2010).
- [99] P. Lochner, A. Kurzmann, J. Kerski, P. Stegmann, J. König, A. D. Wieck, A. Ludwig, A. Lorke, and M. Geller, *Real-Time Detection of Single Auger Recombination Events in a Self-Assembled Quantum Dot*, [Nano Letters](#) **20**, 1631–1636 (2020).
- [100] A. Wojs and P. Hawrylak, *Negatively charged magnetoexcitons in quantum dots*, [Physical Review B](#) **51**, 10880–10885 (1995).
- [101] J. Wurm, A. Rycerz, I. ç. Adagideli, M. Wimmer, K. Richter, and H. U. Baranger, *Symmetry Classes in Graphene Quantum Dots: Universal Spectral Statistics, Weak Localization, and Conductance Fluctuations*, [Physical Review Letters](#) **102**, 056806 (2009).
- [102] A. D. Güçlü and P. Hawrylak, *Optical control of magnetization and spin blockade in graphene quantum dots*, [Physical Review B](#) **87**, 035425 (2013).
- [103] L. Banszerus, S. Möller, K. Hecker, E. Icking, K. Watanabe, T. Taniguchi, F. Hassler, C. Volk, and C. Stampfer, *Particle–hole symmetry protects spin-valley blockade in graphene quantum dots*, [Nature](#) **618**, 51–56 (2023).
- [104] I. Ozfidan, M. Korkusinski, and P. Hawrylak, *Theory of biexcitons and biexciton-exciton cascade in graphene quantum dots*, [Physical Review B](#) **91**, 115314 (2015).
- [105] C. Sun, F. Figge, I. Ozfidan, M. Korkusinski, X. Yan, L.-s. Li, P. Hawrylak, and J. A. McGuire, *Biexciton Binding of Dirac fermions Confined in Colloidal Graphene Quantum Dots*, [Nano Letters](#) **15**, 5472–5476 (2015).
- [106] A. Kurzmann, Y. Kleeorin, C. Tong, R. Garreis, A. Knothe, M. Eich, C. Mittag, C. Gold, F. K. d. Vries, K. Watanabe, T. Taniguchi, V. Fal'ko, Y. Meir, T. Ihn, and K. Ensslin, *Kondo effect and spin–orbit coupling in graphene quantum dots*, [Nature Communications](#) **12**, 6004 (2021).
- [107] B. Trauzettel, D. V. Bulaev, D. Loss, and G. Burkard, *Spin qubits in graphene quantum dots*, [Nature Physics](#) **3**, 192 (2007).
- [108] S. Schnez, F. Molitor, C. Stampfer, J. Güttinger, I. Shorubalko, T. Ihn, and K. Ensslin, *Observation of excited states in a graphene quantum dot*, [Applied Physics Letters](#) **94**, 012107 (2009).
- [109] M. L. Mueller, X. Yan, J. A. McGuire, and L.-s. Li, *Triplet States and Electronic Relaxation in Photoexcited Graphene Quantum Dots*, [Nano Letters](#) **10**, 2679–2682 (2010).
- [110] D. R. da Costa, M. Zarenia, A. Chaves, G. A. Farias, and F. M. Peeters, *Energy levels of bilayer graphene quantum dots*, [Physical Review B](#) **92**, 115437 (2015).

- [111] L. Banszerus, S. Möller, E. Icking, K. Watanabe, T. Taniguchi, C. Volk, and C. Stampfer, *Single-Electron Double Quantum Dots in Bilayer Graphene*, [Nano Letters](#) **20**, 2005–2011 (2020).
- [112] L. Banszerus, A. Rothstein, T. Fabian, S. Möller, E. Icking, S. Trellenkamp, F. Lentz, D. Neumaier, K. Watanabe, T. Taniguchi, F. Libisch, C. Volk, and C. Stampfer, *Electron–Hole Crossover in Gate-Controlled Bilayer Graphene Quantum Dots*, [Nano Letters](#) **20**, 7709–7715 (2020).
- [113] L. Banszerus, S. Möller, C. Steiner, E. Icking, S. Trellenkamp, F. Lentz, K. Watanabe, T. Taniguchi, C. Volk, and C. Stampfer, *Spin-valley coupling in single-electron bilayer graphene quantum dots*, [Nature Communications](#) **12**, 5250 (2021).
- [114] R. Garreis, J. D. Gerber, V. Stará, C. Tong, C. Gold, M. Rössli, K. Watanabe, T. Taniguchi, K. Ensslin, T. Ihn, and A. Kurzmann, *Counting statistics of single electron transport in bilayer graphene quantum dots*, [Physical ReviewRes.](#) **5**, 013042 (2023).
- [115] A. Kurzmann, M. Eich, H. Overweg, M. Mangold, F. Herman, P. Rickhaus, R. Pisoni, Y. Lee, R. Garreis, C. Tong, K. Watanabe, T. Taniguchi, K. Ensslin, and T. Ihn, *Excited States in Bilayer Graphene Quantum Dots*, [Physical Review Letters](#) **123**, 026803 (2019).
- [116] A. Knothe and V. Fal’ko, *Influence of minivalleys and Berry curvature on electrostatically induced quantum wires in gapped bilayer graphene*, [Physical Review B](#) **98**, 155435 (2018).
- [117] A. Kurzmann, H. Overweg, M. Eich, A. Pally, P. Rickhaus, R. Pisoni, Y. Lee, K. Watanabe, T. Taniguchi, T. Ihn, and K. Ensslin, *Charge Detection in Gate-Defined Bilayer Graphene Quantum Dots*, [Nano Letters](#) **19**, 5216–5221 (2019).
- [118] M. Eich, R. Pisoni, A. Pally, H. Overweg, A. Kurzmann, Y. Lee, P. Rickhaus, K. Watanabe, T. Taniguchi, K. Ensslin, and T. Ihn, *Coupled Quantum Dots in Bilayer Graphene*, [Nano Letters](#) **18**, 5042–5048 (2018).
- [119] L. Banszerus, B. Frohn, A. Epping, D. Neumaier, K. Watanabe, T. Taniguchi, and C. Stampfer, *Gate-Defined Electron–Hole Double Dots in Bilayer Graphene*, [Nano Letters](#) **18**, 4785–4790 (2018).
- [120] S. Möller, L. Banszerus, A. Knothe, C. Steiner, E. Icking, S. Trellenkamp, F. Lentz, K. Watanabe, T. Taniguchi, L. I. Glazman, V. I. Fal’ko, C. Volk, and C. Stampfer, *Probing Two-Electron Multiplets in Bilayer Graphene Quantum Dots*, [Physical Review Letters](#) **127**, 256802 (2021).
- [121] M. Ciorga, A. S. Sachrajda, P. Hawrylak, C. Gould, P. Zawadzki, S. Jullian, Y. Feng, and Z. Wasilewski, *Addition spectrum of a lateral dot from Coulomb and spin-blockade spectroscopy*, [Physical Review B](#) **61**, R16315–R16318 (2000).
- [122] C.-Y. Hsieh, Y.-P. Shim, M. Korkusinski, and P. Hawrylak, *Physics of lateral triple quantum-dot molecules with controlled electron numbers*, [Reports on Progress in Physics](#) **75**, 114501 (2012).
- [123] G. Burkard, T. D. Ladd, A. Pan, J. M. Nichol, and J. R. Petta, *Semiconductor spin qubits*, [Reviews of Modern Physics](#) **95**, 025003 (2023).
- [124] F. P. G. de Arquer, D. V. Talapin, V. I. Klimov, Y. Arakawa, M. Bayer, and E. H. Sargent, *Semiconductor quantum dots: Technological progress and future challenges*, [Science](#) **373**, eaaz8541 (2021).
- [125] M. Bayer, O. Stern, P. Hawrylak, S. Fafard, and A. Forchel, *Hidden symmetries in the energy levels of excitonic ‘artificial atoms’*, [Nature](#) **405**, 923–926 (2000).
- [126] P. Hawrylak, G. A. Narvaez, M. Bayer, and A. Forchel, *Excitonic Absorption in a Quantum Dot*, [Physical Review Letters](#) **85**, 389–392 (2000).
- [127] I. Schwartz, D. Cogan, E. R. Schmidgall, Y. Don, L. Gantz, O. Kenneth, N. H. Lindner, and D. Gershoni, *Deterministic generation of a cluster state of entangled photons*, [Science](#) **354**, 434–437 (2016).
- [128] P. Laferrière, E. Yeung, M. Korkusinski, P. J. Poole, R. L. Williams, D. Dalacu, J. Manalo, M. Cygorek, A. Altintas, and P. Hawrylak, *Systematic study of the emission spectra of nanowire quantum dots*, [Applied Physics Letters](#) **118**, 161107 (2021).
- [129] G. Bester, S. Nair, and A. Zunger, *Pseudopotential calculation of the excitonic fine structure of million-atom self-assembled  $In_{1-x}Ga_xAs/GaAs$  quantum dots*, [Physical Review B](#) **67**, 161306 (2003).
- [130] M. Korkusinski, Y. Saleem, A. Dusko, D. Miravet, and P. Hawrylak, *Spontaneous Spin and Valley Symmetry-Broken States of Interacting Massive Dirac Fermions in a Bilayer Graphene Quantum Dot*, [Nano Letters](#) **23**, 7546–7551 (2023).
- [131] M. Müller, C. Kübel, and K. Müllen, *Giant Polycyclic Aromatic Hydrocarbons*, [Chemistry – A European Journal](#) **4**, 2099–2109 (1998).

- [132] J. S. Bunch, Y. Yaish, M. Brink, K. Bolotin, and P. L. McEuen, *Coulomb Oscillations and Hall Effect in Quasi-2D Graphite Quantum Dots*, [Nano Letters](#) **5**, 287–290 (2005).
- [133] N. Mohanty, D. Moore, Z. Xu, T. S. Sreeprasad, A. Nagaraja, A. A. Rodriguez, and V. Berry, *Nanotomy-based production of transferable and dispersible graphene nanostructures of controlled shape and size*, [Nature Communications](#) **3**, 844 (2012).
- [134] T. Yamamoto, T. Noguchi, and K. Watanabe, *Edge-state signature in optical absorption of nanographenes: Tight-binding method and time-dependent density functional theory calculations*, [Physical Review B](#) **74**, 121409 (2006).
- [135] Z. Z. Zhang, K. Chang, and F. M. Peeters, *Tuning of energy levels and optical properties of graphene quantum dots*, [Physical Review B](#) **77**, 235411 (2008).
- [136] A. D. Güçlü, P. Potasz, and P. Hawrylak, *Excitonic absorption in gate-controlled graphene quantum dots*, [Physical Review B](#) **82**, 155445 (2010).
- [137] J. Fernández-Rossier and J. J. Palacios, *Magnetism in Graphene Nanoislands*, [Physical Review Letters](#) **99**, 177204 (2007).
- [138] W. L. Wang, S. Meng, and E. Kaxiras, *Graphene NanoFlakes with Large Spin*, [Nano Letters](#) **8**, 241–245 (2008).
- [139] W. L. Wang, O. V. Yazyev, S. Meng, and E. Kaxiras, *Topological Frustration in Graphene Nanoflakes: Magnetic Order and Spin Logic Devices*, [Physical Review Letters](#) **102**, 157201 (2009).
- [140] A. D. Güçlü, P. Potasz, O. Voznyy, M. Korkusinski, and P. Hawrylak, *Magnetism and Correlations in Fractionally Filled Degenerate Shells of Graphene Quantum Dots*, [Physical Review Letters](#) **103**, 246805 (2009).
- [141] L. A. Ponomarenko, F. Schedin, M. I. Katsnelson, R. Yang, E. W. Hill, K. S. Novoselov, and A. K. Geim, *Chaotic Dirac Billiard in Graphene Quantum Dots*, [Science](#) **320**, 356–358 (2008).
- [142] P. Recher and B. Trauzettel, *Quantum dots and spin qubits in graphene*, [Nanotechnology](#) **21**, 302001 (2010).
- [143] S. K. Hämäläinen, Z. Sun, M. P. Boneschanscher, A. Uppstu, M. Ijäs, A. Harju, D. Vanmaekelbergh, and P. Liljeroth, *Quantum-Confined Electronic States in Atomically Well-Defined Graphene Nanostructures*, [Physical Review Letters](#) **107**, 236803 (2011).
- [144] J. Akola, H. P. Heiskanen, and M. Manninen, *Edge-dependent selection rules in magic triangular graphene flakes*, [Physical Review B](#) **77**, 193410 (2008).
- [145] J. M. Pereira, P. Vasilopoulos, and F. M. Peeters, *Tunable Quantum Dots in Bilayer Graphene*, [Nano Letters](#) **7**, 946–949 (2007).
- [146] M. Zarenia, B. Partoens, T. Chakraborty, and F. M. Peeters, *Electron-electron interactions in bilayer graphene quantum dots*, [Physical Review B](#) **88**, 245432 (2013).
- [147] A. Knothe and V. Fal'ko, *Quartet states in two-electron quantum dots in bilayer graphene*, [Physical Review B](#) **101**, 235423 (2020).
- [148] H. Min, B. Sahu, S. K. Banerjee, and A. H. MacDonald, *Ab initio theory of gate induced gaps in graphene bilayers*, [Physical Review B](#) **75**, 155115 (2007).
- [149] M. Aoki and H. Amawashi, *Dependence of band structures on stacking and field in layered graphene*, [Solid State Communications](#) **142**, 123–127 (2007).
- [150] P. Gava, M. Lazzeri, A. M. Saitta, and F. Mauri, *Ab initio study of gap opening and screening effects in gated bilayer graphene*, [Physical Review B](#) **79**, 165431 (2009).
- [151] L. A. Falkovsky, *Gate-tunable bandgap in bilayer graphene*, [Journal of Experimental and Theoretical Physics](#) **110**, 319–324 (2010).
- [152] M. Albert, D. Miravet, Y. Saleem, K. Sadecka, M. Korkusinski, G. Bester, and P. Hawrylak, *Optical properties of gated bilayer graphene quantum dots with trigonal warping*, [Physical Review B](#) **110**, 155421 (2024).
- [153] A. Kiraz, M. Atatüre, and A. Imamoglu, *Quantum-dot single-photon sources: Prospects for applications in linear optics quantum-information processing*, [Physical Review A](#) **69**, 032305 (2004).
- [154] E. J. Gansen, M. A. Rowe, M. B. Greene, D. Rosenberg, T. E. Harvey, M. Y. Su, R. H. Hadfield, S. W. Nam, and R. P. Mirin, *Operational analysis of a quantum dot optically gated field-effect transistor as a single-photon detector*, [IEEE Journal of Selected Topics in Quantum Electronics](#) **13**, 967–977 (2007).

- [155] A. Shields, M. O'sullivan, I. Farrer, D. Ritchie, R. Hogg, M. Leadbeater, C. Norman, and M. Pepper, *Detection of single photons using a field-effect transistor gated by a layer of quantum dots*, *Applied Physics Letters* **76**, 3673–3675 (2000).
- [156] M. A. Rowe, E. Gansen, M. Greene, R. Hadfield, T. Harvey, M. Su, S. W. Nam, R. Mirin, and D. Rosenberg, *Single-photon detection using a quantum dot optically gated field-effect transistor with high internal quantum efficiency*, *Applied physics letters* **89**, 253505 (2006).
- [157] L. Tang, R. Ji, X. Cao, J. Lin, H. Jiang, X. Li, K. S. Teng, C. M. Luk, S. Zeng, J. Hao, and S. P. Lau, *Deep Ultraviolet Photoluminescence of Water-Soluble Self-Passivated Graphene Quantum Dots*, *ACS Nano* **6**, 5102–5110 (2012).
- [158] S. H. Jin, D. H. Kim, G. H. Jun, S. H. Hong, and S. Jeon, *Tuning the Photoluminescence of Graphene Quantum Dots through the Charge Transfer Effect of Functional Groups*, *ACS Nano* **7**, 1239–1245 (2013).
- [159] S. Zhuo, M. Shao, and S.-T. Lee, *Upconversion and Downconversion Fluorescent Graphene Quantum Dots: Ultrasonic Preparation and Photocatalysis*, *ACS Nano* **6**, 1059–1064 (2012).
- [160] M. Albert, *Optical Properties of Bilayer Graphene Quantum Dots*, *Université d'Ottawa / University of Ottawa* (2024).
- [161] Y.-N. Ren, Q. Cheng, Q.-F. Sun, and L. He, *Continuously Tunable Berry Phase and Valley-Polarized Energy Spectra in Bilayer Graphene Quantum Dots*, *arXiv:2108.07391* (2021).
- [162] S. Wang, M. Z. Hossain, K. Shinozuka, N. Shimizu, S. Kitada, T. Suzuki, R. Ichige, A. Kuwana, and H. Kobayashi, *Graphene field-effect transistor biosensor for detection of biotin with ultrahigh sensitivity and specificity*, *Biosensors and Bioelectronics* **165**, 112363 (2020).
- [163] J. A. Crosse, X. Xu, M. S. Sherwin, and R. B. Liu, *Theory of low-power ultra-broadband terahertz sideband generation in bi-layer graphene*, *Nature Communications* **5**, 4854 (2014).
- [164] K. S. Novoselov, A. Mishchenko, A. Carvalho, and A. H. Castro Neto, *2D materials and van der Waals heterostructures*, *Science* **353** (2016).
- [165] Y. Liu, N. O. Weiss, X. Duan, H.-C. Cheng, Y. Huang, and X. Duan, *Van der Waals heterostructures and devices*, *Nature Reviews Materials* **1**, 1–17 (2016).
- [166] N. Mounet, M. Gibertini, P. Schwaller, D. Campi, A. Merkys, A. Marrazzo, T. Sohier, I. E. Castelli, A. Cepellotti, G. Pizzi, and N. Marzari, *Two-dimensional materials from high-throughput computational exfoliation of experimentally known compounds*, *Nature Nanotechnology* **13**, 246–252 (2018).
- [167] M. Ashton, J. Paul, S. B. Sinnott, and R. G. Hennig, *Topology-Scaling Identification of Layered Solids and Stable Exfoliated 2D Materials*, *Physical Review Letters* **118**, 106101 (2017).
- [168] R. A. Bromley, R. B. Murray, and A. D. Yoffe, *The band structures of some transition metal dichalcogenides. III. Group VIA: trigonal prism materials*, *Journal of Physics C: Solid State Physics* **5**, 759 (1972).
- [169] K. F. Mak, C. Lee, J. Hone, J. Shan, and T. F. Heinz, *Atomically Thin MoS<sub>2</sub>: A New Direct-Gap Semiconductor*, *Physical Review Letters* **105**, 136805 (2010).
- [170] K. S. Novoselov, D. Jiang, F. Schedin, T. J. Booth, V. V. Khotkevich, S. V. Morozov, and A. K. Geim, *Two-dimensional atomic crystals*, *Proceedings of the National Academy of Sciences* **102**, 10451–10453 (2005).
- [171] S. Balendhran, J. Z. Ou, M. Bhaskaran, S. Sriram, S. Ippolito, Z. Vasic, E. Kats, S. Bhargava, S. Zhuiykov, and K. Kalantar-Zadeh, *Atomically thin layers of MoS<sub>2</sub> via a two step thermal evaporation–exfoliation method*, *Nanoscale* **4**, 461–466 (2012).
- [172] K. Kalantar-zadeh, J. Z. Ou, T. Daeneke, M. S. Strano, M. Pumera, and S. L. Gras, *Two-dimensional transition metal dichalcogenides in biosystems*, *Advanced Functional Materials* **25**, 5086–5099 (2015).
- [173] A. Splendiani, L. Sun, Y. Zhang, T. Li, J. Kim, C.-Y. Chim, G. Galli, and F. Wang, *Emerging Photoluminescence in Monolayer MoS<sub>2</sub>*, *Nano Letters* **10**, 1271 (2010).
- [174] A. Chernikov, T. C. Berkelbach, H. M. Hill, A. Rigosi, Y. Li, O. B. Aslan, D. R. Reichman, M. S. Hybertsen, and T. F. Heinz, *Exciton binding energy and nonhydrogenic Rydberg series in monolayer WS<sub>2</sub>*, *Physical Review Letters* **113**, 076802 (2014).
- [175] M. Bieniek, K. Sadecka, L. Szulakowska, and P. Hawrylak, *Theory of Excitons in Atomically Thin Semiconductors: Tight-Binding Approach*, *Nanomaterials* **12** (2022).

- [176] A. Jain, S. P. Ong, G. Hautier, W. Chen, W. D. Richards, S. Dacek, S. Cholia, D. Gunter, D. Skinner, G. Ceder, and K. a. Persson, *The Materials Project: A materials genome approach to accelerating materials innovation*, *APL Materials* **1**, 011002 (2013).
- [177] D. W. Latzke, W. Zhang, A. Suslu, T.-R. Chang, H. Lin, H.-T. Jeng, S. Tongay, J. Wu, A. Bansil, and A. Lanzara, *Electronic structure, spin-orbit coupling, and interlayer interaction in bulk MoS<sub>2</sub> and WS<sub>2</sub>*, *Physical Review B* **91**, 235202 (2015).
- [178] A. Kormányos, G. Burkard, M. Gmitra, J. Fabian, V. Zólyomi, N. D. Drummond, and V. Fal'ko, *K · p theory for two-dimensional transition metal dichalcogenide semiconductors*, *2D Materials* **2**, 022001 (2015).
- [179] Z. Y. Zhu, Y. C. Cheng, and U. Schwingenschlögl, *Giant spin-orbit-induced spin splitting in two-dimensional transition-metal dichalcogenide semiconductors*, *Physical Review B* **84**, 153402 (2011).
- [180] D. Xiao, G.-B. Liu, W. Feng, X. Xu, and W. Yao, *Coupled spin and valley physics in monolayers of MoS<sub>2</sub> and other group-VI dichalcogenides*, *Physical Review Letters* **108**, 196802 (2012).
- [181] T. Habe and M. Koshino, *Spin-dependent refraction at the atomic step of transition-metal dichalcogenides*, *Physical Review B* **91**, 201407 (2015).
- [182] H. Yu, M. Laurien, Z. Hu, and O. Rubel, *Exploration of the bright and dark exciton landscape and fine structure of MoS<sub>2</sub> using G<sub>0</sub>W<sub>0</sub>-BSE*, *Physical Review B* **100**, 125413 (2019).
- [183] K. Beach, M. C. Lucking, and H. Terrones, *Strain dependence of second harmonic generation in transition metal dichalcogenide monolayers and the fine structure of the C exciton*, *Physical Review B* **101**, 155431 (2020).
- [184] R. Soklaski, Y. Liang, and L. Yang, *Temperature effect on optical spectra of monolayer molybdenum disulfide*, *Applied Physics Letters* **104**, 193110 (2014).
- [185] A. Molina-Sánchez, M. Palummo, A. Marini, and L. Wirtz, *Temperature-dependent excitonic effects in the optical properties of single-layer MoS<sub>2</sub>*, *Physical Review B* **93**, 155435 (2016).
- [186] A. Klots, A. Newaz, B. Wang, D. Prasai, H. Krzyzanowska, J. Lin, D. Caudel, N. Ghimire, J. Yan, B. Iva11, K. A. Velizhanin, A. Burger, D. G. Mandrus, N. H. Tolk, S. T. Pantelides, and K. I. Bolotin, *Probing excitonic states in suspended two-dimensional semiconductors by photocurrent spectroscopy*, *Scientific Reports* **4**, 1–7 (2014).
- [187] J. Echeverry, B. Urbaszek, T. Amand, X. Marie, and I. Gerber, *Splitting between bright and dark excitons in transition metal dichalcogenide monolayers*, *Physical Review B* **93**, 121107 (2016).
- [188] C.-K. Yong, M. I. B. Utama, C. S. Ong, T. Cao, E. C. Regan, J. Horng, Y. Shen, H. Cai, K. Watanabe, T. Taniguchi, S. Tongay, H. Deng, A. Zettl, S. G. Louie, and F. Wang, *Valley-dependent exciton fine structure and Autler–Townes doublets from Berry phases in monolayer MoSe<sub>2</sub>*, *Nature Materials* **18**, 1065–1070 (2019).
- [189] A. Molina-Sánchez, D. Sangalli, K. Hummer, A. Marini, and L. Wirtz, *Effect of spin-orbit interaction on the optical spectra of single-layer, double-layer, and bulk MoS<sub>2</sub>*, *Physical Review B* **88**, 045412 (2013).
- [190] Y. Suzuki and K. Watanabe, *Excitons in two-dimensional atomic layer materials from time-dependent density functional theory: mono-layer and bi-layer hexagonal boron nitride and transition-metal dichalcogenides*, *Physical Chemistry Chemical Physics* **22**, 2908–2916 (2020).
- [191] T. C. Berkelbach, M. S. Hybertsen, and D. R. Reichman, *Bright and dark singlet excitons via linear and two-photon spectroscopy in monolayer transition-metal dichalcogenides*, *Physical Review B* **92**, 085413 (2015).
- [192] F. Wu, F. Qu, and A. H. MacDonald, *Exciton band structure of monolayer MoS<sub>2</sub>*, *Physical Review B* **91**, 075310 (2015).
- [193] G.-H. Peng, P.-Y. Lo, W.-H. Li, Y.-C. Huang, Y.-H. Chen, C.-H. Lee, C.-K. Yang, and S.-J. Cheng, *Distinctive signatures of the spin-and momentum-forbidden dark exciton states in the photoluminescence of strained WSe<sub>2</sub> monolayers under thermalization*, *Nano Letters* **19**, 2299–2312 (2019).
- [194] B. Scharf, T. Frank, M. Gmitra, J. Fabian, I. Žutić, and V. Perebeinos, *Excitonic Stark effect in MoS<sub>2</sub> monolayers*, *Physical Review B* **94**, 245434 (2016).
- [195] A. Steinhoff, M. Rosner, F. Jahnke, T. O. Wehling, and C. Gies, *Influence of excited carriers on the optical and electronic properties of MoS<sub>2</sub>*, *Nano Letters* **14**, 3743–3748 (2014).
- [196] A. Steinhoff, J.-H. Kim, F. Jahnke, M. Rosner, D.-S. Kim, C. Lee, G. H. Han, M. S. Jeong, T. Wehling, and C. Gies, *Efficient excitonic photoluminescence in direct and indirect band gap monolayer MoS<sub>2</sub>*, *Nano Letters* **15**, 6841–6847 (2015).

- [197] M. Glazov, T. Amand, X. Marie, D. Lagarde, L. Bouet, and B. Urbaszek, *Exciton fine structure and spin decoherence in monolayers of transition metal dichalcogenides*, [Physical Review B](#) **89**, 201302 (2014).
- [198] M. Selig, G. Berghäuser, A. Raja, P. Nagler, C. Schüller, T. F. Heinz, T. Korn, A. Chernikov, E. Malic, and A. Knorr, *Excitonic linewidth and coherence lifetime in monolayer transition metal dichalcogenides*, [Nature Communications](#) **7**, 1–6 (2016).
- [199] M. Feierabend, G. Berghäuser, A. Knorr, and E. Malic, *Proposal for dark exciton based chemical sensors*, [Nature Communications](#) **8**, 1–6 (2017).
- [200] M. Glazov, E. Ivchenko, G. Wang, T. Amand, X. Marie, B. Urbaszek, and B. Liu, *Spin and valley dynamics of excitons in transition metal dichalcogenide monolayers*, [Physica Status Solidi B](#) **252**, 2349–2362 (2015).
- [201] M. Glazov, L. Golub, G. Wang, X. Marie, T. Amand, and B. Urbaszek, *Intrinsic exciton-state mixing and nonlinear optical properties in transition metal dichalcogenide monolayers*, [Physical Review B](#) **95**, 035311 (2017).
- [202] A. Chaves, R. Ribeiro, T. Frederico, and N. Peres, *Excitonic effects in the optical properties of 2D materials: an equation of motion approach*, [2D Materials](#) **4**, 025086 (2017).
- [203] H. Yu, G.-B. Liu, P. Gong, X. Xu, and W. Yao, *Dirac cones and Dirac saddle points of bright excitons in monolayer transition metal dichalcogenides*, [Nature Communications](#) **5**, 1–7 (2014).
- [204] M. Trushin, M. O. Goerbig, and W. Belzig, *Optical absorption by Dirac excitons in single-layer transition-metal dichalcogenides*, [Physical Review B](#) **94**, 041301 (2016).
- [205] M. Trushin, M. O. Goerbig, and W. Belzig, *Model Prediction of Self-Rotating Excitons in Two-Dimensional Transition-Metal Dichalcogenides*, [Physical Review Letters](#) **120**, 187401 (2018).
- [206] F. Rose, M. Goerbig, and F. Piéchon, *Spin-and valley-dependent magneto-optical properties of MoS<sub>2</sub>*, [Physical Review B](#) **88**, 125438 (2013).
- [207] G. Catarina, J. Have, J. Fernández-Rossier, and N. M. Peres, *Optical orientation with linearly polarized light in transition metal dichalcogenides*, [Physical Review B](#) **99**, 125405 (2019).
- [208] I. Kylänpää and H.-P. Komsa, *Binding energies of exciton complexes in transition metal dichalcogenide monolayers and effect of dielectric environment*, [Physical Review B](#) **92**, 205418 (2015).
- [209] D. W. Kidd, D. K. Zhang, and K. Varga, *Binding energies and structures of two-dimensional excitonic complexes in transition metal dichalcogenides*, [Physical Review B](#) **93**, 125423 (2016).
- [210] T. G. Pedersen, *Exciton Stark shift and electroabsorption in monolayer transition-metal dichalcogenides*, [Physical Review B](#) **94**, 125424 (2016).
- [211] L. Cavalcante, D. R. da Costa, G. Farias, D. Reichman, and A. Chaves, *Stark shift of excitons and trions in two-dimensional materials*, [Physical Review B](#) **98**, 245309 (2018).
- [212] C. Robert, M. A. Semina, F. Cadiz, M. Manca, E. Courtade, T. Taniguchi, K. Watanabe, H. Cai, S. Tongay, B. Lassagne, P. Renucci, T. Amand, X. Marie, M. M. Glazov, and B. Urbaszek, *Optical spectroscopy of excited exciton states in MoS<sub>2</sub> monolayers in van der Waals heterostructures*, [Physical Review Materials](#) **2**, 011001 (2018).
- [213] M. Feierabend, Z. Khatibi, G. Berghäuser, and E. Malic, *Dark exciton based strain sensing in tungsten-based transition metal dichalcogenides*, [Physical Review B](#) **99**, 195454 (2019).
- [214] M. R. Molas, A. O. Slobodeniuk, K. Nogajewski, M. Bartos, Ł. Bala, A. Babiński, K. Watanabe, T. Taniguchi, C. FAugeras, and M. Potemski, *Energy spectrum of two-dimensional excitons in a nonuniform dielectric medium*, [Physical Review Letters](#) **123**, 136801 (2019).
- [215] W.-T. Hsu, J. Quan, C.-Y. Wang, L.-S. Lu, M. Campbell, W.-H. Chang, L.-J. Li, X. Li, and C.-K. Shih, *Dielectric impact on exciton binding energy and quasiparticle bandgap in monolayer WS<sub>2</sub> and WSe<sub>2</sub>*, [2D Materials](#) **6**, 025028 (2019).
- [216] M. F. M. Quintela and N. M. Peres, *A colloquium on the variational method applied to excitons in 2D materials*, [The European Physical Journal B](#) **93**, 1–16 (2020).
- [217] T. C. Berkelbach and D. R. Reichman, *Optical and excitonic properties of atomically thin transition-metal dichalcogenides*, [Annual Review of Condensed Matter Physics](#) **9**, 379–396 (2018).
- [218] F. Ceballos, Q. Cui, M. Z. Bellus, and H. Zhao, *Exciton formation in monolayer transition metal dichalcogenides*, [Nanoscale](#) **8**, 11681–11688 (2016).

- [219] X.-X. Zhang, T. Cao, Z. Lu, Y.-C. Lin, F. Zhang, Y. Wang, Z. Li, J. C. Hone, J. A. Robinson, D. Smirnov, S. G. Louie, and T. F. Heinz, *Magnetic brightening and control of dark excitons in monolayer WSe<sub>2</sub>*, *Nature Nanotechnology* **12**, 883–888 (2017).
- [220] M. R. Molas, A. O. Slobodeniuk, T. Kazimierczuk, K. Nogajewski, M. Bartos, P. Kapuscinski, K. Oreszczuk, K. Watanabe, T. Taniguchi, C. FAugeras, P. Kossacki, D. M. Basko, and M. Potemski, *Probing and manipulating valley coherence of dark excitons in monolayer WSe<sub>2</sub>*, *Physical Review Letters* **123**, 096803 (2019).
- [221] C. Robert, B. Han, P. Kapuscinski, A. Delhomme, C. FAugeras, T. Amand, M. Molas, M. Bartos, K. Watanabe, T. Taniguchi, B. Urbaszek, M. Potemski, and X. Marie, *Measurement of the spin-forbidden dark excitons in MoS<sub>2</sub> and MoSe<sub>2</sub> monolayers*, *Nature Communications* **11**, 1–8 (2020).
- [222] P. Kapuscinski, A. Delhomme, D. Vaclavkova, A. Slobodeniuk, M. Grzeszczyk, M. Bartos, K. Watanabe, T. Taniguchi, C. FAugeras, and M. Potemski, *Rydberg series of dark excitons and the conduction band spin-orbit splitting in monolayer WSe<sub>2</sub>*, *arXiv:2102.12286* (2021).
- [223] M. Bieniek, L. Szulakowska, and P. Hawrylak, *Band nesting and exciton spectrum in monolayer MoS<sub>2</sub>*, *Physical Review B* **101**, 125423 (2020).
- [224] K. He, N. Kumar, L. Zhao, Z. Wang, K. F. Mak, H. Zhao, and J. Shan, *Tightly bound excitons in monolayer WSe<sub>2</sub>*, *Physical Review Letters* **113**, 026803 (2014).
- [225] T. Mueller and E. Malic, *Exciton physics and device application of two-dimensional transition metal dichalcogenide semiconductors*, *npj 2D Materials and Applications* **2**, 29 (2018).
- [226] A. Arora, M. Koperski, A. Slobodeniuk, K. Nogajewski, R. Schmidt, R. Schneider, M. R. Molas, S. M. de Vasconcellos, R. Bratschitsch, and M. Potemski, *Zeeman spectroscopy of excitons and hybridization of electronic states in few-layer WSe<sub>2</sub>, MoSe<sub>2</sub> and MoTe<sub>2</sub>*, *2D Materials* **6**, 015010 (2018).
- [227] J. Xiao, M. Zhao, Y. Wang, and X. Zhang, *Excitons in atomically thin 2D semiconductors and their applications*, *Nanophotonics* **6**, 1309–1328 (2017).
- [228] D. Thomas, *The exciton spectrum of zinc oxide*, *Journal of Physics and Chemistry of Solids* **15**, 86–96 (1960).
- [229] M. Sturge, *Optical absorption of gallium arsenide between 0.6 and 2.75 eV*, *Physical Review* **127**, 768 (1962).
- [230] A. Arora, T. Deilmann, P. Marauhn, M. Drüppel, R. Schneider, M. R. Molas, D. Vaclavkova, S. Michaelis de Vasconcellos, M. Rohlfing, M. Potemski, and R. Bratschitsch, *Valley-contrasting optics of interlayer excitons in Mo- and W-based bulk transition metal dichalcogenides*, *Nanoscale* **10**, 15571–15577 (2018).
- [231] S. Crooker, M. Goryca, J. Li, A. Stier, T. Taniguchi, K. Watanabe, E. Courtade, S. Shree, C. Robert, B. Urbaszek, X. Marie, and S. A. Crooker, *Revealing the exciton masses and dielectric properties of monolayer semiconductors with high magnetic fields*, *Bulletin of the American Physical Society* **65** (2020).
- [232] M. Palummo, M. Bernardi, and J. C. Grossman, *Exciton radiative lifetimes in two-dimensional transition metal dichalcogenides*, *Nano Letters* **15**, 2794–2800 (2015).
- [233] A. Ramasubramaniam, *Large excitonic effects in monolayers of molybdenum and tungsten dichalcogenides*, *Physical Review B* **86**, 115409 (2012).
- [234] D. Lagarde, L. Bouet, X. Marie, C. Zhu, B. Liu, T. Amand, P. Tan, and B. Urbaszek, *Carrier and polarization dynamics in monolayer MoS<sub>2</sub>*, *Physical Review Letters* **112**, 047401 (2014).
- [235] G. Moody, J. Schaibley, and X. Xu, *Exciton dynamics in monolayer transition metal dichalcogenides*, *Journal of the Optical Society of America B* **33**, C39–C49 (2016).
- [236] C. Robert, D. Lagarde, F. Cadiz, G. Wang, B. Lassagne, T. Amand, A. Balocchi, P. Renucci, S. Tongay, B. Urbaszek, and X. Marie, *Exciton radiative lifetime in transition metal dichalcogenide monolayers*, *Physical Review B* **93**, 205423 (2016).
- [237] N. Kumar, Q. Cui, F. Ceballos, D. He, Y. Wang, and H. Zhao, *Exciton diffusion in monolayer and bulk MoSe<sub>2</sub>*, *Nanoscale* **6**, 4915–4919 (2014).
- [238] S. Helmrich, A. W. Achtstein, H. Ahmad, M. Kunz, B. Herzog, O. Schöps, U. Woggon, and N. Owschimikow, *High phonon-limited mobility of charged and neutral excitons in mono- and bilayer MoTe<sub>2</sub>*, *2D Materials* **8**, 025019 (2021).
- [239] Y. Fu, D. He, J. He, A. Bian, L. Zhang, S. Liu, Y. Wang, and H. Zhao, *Effect of dielectric environment on excitonic dynamics in monolayer WS<sub>2</sub>*, *Advanced Materials Interfaces* **6**, 1901307 (2019).

- [240] R. Coehoorn, C. Haas, J. Dijkstra, C. J. F. Flipse, R. A. de Groot, and A. Wold, *Electronic structure of  $MoSe_2$ ,  $MoS_2$ , and  $WSe_2$ . I. Band-structure calculations and photoelectron spectroscopy*, *Physical Review B* **35**, 6195–6202 (1987).
- [241] E. Malic, M. Selig, M. Feierabend, S. Brem, D. Christiansen, F. Wendler, A. Knorr, and G. Berghäuser, *Dark excitons in transition metal dichalcogenides*, *Physical Review Materials* **2**, 014002 (2018).
- [242] M. Drüppel, T. Deilmann, P. Krüger, and M. Rohlfing, *Diversity of trion states and substrate effects in the optical properties of an  $MoS_2$  monolayer*, *Nature Communications* **8**, 1–7 (2017).
- [243] A. Hichri, S. Jaziri, and M. Goerbig, *Charged excitons in two-dimensional transition metal dichalcogenides: Semiclassical calculation of Berry curvature effects*, *Physical Review B* **100**, 115426 (2019).
- [244] X. Xu, Z. Lou, S. Cheng, P. C. Chow, N. Koch, and H.-M. Cheng, *Van der Waals organic/inorganic heterostructures in the two-dimensional limit*, *Chem* **7**, 2989–3026 (2021).
- [245] J. He, K. Hummer, and C. Franchini, *Stacking effects on the electronic and optical properties of bilayer transition metal dichalcogenides  $MoS_2$ ,  $MoSe_2$ ,  $WS_2$ , and  $WSe_2$* , *Physical Review B* **89**, 075409 (2014).
- [246] J. C. Song and N. M. Gabor, *Electron quantum metamaterials in van der Waals heterostructures*, *Nature Nanotechnology* **13**, 986–993 (2018).
- [247] P. E. Faria Junior and J. Fabian, *Signatures of Electric Field and Layer Separation Effects on the Spin-Valley Physics of  $MoSe_2/WSe_2$  Heterobilayers: From Energy Bands to Dipolar Excitons*, *Nanomaterials* **13** (2023).
- [248] K. Sadecka, M. Bieniek, P. E. Faria Junior, A. Wójs, P. Hawrylak, and J. Pawłowski, *Electrically tunable  $MoSe_2/WSe_2$  heterostructure-based quantum dot*, *Physical Review B* **111**, 115421 (2025).
- [249] P. Rivera, J. R. Schaibley, A. M. Jones, J. S. Ross, S. Wu, G. Aivazian, P. Klement, K. Seyler, G. Clark, N. J. Ghimire, J. Yan, D. G. Mandrus, W. Yao, and X. Xu, *Observation of long-lived interlayer excitons in monolayer  $MoSe_2-WSe_2$  heterostructures*, *Nature Communications* **6**, 1–6 (2015).
- [250] K. L. Seyler, P. Rivera, H. Yu, N. P. Wilson, E. L. Ray, D. G. Mandrus, J. Yan, W. Yao, and X. Xu, *Signatures of moiré-trapped valley excitons in  $MoSe_2/WSe_2$  heterobilayers*, *Nature* **567**, 66–70 (2019).
- [251] E. Calman, L. Fowler-Gerace, D. Choksy, L. Butov, D. Niko11, I. Young, S. Hu, A. Mishchenko, and A. Geim, *Indirect excitons and trions in  $MoSe_2/WSe_2$  van der Waals heterostructures*, *Nano Letters* **20**, 1869–1875 (2020).
- [252] F. Volmer, M. Ersfeld, P. E. Faria Junior, L. Waldecker, B. Parashar, L. Rathmann, S. Dubey, I. Cojocariu, V. Feyer, K. Watanabe, T. Taniguchi, C. M. Schneider, L. Plucinski, C. Stampfer, J. Fabian, and B. Beschoten, *Twist angle dependent interlayer transfer of valley polarization from excitons to free charge carriers in  $WSe_2/MoSe_2$  heterobilayers*, *npj 2D Materials and Applications* **7**, 58 (2023).
- [253] B. L. T. Rosa, P. E. F. Junior, A. R. Cadore, Y. Yang, A. Koulas-Simos, C. C. Palekar, S. A. Tongay, J. Fabian, and S. Reitzenstein, *Electrical Manipulation of Intervalley Trions in Twisted  $MoSe_2$  Homobilayers at Room Temperature*, *Advanced Physics Research* **4**, 2400135 (2025).
- [254] Y. Liu, N. O. Weiss, X. Duan, H.-C. Cheng, Y. Huang, and X. Duan, *Van der Waals heterostructures and devices*, *Nature Reviews Materials* **1**, 16042 (2016).
- [255] S. Deb, J. Krause, P. E. Faria Junior, M. A. Kempf, R. Schwartz, K. Watanabe, T. Taniguchi, J. Fabian, and T. Korn, *Excitonic signatures of ferroelectric order in parallel-stacked  $MoS_2$* , *Nature Communications* **15**, 7595 (2024).
- [256] H. Liu, Y. Wu, Z. Wu, S. Liu, V. L. Zhang, and T. Yu, *Coexisting Phases in Transition Metal Dichalcogenides: Overview, Synthesis, Applications, and Prospects*, *ACS Nano* **18**, 2708–2729 (2024).
- [257] B. Amin, N. Singh, and U. Schwingenschlögl, *Heterostructures of transition metal dichalcogenides*, *Physical Review B* **92**, 075439 (2015).
- [258] F. Zhang, W. Li, and X. Dai, *Modulation of electronic structures of  $MoSe_2/WSe_2$  van der Waals heterostructure by external electric field*, *Solid State Communications* **266**, 11–15 (2017).
- [259] X. Duan, C. Wang, J. C. Shaw, R. Cheng, Y. Chen, H. Li, X. Wu, Y. Tang, Q. Zhang, A. Pan, J. Jiang, R. Yu, Y. Huang, and X. Duan, *Lateral epitaxial growth of two-dimensional layered semiconductor heterojunctions*, *Nature Nanotechnology* **9**, 1024–1030 (2014).

- [260] Y. Gong, J. Lin, X. Wang, G. Shi, S. Lei, Z. Lin, X. Zou, G. Ye, R. Vajtai, B. I. Yakobson, H. Terrones, M. Terrones, B. K. Tay, J. Lou, S. T. Pantelides, Z. Liu, W. Zhou, and P. M. Ajayan, *Vertical and in-plane heterostructures from  $WS_2/MoS_2$  monolayers*, *Nature Materials* **13**, 1135–1142 (2014).
- [261] O. Ávalos-Ovando, D. Mastrogiuseppe, and S. E. Ulloa, *Lateral heterostructures and one-dimensional interfaces in 2D transition metal dichalcogenides*, *Journal of Physics: Condensed Matter* **31**, 213001 (2019).
- [262] L. Debbichi, O. Eriksson, and S. Lebègue, *Electronic structure of two-dimensional transition metal dichalcogenide bilayers from ab initio theory*, *Physical Review B* **89**, 205311 (2014).
- [263] B. V. Troeye, A. Lherbier, S. M.-M. Dubois, J.-C. Charlier, and X. Gonze, *First-principles prediction of lattice coherency in van der Waals heterostructures*, [arXiv:1911.06846](https://arxiv.org/abs/1911.06846) (2019).
- [264] E. Cappelluti, R. Roldán, J. A. Silva-Guillén, P. Ordejón, and F. Guinea, *Tight-binding model and direct-gap/indirect-gap transition in single-layer and multilayer  $MoS_2$* , *Physical Review B* **88**, 075409 (2013).
- [265] S. K. Pandey, R. Das, and P. Mahadevan, *Layer-Dependent Electronic Structure Changes in Transition Metal Dichalcogenides: The Microscopic Origin*, *ACS Omega* **5**, 15169–15176 (2020).
- [266] W.-T. Hsu, J. Quan, C.-R. Pan, P.-J. Chen, M.-Y. Chou, W.-H. Chang, A. H. MacDonald, X. Li, J.-F. Lin, and C.-K. Shih, *Quantitative determination of interlayer electronic coupling at various critical points in bilayer  $MoS_2$* , *Physical Review B* **106**, 125302 (2022).
- [267] F. H. Davies, C. J. Price, N. T. Taylor, S. G. Davies, and S. P. Hepplestone, *Band alignment of transition metal dichalcogenide heterostructures*, *Physical Review B* **103**, 045417 (2021).
- [268] A. J. Pearce, E. Mariani, and G. Burkard, *Tight-binding approach to strain and curvature in monolayer transition-metal dichalcogenides*, *Physical Review B* **94**, 155416 (2016).
- [269] F. Ullah, Y. Sim, C. T. Le, M.-J. Seong, J. I. Jang, S. H. Rhim, B. C. Tran Khac, K.-H. Chung, K. Park, Y. Lee, C. Kim, H. Y. Jeong, and Y. S. Kim, *Growth and Simultaneous Valleys Manipulation of Two-Dimensional  $MoSe_2-WSe_2$  Lateral Heterostructure*, *ACS Nano* **11**, 8822–8829 (2017).
- [270] H. Jin, H. Su, X. Li, Y. Yu, H. Guo, and Y. Wei, *Strain-gated nonlinear Hall effect in two-dimensional  $MoSe_2/WSe_2$  van der Waals heterostructure*, *Physical Review B* **104**, 195404 (2021).
- [271] D. Kozawa, A. Carvalho, I. Verzhbitskiy, F. Giustiniano, Y. Miyauchi, S. Mouri, A. Castro Neto, K. Matsuda, and G. Eda, *Evidence for fast interlayer energy transfer in  $MoSe_2/WS_2$  heterostructures*, *Nano Letters* **16**, 4087–4093 (2016).
- [272] N. R. Wilson, P. V. Nguyen, K. Seyler, P. Rivera, A. J. Marsden, Z. P. L. Laker, G. C. Constantinescu, V. Kandyba, A. Bari11, N. D. M. Hine, X. Xu, and D. H. Cobden, *Determination of band offsets, hybridization, and exciton binding in 2D semiconductor heterostructures*, *Science Advances* **3**, e1601832 (2017).
- [273] T. Deilmann, M. Rohlfing, and U. Wurstbauer, *Light–matter interaction in van der Waals hetero-structures*, *Journal of Physics: Condensed Matter* **32**, 333002 (2020).
- [274] R. Y. Kezerashvili and A. Spiridonova, *Magnetoexcitons in transition-metal dichalcogenides monolayers, bilayers, and van der Waals heterostructures*, [arXiv:2012.07125](https://arxiv.org/abs/2012.07125) (2020).
- [275] J. Blackburn, D. Kern, and E. Link-Miller, *Photoinduced charge transfer in transition metal dichalcogenide heterojunctions – towards next generation energy technologies*, *Energy & Environmental Science* **13** (2020).
- [276] Y. Zhao, L. Du, S. Yang, J. Tian, X. Li, C. Shen, J. Tang, Y. Chu, K. Watanabe, T. Taniguchi, R. Yang, D. Shi, Z. Sun, Y. Ye, W. Yang, and G. Zhang, *Optically and magnetically addressable valley pseudospin of interlayer excitons in bilayer  $MoS_2$* , [arXiv:2106.00351](https://arxiv.org/abs/2106.00351) (2021).
- [277] A. T. Hanbicki, H.-J. Chuang, M. R. Rosenberger, C. S. Hellberg, S. V. Sivaram, K. M. McCreary, I. I. Mazin, and B. T. Jonker, *Double indirect interlayer exciton in a  $MoSe_2/WSe_2$  van der Waals heterostructure*, *Acs Nano* **12**, 4719–4726 (2018).
- [278] A. O. Slobodeniuk, Ł. Bala, M. Koperski, M. R. Molas, P. Kossacki, K. Nogajewski, M. Bartos, K. Watanabe, T. Taniguchi, C. FAugeras, and M. Potemski, *Fine structure of K-excitons in multilayers of transition metal dichalcogenides*, *2D Materials* **6**, 025026 (2019).
- [279] S. Das, G. Gupta, and K. Majumdar, *Layer degree of freedom for excitons in transition metal dichalcogenides*, *Physical Review B* **99**, 165411 (2019).
- [280] H. Chen, X. Wen, J. Zhang, T. Wu, Y. Gong, X. Zhang, J. Yuan, C. Yi, J. Lou, P. M. Ajayan, W. Zhuang, G. Zhang, and J. Zheng, *Ultrafast formation of interlayer hot excitons in atomically thin  $MoS_2/WS_2$  heterostructures*, *Nature Communications* **7**, 1–8 (2016).

- [281] K. Kořmider and J. Fernandez-Rossier, *Electronic properties of the  $MoS_2$ - $ws_2$  heterojunction*, *Physical Review B* **87**, 075451 (2013).
- [282] L. Hedin and S. Lundqvist, *Effects of electron-electron and electron-phonon interactions on the one-electron states of solids*, *Academic Press, Solid State Physics* **23**, 1–181 (1970).
- [283] H.-P. Komsa and A. V. Krasheninnikov, *Effects of confinement and environment on the electronic structure and exciton binding energy of  $MoS_2$  from first principles*, *Physical Review B* **86**, 241201 (2012).
- [284] T. Cheiwchanchamnangij and W. R. Lambrecht, *Quasiparticle band structure calculation of monolayer, bilayer, and bulk  $MoS_2$* , *Physical Review B* **85**, 205302 (2012).
- [285] F. Zeng, W.-B. Zhang, and B.-Y. Tang, *Electronic structures and elastic properties of monolayer and bilayer transition metal dichalcogenides  $MX_2$  ( $M = Mo, W, X = O, S, Se, Te$ ): A comparative first-principles study*, *Chinese Physics B* **24**, 097103 (2015).
- [286] W. Li, T. Wang, X. Dai, X. Wang, C. Zhai, Y. Ma, S. Chang, and Y. Tang, *Electric field modulation of the band structure in  $MoS_2/WS_2$  van der Waals heterostructure*, *Solid State Communications* **250**, 9–13 (2017).
- [287] N. Zibouche, M. Schlipf, and F. Giustino, *GW band structure of monolayer  $MoS_2$  using the SternheimerGW method and effect of dielectric environment*, *Physical Review B* **103**, 125401 (2021).
- [288] L. Meckbach, T. Stroucken, and S. W. Koch, *Giant excitation induced bandgap renormalization in TMDC monolayers*, *Applied Physics Letters* **112**, 061104 (2018).
- [289] Z. Gong, G.-B. Liu, H. Yu, D. Xiao, X. Cui, X. Xu, and W. Yao, *Magnetoelectric effects and valley-controlled spin quantum gates in transition metal dichalcogenide bilayers*, *Nature Communications* **4**, 1–6 (2013).
- [290] N. Huo, J. Kang, Z. Wei, S.-S. Li, J. Li, and S.-H. Wei, *Novel and enhanced optoelectronic performances of multilayer  $MoS_2$ - $WS_2$  heterostructure transistors*, *Advanced Functional Materials* **24**, 7025–7031 (2014).
- [291] P. Rivera, K. L. Seyler, H. Yu, J. R. Schaibley, J. Yan, D. G. Mandrus, W. Yao, and X. Xu, *Valley-polarized exciton dynamics in a 2D semiconductor heterostructure*, *Science* **351**, 688–691 (2016).
- [292] B. Miller, A. Steinhoff, B. Pano, J. Klein, F. Jahnke, A. Holleitner, and U. Wurstbauer, *Long-lived direct and indirect interlayer excitons in van der Waals heterostructures*, *Nano Letters* **17**, 5229–5237 (2017).
- [293] P. Nagler, M. V. Ballottin, A. A. Mitigloglu, F. Mooshammer, N. Paradiso, C. Strunk, R. Huber, A. Chernikov, P. C. Christianen, C. Schüller, and T. Korn, *Giant magnetic splitting inducing near-unity valley polarization in van der Waals heterostructures*, *Nature Communications* **8**, 1–6 (2017).
- [294] A. R.-P. Montblanch, D. M. Kara, I. Paradisanos, C. M. Purser, M. S. G. Feuer, E. M. Alexeev, L. Stefan, Y. Qin, M. Blei, G. Wang, A. R. Cadore, P. Latawiec, M. Lončar, S. Tongay, A. C. Ferrari, and M. Atatüre, *Confinement of long-lived interlayer excitons in  $WS_2/WSe_2$  heterostructures*, *Communications Physics* **4**, 119 (2021).
- [295] J. Choi, M. Florian, A. Steinhoff, D. Erben, K. Tran, D. S. Kim, L. Sun, J. Quan, R. Claassen, S. Majumder, J. A. Hollingsworth, T. Taniguchi, K. Watanabe, K. Ueno, A. Singh, G. Moody, F. Jahnke, and X. Li, *Twist Angle-Dependent Interlayer Exciton Lifetimes in van der Waals Heterostructures*, *Physical Review Letters* **126**, 047401 (2021).
- [296] A. A. High, A. T. Hammack, J. R. Leonard, S. Yang, L. V. Butov, T. Ostatnický, M. Vladimirova, A. V. Kavokin, T. C. H. Liew, K. L. Campman, and A. C. Gossard, *Spin currents in a coherent exciton gas*, *Physical Review Letters* **110**, 246403 (2013).
- [297] A. A. High, J. R. Leonard, A. T. Hammack, M. M. Fogler, L. V. Butov, A. V. Kavokin, K. L. Campman, and A. C. Gossard, *Spontaneous coherence in a cold exciton gas*, *Nature* **483**, 584–588 (2012).
- [298] M. Fogler, L. Butov, and K. Novoselov, *High-temperature superfluidity with indirect excitons in van der Waals heterostructures*, *Nature Communications* **5**, 1–5 (2014).
- [299] E. Calman, M. Fogler, L. Butov, S. Hu, A. Mishchenko, and A. Geim, *Indirect excitons in van der Waals heterostructures at room temperature*, *Nature Communications* **9**, 1–5 (2018).
- [300] L. A. Jauregui, A. Y. Joe, K. Pistunova, D. S. Wild, A. A. High, Y. Zhou, G. Scuri, K. De Greve, A. Sushko, C.-H. Yu, T. Taniguchi, K. Watanabe, D. J. Needleman, M. D. Lukin, H. Park, and P. Kim, *Electrical control of interlayer exciton dynamics in atomically thin heterostructures*, *Science* **366**, 870–875 (2019).
- [301] X. Zhu, J. He, R. Zhang, C. Cong, Y. Zheng, H. Zhang, S. Zhang, and L. Chen, *Effects of dielectric screening on the excitonic and critical points properties of  $WS_2/MoS_2$  heterostructures*, *Nanoscale* **12**, 23732–23739 (2020).

- [302] M. Van der Donck and F. Peeters, *Interlayer excitons in transition metal dichalcogenide heterostructures*, *Physical Review B* **98**, 115104 (2018).
- [303] O. L. Berman and R. Y. Kezerashvili, *High-temperature superfluidity of the two-component Bose gas in a transition metal dichalcogenide bilayer*, *Physical Review B* **93**, 245410 (2016).
- [304] P. Nagler, F. Mooshammer, J. Kunstmann, M. V. Ballottin, A. Mitioglu, A. Chernikov, A. Chaves, F. Stein, N. Paradiso, S. Meier, G. Plechinger, C. Strunk, R. Huber, G. Seifert, D. R. Reichman, P. C. M. Christianen, C. Schüller, and T. Korn, *Interlayer excitons in transition-metal dichalcogenide heterobilayers*, *Physica Status Solidi B* **256**, 1900308 (2019).
- [305] E. Lorchat, M. Selig, F. Katsch, K. Yumigeta, S. Tongay, A. Knorr, C. Schneider, and S. Höfling, *Excitons in bilayer MoS<sub>2</sub> displaying a colossal electric field splitting and tunable magnetic response*, *Physical Review Letters* **126**, 037401 (2021).
- [306] M. A. Lampert, *Mobile and immobile effective-mass-particle complexes in nonmetallic solids*, *Physical Review Letters* **1**, 450 (1958).
- [307] R. Sergeev and R. Suris, *Ground-state energy of X- and X+ trions in a two-dimensional quantum well at an arbitrary mass ratio*, *Physics of the Solid State* **43**, 746–751 (2001).
- [308] B. Stébé and A. Ainane, *Ground state energy and optical absorption of excitonic trions in two dimensional semiconductors*, *Superlattices and Microstructures* **5**, 545–548 (1989).
- [309] R. Schilling and D. Mattis, *Bound exciton and hole: an exactly solvable three-body model in any number of dimensions*, *Physical Review Letters* **49**, 808 (1982).
- [310] A. Koudi11, C. Kehl, A. Rodina, J. Geurts, D. Wolverson, and G. Karczewski, *Suris tetrons: possible spectroscopic evidence for four-particle optical excitations of a two-dimensional electron gas*, *Physical Review Letters* **112**, 147402 (2014).
- [311] M. M. Glazov, *Optical properties of charged excitons in two-dimensional semiconductors*, *The Journal of Chemical Physics* **153**, 034703 (2020).
- [312] K. F. Mak, K. He, C. Lee, G. H. Lee, J. Hone, T. F. Heinz, and J. Shan, *Tightly bound trions in monolayer MoS<sub>2</sub>*, *Nature Materials* **12**, 207–211 (2013).
- [313] A. Arora, T. Deilmann, T. Reichenauer, J. Kern, S. M. de Vasconcellos, M. Rohlfing, and R. Bratschitsch, *Excited-state trions in monolayer WS<sub>2</sub>*, *Physical Review Letters* **123**, 167401 (2019).
- [314] G. Plechinger, P. Nagler, A. Arora, R. Schmidt, A. Chernikov, A. G. Del Águila, P. C. Christianen, R. Bratschitsch, C. Schüller, and T. Korn, *Trion fine structure and coupled spin–valley dynamics in monolayer tungsten disulfide*, *Nature Communications* **7**, 1–9 (2016).
- [315] C. Biswas and R. Seibait, *Interlayer trions in 2D transition-metal dichalcogenide heterostructures*, *Journal of the Korean Physical Society* **77**, 850–852 (2020).
- [316] T. Deilmann and K. S. Thygesen, *Interlayer trions in the MoS<sub>2</sub>/WS<sub>2</sub> van der Waals heterostructure*, *Nano Letters* **18**, 1460–1465 (2018).
- [317] M. Kuwabara, D. R. Clarke, and D. A. Smith, *Anomalous superperiodicity in scanning tunneling microscope images of graphite*, *Applied Physics Letters* **56**, 2396–2398 (1990).
- [318] G. Oster, M. Wasserman, and C. Zwerling, *Theoretical interpretation of moiré patterns*, *J. Opt. Soc. Am.* **54**, 169–175 (1964).
- [319] I. Amidror, *The Theory of the Moiré Phenomenon: Volume I: Periodic Layers*, *Springer Dordrecht* **38** (2009).
- [320] B. Hunt, J. D. Sanchez-Yamagishi, A. F. Young, M. Yankowitz, B. J. LeRoy, K. Watanabe, T. Taniguchi, P. Moon, M. Koshino, P. Jarillo-Herrero, and R. C. Ashoori, *Massive Dirac fermions and hofstadter butterfly in a van der Waals heterostructure*, *Science* **340**, 1427–1430 (2013).
- [321] C. R. Dean, L. Wang, P. Maher, C. Forsythe, F. Ghahari, Y. Gao, J. Katoch, M. Ishigami, P. Moon, M. Koshino, T. Taniguchi, K. Watanabe, K. L. Shepard, J. Hone, and P. Kim, *Hofstadter’s butterfly and the fractal quantum Hall effect in moiré superlattices*, *Nature* **497**, 598–602 (2013).
- [322] J. M. B. Lopes dos Santos, N. M. R. Peres, and A. H. Castro Neto, *Graphene Bilayer with a Twist: Electronic Structure*, *Physical Review Letters* **99**, 256802 (2007).
- [323] R. Bistritzer and A. H. MacDonald, *Moiré bands in twisted double-layer graphene*, *Proceedings of the National Academy of Sciences* **108**, 12233–12237 (2011).

- [324] L. J. McGilly, A. Kerelsky, N. R. Finney, K. Shapovalov, E.-M. Shih, A. Ghiotto, Y. Zeng, S. L. Moore, W. Wu, Y. Bai, K. Watanabe, T. Taniguchi, M. Stengel, L. Zhou, J. Hone, X. Zhu, D. N. Basov, C. Dean, C. E. Dreyer, and A. N. Pasupathy, *Visualization of moiré superlattices*, *Nature Nanotechnology* **15**, 580–584 (2020).
- [325] Y. Cao, V. Fatemi, S. Fang, K. Watanabe, T. Taniguchi, E. Kaxiras, and P. Jarillo-Herrero, *Unconventional superconductivity in magic-angle graphene superlattices*, *Nature* **556**, 43–50 (2018).
- [326] J. Kang, J. Li, S.-S. Li, J.-B. Xia, and L.-W. Wang, *Electronic structural moiré pattern effects on MoS<sub>2</sub>/MoSe<sub>2</sub> 2D heterostructures*, *Nano Letters* **13**, 5485–5490 (2013).
- [327] C. Zhang, C.-P. Chuu, X. Ren, M.-Y. Li, L.-J. Li, C. Jin, M.-Y. Chou, and C.-K. Shih, *Interlayer couplings, moiré patterns, and 2D electronic superlattices in MoS<sub>2</sub>/WSe<sub>2</sub> hetero-bilayers*, *Science Advances* **3**, e1601459 (2017).
- [328] F. Wu, T. Lovorn, and A. MacDonald, *Theory of optical absorption by interlayer excitons in transition metal dichalcogenide heterobilayers*, *Physical Review B* **97**, 035306 (2018).
- [329] D. A. Ruiz-Tijerina and V. I. Fal'ko, *Interlayer hybridization and moiré superlattice minibands for electrons and excitons in heterobilayers of transition-metal dichalcogenides*, *Physical Review B* **99**, 125424 (2019).
- [330] K. Tran, J. Choi, and A. Singh, *Moiré and beyond in transition metal dichalcogenide twisted bilayers*, *2D Materials* **8**, 022002 (2020).
- [331] A. Weston, Y. Zou, V. Enaldiev, A. Summerfield, N. Clark, V. Zólyomi, A. Graham, C. Yelgel, S. Magorian, M. Zhou, et al., *Atomic reconstruction in twisted bilayers of transition metal dichalcogenides*, *Nature Nanotechnology* **15**, 592–597 (2020).
- [332] G. Scuri, T. I. Andersen, Y. Zhou, D. S. Wild, J. Sung, R. J. Gelly, D. Bérubé, H. Heo, L. Shao, A. Y. Joe, A. M. Mier Valdivia, T. Taniguchi, K. Watanabe, M. Lončar, P. Kim, M. D. Lukin, and H. Park, *Electrically tunable valley dynamics in twisted WSe<sub>2</sub>/WSe<sub>2</sub> bilayers*, *Physical Review Letters* **124**, 217403 (2020).
- [333] S. Shabani, D. Halbertal, W. Wu, M. Chen, S. Liu, J. Hone, W. Yao, D. N. Basov, X. Zhu, and A. N. Pasupathy, *Deep moiré potentials in twisted transition metal dichalcogenide bilayers*, *Nature Physics*, 1–6 (2021).
- [334] I. Maity, P. K. Maiti, H. Krishnamurthy, and M. Jain, *Reconstruction of moiré lattices in twisted transition metal dichalcogenide bilayers*, *Physical Review B* **103**, L121102 (2021).
- [335] A. J. H. Jones, R. Muzzio, S. Pakdel, D. Biswas, D. Curcio, N. Lanatà, P. Hofmann, K. M. McCreary, B. T. Jonker, K. Watanabe, T. Taniguchi, S. Singh, R. J. Koch, C. Jozwiak, E. Rotenberg, A. Bostwick, J. A. Miwa, J. Katoch, and S. Ulstrup, *Visualizing band structure hybridization and superlattice effects in twisted MoS<sub>2</sub>/WS<sub>2</sub> heterobilayers*, *arXiv:2106.00403* (2021).
- [336] H. Yu, G.-B. Liu, J. Tang, X. Xu, and W. Yao, *Moiré excitons: From programmable quantum emitter arrays to spin-orbit-coupled artificial lattices*, *Science Advances* **3**, e1701696 (2017).
- [337] F. Wu, T. Lovorn, and A. H. MacDonald, *Topological Exciton Bands in Moiré Heterojunctions*, *Physical Review Letters* **118**, 147401 (2017).
- [338] S. Brem, C. Linderälv, P. Erhart, and E. Malic, *Tunable Phases of Moiré Excitons in van der Waals Heterostructures*, *Nano Letters* **20**, 8534–8540 (2020).
- [339] H. Guo, X. Zhang, and G. Lu, *Shedding light on moiré excitons: A first-principles perspective*, *Science Advances* **6**, eabc5638 (2020).
- [340] A. M. van der Zande, J. Kunstmann, A. Chernikov, D. A. Chenet, Y. You, X. Zhang, P. Y. Huang, T. C. Berkelbach, L. Wang, F. Zhang, M. S. Hybertsen, D. A. Muller, D. R. Reichman, T. F. Heinz, and J. C. Hone, *Tailoring the Electronic Structure in Bilayer Molybdenum Disulfide via Interlayer Twist*, *Nano Letters* **14**, 3869–3875 (2014).
- [341] P. K. Nayak, Y. Horbatenko, S. Ahn, G. Kim, J.-U. Lee, K. Y. Ma, A.-R. Jang, H. Lim, D. Kim, S. Ryu, H. Cheong, N. Park, and H. S. Shin, *Probing Evolution of Twist-Angle-Dependent Interlayer Excitons in MoSe<sub>2</sub>/WSe<sub>2</sub> van der Waals Heterostructures*, *ACS Nano* **11**, 4041–4050 (2017).
- [342] W.-T. Hsu, B.-H. Lin, L.-S. Lu, M.-H. Lee, M.-W. Chu, L.-J. Li, W. Yao, W.-H. Chang, and C.-K. Shih, *Tailoring excitonic states of van der Waals bilayers through stacking configuration, band alignment, and valley spin*, *Science Advances* **5** (2019).

- [343] P. Merkl, F. Mooshammer, S. Brem, A. Girnghuber, K.-Q. Lin, L. Weigl, M. Liebich, C.-K. Yong, R. Gillen, J. Maultzsch, J. M. Lupton, E. Malic, and R. Huber, *Twist-tailoring Coulomb correlations in van der Waals homobilayers*, [Nature Communications](#) **11**, 1–7 (2020).
- [344] N. Zhang, A. Surrente, M. Baranowski, D. K. Maude, P. Gant, A. Castellanos-Gomez, and P. Plochocka, *Moiré intralayer excitons in a  $MoSe_2/MoS_2$  heterostructure*, [Nano Letters](#) **18**, 7651–7657 (2018).
- [345] E. M. Alexeev, D. A. Ruiz-Tijerina, M. Da1lich, M. J. Hamer, D. J. Terry, P. K. Nayak, S. Ahn, S. Pak, J. Lee, J. I. Sohn, M. R. Molas, M. Koperski, K. Watanabe, T. Taniguchi, K. S. Novoselov, R. V. Gorbachev, H. S. Shin, V. I. Fal’ko, and A. I. Tartakovskii, *Resonantly hybridized excitons in moiré superlattices in van der Waals heterostructures*, [Nature](#) **567**, 81–86 (2019).
- [346] C. Jin, E. C. Regan, A. Yan, M. I. B. Utama, D. Wang, S. Zhao, Y. Qin, S. Yang, Z. Zheng, S. Shi, K. Watanabe, T. Taniguchi, S. Tongay, A. Zettl, and F. Wang, *Observation of moiré excitons in  $WSe_2/WS_2$  heterostructure superlattices*, [Nature](#) **567**, 76–80 (2019).
- [347] C. Jin, E. C. Regan, D. Wang, M. I. B. Utama, C.-S. Yang, J. Cain, Y. Qin, Y. Shen, Z. Zheng, K. Watanabe, T. Taniguchi, S. Tongay, A. Zettl, and F. Wang, *Identification of spin, valley and moiré quasi-angular momentum of interlayer excitons*, [Nature Physics](#) **15**, 1140–1144 (2019).
- [348] K. Tran, G. Moody, F. Wu, X. Lu, J. Choi, K. Kim, A. Rai, D. A. Sanchez, J. Quan, A. Singh, J. Embley, A. Zepeda, M. Campbell, T. Autry, T. Taniguchi, K. Watanabe, N. Lu, S. K. Banerjee, K. L. Silverman, S. Kim, E. Tutuc, L. Yang, A. H. MacDonald, and X. Li, *Evidence for moiré excitons in van der Waals heterostructures*, [Nature](#) **567**, 71–75 (2019).
- [349] J. Choi, W.-T. Hsu, L.-S. Lu, L. Sun, H.-Y. Cheng, M.-H. Lee, J. Quan, K. Tran, C.-Y. Wang, M. Staab, K. Jones, T. Taniguchi, K. Watanabe, M.-W. Chu, S. Gwo, S. Kim, C.-K. Shih, X. Li, and W.-H. Chang, *Moiré potential impedes interlayer exciton diffusion in van der Waals heterostructures*, [Science Advances](#) **6**, eaba8866 (2020).
- [350] Y. Shimazaki, I. Schwartz, K. Watanabe, T. Taniguchi, M. Kroner, and A. Imamoğlu, *Strongly correlated electrons and hybrid excitons in a moiré heterostructure*, [Nature](#) **580**, 472–477 (2020).
- [351] M. Förg, A. S. Baimuratov, S. Y. Kruchinin, I. A. Vovk, J. Scherzer, J. Förste, V. Funk, K. Watanabe, T. Taniguchi, and A. Högele, *Moiré excitons in  $MoSe_2-wse_2$  heterobilayers and heterotrilayers*, [Nature Communications](#) **12**, 1–7 (2021).
- [352] T. I. Andersen, G. Scuri, A. Sushko, K. De Greve, J. Sung, Y. Zhou, D. S. Wild, R. J. Gelly, H. Heo, D. Bérubé, A. Y. Joe, L. A. Jauregui, K. Watanabe, T. Taniguchi, P. Kim, H. Park, and M. D. Lukin, *Excitons in a reconstructed moiré potential in twisted  $WSe_2/WSe_2$  homobilayers*, [Nature Materials](#) **20**, 480–487 (2021).
- [353] X. Lu, X. Li, and L. Yang, *Modulated interlayer exciton properties in a two-dimensional moiré crystal*, [Physical Review B](#) **100**, 155416 (2019).
- [354] J. Michl, C. C. Palekar, S. A. Tarasenko, F. Lohof, C. Gies, M. von Helversen, R. Sailus, S. Tongay, T. Taniguchi, K. Watanabe, T. Heindel, B. Rosa, M. Rödel, T. Shubina, S. Höfling, S. Reitzenstein, C. Anton-Solanas, and C. Schneider, *Intrinsic circularly polarized exciton emission in a twisted van der Waals heterostructure*, [Physical Review B](#) **105**, L241406 (2022).
- [355] E. Scellina, X. Liu, Z. Hu, A. Fieramosca, Y. Huang, W. Du, S. Liu, J. Zhao, K. Watanabe, T. Taniguchi, and Q. Xiong, *Evidence for moiré trions in twisted  $MoSe_2$  homobilayers*, [Nano Letters](#) (2021).
- [356] I. Bloch, *Ultracold quantum gases in optical lattices*, [Nature Physics](#) **1**, 23–30 (2005).
- [357] W. Wang and X. Ma, *Strain-induced trapping of indirect excitons in  $MoSe_2/WSe_2$  heterostructures*, [ACS Photonics](#) **7**, 2460–2467 (2020).
- [358] A. Tartakovskii, *Moiré or not*, [Nature Materials](#) **19**, 581–582 (2020).
- [359] M. Brotons-Gisbert, H. Baek, A. Molina-Sánchez, A. Campbell, E. Scerri, D. White, K. Watanabe, T. Taniguchi, C. Bonato, and B. D. Gerardot, *Spin-layer locking of interlayer excitons trapped in moiré potentials*, [Nature Materials](#) **19**, 630–636 (2020).
- [360] W. Li, X. Lu, S. Dubey, L. Devenica, and A. Srivastava, *Dipolar interactions between localized interlayer excitons in van der Waals heterostructures*, [Nature Materials](#) **19**, 624–629 (2020).
- [361] D. N. Shanks, F. Mahdikhanyarvejahany, C. Muccianti, A. Alfrey, M. R. Koehler, D. G. Mandrus, T. Taniguchi, K. Watanabe, H. Yu, B. J. LeRoy, and J. R. Schaibley, *Nanoscale trapping of interlayer excitons in a 2D semiconductor heterostructure*, [Nano Letters](#) **21**, 5641–5647 (2021).

- [362] J. Wang, Q. Shi, E.-M. Shih, L. Zhou, W. Wu, Y. Bai, D. Rhodes, K. Barmak, J. Hone, C. R. Dean, and X.-Y. Zhu, *Diffusivity Reveals Three Distinct Phases of Interlayer Excitons in  $\text{MoSe}_2/\text{WSe}_2$  Heterobilayers*, *Physical Review Letters* **126**, 106804 (2021).
- [363] M. Brotons-Gisbert, H. Baek, A. Campbell, K. Watanabe, T. Taniguchi, and B. D. Gerardot, *Moiré-Trapped Interlayer Trions in a Charge-Tunable  $\text{WSe}_2/\text{MoSe}_2$  Heterobilayer*, *Physical Review X* **11**, 031033 (2021).
- [364] H. Baek, M. Brotons-Gisbert, A. Campbell, V. Vitale, J. Lischner, K. Watanabe, T. Taniguchi, and B. D. Gerardot, *Optical read-out of Coulomb staircases in a moiré superlattice via trapped interlayer trions*, *Nature Nanotechnology* **16**, 1237–1243 (2021).
- [365] C.-X. Liu, *Unconventional superconductivity in bilayer transition metal dichalcogenides*, *Physical Review Letters* **118**, 087001 (2017).
- [366] Z. Wang, D. A. Rhodes, K. Watanabe, T. Taniguchi, J. C. Hone, J. Shan, and K. F. Mak, *Evidence of high-temperature exciton condensation in two-dimensional atomic double layers*, *Nature* **574**, 76–80 (2019).
- [367] Z. Bi and L. Fu, *Excitonic density wave and spin-valley superfluid in bilayer transition metal dichalcogenide*, *Nature Communications* **12**, 1–10 (2021).
- [368] E. C. Regan, D. Wang, C. Jin, M. I. B. Utama, B. Gao, X. Wei, S. Zhao, W. Zhao, Z. Zhang, K. Yumigeta, M. Blei, J. D. Carlström, K. Watanabe, T. Taniguchi, S. Tongay, M. Crommie, A. Zettl, and F. Wang, *Mott and generalized wigner crystal states in  $\text{WSe}_2/\text{WS}_2$  moiré superlattices*, *Nature* **579**, 359–363 (2020).
- [369] M. H. Naik and M. Jain, *Ultraflatbands and shear solitons in moiré patterns of twisted bilayer transition metal dichalcogenides*, *Physical Review Letters* **121**, 266401 (2018).
- [370] H. Pan, F. Wu, and S. D. Sarma, *Band topology, Hubbard model, Heisenberg model, and Dzyaloshinskii-Moriya interaction in twisted bilayer  $\text{WSe}_2$* , *Physical Review Research* **2**, 033087 (2020).
- [371] F. Wu, T. Lovorn, E. Tutuc, and A. H. MacDonald, *Hubbard Model Physics in Transition Metal Dichalcogenide Moiré Bands*, *Physical Review Letters* **121**, 026402 (2018).
- [372] F. Wu, T. Lovorn, E. Tutuc, I. Martin, and A. H. MacDonald, *Topological Insulators in Twisted Transition Metal Dichalcogenide Homobilayers*, *Physical Review Letters* **122**, 086402 (2019).
- [373] Y. Nakamura and Y. Yanase, *Odd-parity superconductivity in bilayer transition metal dichalcogenides*, *Physical Review B* **96**, 054501 (2017).
- [374] O. Zheliuk, J. Lu, Q. Chen, A. El Yumin, S. Golightly, and J. Ye, *Josephson coupled ising pairing induced in suspended  $\text{MoS}_2$  bilayers by double-side ionic gating*, *Nature Nanotechnology* **14**, 1123–1128 (2019).
- [375] D. Costanzo, S. Jo, H. Berger, and A. F. Morpurgo, *Gate-induced superconductivity in atomically thin  $\text{MoS}_2$  crystals*, *Nature Nanotechnology* **11**, 339–344 (2016).
- [376] J. Eisenstein and A. H. MacDonald, *Bose–einstein condensation of excitons in bilayer electron systems*, *Nature* **432**, 691–694 (2004).
- [377] M. Wurdack, E. Estrecho, S. Todd, T. Yun, M. Pieczarka, S. K. Earl, J. A. Davis, C. Schneider, A. G. Truscott, and E. A. Ostrovskaya, *Motional narrowing, ballistic transport, and trapping of room-temperature exciton polaritons in an atomically-thin semiconductor*, *Nature Communications* **12**, 5366 (2021).
- [378] S.-Y. Chen, M. Pieczarka, M. Wurdack, E. Estrecho, T. Taniguchi, K. Watanabe, J. Yan, E. A. Ostrovskaya, and M. S. Fuhrer, *Long-lived populations of momentum- and spin-indirect excitons in monolayer  $\text{WSe}_2$* , *arXiv:2103.11591* (2020).
- [379] F.-C. Wu, F. Xue, and A. MacDonald, *Theory of two-dimensional spatially indirect equilibrium exciton condensates*, *Physical Review B* **92**, 165121 (2015).
- [380] B. Debnath, Y. Barlas, D. Wickramaratne, M. R. Neupane, and R. K. Lake, *Exciton condensate in bilayer transition metal dichalcogenides: strong coupling regime*, *Physical Review B* **96**, 174504 (2017).
- [381] Y. E. Lozovik and V. Yudson, *A new mechanism for superconductivity: pairing between spatially separated electrons and holes*, *Soviet Journal of Experimental and Theoretical Physics* **71**, 738 (1976).
- [382] O. L. Berman and R. Y. Kezerashvili, *Superfluidity of dipolar excitons in a transition metal dichalcogenide double layer*, *Physical Review B* **96**, 094502 (2017).
- [383] D. Soriano and J. Lado, *Exchange-bias controlled correlations in magnetically encapsulated twisted van der Waals dichalcogenides*, *Journal of Physics D: Applied Physics* **53**, 474001 (2020).

- [384] Y. Cao, V. Fatemi, A. Demir, S. Fang, S. L. Tomarken, J. Y. Luo, J. D. Sanchez-Yamagishi, K. Watanabe, T. Taniguchi, E. Kaxiras, R. C. Ashoori, and P. Jarillo-Herrero, *Correlated insulator behaviour at half-filling in magic-angle graphene superlattices*, *Nature* **556**, 80–84 (2018).
- [385] S. Carr, S. Fang, Z. Zhu, and E. Kaxiras, *Exact continuum model for low-energy electronic states of twisted bilayer graphene*, *Physical Review Research* **1**, 013001 (2019).
- [386] L. Wang, E.-M. Shih, A. Ghiotto, L. Xian, D. A. Rhodes, C. Tan, M. Claassen, D. M. Kennes, Y. Bai, B. Kim, K. Watanabe, T. Taniguchi, X. Zhu, J. Hone, A. Rubio, A. Pasupathy, and C. R. Dean, *Magic continuum in twisted bilayer  $WSe_2$* , arXiv:1910.12147 (2019).
- [387] Z. Zhang, Y. Wang, K. Watanabe, T. Taniguchi, K. Ueno, E. Tutuc, and B. J. LeRoy, *Flat bands in twisted bilayer transition metal dichalcogenides*, *Nature Physics* **16**, 1093–1096 (2020).
- [388] L. Wang, E.-M. Shih, A. Ghiotto, L. Xian, D. A. Rhodes, C. Tan, M. Claassen, D. M. Kennes, Y. Bai, B. Kim, K. Watanabe, T. Taniguchi, X. Zhu, J. Hone, A. Rubio, A. N. Pasupathy, and C. R. Dean, *Correlated electronic phases in twisted bilayer transition metal dichalcogenides*, *Nature Materials*, 1–6 (2020).
- [389] S. Pavlović and F. M. Peeters, *Electronic properties of triangular and hexagonal  $MoS_2$  quantum dots*, *Physical Review B* **91**, 155410 (2015).
- [390] C. C. Price, N. C. Frey, D. Jariwala, and V. B. Shenoy, *Engineering Zero-Dimensional Quantum Confinement in Transition-Metal Dichalcogenide Heterostructures*, *ACS Nano* **13**, 8303–8311 (2019).
- [391] X.-X. Song, Z.-Z. Zhang, J. You, D. Liu, H.-O. Li, G. Cao, M. Xiao, and G.-P. Guo, *Temperature dependence of Coulomb oscillations in a few-layer two-dimensional  $WS_2$  quantum dot*, *Scientific Reports* **5**, 16113 (2015).
- [392] J. Pawłowski, *Spin-valley system in a gated  $MoS_2$ -monolayer quantum dot*, *New Journal of Physics* **21**, 123029 (2019).
- [393] L. Szulakowska, M. Cygorek, M. Bieniek, and P. Hawrylak, *Valley- and spin-polarized broken-symmetry states of interacting electrons in gated  $MoS_2$  quantum dots*, *Physical Review B* **102**, 245410 (2020).
- [394] A. Kormányos, V. Zólyomi, N. D. Drummond, and G. Burkard, *Spin-Orbit Coupling, Quantum Dots, and Qubits in Monolayer Transition Metal Dichalcogenides*, *Physical Review X* **4**, 011034 (2014).
- [395] M. Brooks and G. Burkard, *Spin-degenerate regimes for single quantum dots in transition metal dichalcogenide monolayers*, *Physical Review B* **95**, 245411 (2017).
- [396] R. Pisoni, Z. Lei, P. Back, M. Eich, H. Overweg, Y. Lee, K. Watanabe, T. Taniguchi, T. Ihn, and K. Ensslin, *Gate-tunable quantum dot in a high quality single layer  $MoS_2$  van der Waals heterostructure*, *Applied Physics Letters* **112**, 123101 (2018).
- [397] S. Bhandari, K. Wang, K. Watanabe, T. Taniguchi, P. Kim, and R. M. Westervelt, *Imaging quantum dot formation in  $MoS_2$  nanostructures*, *Nanotechnology* **29**, 42LT03 (2018).
- [398] J. Fouladi-Oskouei, S. Shojaei, and Z. Liu, *Robust tunable excitonic features in monolayer transition metal dichalcogenide quantum dots*, *Journal of Physics: Condensed Matter* **30**, 145301 (2018).
- [399] F. Qu, A. C. Dias, J. Fu, L. Villegas-Lelovsky, and D. L. Azevedo, *Tunable spin and valley dependent magneto-optical absorption in molybdenum disulfide quantum dots*, *Scientific Reports* **7**, 41044 (2017).
- [400] H. Eschrig, *The fundamentals of density functional theory*, *Springer* **32** (1996).
- [401] R. M. Martin and R. M. Martin, *Electronic structure: basic theory and practical methods*, *Cambridge university press* (2004).
- [402] R. M. Dreizler and E. K. Gross, *Density functional theory: an approach to the quantum many-body problem*, *Springer Science & Business Media* (2012).
- [403] P. Giannozzi, S. Baroni, N. Bonini, M. Calandra, R. Car, C. Cavazzoni, D. Ceresoli, G. L. Chiarotti, M. Cococcioni, I. Dabo, A. D. Corso, S. de Gironcoli, S. Fabris, G. Fratesi, R. Gebauer, U. Gerstmann, C. Gougousis, A. Kokalj, M. Lazzeri, L. Martin-Samos, N. Marzari, F. Mauri, R. Mazzarello, S. Paolini, A. Pasquarello, L. Paulatto, C. Sbraccia, S. Scandolo, G. Sclauzero, A. P. Seitsonen, A. Smogunov, P. Umari, and R. M. Wentzcovitch, *QUANTUM ESPRESSO: a modular and open-source software project for quantum simulations of materials*, *Journal of Physics: Condensed Matter* **21**, 395502 (2009).
- [404] P. Blaha, K. Schwarz, F. Tran, R. Laskowski, G. K. H. Madsen, and L. D. Marks, *WIEN2k: An APW+lo program for calculating the properties of solids*, *The Journal of Chemical Physics* **152**, 074101 (2020).
- [405] J. Hafner, *Ab-initio simulations of materials using VASP: Density-functional theory and beyond*, *Journal of Computational Chemistry* **29**, 2044–2078 (2008).

- [406] X. Gonze, J.-M. Beuken, R. Caracas, F. Detraux, M. Fuchs, G.-M. Rignanese, L. Sindic, M. Verstraete, G. Zerah, F. Jollet, M. Torrent, A. Roy, M. Mikami, P. Ghosez, J.-Y. Raty, and D. Allan, *First-principles computation of material properties: the ABINIT software project*, [Computational Materials Science](#) **25**, 478–492 (2002).
- [407] X. Gonze, B. Amadon, P.-M. Anglade, J.-M. Beuken, F. Bottin, P. Boulanger, F. Bruneval, D. Caliste, R. Caracas, M. Côté, T. Deutsch, L. Genovese, P. Ghosez, M. Giantomassi, S. Goedecker, D. Hamann, P. Hermet, F. Jollet, G. Jomard, S. Leroux, M. Mancini, S. Mazevet, M. Oliveira, G. Onida, Y. Pouillon, T. Rangel, G.-M. Rignanese, D. Sangalli, R. Shaltaf, M. Torrent, M. Verstraete, G. Zerah, and J. Zwanziger, *ABINIT: First-principles approach to material and nanosystem properties*, [Computer Physics Communications](#) **180**, 2582–2615 (2009).
- [408] X. Gonze, F. Jollet, F. A. Araujo, D. Adams, B. Amadon, T. Applencourt, C. Audouze, J.-M. Beuken, J. Bieder, A. Bokhanchuk, E. Bousquet, F. Bruneval, D. Caliste, M. Côté, F. Dahm, F. D. Pieve, M. Delaveau, M. D. Gennaro, B. Dorado, C. Espejo, G. Geneste, L. Genovese, A. Gerossier, M. Giantomassi, Y. Gillet, D. Hamann, L. He, G. Jomard, J. L. Janssen, S. L. Roux, A. Levitt, A. Lherbier, F. Liu, I. Lukačević, A. Martin, C. Martins, M. Oliveira, S. Poncé, Y. Pouillon, T. Rangel, G.-M. Rignanese, A. Romero, B. Rousseau, O. Rubel, A. Shukri, M. Stankovski, M. Torrent, M. V. Setten, B. V. Troeye, M. Verstraete, D. Waroquiers, J. Wiktor, B. Xu, A. Zhou, and J. Zwanziger, *Recent developments in the ABINIT software package*, [Computer Physics Communications](#) **205**, 106–131 (2016).
- [409] J. Kohanoff, *Electronic structure calculations for solids and molecules: theory and computational methods*, [Cambridge University Press](#) (2006).
- [410] M. J. Winiarski, *Badanie struktury elektronowej nadprzewodników zawierających atomy żelazowców*, (2013).
- [411] P. Hohenberg and W. Kohn, *Inhomogeneous Electron Gas*, [Physical Review](#) **136**, B864–B871 (1964).
- [412] W. Kohn and L. J. Sham, *Self-Consistent Equations Including Exchange and Correlation Effects*, [Physical Review](#) **140**, A1133–A1138 (1965).
- [413] D. Pines, *Elementary excitations in solids*, [CRC Press](#) (2018).
- [414] H. Hellmann, *A New Approximation Method in the Problem of Many Electrons*, [The Journal of Chemical Physics](#) **3**, 61–61 (1935).
- [415] J. C. Phillips and L. Kleinman, *New Method for Calculating Wave Functions in Crystals and Molecules*, [Physical Review Physical Review Materials](#) **116**, 287–294 (1959).
- [416] D. R. Hamann, M. Schlüter, and C. Chiang, *Norm-Conserving Pseudopotentials*, [Physical Review Letters](#) **43**, 1494–1497 (1979).
- [417] D. Vanderbilt, *Soft self-consistent pseudopotentials in a generalized eigenvalue formalism*, [Physical Review B](#) **41**, 7892–7895 (1990).
- [418] P. E. Blöchl, *Projector augmented-wave method*, [Physical Review B](#) **50**, 17953–17979 (1994).
- [419] G. Kresse and D. Joubert, *From ultrasoft pseudopotentials to the projector augmented-wave method*, [Physical Review B](#) **59**, 1758–1775 (1999).
- [420] J. P. Perdew, K. Burke, and M. Ernzerhof, *Generalized Gradient Approximation Made Simple*, [Physical Review Letters](#) **77**, 3865–3868 (1996).
- [421] V. I. Anisimov, J. Zaanen, and O. K. Andersen, *Band theory and Mott insulators: Hubbard  $U$  instead of Stoner  $I$* , [Physical Review B](#) **44**, 943–954 (1991).
- [422] A. I. Liechtenstein, V. I. Anisimov, and J. Zaanen, *Density-functional theory and strong interactions: Orbital ordering in Mott-Hubbard insulators*, [Physical Review B](#) **52**, R5467–R5470 (1995).
- [423] B. Himmetoglu, A. Floris, S. de Gironcoli, and M. Cococcioni, *Hubbard-corrected DFT energy functionals: The LDA+ $U$  description of correlated systems*, [International Journal of Quantum Chemistry](#) **114**, 14–49 (2014).
- [424] A. D. Becke, *Density-functional exchange-energy approximation with correct asymptotic behavior*, [Physical Review A](#) **38**, 3098–3100 (1988).
- [425] J. Heyd, G. E. Scuseria, and M. Ernzerhof, *Hybrid functionals based on a screened Coulomb potential*, [The Journal of Chemical Physics](#) **118**, 8207–8215 (2003).
- [426] E. Runge and E. K. U. Gross, *Density-Functional Theory for Time-Dependent Systems*, [Physical Review Letters](#) **52**, 997–1000 (1984).

- [427] J. D. Head and M. C. Zerner, *A Broyden—Fletcher—Goldfarb—Shanno optimization procedure for molecular geometries*, [Chemical Physics Letters](#) **122**, 264–270 (1985).
- [428] M. C. Payne, M. P. Teter, D. C. Allan, T. A. Arias, and J. D. Joannopoulos, *Iterative minimization techniques for ab initio total-energy calculations: molecular dynamics and conjugate gradients*, [Reviews of Modern Physics](#) **64**, 1045–1097 (1992).
- [429] G. Kresse and J. Furthmüller, *Efficient iterative schemes for ab initio total-energy calculations using a plane-wave basis set*, [Physical Review B](#) **54**, 11169–11186 (1996).
- [430] J. C. Slater, *Atomic Shielding Constants*, [Physical Review Physical Review Materials](#) **36**, 57–64 (1930).
- [431] Y. Saleem, *Electronic and Optical Properties of 2D Materials*, [Université d'Ottawa / University of Ottawa](#) (2023).
- [432] A. H. Castro Neto, F. Guinea, N. M. R. Peres, K. S. Novoselov, and A. K. Geim, *The electronic properties of graphene*, [Reviews of Modern Physics](#) **81**, 109–162 (2009).
- [433] X. Xu, W. Yao, D. Xiao, and T. F. Heinz, *Spin and pseudospins in layered transition metal dichalcogenides*, [Nature Physics](#) **10**, 343–350 (2014).
- [434] H. Zeng, J. Dai, W. Yao, D. Xiao, and X. Cui, *Valley polarization in MoS<sub>2</sub> monolayers by optical pumping*, [Nature Nanotechnology](#) **7**, 490–493 (2012).
- [435] L. Szulakowska, *Electron-electron interactions and optical properties of two-dimensional nanocrystals*, [Université d'Ottawa / University of Ottawa](#) (2020).
- [436] J. W. McClure, *Diamagnetism of Graphite*, [Physical Review Physical Review Materials](#) **104**, 666–671 (1956).
- [437] M. O. Goerbig, *Electronic properties of graphene in a strong magnetic field*, [Reviews of Modern Physics](#) **83**, 1193–1243 (2011).
- [438] O. L. de Lange and R. E. Raab, *Ladder operators for orbital angular momentum*, [American Journal of Physics](#) **54**, 372–375 (1986).
- [439] C. L. Kane and E. J. Mele, *Quantum spin hall effect in graphene*, [Physical Review Letters](#) **95**, 226801 (2005).
- [440] E. Anderson, Z. Bai, C. Bischof, S. Blackford, J. Demmel, J. Dongarra, J. Du Croz, A. Greenbaum, S. Hammarling, A. McKenney, and D. Sorensen, *LAPACK Users' Guide, Third Edition*, [Society for Industrial and Applied Mathematics](#) (1999).
- [441] P. Hawrylak, *Far infrared absorption by screened D-states in quantum wells in a strong magnetic field*, [Solid State Communications](#) **88**, 475–479 (1993).
- [442] S.-J. Cheng, W. Sheng, and P. Hawrylak, *Theory of excitonic artificial atoms: InGaAs/GaAs quantum dots in strong magnetic fields*, [Physical Review B](#) **68**, 235330 (2003).
- [443] S. Raymond, S. Studenikin, A. Sachrajda, Z. Wasilewski, S. J. Cheng, W. Sheng, P. Hawrylak, A. Babinski, M. Potemski, G. Ortner, and M. Bayer, *Excitonic Energy Shell Structure of Self-Assembled InGaAs/GaAs Quantum Dots*, [Physical Review Letters](#) **92**, 187402 (2004).
- [444] M. Korkusinski, *Correlations in semiconductor quantum dots*, [Université d'Ottawa / University of Ottawa](#) (2004).
- [445] D. Y. Qiu, F. H. da Jornada, and S. G. Louie, *Screening and many-body effects in two-dimensional crystals: monolayer MoS<sub>2</sub>*, [Physical Review B](#) **93**, 235435 (2016).
- [446] P. Cudazzo, I. V. Tokatly, and A. Rubio, *Dielectric screening in two-dimensional insulators: implications for excitonic and impurity states in graphene*, [Physical Review B](#) **84**, 085406 (2011).
- [447] N. S. Rytova, *Screened potential of a point charge in a thin film*, [Proc. MSU, Phys. Astron.](#) **3**, 30 (1967).
- [448] L. Keldysh, *Coulomb interaction in thin semiconductor and semimetal films*, [Soviet Journal of Experimental and Theoretical Physics Letters](#) **29**, 658 (1979).
- [449] S. Ovesen, S. Brem, C. Linderålv, M. Kuisma, T. Korn, P. Erhart, M. Selig, and E. Malic, *Interlayer exciton dynamics in van der Waals heterostructures*, [Communications Physics](#) **2**, 1–8 (2019).
- [450] K. Sadecka, *Inter- and Intralayer Excitonic Spectrum of MoSe<sub>2</sub>/WSe<sub>2</sub> Heterostructure*, [Acta Physica Polonica, A.](#) **141** (2022).
- [451] Y. Nambu, *Force potentials in quantum field theory*, [Progress of Theoretical Physics](#) **5**, 614–633 (1950).

- [452] E. E. Salpeter and H. A. Bethe, *A Relativistic Equation for Bound-State Problems*, [Physical Review](#) **84**, 1232–1242 (1951).
- [453] F. J. Dyson, *The S Matrix in Quantum Electrodynamics*, [Physical Review Physical Review Materials](#) **75**, 1736–1755 (1949).
- [454] J. Schwinger, *On the Green's functions of quantized fields. I*, [Proceedings of the National Academy of Sciences](#) **37**, 452–455 (1951).
- [455] L. Hedin, *New Method for Calculating the One-Particle Green's Function with Application to the Electron-Gas Problem*, [Physical Review Physical Review Materials](#) **139**, A796–A823 (1965).
- [456] F. Aryasetiawan and O. Gunnarsson, *The GW method*, [Reports on Progress in Physics](#) **61**, 237 (1998).
- [457] A. Marini, C. Hogan, M. Grüning, and D. Varsano, *Yambo: an ab initio tool for excited state calculations*, [Computer Physics Communications](#) **180**, 1392–1403 (2009).
- [458] J. Deslippe, G. Samsonidze, D. A. Strubbe, M. Jain, M. L. Cohen, and S. G. Louie, *BerkeleyGW: A massively parallel computer package for the calculation of the quasiparticle and optical properties of materials and nanostructures*, [Computer Physics Communications](#) **183**, 1269–1289 (2012).
- [459] P. Giannozzi, O. Andreussi, T. Brumme, O. Bunau, M. B. Nardelli, M. Calandra, R. Car, C. Cavazzoni, D. Ceresoli, M. Cococcioni, N. Colonna, I. Carnimeo, A. D. Corso, S. de Gironcoli, P. Delugas, R. A. DiStasio, A. Ferretti, A. Floris, G. Fratesi, G. Fugallo, R. Gebauer, U. Gerstmann, F. Giustino, T. Gorni, J. Jia, M. Kawamura, H.-Y. Ko, A. Kokalj, E. Küçükbenli, M. Lazzeri, M. Marsili, N. Marzari, F. Mauri, N. L. Nguyen, H.-V. Nguyen, A. Otero-de-la-Roza, L. Paulatto, S. Poncé, D. Rocca, R. Sabatini, B. Santra, M. Schlipf, A. P. Seitsonen, A. Smogunov, I. Timrov, T. Thonhauser, P. Umari, N. Vast, X. Wu, and S. Baroni, *Advanced capabilities for materials modelling with Quantum ESPRESSO*, [IOP Publishing](#) **29**, 465901 (2017).
- [460] D. Sangalli, A. Ferretti, H. Miranda, C. Attaccalite, I. 3ri, E. Cannuccia, P. Melo, M. Marsili, F. Paleari, A. Marrazzo, G. Prandini, P. Bonfà, M. O. Atambo, F. Affinito, M. Palummo, A. Molina-Sánchez, C. Hogan, M. Grüning, D. Varsano, and A. Marini, *Many-body perturbation theory calculations using the yambo code*, [Journal of Physics: Condensed Matter](#) **31**, 325902 (2019).
- [461] G. C. Wick, *The Evaluation of the Collision Matrix*, [Physical Review Physical Review Materials](#) **80**, 268–272 (1950).
- [462] J. C. Ward, *An Identity in Quantum Electrodynamics*, [Physical Review Physical Review Materials](#) **78**, 182–182 (1950).
- [463] L. Szulakowska, M. Bieniek, and P. Hawrylak, *Electronic structure, magnetoexcitons and valley polarized electron gas in 2D crystals*, [Solid-State Electronics](#) **155**, 105–110 (2019).
- [464] C. R. Dean, A. F. Young, I. Meric, C. Lee, L. Wang, S. Sorgenfrei, K. Watanabe, T. Taniguchi, P. Kim, K. L. Shepard, and J. Hone, *Boron nitride substrates for high-quality graphene electronics*, [Nature Nanotechnology](#) **5**, 722–726 (2010).
- [465] M. Bayer, G. Ortner, O. Stern, A. Kuther, A. A. Gorbu11, A. Forchel, P. Hawrylak, S. Fafard, K. Hinzer, T. L. Reinecke, S. N. Walck, J. P. Reithmaier, F. Klopff, and F. Schäfer, *Fine structure of neutral and charged excitons in self-assembled In(Ga)As/(Al)GaAs quantum dots*, [Physical Review B](#) **65**, 195315 (2002).
- [466] B. J. Wittek, R. W. Heeres, U. Perinetti, E. P. A. M. Bakkers, L. P. Kouwenhoven, and V. Zwiller, *Measurement of the g-factor tensor in a quantum dot and disentanglement of exciton spins*, [Physical Review B](#) **84**, 195305 (2011).
- [467] M. Ediger, G. Bester, A. Badolato, P. M. Petroff, K. Karrai, A. Zunger, and R. J. Warburton, *Peculiar many-body effects revealed in the spectroscopy of highly charged quantum dots*, [Nature Physics](#) **3**, 774–779 (2007).
- [468] G. A. Narvaez, G. Bester, and A. Zunger, *Excitons, biexcitons, and trions in self-assembled (In,Ga)As/GaAs quantum dots: Recombination energies, polarization, and radiative lifetimes versus dot height*, [Physical Review B](#) **72**, 245318 (2005).
- [469] A. Torche and G. Bester, *First-principles many-body theory for charged and neutral excitations: Trion fine structure splitting in transition metal dichalcogenides*, [Physical Review B](#) **100**, 201403 (2019).
- [470] A. Chafai, I. Essaoudi, A. Ainane, and C. Duque, *Insight into negative trions binding energy behavior inside type-I and reversed type-I core/shell quantum dots: A variational analysis*, [OAJ Materials and Devices](#) **7** (2023).

- [471] P. Hawrylak, *Optical properties of a two-dimensional electron gas: Evolution of spectra from excitons to Fermi-edge singularities*, *Physical Review B* **44**, 3821–3828 (1991).
- [472] P. Hawrylak and M. Potemski, *Theory of photoluminescence from an interacting two-dimensional electron gas in strong magnetic fields*, *Physical Review B* **56**, 12386–12394 (1997).
- [473] J. Klein, A. Hötger, M. Florian, A. Steinhoff, A. Delhomme, T. Taniguchi, K. Watanabe, F. Jahnke, A. W. Holleitner, M. Potemski, C. FAuger, J. J. Finley, and A. V. Stier, *Controlling exciton many-body states by the electric-field effect in monolayer MoS<sub>2</sub>*, *Physical Review Research* **3**, L022009 (2021).
- [474] J. Klein, M. Florian, A. Hötger, A. Steinhoff, A. Delhomme, T. Taniguchi, K. Watanabe, F. Jahnke, A. W. Holleitner, M. Potemski, C. FAuger, A. V. Stier, and J. J. Finley, *Trions in MoS<sub>2</sub> are quantum superpositions of intra- and intervalley spin states*, *Physical Review B* **105**, L041302 (2022).
- [475] K. Oreszczuk, A. Rodek, M. Goryca, T. Kazimierczuk, M. Raczyński, J. Howarth, T. Taniguchi, K. Watanabe, M. Potemski, and P. Kossacki, *Enhancement of electron magnetic susceptibility due to many-body interactions in monolayer MoSe<sub>2</sub>*, *2D Materials* **10**, 045019 (2023).
- [476] S. Grimme, J. Antony, S. Ehrlich, and H. Krieg, *A consistent and accurate ab initio parametrization of density functional dispersion correction (DFT-D) for the 94 elements H-Pu*, *The Journal of Chemical Physics* **132**, 154104 (2010).
- [477] B. Bradlyn, J. Cano, Z. Wang, M. Vergniory, C. Felser, R. J. Cava, and B. A. Bernevig, *Beyond Dirac and Weyl fermions: Unconventional quasiparticles in conventional crystals*, *Science* **353** (2016).
- [478] M. Bayer, G. Ortner, O. Stern, A. Kuther, A. A. Gorbunov, A. Forchel, P. Hawrylak, S. Fafard, K. Hinzer, T. L. Reinecke, S. N. Walck, J. P. Reithmaier, F. Klopf, and F. Schäfer, *Fine structure of neutral and charged excitons in self-assembled In(Ga)As/(Al)GaAs quantum dots*, *Physical Review B* **65**, 195315 (2002).
- [479] A. H. Trojnar, E. S. Kadantsev, M. Korkusiński, and P. Hawrylak, *Theory of fine structure of correlated exciton states in self-assembled semiconductor quantum dots in a magnetic field*, *Physical Review B* **84**, 245314 (2011).
- [480] A. Srivastava and A. ç. Imamo ğlu, *Signatures of Bloch-Band Geometry on Excitons: Nonhydrogenic Spectra in Transition-Metal Dichalcogenides*, *Physical Review Letters* **115**, 166802 (2015).
- [481] S. Gao, L. Yang, and C. D. Spataru, *Interlayer coupling and gate-tunable excitons in transition metal dichalcogenide heterostructures*, *Nano Letters* **17**, 7809–7813 (2017).
- [482] G.-B. Liu, W.-Y. Shan, Y. Yao, W. Yao, and D. Xiao, *Three-band tight-binding model for monolayers of group-VIB transition metal dichalcogenides*, *Physical Review B* **88**, 085433 (2013).
- [483] A. Altıntaş, M. Bieniek, A. Dusko, M. Korkusiński, J. Pawłowski, and P. Hawrylak, *Spin-valley qubits in gated quantum dots in a single layer of transition metal dichalcogenides*, *Physical Review B* **104**, 195412 (2021).
- [484] J. Pawłowski, D. Żebrowski, and S. Bednarek, *Valley qubit in a gated MoS<sub>2</sub> monolayer quantum dot*, *Physical Review B* **97**, 155412 (2018).
- [485] J. Pawłowski, J. E. Tiessen, R. Dax, and J. Shi, *Electrical manipulation of valley qubit and valley geometric phase in lateral monolayer heterostructures*, *Physical Review B* **109**, 045411 (2024).
- [486] A. Y. Joe, K. Pistunova, K. Kaasbjerg, K. Wang, B. Kim, D. A. Rhodes, T. Taniguchi, K. Watanabe, J. Hone, T. Low, L. A. Jauregui, and P. Kim, *Transport Study of Charge-Carrier Scattering in Monolayer WSe<sub>2</sub>*, *Physical Review Letters* **132**, 056303 (2024).
- [487] M. Bieniek, L. Szulakowska, and P. Hawrylak, *Effect of valley, spin, and band nesting on the electronic properties of gated quantum dots in a single layer of transition metal dichalcogenides*, *Physical Review B* **101**, 035401 (2020).
- [488] M. B. Plenio, V. Vedral, and P. L. Knight, *Quantum error correction in the presence of spontaneous emission*, *Physical Review A* **55**, 67–71 (1997).
- [489] J. Wilson and A. Yoffe, *The transition metal dichalcogenides discussion and interpretation of the observed optical, electrical and structural properties*, *Advances in Physics* **18**, 193–335 (1969).
- [490] C. Qian, M. Troue, J. Figueiredo, P. Soubelet, V. Villafañe, J. Beierlein, S. Klemmt, A. V. Stier, S. Höfling, A. W. Holleitner, and J. J. Finley, *Lasing of moiré trapped MoSe<sub>2</sub>/WSe<sub>2</sub> interlayer excitons coupled to a nanocavity*, *Science Advances* **10**, eadk6359 (2024).

- [491] V. Vitale, K. Atalar, A. A. Mostofi, and J. Lischner, *Flat band properties of twisted transition metal dichalcogenide homo- and heterobilayers of  $MoS_2$ ,  $MoSe_2$ ,  $WS_2$  and  $WSe_2$* , *2D Materials* **8**, 045010 (2021).
- [492] J. C. Slater and G. F. Koster, *Simplified LCAO Method for the Periodic Potential Problem*, *Physical Review* **94**, 1498–1524 (1954).
- [493] M. Bieniek, M. Korkusiński, L. Szulakowska, P. Potasz, I. Ozfidan, and P. Hawrylak, *Band nesting, massive Dirac fermions, and valley Landé and Zeeman effects in transition metal dichalcogenides: A tight-binding model*, *Physical Review B* **97**, 085153 (2018).
- [494] K. V. Price, R. M. Storn, and J. A. Lampinen, *Differential Evolution: A Practical Approach to Global Optimization*, Springer, 37–134 (2005).
- [495] P. E. Faria Junior and J. Fabian, *Signatures of Electric Field and Layer Separation Effects on the Spin-Valley Physics of  $MoSe_2/WSe_2$  Heterobilayers: From Energy Bands to Dipolar Excitons*, *Nanomaterials* **13** (2023).
- [496] L. Szulakowska, M. Cygorek, M. Bieniek, and P. Hawrylak, *Valley-and spin-polarized broken-symmetry states of interacting electrons in gated  $MoS_2$  quantum dots*, *Physical Review B* **102**, 245410 (2020).
- [497] A. Varlet, D. Bischoff, P. Simonet, K. Watanabe, T. Taniguchi, T. Ihn, K. Ensslin, M. Mucha-Kruczyński, and V. I. Fal’ko, *Anomalous Sequence of Quantum Hall Liquids Revealing a Tunable Lifshitz Transition in Bilayer Graphene*, *Physical Review Letters* **113**, 116602 (2014).
- [498] H. Overweg, A. Knothe, T. Fabian, L. Linhart, P. Rickhaus, L. Wernli, K. Watanabe, T. Taniguchi, D. Sánchez, J. Burgdörfer, F. Libisch, V. I. Fal’ko, K. Ensslin, and T. Ihn, *Topologically Nontrivial Valley States in Bilayer Graphene Quantum Point Contacts*, *Physical Review Letters* **121**, 257702 (2018).
- [499] R. Garreis, A. Knothe, C. Tong, M. Eich, C. Gold, K. Watanabe, T. Taniguchi, V. Fal’ko, T. Ihn, K. Ensslin, and A. Kurzmann, *Shell Filling and Trigonal Warping in Graphene Quantum Dots*, *Physical Review Letters* **126**, 147703 (2021).
- [500] A. M. Seiler, N. Jacobsen, M. Statz, N. Fernandez, F. Falorsi, K. Watanabe, T. Taniguchi, Z. Dong, L. S. Levitov, and R. T. Weitz, *Probing the tunable multi-cone band structure in Bernal bilayer graphene*, *Nature Communications* **15**, 3133 (2024).
- [501] D. Miravet, A. Altıntaş, A. W. Rodrigues, M. Bieniek, M. Korkusinski, and P. Hawrylak, *Interacting holes in gated  $WSe_2$  quantum dots*, *Physical Review B* **108**, 195407 (2023).
- [502] J. Pawłowski, D. Miravet, M. Bieniek, M. Korkusinski, J. Boddison-Chouinard, L. Gaudreau, A. Luican-5er, and P. Hawrylak, *Interacting holes in a gated  $WSe_2$  quantum channel: Valley correlations and zigzag Wigner crystal*, *Physical Review B* **110**, 125147 (2024).
- [503] D. Miravet, L. Szulakowska, M. Bieniek, K. Sadecka, M. Korkusiński, and P. Hawrylak, *Theory of excitonic complexes in gated  $WSe_2$  quantum dots*, *Physical Review B* **110**, 235404 (2024).
- [504] J. Jadcak, J. Kutrowska-Girzycka, M. Bieniek, T. Kazimierczuk, P. Kossacki, J. J. Schindler, J. Debus, K. Watanabe, T. Taniguchi, C. H. Ho, A. Wójs, P. Hawrylak, and L. Bryja, *Probing negatively charged and neutral excitons in  $MoS_2/hBN$  and  $hBN/MoS_2/hBN$  van der Waals heterostructures*, *Nanotechnology* **32**, 145717 (2021).
- [505] J. Pawłowski, M. Bieniek, and T. Wozniak, *Valley Two-Qubit System in a  $MoS_2$ -Monolayer Gated Double Quantum Dot*, *Physical Review Applied* **15**, 054025 (2021).